Study to Address Sedimentation and Erosion Impacting Infrastructure on the Southern Jicarilla Apache Nation, New Mexico

Kevin M. Hobbs, Andrew P. Jochems, Faustin N. Kumah, Phil L. Miller, Navid Mojtabai, Kristin S. Pearthree, Mehrdad Razavi, and Clinton P. Richardson

OPEN-FILE REPORT

Study to Address Sedimentation and Erosion Impacting Infrastructure on the Southern Jicarilla Apache Nation, New Mexico

Kevin M. Hobbs[1], Andrew P. Jochems[1], Faustin N. Kumah[2], Phil L. Miller[1], Navid Mojtabai[2], Kristin S. Pearthree[1], Mehrdad Razavi[2], and Clinton P. Richardson[3]

[1]New Mexico Bureau of Geology and Mineral Resources

[2]Department of Mineral Engineering, New Mexico Institute of Mining and Technology

[3]Department of Civil and Environmental Engineering, New Mexico Institute of Mining and Technology

Open-File Report 620—Study to Address Sedimentation and Erosion Impacting Infrastructure on the Southern Jicarilla Apache Nation, New Mexico

Kevin M. Hobbs, Andrew P. Jochems, Faustin N. Kumah, Phil L. Miller, Navid Mojtabai, Kristin S. Pearthree, Mehrdad Razavi, and Clinton P. Richardson

Cover Photo: Hoodoo of San Jose Formation sandstone on a pedestal of mudstone in an eroding piñon-juniper woodland landscape of the Jicarilla Apache Nation.
Photo by Kevin M. Hobbs

CONTENTS

Figures

Tables

UNIT ABBREVIATIONS

ft	foot, feet
m	meter, meters
cm	centimeter, centimeters
acre-ft	acre-feet
ha	hectare
cfs	cubic feet per second
C	Celsius
F	Fahrenheit
s	second
hr	hour
yr	year
Ma	mega-annum (i.e., millions of years before the present)
ka	kilo-annum (i.e., thousands of years before the present)
YBP	years before present
GIS	geographic information system
UAV	uncrewed aerial vehicle, also known as a "drone"
JAN	Jicarilla Apache Nation
NMBGMR	New Mexico Bureau of Geology and Mineral Resources
NMT	New Mexico Tech
SJB	San Juan Basin
USGS	U.S. Geological Survey

EXECUTIVE SUMMARY

This report gives a detailed treatment of the geologic, hydrologic, and engineering factors affecting erosion and sedimentation in the upper Cañon Largo watershed on the southern Jicarilla Apache Nation, New Mexico. We summarize previous studies of geology and hydrology and provide new detail on stream dynamics, sediment transport, and rates of erosion and sedimentation. Two new maps[1] are complements to and were produced concurrently with this report: the *Geologic Map of the Cañon Largo Watershed on the Jicarilla Apache Nation, Rio Arriba and Sandoval Counties, New Mexico,* which presents detailed surficial geologic mapping and descriptions at the 1:50,000 scale, and the *Erosion and Sedimentation Hazard Map of the Cañon Largo Watershed on the Jicarilla Apache Nation, Rio Arriba and Sandoval Counties, New Mexico,* which displays the computed level of risks associated with the potential for an erosion or sedimentation event, also at the 1:50,000 scale. Each of these maps has its own associated report.

The Cañon Largo watershed is a major ephemeral tributary to the San Juan River and drains the majority of the southern Jicarilla Apache Nation. The watershed also includes portions of the Navajo Nation, the Santa Fe and Carson National Forests, New Mexico State Trust lands, Bureau of Land Management lands, and private property. Its headwaters lie on the Continental Divide on and upstream of the Jicarilla Apache Nation, and it flows for approximately 100 km (62 mi) to the northwest toward the San Juan River, which it joins at Blanco, New Mexico. The watershed occupies portions of the central and eastern San Juan Basin at elevations of approximately 1,700 m (5,600 ft) to 2,500 m (8,200 ft). There are over 8,000 operating oil and gas wells in the watershed as of this writing.

All streams in the watershed are dry for the majority of any year. Episodes of streamflow can occur after any precipitation event, but are most common during the summer monsoon season and during snowmelt events in late winter. Though they are uncommon, medium- and high-magnitude streamflow events affect landscapes in the watershed through the erosive processes of incision, headcutting, lateral migration of cutbanks, rilling, and soil piping, as well as through the process of sedimentation in streambeds, alluvial fans, and broad flats. These processes can also have significant and deleterious effects on the human infrastructure in the watershed, including erosion of roads and fences, undercutting of pipelines, restriction of vehicle access, and burial of rights-of-way, highways, cattleguards, and fences under sediment. A desire for increased knowledge of the causes, rates, and remedies of these effects on infrastructure led the Jicarilla Apache Nation Oil and Gas Administration to fund this study.

The Cañon Largo watershed is in an episode of overall erosion; that is, most streams in the watershed are transporting more sediment out of the watershed than they are depositing in the watershed. The effects of this erosion include lowering of streambeds through incision, widening of arroyos through lateral migration of cutbanks, and regolith loss on upland slopes. Causes of erosion are difficult to ascertain, but likely include long-term increases in stream power related to changes in climate and/or vegetation composition and density, improper infrastructure construction and/or maintenance practices, or some combination of these two. The current erosion cycle in the Cañon Largo watershed is not

[1]Maps are available for download at https://geoinfo.nmt.edu/publications/openfile/details.cfml?Volume=620

unique among similar watersheds in the southwestern United States; in the late nineteenth century, many such systems began major incision, which continues today. Until the Cañon Largo watershed reaches a new equilibrium of stream power, gradient, sediment supply, and climate conditions, the effects of erosion on the landscapes and infrastructure of the area are likely to increase in both magnitude and geographic extent. Watershed-scale erosion in the Cañon Largo watershed is unlikely to be remedied through human intervention. Engineering practices instead can focus on protecting specific points of infrastructure, adapting existing infrastructure to anticipated erosion, and making informed decisions about the type and location of future infrastructure before construction.

Even while the Cañon Largo watershed is in a decades-long erosive episode, there are particular locations within it that are undergoing sedimentation. The sediment supply in the watershed is mostly being transported out of the study area; however, in certain localities, it is being deposited. Some deposition occurs in alluvial fans and arroyo beds through non-anthropogenic processes. The deposition that affects infrastructure, however, occurs mostly at or upstream of human impediments to streamflow, including culverts, well pads, and places where roads cross streams at grade. Sedimentation at such locations is often preventable through engineering practices.

Raindrop impressions and mud cracks in alluvium of Medio Canyon, Jicarilla Apache Nation. *Photo by Kevin M. Hobbs*

I. INTRODUCTION

Kevin M. Hobbs

This report is a result of the Study to Address Sedimentation and Erosion Impacting Infrastructure on the Southern Jicarilla Apache Nation, New Mexico, conducted by the New Mexico Bureau of Geology and Mineral Resources (NMBGMR) under contract to the Jicarilla Apache Nation. The information presented here first gives a detailed treatment of the geologic and hydrologic products and processes of the study area as they pertain to erosion and sedimentation, and second recommends engineering and construction best practices for addressing the effects of erosion and sedimentation on the area's infrastructure. In addition, this report includes a background on the study area's topography, geography, vegetation, hydrology, and climate.

GEOGRAPHIC AND TOPOGRAPHIC SETTING

The Cañon Largo watershed is located in San Juan, Rio Arriba, and Sandoval Counties, New Mexico (Fig. 1.1), and is a major ephemeral tributary to the San Juan River. The watershed is bound on the west by a topographic divide extending from Harris Mesa to Huerfano Mountain, separating it from smaller tributaries to the San Juan River such as Muñoz Canyon, Armenta Canyon, Kutz Arroyo, and Gallegos Canyon. It is bound on the southwest by Sisnathyel Mesa, a topographic divide separating it from southwest-flowing tributaries to the Chaco River, itself a tributary to the San Juan River. The watershed is bound on the south and east by the Continental Divide, separating it from tributaries to the Rio Chama and Rio Puerco, themselves tributaries to the Rio Grande. It is bound on the north by a topographic divide extending from Manzanares Mesa in the west to the Continental Divide in the headwaters of Burro Canyon; this divide separates it from Gobernador and La Jara Canyons, themselves

tributaries to the San Juan River's impoundment at Navajo Lake. Elevations in the watershed range from approximately 1,690 m (5,540 ft) at the confluence of the San Juan River and Cañon Largo to approximately 2,490 m (8,150 ft) on the Continental Divide at the head of Tapicito Creek. The longest streamflow path in the watershed is approximately 110 km (69 mi), and the watershed is roughly 95 km (59 mi) long by 62 km (38 mi) wide at its greatest dimensions. The Cañon Largo watershed is designated by the U.S. Geological Survey (USGS) with the hydrologic unit code (HUC) of 14080103 and has a surface extent of 4,439 km^2 (1,714 mi^2 = 443,924 ha). The watershed occupies the central and eastern portions of the San Juan Basin, a geologic structural basin. Essentially all bedrock in the watershed comprises Paleogene-aged sedimentary rocks of the Nacimiento and San Jose Formations. Quaternary-aged alluvial and eolian surficial sedimentary units cover considerable portions of the watershed.

Ranching and hydrocarbon extraction form the basis of the regional economy. Except for the San Juan River, there is no natural perennial surface water in the watershed. Because of this, groundwater is a heavily utilized resource in the area. Oil and gas extraction in the watershed began in the 1940s, intensified in the 1970s and 1980s, and continues into the 2020s. According to New Mexico Oil Conservation Division data, there are 10,953 oil and gas wells in the watershed, 8,034 of which are active as of November 2022. Average well density in the watershed is 2.5/km^2 (6.4/mi^2). Hydrocarbon development in the area continues as unconventional gas reservoirs in the Mancos Shale are exploited. The roads, pipelines, and pads built and used for the hydrocarbon industry in the watershed make up the vast majority of infrastructure in the region; stock ponds and county- and state-maintained roads make up a smaller proportion of total infrastructure.
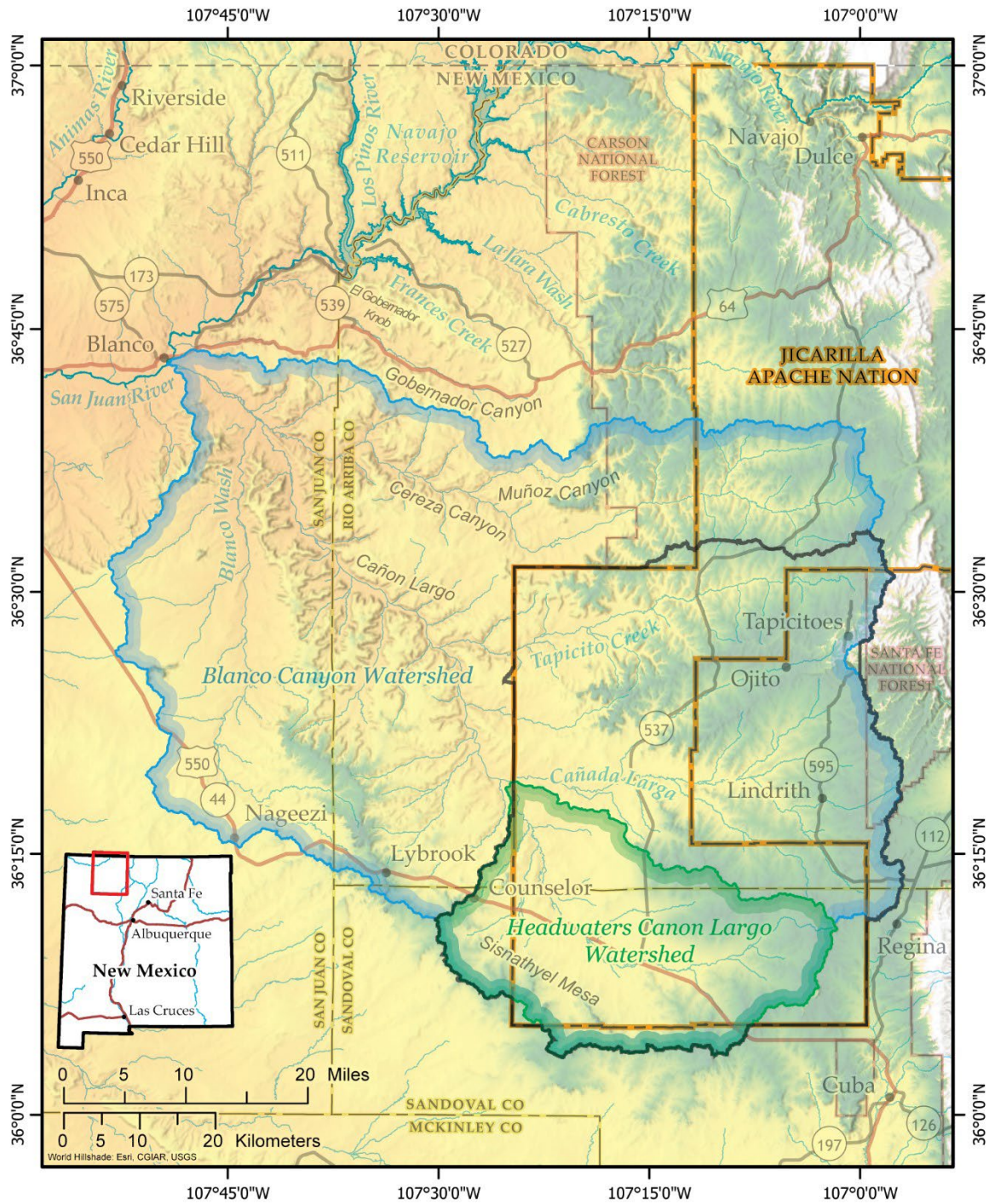
Figure 1.1. Map showing the outline of the Cañon Largo watershed (blue outline), the southern Jicarilla Apache Nation (orange outline), and the extent of the study area (black outline).

Human populations within the Cañon Largo watershed are small and in low densities. There are two population centers within the watershed: Counselor (population about 500) and Lindrith (population about 200). Other residents of the watershed occupy widely dispersed ranches and homesteads. The majority of the watershed comprises lands administered by the U.S. Bureau of Land Management, but significant portions of the watershed also comprise lands of the Jicarilla Apache Nation, the Navajo Nation, the Santa Fe and Carson National Forests, the State of New Mexico, and private landowners. This study focused on the portions of the watershed within or upstream of the southern Jicarilla Apache Nation Reservation, which includes upper Cañon Largo and its tributaries Tancosa Wash, Cañada Larga, and Tapicito Creek.

Landforms in the Cañon Largo watershed include sandstone mesas ranging in height from 40 to 300 m (130–1,000 ft) above surrounding valleys, sand-bed arroyos, high-elevation grass- and shrub-dominated plains, mudstone badlands, and broad valley bottoms. Large areas of uplands in the watershed contain stabilized eolian sand sheets that make up kilometers-wide plains of little topographic relief, especially in the west near Huerfano Mountain and in upper Cañon Largo on the southern Jicarilla Apache Nation near the intersection of U.S. Highway 550 and New Mexico Highway 537.

VEGETATION

Vegetation in the watershed comprises five U.S. Environmental Protection Agency Level IV Ecoregions: 20c (Semiarid Benchlands and Tablelands), 21d (Foothill Woodlands and Shrublands), 21f (Sedimentary Mid-Elevation Forests), 22i (San Juan/Chaco Tablelands and Mesas), and 22n (Near-Rockies Valleys and Mesas; Griffith et al., 2006). Plant communities in the watershed vary based on elevation, substrate composition, and aspect. In general, grasses and shrubs dominate in the watershed's lower elevations, while ponderosa pine (*Pinus ponderosa*) and Douglas-fir (*Pseudotsuga menziesii*) are relegated to the watershed's higher elevations. Junipers (*Juniperus monosperma* and *J. scopulorum*) and piñon (*Pinus edulis*) make up woodlands where sandy soils with shallow bedrock dominate in the watershed's middle elevations. Gambel oak (*Quercus gambelii*) is less common

than piñon or juniper but is found throughout the watershed, particularly at the base of sandstone cliffs and on thin soil among piñon-juniper and ponderosa pine woodlands. Unconsolidated sedimentary units, such as alluvium and eolian deposits, typically support shrub- and grass-dominated plant communities at all elevations in the watershed. Small bedrock outcrops surrounded by tree-free alluvium are often marked by junipers or piñon. Big sagebrush (*Artemisia tridentata*), snakeweed (*Gutierrezia sarothrae*), four-wing saltbush (*Atriplex canescens*), and chamisa (*Ericameria nauseosa*) are perhaps the most common flora throughout the watershed and can be found at essentially every elevation and aspect. North and east aspects typically support more woodlands and forests than do south and west aspects at the same elevation. Riparian woody vegetation, mostly comprising cottonwood (*Populus deltoides*) and saltcedar (*Tamarix ramosissima*) with minor willow (*Salix* spp.*,* primarily *S. exigua*), is confined to the floors of large arroyos and near bedrock springs and seeps.

HYDROLOGY

The hydrology of the Cañon Largo watershed is relatively unstudied for a watershed of its size. What little quantitative data exist are derived from a USGS gaging station approximately 7 km (4 mi) up Cañon Largo from its confluence with the San Juan River. This gaging station (given the designation "USGS 09356565 CANYON LARGO NR BLANCO, NM") was at an elevation of 1,720 m (5,640 ft) where San Juan County Road 4450 crosses Cañon Largo on a steel truss bridge. This gaging station was active from October 1978 through October 1981, collecting daily measurements for a total of 1,466 days. On 690 of those days, there was no observed streamflow. On 305 of the total 1,466 observation days, the observed average discharge was greater than 0 but less than 0.003 m³/s (0.1 ft³/s). Observed discharge exceeded 0.03 m³/s (1 ft³/s) on 247 of the total 1,466 observation days. There were 224 days when streamflow was greater than 0.003 m³/s but less than 0.03 m³/s. On the 776 days with observed streamflow, average discharge was 0.91 m³/s (32 ft³/s), whereas median discharge was 0.001 m³/s (0.23 ft³/s). Of the highest 10% (n = 78) of average daily discharge events at the gaging station, 43 occurred during the months of February or March, whereas only 18 occurred during the monsoon months of July,

August, and September, suggesting that snowmelt runoff can be a significant contributor to streamflow in Cañon Largo. It should be noted that these data only represent three years, and that year-to-year variations in timing and amount of streamflow in arid-region streams can be impacted profoundly by individual storm events.

CLIMATE

The watershed's climate is cold semiarid. Given the relatively low relief and location within the central San Juan Basin, there is only a slight orographic precipitation effect within the watershed, which receives a mean annual precipitation of 33 cm (13 in.) at Navajo Dam (10 km [6 mi] north of the watershed at an elevation of 1,760 m [5,770 ft]; period of record 1963–2016) and 37 cm (14.5 in.) at Lindrith (within the watershed at an elevation of 2,240 m [7,350 ft]; period of record 1971–2016). Climate records at the aforementioned sites are obtained from weather stations taking daily measurements over the periods of record and summarized by the Western Regional Climate Center of the National Oceanic and Atmospheric Administration. At Navajo Dam, near the watershed's outlet, the average July high and low temperatures are 33°C (91°F) and 16°C (60°F), respectively; average January high and low temperature are 4°C (40°F) and -7°C (19°F), respectively. Monsoon precipitation in July, August, and September accounts for 32% of the average annual precipitation at Navajo Dam. Navajo Dam receives an annual average of 31 cm (12 in.) of snowfall. At Lindrith, near the watershed's headwaters, the average July high and low temperatures are 30°C (86°F) and 11°C (52°F), respectively; average January high and low temperature are 5°C (41°F) and -11°C (12°F), respectively. Monsoon precipitation in July, August, and September accounts for 39% of the average annual precipitation at Lindrith. Lindrith receives an annual average of 152 cm (60 in.) of snowfall.

II. METHODS

Kevin M. Hobbs

Detailed methods for specific analyses and calculations are described in each following chapter. What follows here is a general description of study-wide methodology applicable to more than one objective, analysis, or calculation of the study.

FIELD METHODS

All field work was undertaken in 2021 and 2022. Geologic mapping methodology is detailed in the report to the *Geologic Map of the Cañon Largo Watershed on the Jicarilla Apache Nation, Rio Arriba and Sandoval Counties, New Mexico*, but followed the methods of Compton (1962) and Lisle et al. (2011). All field visits to the Jicarilla Apache Nation were completed with an appropriate and current work permit acquired from the Jicarilla Apache Nation Department of Labor. Field visits to surrounding areas of the watershed under the administration of the U.S. Forest Service, the U.S. Bureau of Land Management, or private citizen landowners were conducted under proper procedures for each field site and its pertinent managing agency and/or owner. Materials collected during field visits to the Jicarilla Apache Nation include sediment-hosted charcoal for radiometric age analysis and sediment samples from selected sites for geotechnical analyses. All collected materials underwent destructive analyses and therefore were not returned to their collection sites. The total amount of collected material was less than 10 kg (22 lbs). All quantitative measurements collected in the field were measured in metric units. Survey data were collected with a Trimble CenterPoint RTX GPS with Trimble Netr9 reference receiver and Zephyr Model 2 antenna. Non-survey coordinates were collected with a Garmin GPSMAP 62 handheld GPS. Aerial imagery was collected with a DJI Phantom 4 Pro uncrewed aerial vehicle (UAV).

Specific study sites (A, B, and C) were selected on the basis of field visits with JAN Oil and Gas Administration representatives (Fig. 2.1). These sites were selected on the basis of observed erosion and/or sedimentation threats to existing infrastructure.

GEOSPATIAL ANALYTICAL METHODS

Geospatial analyses were conducted with ArcGIS Pro, ArcMap 10.8.1, and ArcMap Drone2Map software. All GIS data were collected and analyzed in the NAD83 UTM zone 13N coordinate system with the central meridian placed at -105° longitude. Linear units were set at 1.0 m. All primary data (those that existed prior to this study and were used as input for analyses) and generated data (those that are the result of measurements or analyses conducted for this study) are archived with NMBGMR and are available upon request free of charge.
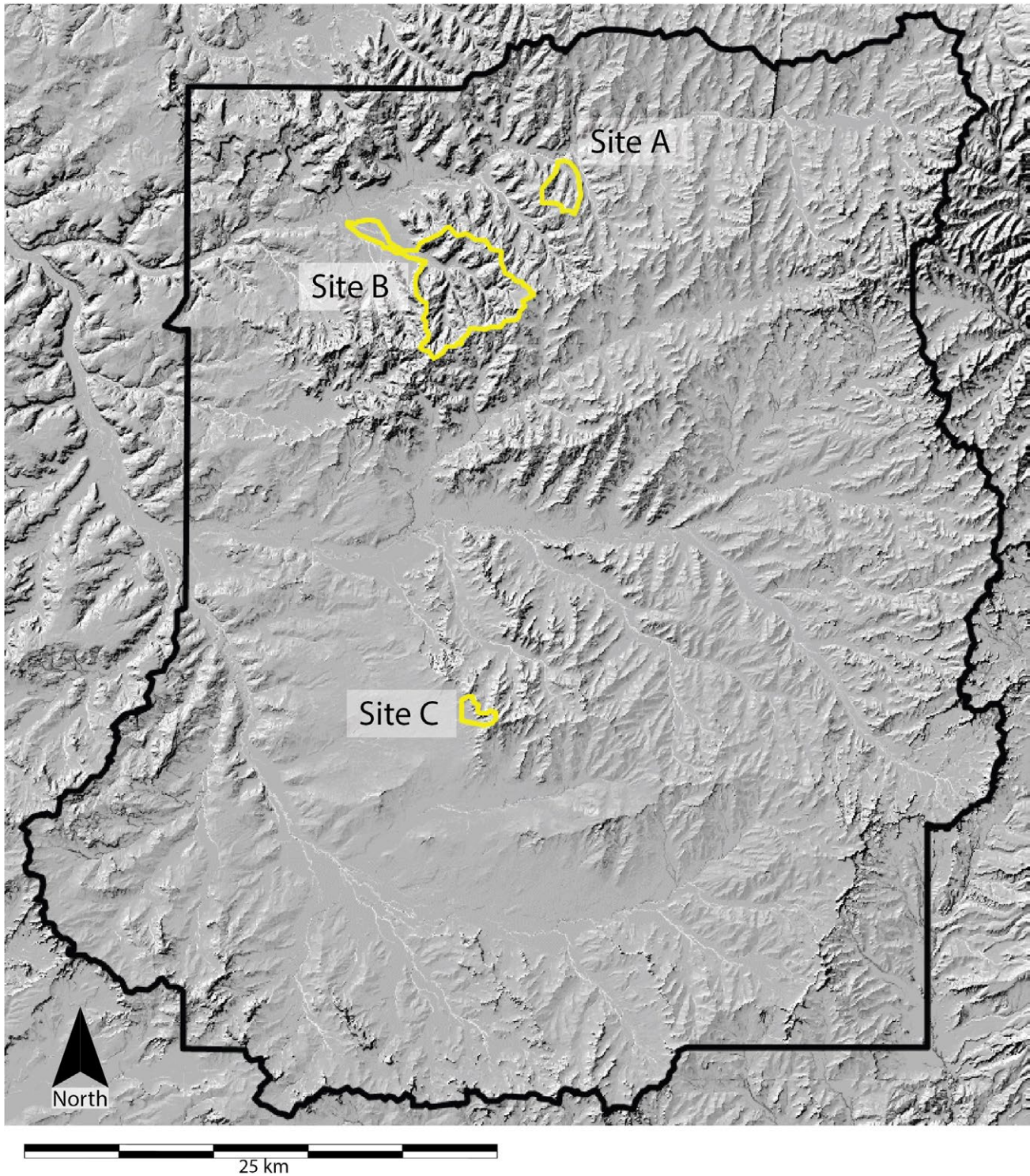
Figure 2.1. Hillshade digital elevation model of the upper Cañon Largo watershed on the Jicarilla Apache Nation. Black outline shows the boundary of the study area. Yellow outlines show the watershed boundaries of selected study Sites A, B, and C.

III. GEOLOGY

Kevin M. Hobbs

The geologic framework of the study area has two main components: (1) relatively flat-lying sedimentary rocks of the Paleogene Period and (2) unconsolidated sediments of the Quaternary Period on broad plains and in valley bottoms (Fig. 3.1).

Additionally, there are five small igneous dikes in the eastern portion of the watershed near the headwaters of Tapicito Creek and Carrizo Canyon. These dikes have little impact on geomorphology,

hydrology, erosion, or sedimentation in the watershed. Detailed descriptions of individual geologic units and their stratigraphic and geographic relationships to each other are in the *Geologic Map of the Cañon Largo Watershed on the Jicarilla Apache Nation, Rio Arriba and Sandoval Counties, New Mexico,* included as a supplement to this report and available for free download from NMBGMR at **https://geoinfo.nmt.edu/publications/openfile/details.cfml?Volume=620**

Mesa-top sands and eolian sand sheets (<2.6 Ma)

Older alluvium (<8 to 1.48 ka)

Young alluvium (1.4 to 0.1 ka)

Active alluvium

Fans and sheetwash deposits

Trachybasalt dikes (ca. 25 Ma)

San Jose Formation (ca. 57 to 54 Ma)

Nacimiento Formation (ca. 65 to 62 Ma)

Older sedimentary rocks (>65 Ma)
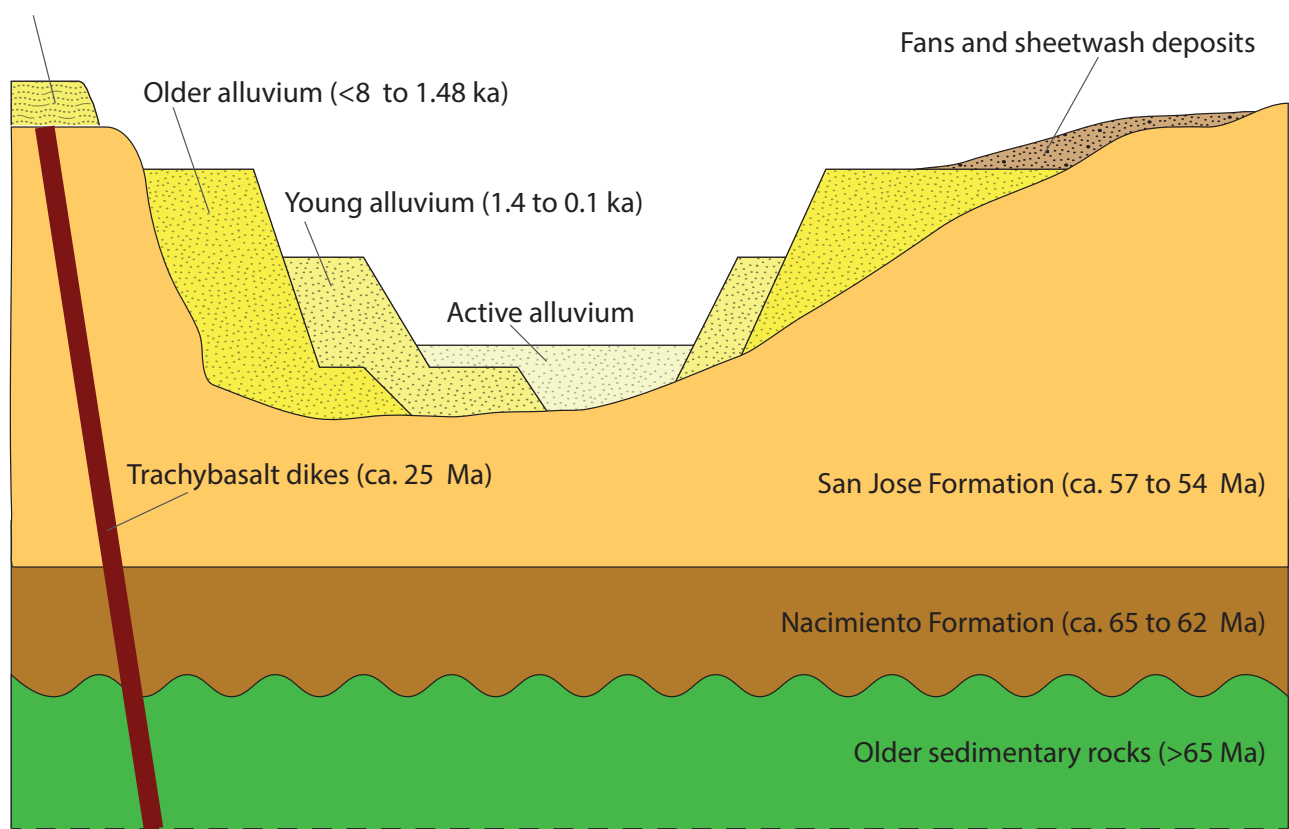
Figure 3.1. Schematic cross-sectional diagram showing the relationships among major geologic units in the upper Cañon Largo watershed. Not to scale.

That map, its report, and the data within serve as baseline geological data for many of the other analyses and surveys in this study. Full GIS data for that map may be requested free of charge at any time from NMBGMR.

STRATIGRAPHY

The older sedimentary rocks in the study area comprise mudstones, siltstones, sandstones, and conglomerates of the Paleocene Nacimiento Formation and Eocene San Jose Formation. The sediments in these formations were deposited as mud, sand, and gravel by rivers in the San Juan Basin during the Laramide orogeny, a mountain-building episode whose topographic and deformational effects are recorded in rocks and landscapes throughout western North America. These Paleogene sediments were derived from the erosion of older sedimentary rocks and crystalline basement rocks in the mountains surrounding the San Juan Basin. Although the Nacimiento and San Jose Formations are not known reservoirs for hydrocarbons, they overlie productive geologic reservoirs of oil and natural gas. In the Cañon Largo watershed, the Nacimiento and San Jose Formations are the stratigraphically highest sedimentary rock units in a 4,100-m-thick (13,500-ft-thick) package of Phanerozoic sedimentary rocks from the Paleozoic, Mesozoic, and Cenozoic Eras (thickness data derived from Magnolia Oil Company Jicarilla Well #1A, Township 23N, Range 2W, SW1/4 SE1/4, Section 18, API# 30-039-05054, total depth 4,131 m [13,550 ft)]). The majority of the area of the Cañon Largo watershed contains the Eocene San Jose Formation as the highest exposed bedrock unit. The Paleocene Nacimiento Formation crops out in the highest tributary headwaters of Cañon Largo near Counselor, along Blanco Wash, and along the deepest portions of Cañon Largo downstream of its confluence with Tapicito Creek.

Unconsolidated Quaternary sediments are found covering much of the surface of the watershed, including on broad upland plains, on shallow slopes, and in the floors of valleys and canyons. These units are summarized in Table 3.1. On upland plains, stabilized eolian sand sheets cover broad expanses of little topographic relief. Although these former sand dunes are stabilized with vegetation (primarily grasses and sagebrush), eolian dune forms are still clearly visible in aerial imagery (Fig. 3.2). In the valleys of arroyos and larger canyons of the watershed, clay- through gravel-sized sediments were originally deposited by flowing water throughout the late Quaternary Period. These sediments, called alluvium, are predominantly sandy and generally form three different levels in larger canyons, each representing a different episode of erosion and deposition (Fig. 3.3): the lowest alluvium (called here "active alluvium" [Qaa]) is found in arroyo beds and represents sediments transported and deposited by present-day fluvial processes, the alluvium herein called "young alluvium" (Qay) is found on flat-topped terraces 1 to 2.5 m higher than modern arroyo beds and was deposited approximately 100 to 1,500 years ago, and the highest and oldest alluvium (called here "older alluvium" [Qao]) is found on expansive flat-topped terraces 3.5 to 9 m higher than modern arroyo beds. The progressive incision of arroyo beds from approximately 1,500 years ago to the present is one of the fundamental causes of erosion-related issues with human infrastructure in the region. Occupying a smaller total area than eolian or valley-floor alluvial deposits in the watershed, sheetwash deposits and alluvial fan deposits are found throughout Cañon Largo and its tributaries.

STRUCTURE

The entire Cañon Largo watershed lies within a geologic deformation structure called the San Juan Basin (SJB). The SJB, like all structural basins, is defined by layers of rock that dip downward toward the center of the basin. A basin's structural center is located where layers of rocks are roughly flat-lying, like the bottom of a bowl. In a symmetrical basin, the structural center is at the same location as the geographic center. The SJB, however, is highly asymmetrical: the rock layers on the northern and eastern sides of the basin dip more steeply than those on the southern and western sides. The SJB's three-dimensional shape is therefore similar to an upturned oyster shell; the basin's structural center is close to its eastern edge and bisects the Cañon Largo watershed. Because of this, the bedrock units in the watershed have relatively low dip angles of less than 10° from horizontal. The SJB's structural axis is defined by opposing shallow dip angles in the upper Cañon Largo watershed, especially in the headwaters of Tapicito Creek and Cañada Larga. Being at the structural center of the SJB, the watershed contains the youngest and stratigraphically highest bedrock

Table 3.1. Summary description of geologic units mapped on the *Geologic Map of the Cañon Largo Watershed on the Jicarilla Apache Nation, Rio Arriba and Sandoval Counties, New Mexico.*

Geologic Unit	Composition	Landscape Position	Age
Artificial fill (aft)	clay, silt, sand, and pebbles	dams, berms, roads, well pads	<0.1 ka
Disturbed ground (ad)	dependent upon underlying geologic composition	human-made disturbance areas	<0.1 ka
Active alluvium (Qaa)	clay, silt, sand, and pebbles	beds of active arroyos	<0.1 ka
Young alluvium (Qay)	clay, silt, sand, and pebbles	terraces 1–2.5 m above active arroyo beds	1.4 to ~0.1 ka
Older alluvium (Qao)	clay, silt, sand, and pebbles	terraces 3.5–9 m above active arroyo beds	8.0 to ~1.48 ka
Sheetwash deposits (Qsw)	clay, silt, sand, and pebbles	gentle slopes where active water flow is not confined to channels	>5.8 ka to present
Older sheetwash deposits (Qswo)	clay, silt, sand, and pebbles	gentle slopes with inactive non-channelized flow; higher landscape position than Qsw	Pleistocene to Holocene
Fan deposits (Qf)	silt, sand, pebbles, and cobbles	active alluvial fans	Holocene to present
Older fan deposits (Qfo)	silt, sand, pebbles, and cobbles	inactive alluvial fans; higher landscape position than Qf	Holocene
Eolian deposits derived from sand-bed arroyos and within valley floors (Qea)	silt and sand	dunes within valleys	~0.2 ka to present
Inactive stabilized eolian deposits derived from sand-bed arroyos and within valley floors (Qeao)	silt and sand	vegetated dunes within valleys	Holocene
Mesa-top sands (Qsm)	silt, sand, and pebbles	topographically isolated small mesas	Holocene
Eolian sand sheets (Qes)	silt and sand	broad low-relief surfaces outside valleys	Pleistocene to Holocene
Landslide deposits (Qls)	cobbles, boulders, and toreva blocks	margins of bedrock cliffs in large valleys	Holocene
Intrusive dikes of the Dulce dike swarm (P$_E$i)	trachybasalt and basaltic trachyandesite	linear ridges in upper Tapicito Creek drainage	Oligocene, ca. 25.0 Ma
Regina, Llaves, and Tapicitos Members of the San Jose Formation, undivided (P$_E$sju)	mudstone, sandstone, and conglomerate	upland slopes and uplands	Eocene
Cuba Mesa Member of the San Jose Formation (P$_E$sjc)	mudstone, sandstone, and conglomerate	upland slopes and uplands	Eocene
Escavada Member of the Nacimiento Formation (P$_E$ne)	mudstone and sandstone	small outcrops below cliffs on Sisnathyel Mesa	Paleocene

units in the basin; older sedimentary rock units are found outside the watershed in all directions toward the SJB margins.

While the SJB structural axis is the largest and best-expressed deformation structure within the Cañon Largo watershed, there also exist smaller deformation structures in the form of joints and faults. Joints are fractures in rock along which there has been no motion, like a crack in window glass. Joints are observed in most sandstones of the watershed, and often form parallel to cliff faces, facilitating cliff retreat through mass wasting. Joints also serve as conduits for water flow, either through infiltration from downward-percolating precipitation water or through lateral flow as groundwater. For these reasons, plant roots often exploit joints in sandstones. Joints sometimes form in a geometric pattern or parallel orientation in response to regional tectonic stress (e.g., Bump and Davis, 2003). This pattern, called systematic jointing, is likely found within the Cañon Largo watershed, but sufficient data have not been collected to verify or deny its existence. Joints also are reported to form in association with igneous dikes such as those present in the headwaters of the Cañon Largo watershed (e.g., Delaney et al., 1986), and many second- and third-order stream valleys in upper Tapicito Creek and Cañon de los Ojitos are parallel to known dikes in the area. Whether or not these dike-parallel valleys are geomorphically controlled by preexisting bedrock joints has not been determined but is worthy of future investigations. Many of the watershed's bedrock strata are mudstones, which may be less likely than well-cemented sandstones to form or record joints. Joints in mudstones often are more difficult to observe because of that rock type's tendency to have poor outcrop qualities. A thorough study on mudstone jointing in the Nacimiento and/or San Jose Formations has not been conducted.

Faults are fractures in rock across which there has been movement. Several small faults are observed in the Cañon Largo watershed, though only one is large enough to appear at the 1:50,000 scale at which the upper watershed was mapped. These faults are meters to tens of meters in observed length and have displacements of decimeters to meters. A full study on fault geometry and kinematics was not undertaken for this report. However, faults in the watershed likely have little influence on surface hydrology, erosion, or sedimentation.
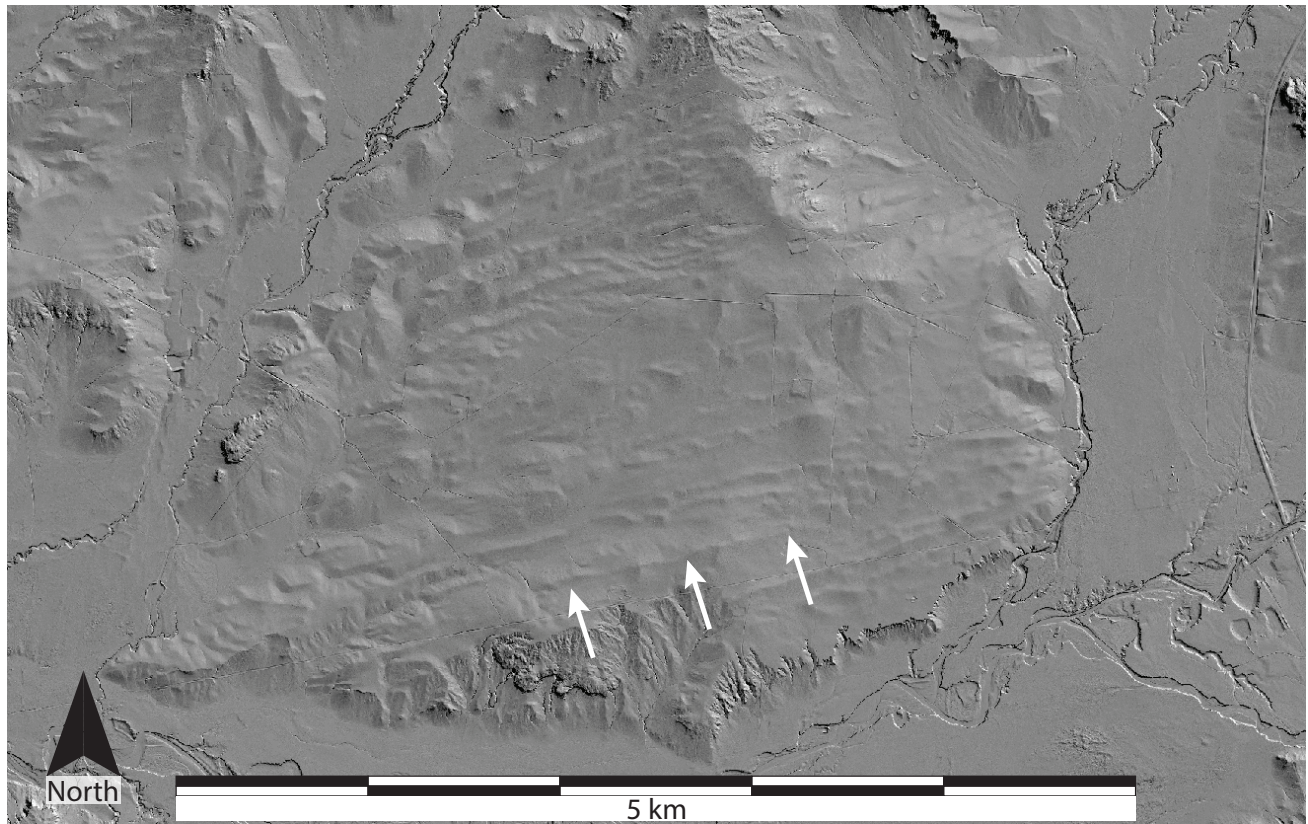
Figure 3.2. Hillshade digital elevation model of stabilized eolian sands showing kilometers-long linear dune forms, one of which is indicated with white arrows. Dune orientation suggests a paleowind average direction of 071°. Center of image is at approximately 36.33° N, -107.31° W. The confluence of south-flowing Cañon de los Ojitos with west-flowing Cañada Larga is at bottom right. New Mexico Highway 537 is at far right.
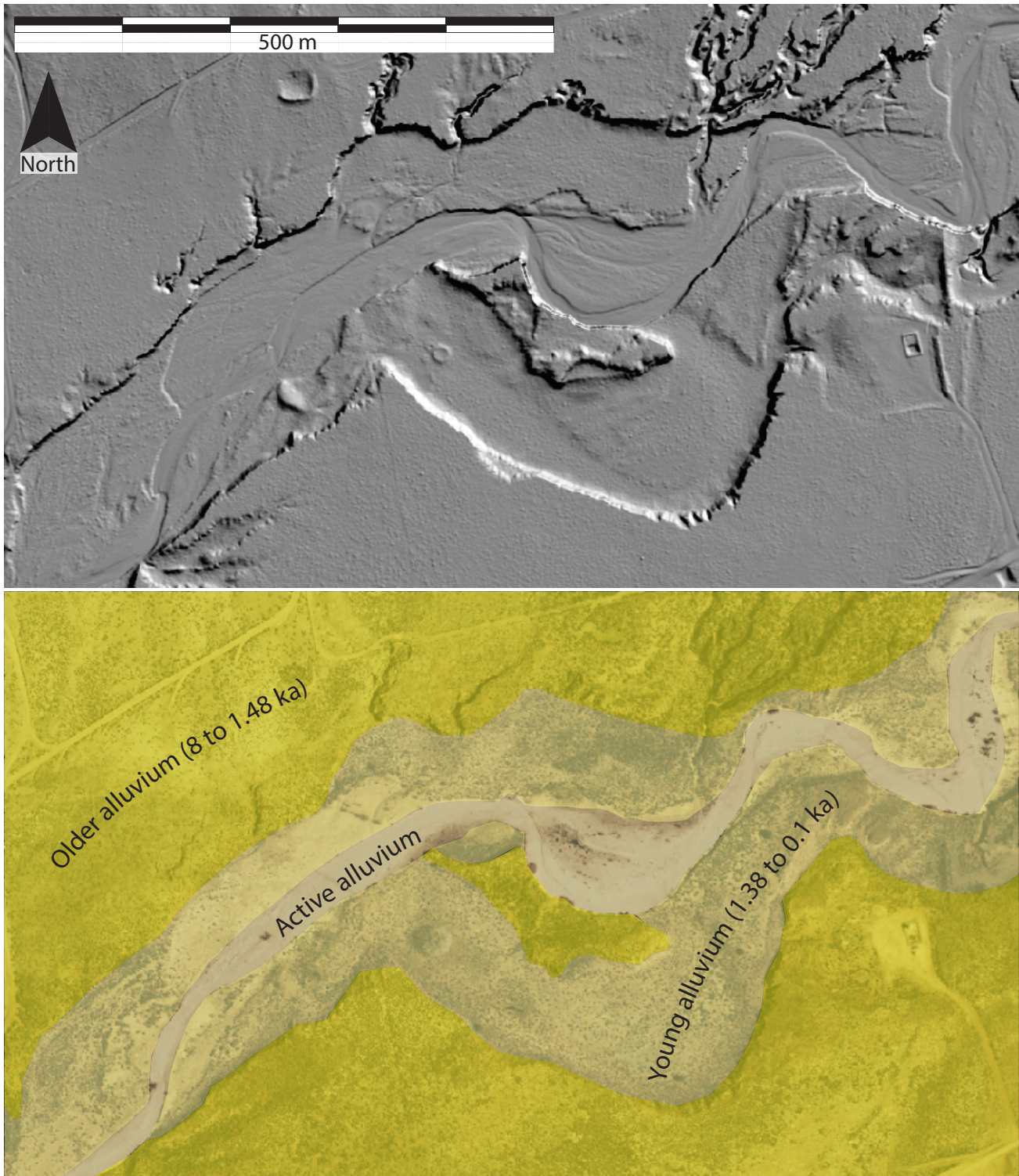
Figure 3.3. Hillshade digital elevation model (top) and orthophotograph (bottom) showing two terraces of alluvium in Tapicito Creek near Las Norias Canyon. The older alluvium surface stands 3.5–9 m higher than the active stream bed. The young alluvium surface stands 1–2.5 m above the active stream bed, but can be inundated during high-flow events. Active alluvium is largely unvegetated and undergoes dynamic fluvial changes during any streamflow event. Center of image is at approximately 36.48° N, -107.29° W. Scale applies to both images.

IV. LITERATURE REVIEW OF EROSION AND SEDIMENTATION ENGINEERING ISSUES

Faustin Kumah, Navid Mojtabai, and Mehrdad Razavi

OVERVIEW OF SOIL EROSION

For most of our history, humans have dealt with the impacts of soil erosion (Isaka and Ashraf, 2017). This phenomenon is a geomorphological activity whereby soil particles, rock fragments, soil aggregates, and organic materials detached from their initial position move to another area through various mechanisms (Poesen, 2018). If the sediment load in the flow is less than the flow's sediment transport capacity, sediment particles are dislodged from their present locations (erosion); conversely, deposition occurs whenever the flow's sediment load surpasses its transport capacity (Aksoy and Kavvas, 2005). It is a crucial process for soil formation (Lal, 2001); however, it is also the most prevalent form of soil degradation (Aiello et al., 2015; Maruffi et al., 2022), with an estimated surface soil loss rate of 25 to 40 billion tons eroded yearly (Kucuker and Giraldo, 2022). Hence, it is a critical environmental concern that threatens agricultural (Renschler et al., 1999; Pandey et al., 2016) and hydrologic systems' productivity and sustainability (Pandey et al., 2016; Ahmad, 2018). Additionally, the transportation of sediments and deposition during erosion negatively impacts streams, lakes, reservoirs, and estuaries (Li et al., 2017). Unfortunately, soil erosion rates are higher than soil formation rates and are exacerbated on sloping land, jeopardizing sustainable agriculture (Pimentel, 2006).

Soil erosion is a complicated environmental phenomenon (Aiello et al., 2015; Senanayake et al., 2022) because it results from the intricate interplay of natural and human-caused forces, which vary over space and time (Zi et al., 2016; Phinzi and Ngetar, 2019). Many elements influence this complicated process, including overland flow (Zi et al., 2016), rainfall (Senanayake et al., 2022), soil, terrain, vegetation, land use management strategies (Ke and Zhang, 2022), and climate change (Yang et al., 2003; Ma et al., 2021). This heterogeneity is further impacted by soil particle redistribution during runoff cycles, which causes long-term landscape changes and, in turn, influences the hydrologic processes occurring on specific hill slopes (Kim et al., 2015). Human activity and concomitant land use change are the principal causes of rapid soil erosion rates (Isaka and Ashraf, 2017), severely affecting the nitrogen and carbon cycles, soil health, and global socioeconomic circumstances (Borrelli et al., 2017). A thorough examination identified various general characteristics, which proved that positive relations exist between erosion rate with slope and annual precipitation, and demonstrated that the effect of land use is significant, with forest and shrublands producing the lowest erosion rates and agricultural lands producing the highest erosion rates (García-Ruiz et al., 2015). Even though soil erosion in natural ecosystems occurs extremely slowly throughout geologic time scales, the associated collective influence on soil quality over billions of years is enormous (Pimentel, 2006). Figure 4.1 shows the spatial patterns of the soil erosion field rate measurements (Borrelli et al., 2021).

SOIL EROSION AND SEDIMENT TRANSPORT MODELING APPROACHES

Forecasting soil erosion is essential at a range of time and spatial levels, from the field scale, where it impacts individual farmers, to regional or global scales, when it may become a crucial input to planning considerations (Kirkby et al., 1998). Erosion studies use several approaches to quantify the
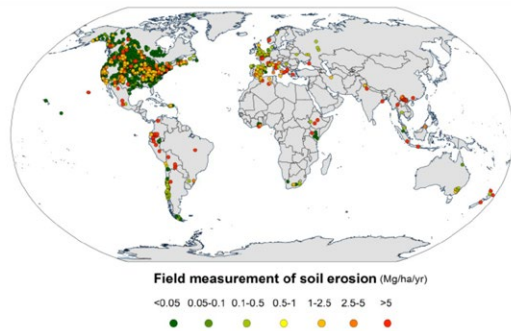
Figure 4.1. Spatial distribution of soil erosion field measurements in Robinson projection (Borrelli et al., 2021).

material eroded off hillslopes, transferred to channels, and transported to other channels, lakes, and oceans (García-Ruiz et al., 2015).

Field measuring methods vary in labor cost, accuracy, and equipment (Stroosnijder, 2005), and they are valuable for monitoring erosion processes in detail; nevertheless, they are costly, time-consuming, and site-specific, making generalizing field survey data problematic (Zhang et al., 1996). Essentially, such field approaches have inherent errors in the data collected, may not be adequately responsive to site modifications, and do not depict natural runoff dynamics (Arriola-Valverde et al., 2020). Furthermore, logistics and accessibility of monitoring sites for collecting data may be challenging (Arriola-Valverde et al., 2020).

Computer models are useful for simulating soil erosion at watershed scales because they account for many of the intricate interconnections of soil erosion mechanisms in time and space (Kim et al., 2015). Modeling offers a quantitative and consistent way to assess soil erosion and sediment yield under various scenarios, and it is required to guide comprehensive soil erosion management (Igwe et al., 2017). There are many soil erosion and sediment yield models available, which vary in terms of erosion processes they examine, complexity, data requirements, and their applications (Pandey et al., 2016), that scientists are using as a basis for formalizing their theoretical assessment of the mechanisms that govern soil particle detachment, transport, and deposition (Uri, 2001). And while there are many scientific publications on this issue, there are still substantial research gaps, so we still do not know practically everything about soil erosion and its control (Poesen, 2018). A literature

survey found a dearth of knowledge on soil erosion mechanisms in forest intermountain watersheds (Borrelli et al., 2014). Accordingly, there is a need to develop baseline data on soil-erosion models that details the mechanisms and models primarily used and in which regions, determines how frequently researchers evaluate the results of these models, and generally outlines what we currently know about the applications of these models worldwide (Borrelli et al., 2021).

Over the last few decades, many alternative models and relationships have been presented to explain and forecast soil erosion by water and related sediment output, with differing aims, time and spatial scale, and conceptual base (de Vente and Poesen, 2005). Most erosion and sediment parameters are scale-dependent; hence, these models are developed for various applications of spatial and temporal scales (Pandey et al., 2016). Current research reveals that there is no fixed trend relationship between drainage basin area and sediment yield; estimating sediment yield based exclusively on the drainage area of the basin is problematic, and data regarding spatially distributed factors, such as soil, land use, climate, topography, and dominant erosion processes, are required (de Vente et al., 2007). García-Ruiz et al. (2015) found a negative relationship between erosion rate and study area size; considerable variations between methods of measurements, with radioisotope, bathymetric, and modeling producing the highest rates and the direct sediment method producing the lowest erosion rates; and a significant effect of experiment duration.

Based on the physical processes reproduced by the model, the model's equations characterizing these processes, and the model's data dependency, models are typically classified as either empirical (or statistical or metric), conceptual, or physics-based (Merritt et al., 2003). Even physics-based models maintain some empiricism in their model methods; therefore, most models do not fall perfectly into one category (de Vente and Poesen, 2005; Pandey et al., 2016). The best model for a specific region is determined by the modeling objectives and the prevailing soil erosion and sediment transport processes and, therefore, by driving environmental conditions (de Vente et al., 2013).

EMPIRICAL MODELS

Empirical models are the most basic of the three model categories (Merritt et al., 2003). Estimating soil erosion utilizing empirical models has long been an important research issue (Aiello et al., 2015). Numerous empirical models have been presented to forecast soil erosion caused by water and the resulting sediment output because of their ease of use and implementation due to the minimum data requirements (Aiello et al., 2015; Abdullah et al., 2017). However, empirical solutions derived from observations apply to the particular area where the data were obtained, and they have been developed based on the correlation of numerous factors utilizing empirical data that is site-specific (Aksoy and Kavvas, 2005; Chandramohan et al., 2015; Abdullah et al., 2017).

These are primarily based on practical field studies in which soil loss rates from various slopes and surfaces were monitored and linked to variables such as gradient, soil type, plant cover, climate index, and flow channel length (Coulthard et al., 2012). Empirical models do not deduce mechanisms at work but instead focus on observable or stochastic correlations between causal factors and simulated output (Merritt et al., 2003). With the assessment of sediment settling and transport patterns at the regional scale, empirical models may be used to forecast average sedimentation, rates of soil erosion, and surface runoff using the Soil Conservation Service (SCS) curve number (Raza et al., 2021). When soil qualities do not fluctuate geographically and spatially detailed meteorological data are not obtainable, robust empirical modeling can yield more credible outcomes than more complicated and dynamic models (Raza et al., 2021).

The Universal Soil Loss Equation (USLE) and its variants (such as Revised USLE [RUSLE], RUSLE2, RUSLE3D, Unit Stream Power-Based Erosion Deposition [USPED], and Modified USLE [MUSLE]) are widely recognized and practical models, but their application has significant constraints. Because they are empirical, they require proper parameterization and validation, predict erosion only at the slope's base, utilize yearly timeframes, and may only be used if a parameter database is available (Coulthard et al., 2012). However, long-term modeling capabilities with these models produce reliable results, including USLE,

MUSLE, RUSLE, and Modular Soil Erosion System (MOSES), at both the hillslope and catchment levels (Raza et al., 2021).

Empirical models are valuable tools for predicting erosion, but they are unable to be applied outside the scope of scenarios they were initially designed for (Santos et al., 1998). Moreover, they forecast the rate of soil erosion from a plot without considering the physical processes at work in that area (Coulthard et al., 2012). Nonetheless, with the advancement of new technologies and the use of remote sensing systems, the accuracy of empirical models forecasting the degree of erosion and measuring sediment output has significantly improved, so they give more accurate basin erosion zonation and sediment output (Rajabi et al., 2022). Table 4.1 summarizes some empirical soil erosion models that are commonly used (Aksoy and Kavvas, 2005; Raza et al., 2021).

CONCEPTUAL MODELS

In conceptual models, sediment-producing events like rainfall and runoff are handled as system inputs, with sediment yields as the output (Chandramohan et al., 2015). The model tends to incorporate a generic representation of the catchment mechanisms as a succession of internal storages rather than the exact intricacies of process interactions, which need extensive catchment knowledge (Pandey et al., 2016). This enables conceptual models to give qualitative and numerical estimates of the consequences of changes in land use without demanding vast volumes of geographically and temporally dispersed data as inputs for modeling (Merritt et al., 2003).

Modelers attempted to develop models that are less complicated than physics-based models yet provide more exact forecasts than the USLE or its successors. This led modelers to create frameworks that conceptualized the erosion process such that there exists a non-physical but theoretically relevant relationship between the components simulated by the model (Aksoy and Kavvas, 2005).

The equations from empirical approaches are used in most conceptual models; hence, they are typically placed between physical and empirical models (Raza et al., 2021). Based on crop and soil management at daily time steps, these conceptual models may forecast the temporal and geographical

Table 4.1. Empirical soil erosion models (Aksoy and Kavvas, 2005; Raza et al., 2021).

Model Name	Input Variables	Governing Equations
USLE	Climate data, topography, land use/land cover, field management practices, crop management factor	Universal Soil Loss Equation
MUSLE	Volume flow rate, peak flow rate, erosion control practices, crop management factor, climate data, topography, land use/land cover, field management practices	Modified Universal Soil Loss Equation
RUSLE	Climate data, topography, land use/land cover, field management practices, crop management factor	Revised Universal Soil Loss Equation
SEDD	Digital elevation model (DEM), land use map, climate, human influence	Universal Soil Loss Equation

distribution of soil detachment and sedimentation at the field scale (Raza et al., 2021). Santos et al. (1998) developed a conceptual model utilizing an empirical soil erosion model; a physics-based model was employed to produce synthetic data to validate the model and minimize resource requirements in generating a database based on field measurements. Automated Geospatial Watershed Assessment and USPED are also integrated conceptual models that use statistical methods to assess the overall number of storages and their configurations (Raza et al., 2021). Table 4.2 summarizes some conceptual erosion models (Merritt et al., 2003; Raza et al., 2021).

PHYSICS-BASED MODELS

On the other hand, physics-based models enable access to the geographical and temporal variability of sediment entrainment, transport, and deposition processes and knowledge of the fundamental sediment-generating processes (Chandramohan et al., 2015). Thus, these models are the outcome of more recent efforts to more thoroughly capture the complexity of soil erosion, transport, and deposition processes to describe and forecast the dynamic

behavior of the earth system as a whole (Borrelli et al., 2021). Mathematical expressions representing particular processes in these models are based on many assumptions and consider empirical/conceptual methods (Pandey et al., 2016). Foster's equation (used in the WEPP and CREAMS models), Engelund and Hansen's equation (used in the TOPOG model), and Rose's equation (used in the GUEST model) are all regularly utilized mathematical algorithms for sediment transport in various physics-based erosion models (Merritt et al., 2003). However, unlike empirical or conceptual models, physics-based spatially dispersed models may be utilized to identify critical regions by giving the output at any desired place within the watershed, especially when time and money are restrictions for vast watersheds (Pandey et al., 2016).

Even though these models employ various approximations to simplify the system (nature) in developing erosion and sediment transport processes by minimizing the number of dimensions in the governing equations (Aksoy and Kavvas, 2005), physics-based models are typically complicated and need significant input data with high spatial and temporal resolution (e.g., soil characteristics,

Table 4.2. Conceptual soil erosion models (Merritt et al., 2003; Raza et al., 2021).

Model Name	Input Variables	Governing Equations
AGNPS (Agricultural Non-Point Source Pollution Model)	Climate, topography, soil characteristics, land use	SCS curve number, USLE, Foster's equation
CAESAR (Cellular Automaton Evolutionary Slope and River Model)	DEM, rainfall, flow parameters, slope processes, bedrock depth, the value of Manning coefficient	Einstein's equation, Wilcock and Crowe's equation
IQQM (Integrated Water Quality and Quantity Model)	Topography, river system configuration, evapotranspiration	Conceptual Sacramento model, QUAL2E model
LASCAM (Large Scale Catchment Model)	Sediment load, runoff, salt fluxes	USLE, stream sediment capacity
SWRRB (Simulator for Water Resources in Rural Basins)	Rainfall data, soil characteristics, land use	MUSLE, sediment balance equation

hydrology, topography, and vegetation), resulting in expensive and complex implementation (Arriola-Valverde et al., 2020). Furthermore, model calibration takes time (Golkarian et al., 2023). Notwithstanding their drawbacks, these physics-based models generate soil erosion and sediment yield output at any desired location within the watershed with greater simulation accuracy than empirical or conceptual models (Pandey et al., 2016); hence, they have been widely employed (Aksoy and Kavvas, 2005). Table 4.3 summarizes physics-based models developed between 2006 and 2011 from a database compiled by Pandey et al. (2016).

LIMITATIONS OF SOIL EROSION MODELS

Because the erosion process has numerous uncertainties that are challenging to address analytically, no viable model for predicting sediment output with the highest level of precision has been created (Santos et al., 1998). Natural complexity, regional heterogeneity, and a lack of available data are some environmental modeling challenges (Jakeman et al., 1999). Selecting required input parameters is challenging because all essential data for any field of study are rarely accessible (Golkarian et al., 2023). Model performance and accuracy remain fundamental challenges in model development, especially with spatially distributed models (Merritt et al., 2003). Soil erosion models may have various issues, including over-parameterization, unrealistic input requirements, unsuitability of

model assumptions or parameter values to local circumstances, and insufficient documentation of model testing and subsequent performance (Merritt et al., 2003).

Using large datasets to test various empirical or physics-based soil erosion models has repeatedly demonstrated that these models typically over-predict soil erosion for small, measured values and under-predict for higher measured values (Nearing, 1998). While physics-based models offer the most theoretical promise for use in environmental scenario analyses, they are frequently optimized for the local conditions of relatively small catchments, and therefore produce poor validation outcomes when applied to diverse catchments or situations (de Vente et al., 2007). Many empirical, conceptual, and physics-based erosion and sediment transport models only address overland flow erosion, with only a few models considering gully erosion (Merritt et al., 2003). Currently, the mechanisms and interactions driving soil erosion under climate warming are very unpredictable; therefore, these interactions should be investigated extensively, particularly in wind erosion models (Ma et al., 2021).

The models to predict erosion must be calibrated and validated using measurements (Stroosnijder, 2005). However, because soil erosion measurements have numerous drawbacks (such as high work/time inputs and restrictions to small spatial and temporal scales), many modeling studies lack validation, so many soil erosion modeling applications should be regarded as indications of the best hypotheses

Table 4.3. Physics-based soil erosion models (Pandey et al., 2016).

Model Name	Input Variables	Governing Equations
AnnAGNPS (Annualized Agricultural Non-Point Source Model)	Climate, soil, topography, channel, cultural practices	RUSLE, modified Einstein deposition equation, Bagnold transport equation
APEX (Agricultural Policy/Environmental eXtender; EPIC model extension)	Climate, crop, watershed characteristics	USLE, MUSLE, and RUSLE, along with their modifications
HYPE (Hydrological Predictions for the Environment)	Climate, soil, land use, topography	Land use and soil type-based empirical and conceptual equations
IDEAL (Integrated Design and Evaluation of Loading Model)	Climate, soil, land cover	MUSLE, event mean concentrations, and runoff volume
MEFIDIS (Modelo de Erosão FÍsico e DIStribuído)	Climate, soil, land use, topography, channel section	Kinetic rainfall energy approach, sediment transport capacity approach
PALMS (Precision Agricultural Landscape Modeling System)	Climate, soil, crop, surface mask, topography	MUSLE
RHEM (Rangeland Hydrology and Erosion Model)	Climate, soil, land cover, topography	Splash erosion and transport equation

currently available rather than predictive models (Borrelli et al., 2021). Comprehensively, García-Ruiz et al. (2015) demonstrated that models have limited predictive power, using a scatterplot of predicted versus observed erosion rates. The scatterplot illustrates a good average relationship; however, the prediction interval (the range that includes 95% of the observations) covers almost two orders of magnitude, but the variable's whole range spans more than four orders of magnitude (García-Ruiz et al., 2015).

Despite the constraints of various soil erosion models, research findings indicate that a low-cost modeling-based strategy, which minimizes costly data collection techniques, can yield exciting information regarding runoff and soil erosion analysis (Straffelini et al., 2022).

OVERVIEW OF CLOSE-RANGE PHOTOGRAMMETRY

Small-format aerial photography captured by uncrewed aerial vehicles (UAVs) is gaining acceptance and use in a variety of natural resources planning and geospatial research applications (d'Oleire-Oltmanns et al., 2012). Although the military has employed UAVs for decades, their deployment for scientific and other civilian applications is relatively new (d'Oleire-Oltmanns et al., 2012). Many techniques for reconstructing DEMs from aerial photography have been developed, including the standard close-range stereo photogrammetry (CRP) and the unique structure from motion (SfM) technique (Li et al., 2018).

By employing scaling information supplied by calibration, stereo photogrammetry permits the reconstruction of a depth (also known as disparity) map, which may then be translated into a metric point cloud and, subsequently, a DEM (Li et al., 2018). Traditional CRP techniques rely on a kernel-based cross-correlation technique, typically calculated by a simple image convolution operator between the patches of two images; hence, these cross-correlation-based algorithms become much more sensitive to variations in pixel density, image scale, illumination, and rotation (Mali et al., 2021).

Structure from motion photogrammetry uses several photos to recreate camera motion and scene rendering without the requirement for calibration, and scaling is often handled via ground control points and independent assessments (Li et al., 2018). To detect conjugated pixels, the SfM employs standard techniques, including affine-SIFT, speeded-up robust features, and scale-invariant feature transform algorithms (SIFT), which use color gradients and multiscale image brightness (Mali and Kuiry, 2018).

The evolution of these digital photogrammetry techniques has been made possible through computer vision approaches (Wrobel, 1991) and visual perception research fields (Eltner et al., 2016) to construct high-resolution 3D and 2.5D models (Arriola-Valverde et al., 2020). These models can be created from a group of uncalibrated photographs (Eltner et al., 2016) with a wide range of image sensors, from relatively low-cost cameras to highly specialized multiband hyperspectral cameras (Cramer, 2008). In a study conducted in Italy on beach dunes, the photogrammetry technique proved efficient, with vertical precision equivalent to terrestrial lidar technology (Laporte-Fauret et al., 2019).

The digital photogrammetric technique may be used with various UAV platforms, but it needs enormous computer resources and many hours of processing time; however, this is offset by a more straightforward and less error-prone data collecting phase when compared to manual quantification techniques (Arriola-Valverde et al., 2020). The use of ground control points is time-consuming because extensive fieldwork is required to establish and measure the locations of the ground control points during data collection (Eltner et al., 2016). Following that, extra time and labor are necessary during postprocessing to identify the ground control points in the pictures; however, progress toward automatic ground control point identification is being explored (Eltner et al., 2016).

Image processing that produces high-detail outcomes is labor-intensive and needs to be improved in the future (d'Oleire-Oltmanns et al., 2012). Systematic advancements in geo-referencing are anticipated to increase the adaptability of multitemporal topographic data extraction (Eltner and Sofia, 2020). Developing soil erosion models using photogrammetric products, in conjunction with other kinds of sensors, may offer a much more robust,

accurate, and dependable solution than approaches that rely heavily on soil samples collected and other input variables (Arriola-Valverde et al., 2020). Also, advances in time-lapse photogrammetry are projected to increase temporal resolution at unprecedented scales (Eltner and Sofia, 2020).

SELECTED APPLICATIONS OF UAV-BASED PHOTOGRAMMETRY IN SOIL EROSION STUDIES

Using a high-resolution topographic dataset is critical for geomorphological research, especially for systems with complex morphology (Eltner and Sofia, 2020). Presently, an extensive array of proprietary and open-source software packages, and recent fast advancements in UAV technology, enable geoscientists and other non-expert users to generate high-quality aerial surveying and orthophotography 3D and 4D models of intricate geomorphological features at low cost (Eltner et al., 2016).

Laporte-Fauret et al. (2019) used photogrammetry via UAV to monitor coastal dune morphological changes and the upper beach at Truc Vert, in southwestern France, at high frequency (after each storm). The area surveyed was 1 km^2, and with a flight time of less than 2 hr, a digital surface model with a root-mean-square vertical error and bias of 0.05 m and -0.03 m was obtained. The monitoring covered six months over the winter, and the authors proved that determining large-scale morphological evolution at a high temporal resolution and a low cost using photogrammetry techniques is well-adapted for use in areas where coastal data are lacking.

d'Oleire-Oltmanns et al. (2012) presented a photogrammetry application for soil erosion monitoring by employing a fixed-wing UAV to close the data gap between the satellite scale and field scale and to quantify gully volume in Morocco. Ground control points were installed for photographs acquired at a flight height of 70 m to ensure high-precision triangulation results for the photogrammetric imagery blocks; root-mean-square horizontal error obtained ranged between 0.009 and 0.027 m, and 0.007 m error in the vertical direction. Photographs were also acquired at a flight height of 400 m, and direct georeferencing techniques rather than ground control points manually installed on the field were employed because of the extensive survey

area; root-mean-square horizontal error obtained ranged between 0.09 and 0.30 m, and between 0.3 and 0.8 m error in the vertical direction.

Stöcker et al. (2015) demonstrated that using UAV and close-range photogrammetry integrated with terrestrial data could be employed in 3D digital modeling of intricate gully morphologies that are difficult to measure. The study was undertaken during the winter season for three months to assess multi-temporal 3D volume changes, and the integrated model had a resolution of 0.5 cm at an accuracy of 1 cm. It was also concluded that for the 170-m^2 gully area, the 5-m^3 positive volume balance was induced by human factors.

Using UAV, Peternel et al. (2017) conducted photogrammetry over a 22.5-month assessment timeframe to monitor and quantify the patterns of surface movement at a landslide in northwestern Slovenia. It was coupled with tachymetric geodetic data to ensure precise control of photogrammetric surface displacement analysis. According to the final analyses, the movement pattern near the toe of the landslide revealed a continuous downslope movement of the whole region, with isolated surges and shallow slides. Overall, the precision of the data points was evaluated using ground control point error, which was calculated by matching ground control point locations derived by photogrammetry to ground control positions recorded with a theodolite, and it varied from 0.02 to 0.03 m.

Eltner et al. (2015) employed UAV data to automatically measure rill and interrill loess soil erosion over a 600-m^2 field plot. Using SfM image processing techniques, high-resolution aerial footage obtained by a UAV was utilized to automatically build exact digital surface models of high spatial resolution. For multi-temporal change detection, they examined soil surface roughness, rill formation, and volumetric quantifications. Volumetric calculations indicated that erosion volumes were large, reaching up to 121 tons/ha during summer thunderstorm events, with an overall accuracy of less than 1 cm obtained from the digital surface models generated.

Culverts conveying water during flow event in Las Norias Canyon, Jicarilla Apache Nation. *Photo by Kevin M. Hobbs*

V. GEOTECHNICAL SITE INVESTIGATION

Faustin Kumah, Navid Mojtabai, and Mehrdad Razavi

INTRODUCTION

The details of the various soil mechanics tests conducted on the samples collected at the surface and at 6 in. of depth during the field investigation are presented here. Specific gravity, moisture content, direct shear, particle size distribution, and constant-head permeability were among the tests performed. A total of 19 samples were collected for analysis. Table 5.1 shows the sampling locations. Figures 5.1 through 5.3 show the sampling locations marked on aerial imagery.

MOISTURE CONTENT AND COLOR

Moisture content (MC) is the proportion of the mass of water to the mass of solids in a soil sample expressed as a percentage. This is determined by weighing the soil specimen, oven-drying it at approximately 110°C for 24 hr, and then weighing it again (ASTM D2216; Craig, 2004). The color (as determined using the Munsell Color Chart) and the summary of the results of the natural moisture content test are presented in Table 5.2.

Table 5.1. Sampling locations.

Waypoint	Latitude	Longitude	Elevation (m)
622	36.488164	-107.199764	2,099.80
623	36.487360	-107.199245	2,103.08
624	36.487217	-107.199336	2,104.31
625	36.486539	-107.199740	2,111.04
626	36.486294	-107.199862	2,121.67
627	36.485678	-107.200719	2,153.93
628	36.485701	-107.197138	2,112.64
629	36.489708	-107.201312	2,092.44
630	36.461983	-107.319756	2,013.39
631	36.461663	-107.320402	2,007.79
632	36.459268	-107.312613	2,017.24
633	36.459912	-107.312239	2,014.45
634	36.235714	-107.255007	2,175.18
635	36.236699	-107.255249	2,173.80
636	36.234032	-107.246143	2,203.12

Table 5.2. Natural moisture content (MC) and color of soil samples.

Waypoint	Sample Depth	MC (%)	Color
622	Surface	4.06	10 YR - 4/3 (Brown)
622	6 in.	9.32	10 YR - 4/3 (Brown)
623	Surface	6.76	2.5 YR - 4/3 (Olive brown)
623	6 in.	13.28	10 YR - 5/3 (Brown)
625	Surface	8.97	10 YR - 4/2 (Brown)
626	0–6 in.	3.80	2.5 YR - 5/3 (Light olive brown)
627	Surface	9.12	5 Y - 5/3 (Olive)
628	Surface	5.34	10 YR - 4/3 (Brown)
628	6 in.	12.00	10 YR - 4/3 (Brown)
629	Surface	3.64	10 YR - 5/3 (Brown)
629	6 in.	13.26	10 YR - 4/3 (Brown)
630	0–6 in.	4.90	10 YR - 5/3 (Brown)
631	Surface	1.22	10 YR - 5/3 (Brown)
632	Surface	1.53	10 YR - 5/3 (Brown)
633	Surface	1.86	10 YR - 5/3 (Brown)
634	Surface	3.75	10 YR - 5/3 (Brown)
635	Surface	5.77	10 YR - 5/3 (Brown)
636	Surface	2.85	10 YR - 5/3 (Brown)

Figure 5.1. Sampling locations at Site A. Refer to Figure 2.1 for locations of sampling sites.
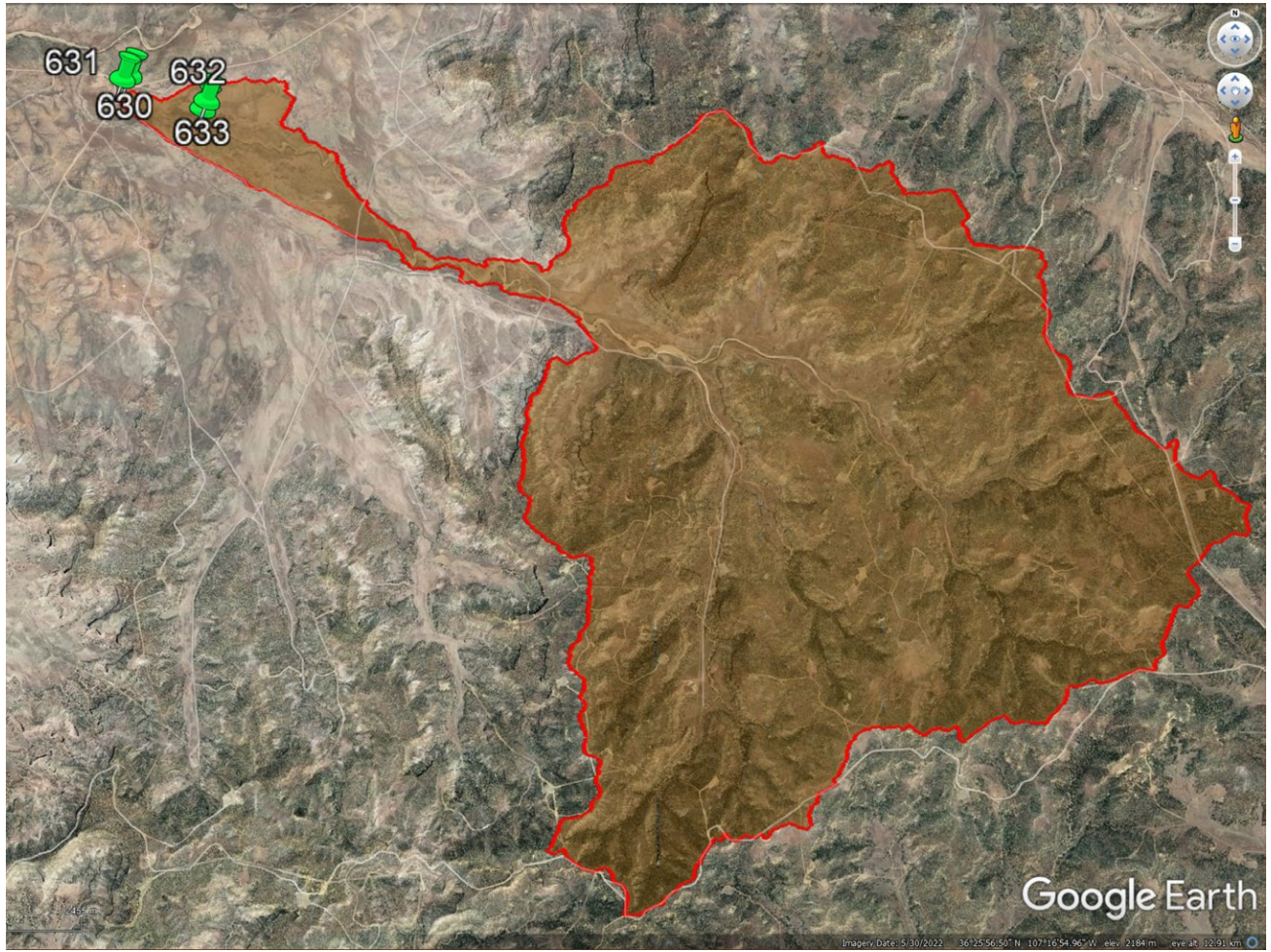
Figure 5.2. Sampling locations at Site B.
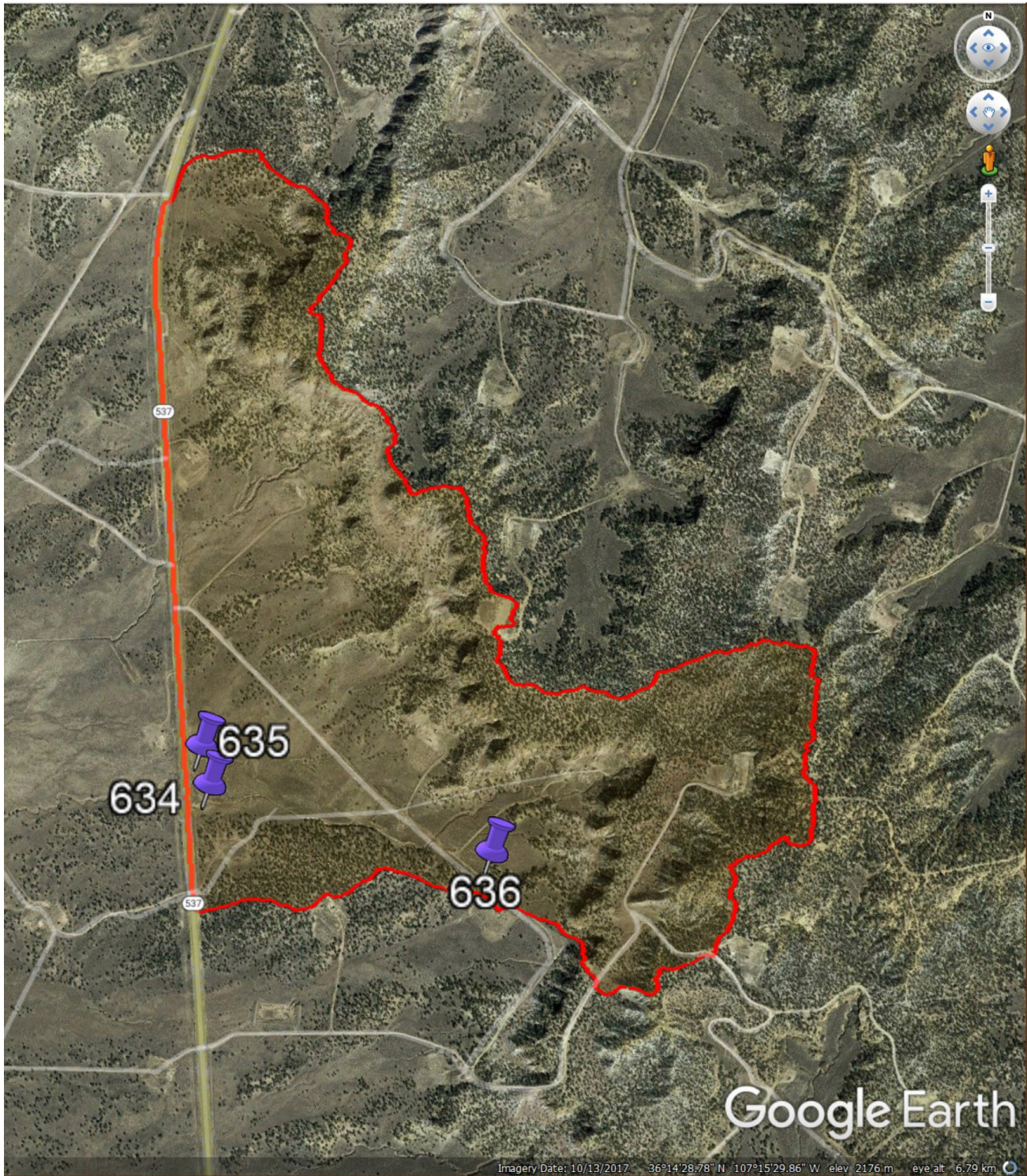
Figure 5.3. Sampling locations at Site C.

GRAIN SIZE DISTRIBUTION

The grain size distribution (GSD) of the soil specimen involves identifying the percentage mass of its particles in various ranges of standard sizes (Craig, 2004). A representative soil sample is oven-dried and run through a set of standard test sieves with decreasing mesh sizes using a sieve shaker (ASTM D-422). The mass of the soil specimen remaining on the individual sieves is measured, then the cumulative mass percentage of soil particles passing through the individual sieves is computed. The U.S. standard sieve numbers used in the stack are 4, 10, 40, 60, 100, 140, and 200. The GSD plots are shown in Figures 5.4 through 5.6.
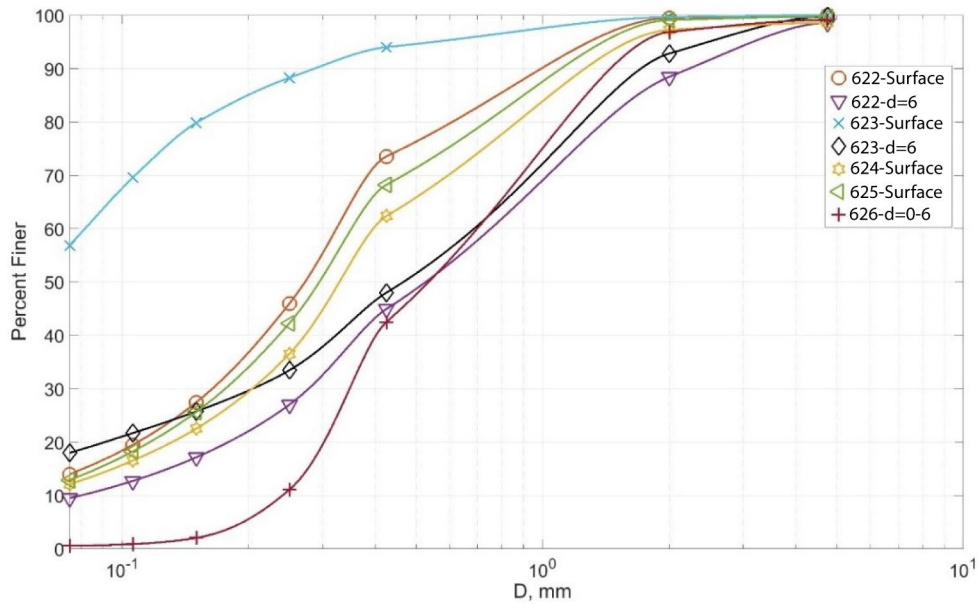
Figure 5.4. Percent finer vs. grain size (samples 622–626).
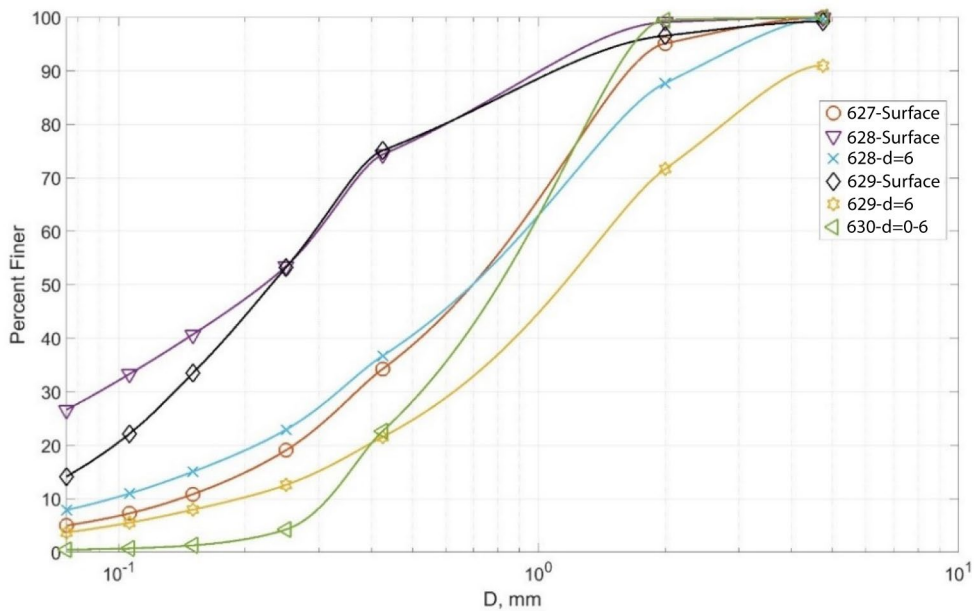
Figure 5.5. Percent finer vs. grain size (samples 627–630).

25
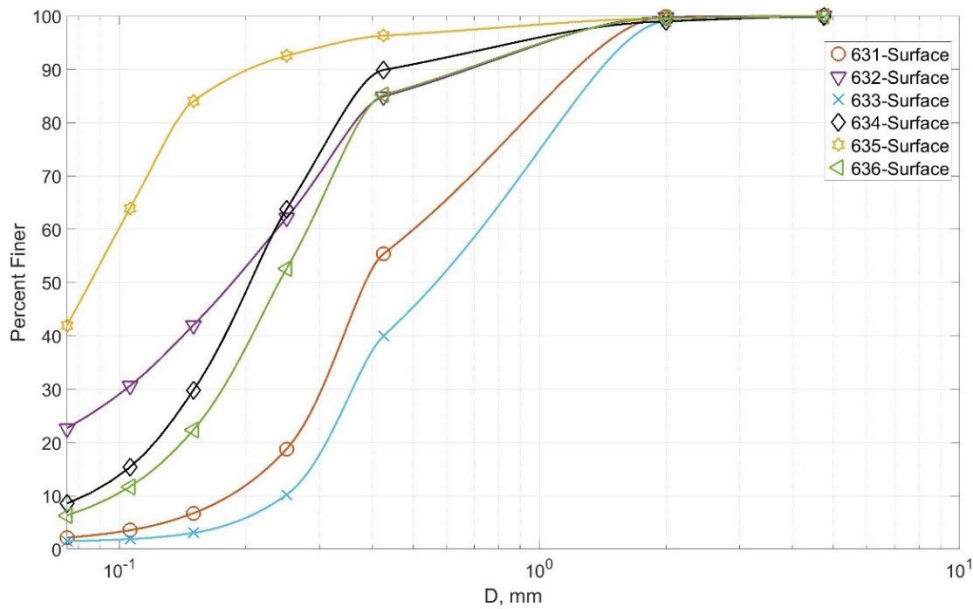
Figure 5.6. Percent finer vs. grain size (samples 631–636).

Specimens were characterized based on the Unified Soil Classification System (USCS), with the classification results shown in Table 5.3. Coarse samples (≥50% passing through U.S. standard number 4 sieve, but <50% passing through U.S. standard number 200 sieve) are classified as sands, and these were further defined as clean sand (<5% fine fraction passing through U.S. standard number 200 sieve) or sands with fines (>12% fine fraction passing through U.S. standard number 200 sieve). The soil sample collected at the surface at waypoint 623 is classified as fine-grained soil because it has more than 50% passing the U.S. standard number 200 sieve (>50% fine fraction). Generally, the plots of percent finer versus grain size for all the samples show a smooth, concave distribution typical of well-graded soils (Craig, 2004).

Figure 5.7 shows the gradation of soil samples after sieve analysis in the laboratory. No meaningful statistical correlation was found between the GSD and the elevation at the sampling locations. However, increasing the number of samples and spreading the locations over the entire study area may lead to a statistical correlation between the sampling location and GSD.

SPECIFIC GRAVITY

The specific gravity (G_S) of soil solids is defined as the ratio of the mass of soil particles to the mass of water (of an equivalent volume; Das and Sobhan, 2014). The specific gravity test was performed according to ASTM D-854. The summary of the specific gravity test results is shown in Table 5.4. The G_S ranges from 2.50 to 2.68, with the average G_S for all samples being 2.61, which is very close to the typical specific gravity of quartz (2.65).

PARTICLE SHAPE

Soil particles were analyzed using a microscope and determined to be sub-angular to angular. Figures 5.8 through 5.11 show images of soil particles taken using the microscope.

Table 5.3. USCS classification of soil samples.

Waypoint	Sample Depth	Gravel Fraction (%)	Sand Fraction (%)	Fine Fraction (%)	USCS Classification
622	Surface	0.04	85.99	13.97	Sands with fines
622	6 in.	1.47	89.05	9.48	Sands
623	Surface	0.00	43.16	56.84	Fine-grained
623	6 in.	0.24	81.79	17.97	Sands with fines
624	Surface	1.45	86.47	12.08	Sands with fines
625	Surface	0.28	86.85	12.87	Sands with fines
626	0–6 in.	0.88	98.56	0.56	Clean sands
627	Surface	0.08	94.94	4.98	Clean sands
628	Surface	0.04	73.34	26.62	Sands with fines
628	6 in.	0.32	91.83	7.85	Sands
629	Surface	0.80	85.09	14.11	Sands with fines
629	6 in.	9.02	87.31	3.67	Clean sands
630	0–6 in.	0.00	99.52	0.48	Clean sands
631	Surface	0.00	97.85	2.15	Clean sands
632	Surface	0.00	77.34	22.66	Sands with fines
633	Surface	0.12	98.40	1.48	Clean sands
634	Surface	0.12	91.34	8.54	Sands
635	Surface	0.00	58.08	41.92	Sands with fines
636	Surface	0.08	93.61	6.31	Sands

Table 5.4. Specific gravity results.

Waypoint	Sample Depth	Test I	Test II	Test III	Mean Specific Gravity
622	Surface	2.61	2.61	2.60	2.61
622	6 in.	2.59	2.59	2.56	2.58
623	Surface	2.50	2.50	2.50	2.50
623	6 in.	2.55	2.53	2.55	2.54
624	Surface	2.63	2.61	2.61	2.61
625	Surface	2.63	2.60	2.62	2.62
626	0–6 in.	2.64	2.67	2.63	2.65
627	Surface	2.59	2.61	2.61	2.60
628	Surface	2.55	2.55	2.50	2.54
628	6 in.	2.60	2.59	2.57	2.59
629	Surface	2.66	2.63	2.62	2.64
629	6 in.	2.60	2.63	2.64	2.62
630	0–6 in.	2.70	2.67	2.67	2.68
631	Surface	2.62	2.66	2.65	2.64
632	Surface	2.61	2.61	2.58	2.60
633	Surface	2.63	2.66	2.66	2.65
634	Surface	2.66	2.62	2.61	2.63
635	Surface	2.61	2.62	2.59	2.61
636	Surface	2.62	2.64	2.64	2.63
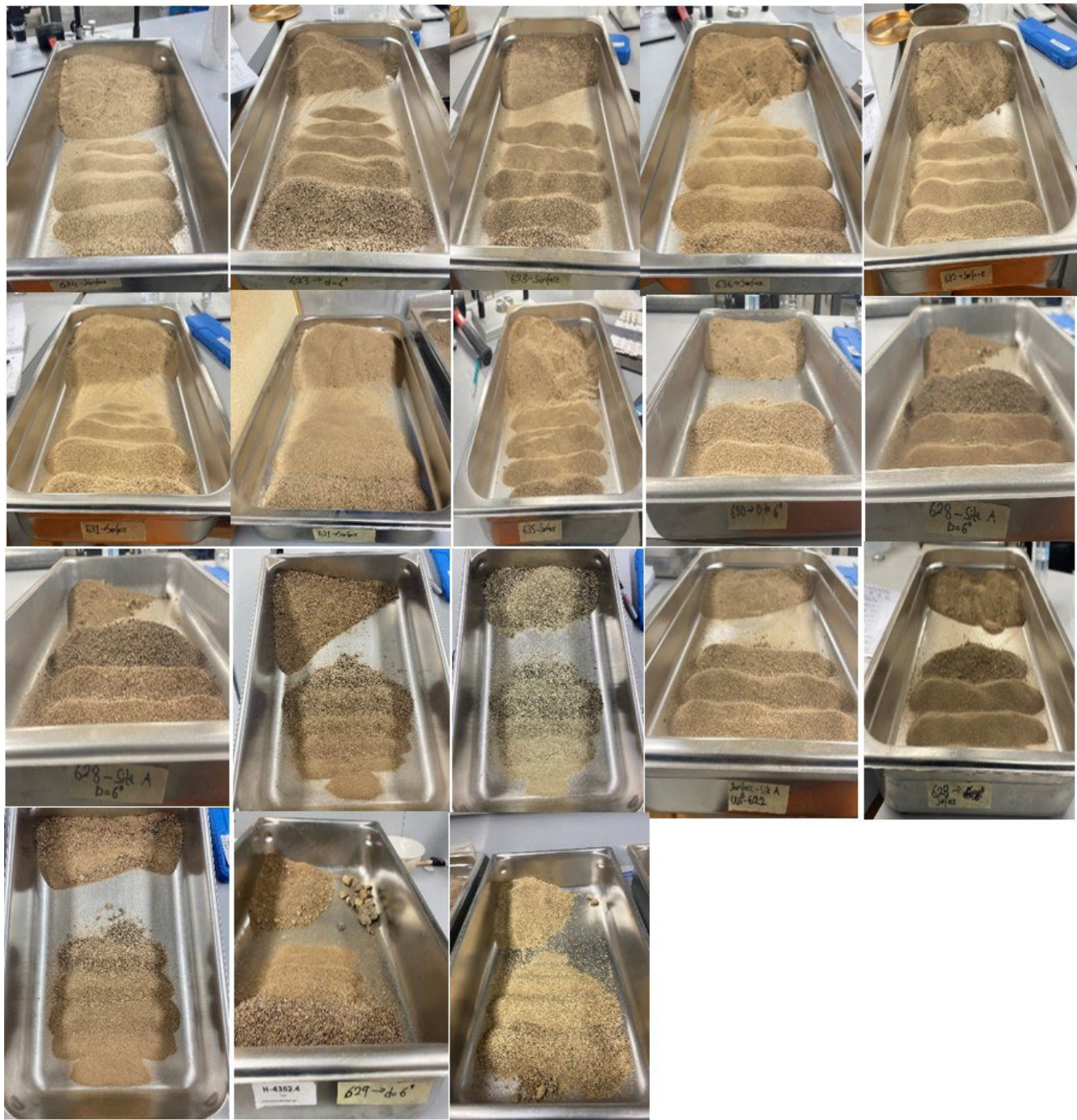
Figure 5.7. Gradation of soil samples after sieve analysis in the lab.

Figure 5.8. Particle shape (sample 624, surface).

Figure 5.9. Particle shape (sample 626, 0–6 in.).

Figure 5.10. Particle shape (sample 631, surface).

Figure 5.11. Particle shape (sample 636, surface).

DIRECT SHEAR TEST

In order to estimate the soil's angle of internal friction, ϕ, which measures its resistance to failure, the direct shear test was conducted. Three samples from each site were analyzed according to ASTM D-3080. The results of this test are summarized in Table 5.5. The ϕ values obtained fall within the range of loose to medium sand with angular grains as presented in Das and Sobhan (2014). The angularity of the soil particles is also evident in the particle shape analyzed under the microscope.

CONSTANT HEAD PERMEABILITY

To determine the soil's hydraulic conductivity (K), the constant head permeability test was performed according to ASTM D-2434. It is a function of the mean size of the pores in the soil. The K values obtained are within the range of very fine sand (Table 5.6), as presented in Craig (2004).

Table 5.5. Direct shear test results.

Waypoint	Sample Depth	Angle of Internal Friction (°)
622	6 in.	36
623	6 in.	38
624	Surface	40
626	0–6 in.	41
627	Surface	34
631	Surface	39
632	Surface	35
635	Surface	40
636	Surface	32

Table 5.6. Coefficient of permeability results.

Waypoint	Sample Depth	K (20°C, cm/s)
629	6 in.	3.4×10^{-3}
631	Surface	7.3×10^{-2}
627	Surface	2.9×10^{-3}
632	Surface	5.2×10^{-2}
635	Surface	8.5×10^{-3}
636	Surface	7.4×10^{-2}

Aerial photograph of roads, culverts, and cutbanks on Las Norias Canyon, Jicarilla Apache Nation. *Photo by New Mexico Bureau of Geology*

VI. CLOSE-RANGE PHOTOGRAMMETRY

Faustin Kumah, Navid Mojtabai, Mehrdad Razavi, and Kevin M. Hobbs

INTRODUCTION

In order to document and quantify erosion and sedimentation at three study sites in the upper Cañon Largo watershed, we conducted UAV-based photogrammetric surveys over an 11-month study period. Photographs collected via UAV were used to create high-resolution topographic models of the study sites. Comparisons of these models allow us to document elevation change related to sedimentation and erosion. The UAV photogrammetric workflow is categorized into three different phases: aerial data acquisition, data processing, and, lastly, analysis of processed imagery. The subsequent sections discuss each stage.

METHODS

Data acquisition

Four field campaigns took place on 17 August 2021, 16 November 2021, 28 July 2022, and 29 July 2022. However, on 29 July 2022, data could only be acquired for Site C due to limited battery capacity and a precipitation event.

We acquired georeferenced images by establishing an autonomous flight plan for the study areas. This study used the DJI Phantom 4 Pro UAV for image acquisition using the DJI FC6310 sRGB camera. The images had a 3:2 aspect ratio with dimensions of 5472 × 3648 pixels at 72 dots per inch (dpi) and a 100 ISO value. The flights were completed at 395 ft above ground level (between 2,000 and 2,200 m above sea level, depending on ground level elevation) to obtain high-resolution imagery. Approximately 443 to 956 images per field campaign per study area were taken, and the camera parameters were fixed for each photogrammetric survey. This

study's estimated ground sampling distance (GSD) at that altitude is 3.25 cm/pixel. Theoretically, the GSD is computed as follows (Arriola-Valverde et al., 2020):

$$GSD \left(\frac{cm}{pixel} \right) = \frac{100 \times S \times h}{f_l \times I_w}$$

where S is the image sensor width in millimeters, h is the height of flight in meters, f_l is the focal length of the image sensor in millimeters, and I_w is the sensor resolution in pixels.

Eight square ground control points (GCP; 24 × 24 in.) with a defined coordinate system were installed on each study area and assessed repeatedly during the survey period to ensure the consistency of each photogrammetric survey and to increase the accuracy of the triangulation process. These GCPs are shown in Figures 6.1 through 6.3 for each of the drone sites. A Trimble CenterPoint RTX GPS with Zephyr 2 antenna was used to define the coordinates and elevations of the GCPs (Table 6.1); the horizontal accuracy was <1 cm and the vertical accuracy was <2.5 cm at each site. Finally, the drone images were saved in JPG format and exported for processing.

Table 6.1. Coordinates and elevations of ground control points.

GCP	Northing	Easting	Elevation (m above sea level)
a1a	4040170.0	303240.4	2,105.63
a1b	4040064.0	303183.4	2,105.57
a1c	4040225.0	303172.9	2,103.58
a1d	4040261.0	303000.3	2,100.50
a1e	4040388.0	302997.0	2,098.90
a1f	4040432.0	302795.4	2,095.86
a1g	4040481.0	302844.0	2,094.05
a1h	4040541.0	302759.9	2,091.93
b1a	4037376.0	293055.1	2,018.18
b1b	4037306.0	293000.1	2,017.81
b1c	4037425.0	292730.2	2,014.58
b1d	4037484.0	292608.3	2,011.87
b1e	4037505.0	292456.4	2,009.07
b1f	4037476.0	292403.9	2,008.59
b1g	4037614.0	292261.4	2,007.76
b1h	4037664.0	292126.9	2,005.96
c1a	4012397.0	298227.7	2,212.53
c1b	4012418.0	298130.9	2,202.59
c1c	4012490.0	298016.5	2,202.76
c1d	4012422.0	297884.6	2,194.45
c1e	4012473.0	297729.7	2,188.64
c1f	4012473.0	297537.7	2,181.81
c1g	4012527.0	297343.1	2,176.85
c1h	4012483.0	297264.1	2,173.20

Data processing

PhotoModeler Premium (version 2022.2.0.127), a close-range photogrammetry and image-based modeling application software developed by PhotoModeler Technologies (Vancouver, Canada), was utilized for image processing. The defined coordinate and elevation values of the GCPs in comma-separated values (CSV) file format and UAV imagery were imported into the software. Ground control points are typically used in photogrammetric workflows to facilitate stereo-model construction and geometrical referencing through triangulation of the bundle block (d'Oleire-Oltmanns et al., 2012). After data importation, the imported coordinates (x, y, z) are assigned to matching GCPs on the imported drone imagery, as shown in Figure 6.4.

From camera calibration through digital surface model (DSM) reconstruction, PhotoModeler features a fully integrated workflow that includes both dense and sparse point cloud, mesh, and texture calculations. A dense point cloud of the 3D model is created and exported as a CSV file for image analysis in MATLAB. Before the dense point clouds were created, it was ensured that the overall residuals at the end of image processing were below 3.0. Figures 6.5 through 6.7 show the 3D models generated for the three sites.

Image analysis

The dense point cloud (in CSV format) for each site was imported into MATLAB. A MATLAB code, called the soil erosion-deposition (SED) code, was developed to compare the 3D point clouds at two different times to determine the volumes of the eroded and deposited materials. The SED code can plot erosion contours, deposition contours, and 3D views of the ground elevations (Fig. 6.8). The DSMs reconstructed from August drone imagery were compared with DSMs reconstructed from 28 July 2022 drone imagery. Then, various output products were analyzed, including the elevation contours and erosion-deposition contours showing areas of soil gain (deposition) and soil loss (erosion), to quantify the total soil loss or gain volume per unit area.

The accuracy of the DSMs generated from the photogrammetric process was assessed by comparing the elevation of the visible immovable features, such as the road, in August 2021 and July 2022. To validate the output of PhotoModeler, ArcGIS Drone2Map software was also used to reconstruct the DSM of the sites using all photos and only nadir images, with the nadir imagery producing a higher accuracy. Accuracies of approximately 3 cm and 30 cm for the z-values were observed for DSM analyses done using ArcGIS Drone2Map (using only the nadir drone images) and Photomodeler, respectively. The 3-cm accuracy could not be replicated using PhotoModeler even after oblique images were removed to reconstruct the DSM. These accuracies were then used to generate a range of soil erosion and deposition volumes using the SED code by adjusting the z-values of the point cloud in MATLAB.
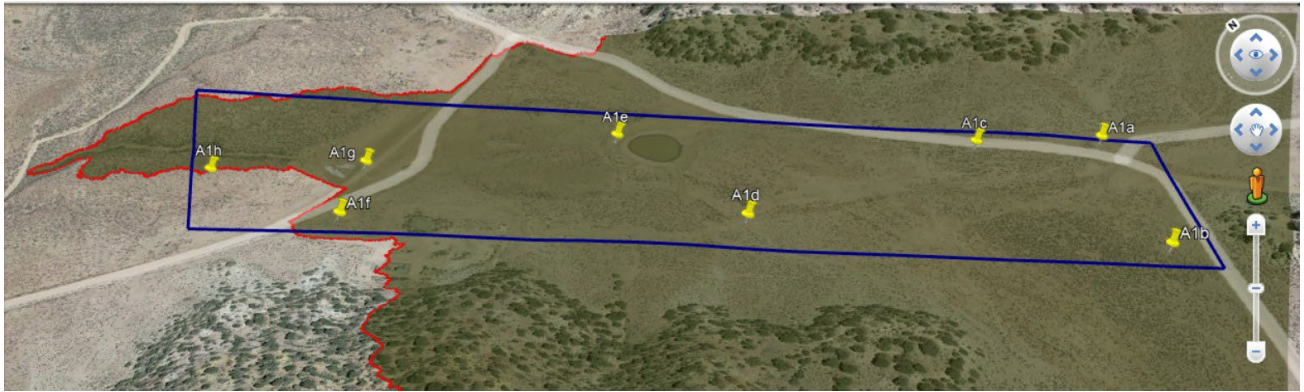
Figure 6.1. Boundaries of the aerial photography zone in Site A.
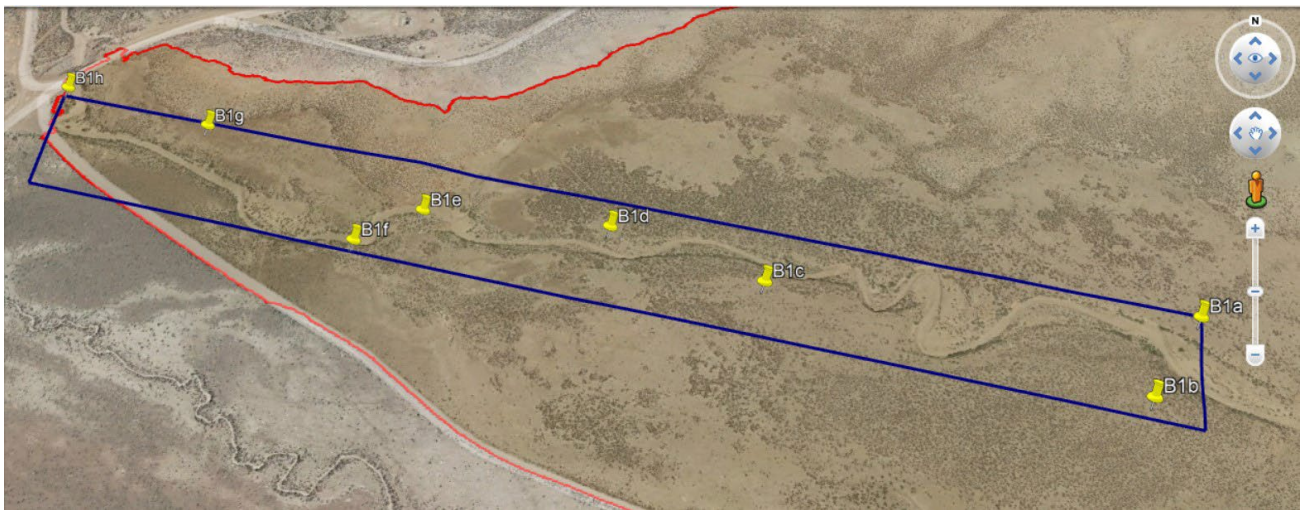
Figure 6.2. Boundaries of the aerial photography zone in Site B.

Figure 6.3. Boundaries of the aerial photography zone in Site C.
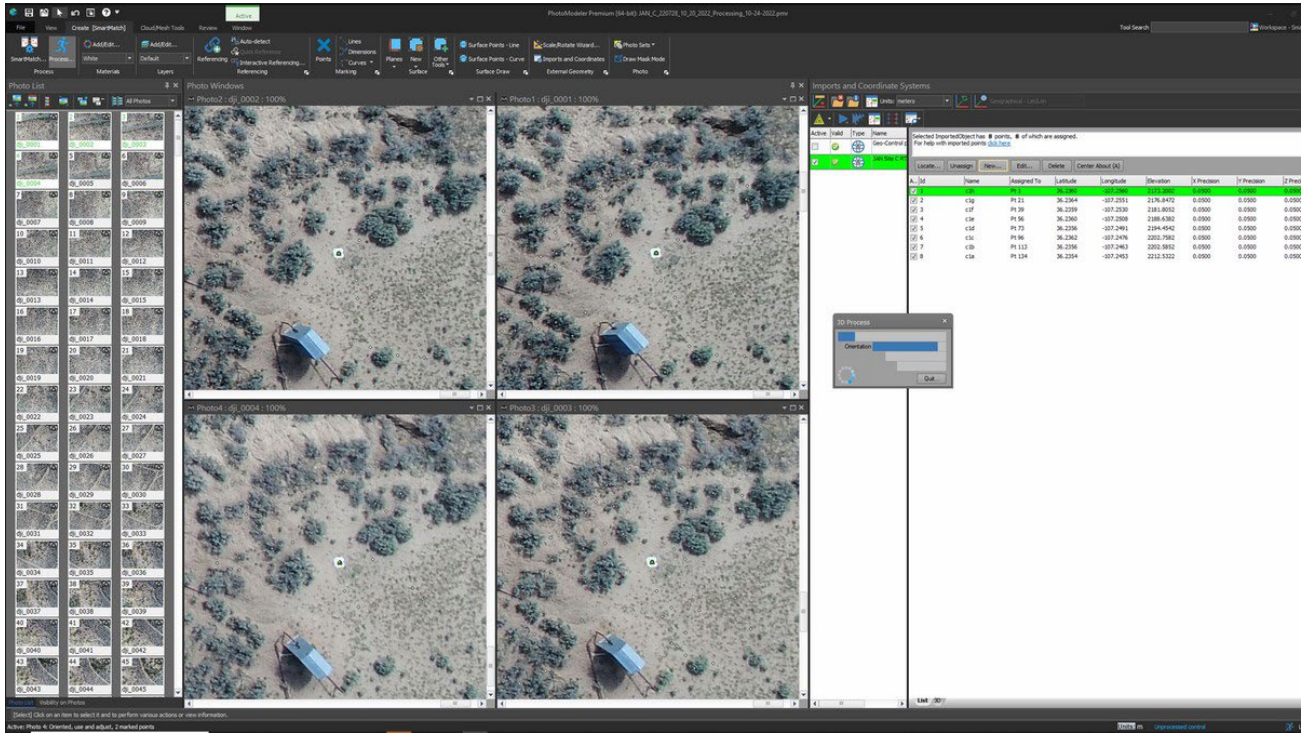
Figure 6.4. Data processing in PhotoModeler.
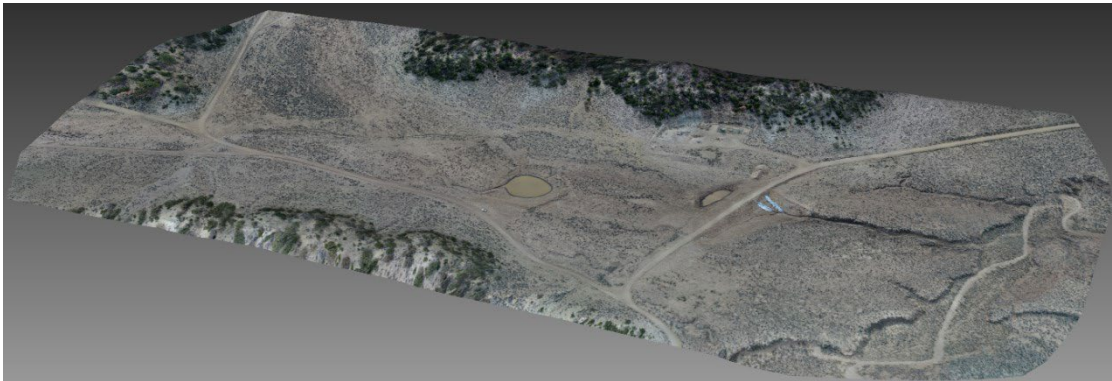
Figure 6.5. 3D model of the photographed zone in Site A.
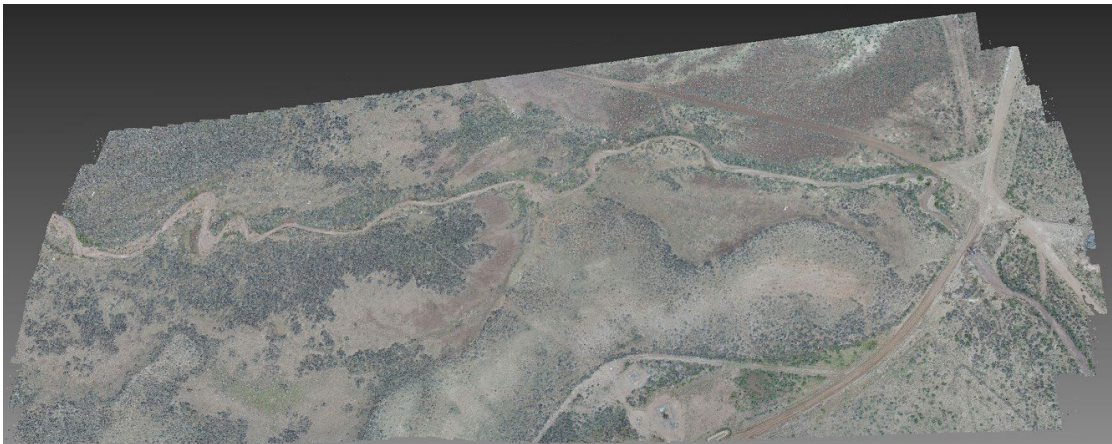
Figure 6.6. 3D model of the photographed zone in Site B.
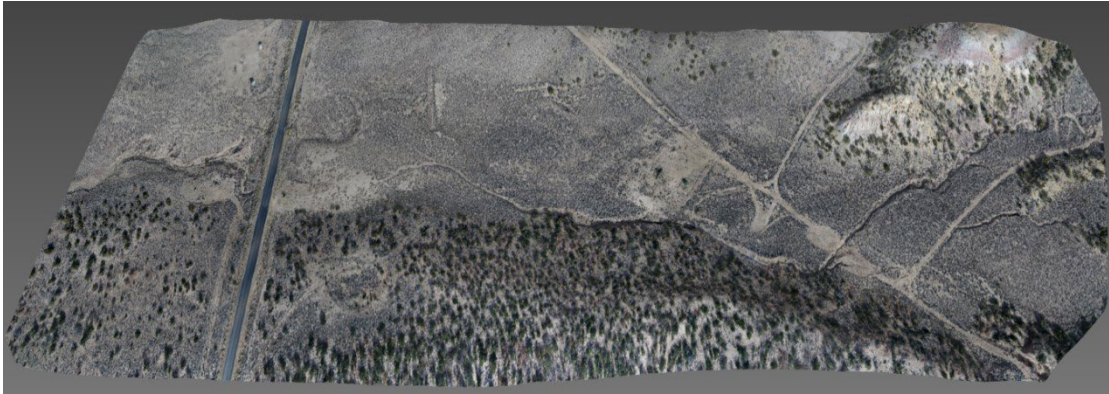
Figure 6.7. 3D model of the photographed zone in Site C.
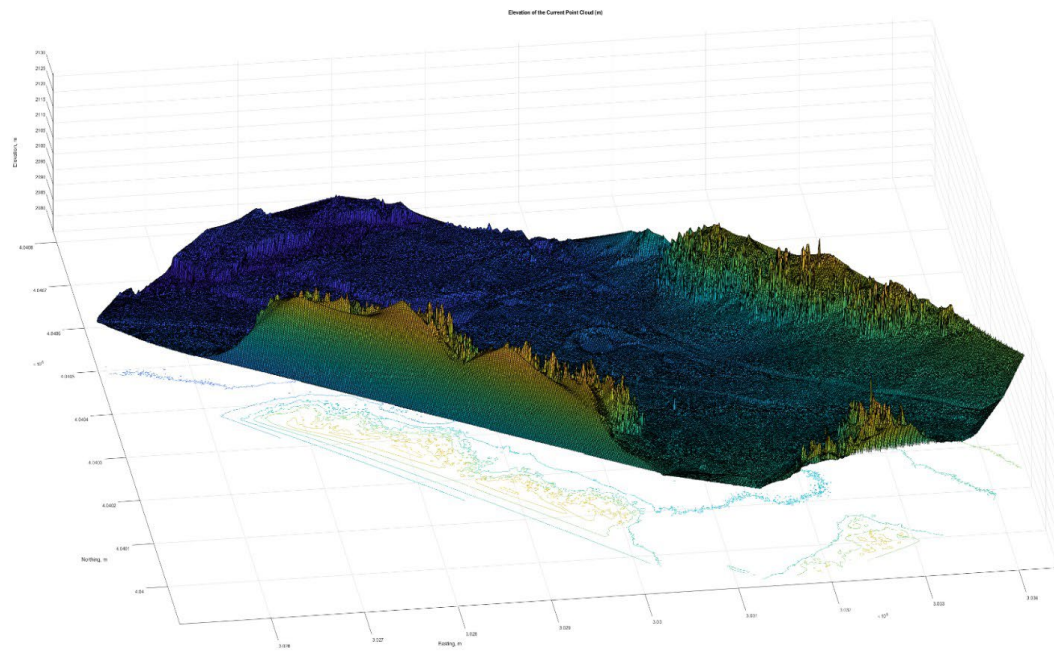
Figure 6.8. Point cloud for Site A generated using the SED code.

RESULTS

Maps derived from intermediate DSMs, digital terrain models, and orthomosaics are included in Appendix 1; GIS data of these models and orthomosaics can be requested free of charge from NMBGMR at https://geoinfo.nmt.edu/. Drone2Map- and PhotoModeler-generated point clouds were analyzed using the SED code in the MATLAB environment to compare the point clouds. PhotoModeler results yielded inaccuracies over ten times greater than those derived from Drone2Map analyses; they are therefore not presented in graphical form here. Figures 6.9 through 6.11 show erosion (yellow-orange-red) and deposition (green-blue) zones from Drone2Map analyses. The majority of all three sites experienced less than 5 cm of elevation change during the study period.

Tables 6.2 and 6.3 show soil loss results obtained from image processing analyses obtained from both Drone2Map and PhotoModeler; Table 6.2 shows Drone2Map results and Table 6.3 summarizes the range of PhotoModeler results obtained from the various analyses.

Table 6.2. Estimates of soil loss at three study sites based on Drone2Map digital elevation model results using SED code.

Site	Average Soil Loss per Unit Area (m^3/m^2)	Average Soil Gain per Unit Area (m^3/m^2)	Total Soil Loss Volume (m^3)	Total Soil Gain Volume (m^3)	Image Area (m^2)
A	0.0138	0.1297	3,500.4	32,805	252,950
B	0.0202	0.0298	8,128.9	12,008	402,350
C	0.0127	0.1006	4,421.5	35,166	349,420

Table 6.3. Minimum and maximum soil loss estimates at three study sites based on parametric analyses using SED code and PhotoModeler digital elevation map results.

	Average Soil Loss per Unit Area (m^3/m^2)	Average Soil Gain per Unit Area (m^3/m^2)	Total Soil Loss Volume (m^3)	Total Soil Gain Volume (m^3)
Site A-Min	0.2269	0.1273	101,410	56,874
Site A-Max	0.5430	0.7256	242,640	324,220
Site B-Min	0.0042	0.1018	2,695	65,754
Site B-Max	0.2190	0.8013	141,470	517,590
Site C-Min	0.0759	0.0691	44,720	100,410
Site C-Max	0.4867	0.5728	286,570	406,830

Elevation change between August 17, 2021, and July 28, 2022, at Study Site A. Background orthophotomosaic was collected via UAV on July 28, 2022. Legend values are in meters. Areas on map that are not colored represent values of elevation change less than 0.05 m. The two areas of significant elevation gain in the north-center portion of the map are areas with standing water during at least one of the UAV flights; the calculated values in those two areas do not reflect real conditions.

Figure 6.9. Drone2Map-derived estimates of elevation change at Site A.
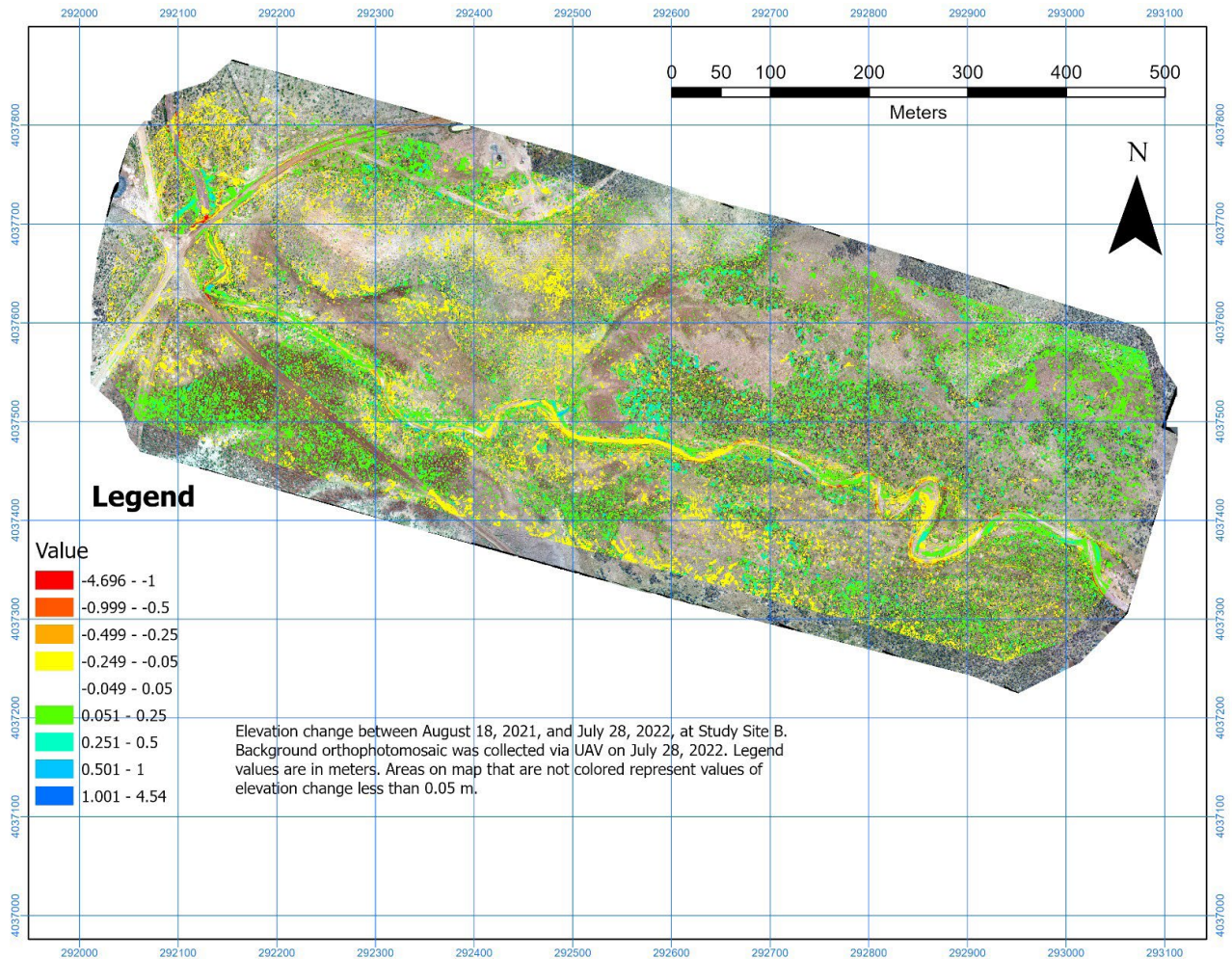
Figure 6.10. Drone2Map-derived estimates of elevation change at Site B.
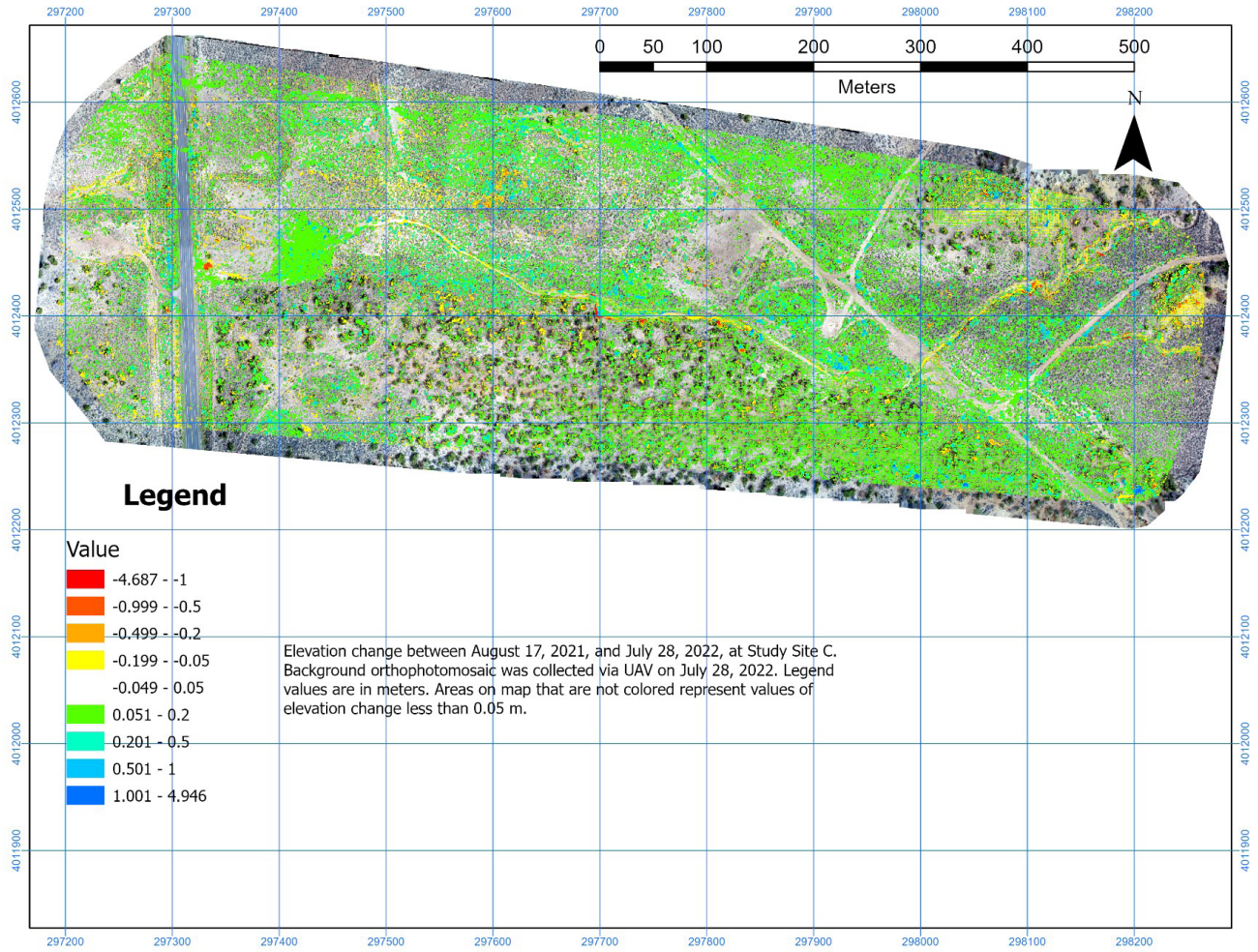
Figure 6.11. Drone2Map-derived estimates of elevation change at Site C.

DISCUSSION

In areas lacking woody vegetation, the close-range photogrammetry results above accurately record erosion- and sedimentation-induced elevation changes as small as 3 cm. This is useful in areas of significant sedimentation, such as alluvial fans, gully-mouth fans, and arroyo beds. Dispersed sedimentation over wide areas is more difficult to quantify with this method, especially if it occurs among woody vegetation. As seen in Figures 6.9 through 6.11, this method captures elevation changes related to changes in vegetation height. True lidar (light detection and ranging) analyses can remove vegetation-induced issues with photogrammetry if elevation changes among woody vegetation require quantification in future studies.

Estimates of soil loss derived from Drone2Map analyses (Table 6.2) are on the same order of magnitude as those derived from sediment transport analyses (Table 8.6) using entirely different techniques. Because of these similarities, there can be some confidence in UAV-derived estimates of sedimentation and erosion in the study area.

Future UAV-derived close-range photogrammetry surveys can benefit from planning surveys at times when sun angle and elevation are similar to previous surveys in order to minimize shadow effects. Overcast weather conditions produce more accurate results than do bright, sunny conditions due to the strong contrast between light and shadow during sunny conditions.

VII. PROCESS RATE DATA

Kevin M. Hobbs

INTRODUCTION

Determining the rates of erosion and sedimentation processes in the study area requires some understanding of the magnitude of erosion and sedimentation changes that might affect infrastructure. For instance, the incision (here defined as focused, downward erosion of a stream caused by flowing water; i.e., erosive deepening) of an arroyo or rill to an arbitrary depth of 50 cm is likely to occur during nearly any high-intensity, short-duration precipitation event in the Cañon Largo watershed and is easy to recognize with either repeat field observation or remote sensing techniques. The incision of arroyos or rills to a depth of 5 cm, however, is much more difficult to recognize but more likely to occur even in lower-intensity (and therefore more common) precipitation events. Even low-magnitude erosion in the study area is likely to occur as focused incision during one erosion event rather than as overall landscape lowering during the same erosion event. In other words, single-event erosion occurs mostly in stream channels or rill bottoms (Fig. 7.1). Given time, however, the location of incision varies as streams and rills migrate across a landscape, and the cumulative effects of many single erosion events can lead to the lowering of an entire landscape.

Whereas incision is likely to be concentrated in isolated localities in arroyos or rills, sedimentation can occur over broader areas. Because of this, the observed effects of sedimentation often are geographically less concentrated than the effects of erosion and are best monitored with repeat elevation surveys (e.g., Fig. 7.2). Sedimentation does occur in the beds of arroyos; in fact, sedimentation in arroyos is a regular subject of study among arid-regions geomorphologists, and seems to be intrinsic to the evolution of arroyo systems (Schumm and Hadley, 1957; Bull, 1997). Arroyo-bed sedimentation,

however, is unlikely to affect infrastructure given the lack of infrastructure in arroyo beds. This study therefore focused on sedimentation occurring outside of arroyo beds.

We applied three methods to estimate the rates of sedimentation and erosion in the upper Cañon Largo watershed on the Jicarilla Apache Nation. First, we obtained dates from organic material buried in alluvial sediments in large valleys (Fig. 7.3). The ages of these organic materials are assumed to be essentially the date of sedimentation, for reasons detailed below. These dates allow us to estimate the timing of large-scale sedimentation episodes whose duration is measured in hundreds to thousands of years. Erosion and/or sedimentation episodes that are determined by this method have larger magnitude and longer duration than those determined by other methods described below. However, this method does not allow the same level of precision in estimates of timing or sediment volume as do other methods.

Second, we analyzed historical aerial photographs of key locations within the study area in order to determine the lateral migration of stream channels and their associated cutbanks. The migration of cutbanks in large valleys does not necessarily deepen arroyos, but it both increases sediment load of streams as well as detrimentally affects infrastructure. The time scales of erosion episodes elucidated with this method range from years to decades.

Third, we conducted repeat elevation surveys of three study sites within the upper Cañon Largo watershed in order to quantify centimeter-scale sedimentation and erosion over the period of study in 2021 and 2022. To complete this method, we employed an uncrewed aerial vehicle (UAV) to collect overlapping aerial photographs of the three study sites. The photographs were then converted to digital elevation models that were analyzed in GIS to
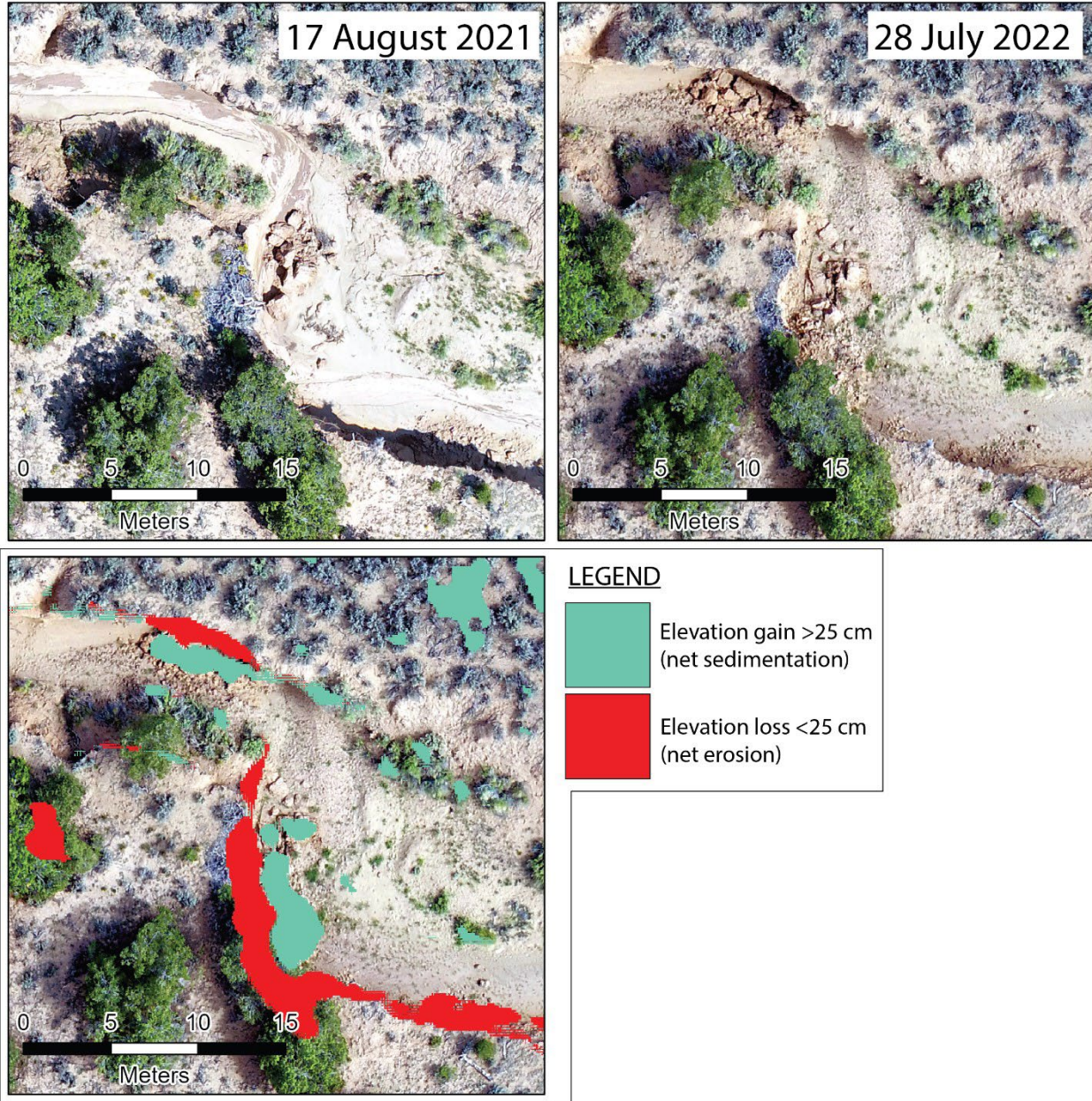
Figure 7.1. Top: Repeat photographs showing an arroyo in Site C in August 2021 and July 2022. Bottom: Annotated photograph showing areas of elevation loss (red) and gain (green) over the 12-month study period. All elevation loss in this reach was due to bank collapse.
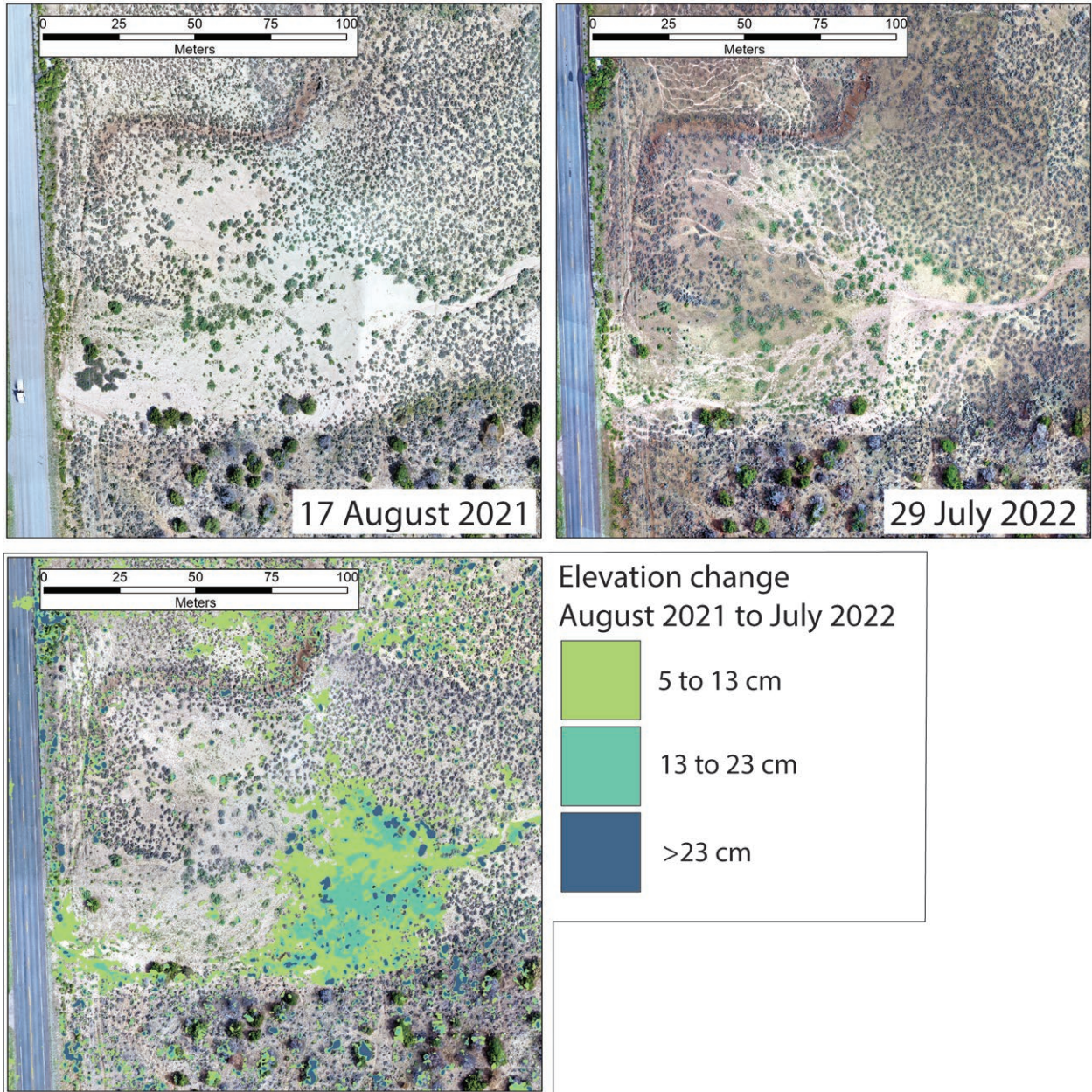
Figure 7.2. Top: Repeat photographs showing an alluvial fan in Site C in August 2021 and July 2022. New Mexico Highway 537 is in the far left of the images. Bottom: Annotated photograph showing areas and magnitudes of sedimentation over the 12-month study period.

Figure 7.3. Sediment-hosted charcoal from older alluvium (map unit Qao) in Tapicito Creek at 36.494481° N, -107.197067° W. Black arrows point to concentrations or large individual pieces of charcoal. The sediment hosting the charcoal is a weakly consolidated silty fine to medium sand. This charcoal was dated to 3,700 ± 30 YBP. Note: The scale was accidentally placed upside down in the field; the photograph is right side up.

determine elevation changes during the study period. The time scales of erosion and/or sedimentation episodes revealed with this method range from days to weeks; the entire study period was approximately 11 months. The magnitude of sedimentation and erosion detectable with this method is as low as 3 cm.

METHODS

Sediment-hosted charcoal was collected in the field while mapping for the *Geologic Map of the Cañon Largo Watershed on the Jicarilla Apache Nation, Rio Arriba and Sandoval Counties, New Mexico*. The sediments hosting the charcoal were described and measured using standard stratigraphic and geologic mapping techniques. Only charcoal was collected for radiometric dating due to its inability to form in-situ, unlike other organic particles that might reflect post-depositional processes (for instance, a wood fragment hosted in alluvial sediments might have been buried during sediment deposition and therefore yield a radiometric age similar to that of the depositional age of the sediments it is found within, or it might be a fragment of a tree root that grew into the sediments many thousands of years after sediment deposition). Charcoal was collected in aluminum foil and shipped to Beta Analytic Inc., a commercial radiometric dating laboratory in Miami, Florida. There, the individual charcoal samples were radiocarbon dated using accelerated mass spectrometry methods. All samples were consumed during analysis.

Lateral migration of cutbanks was estimated using historical aerial photographs available on Google Earth. For all sites, the oldest available imagery dates were from October 1997, and the most-recent imagery dates were either from October 2019 or May 2022. The distance of lateral migration was measured to the nearest meter with the "Ruler" tool in the Google Earth program. Sites were selected

based on the magnitude of cutbank migration and proximity to infrastructure. The areas with the greatest lateral migration include Tapicito Creek downstream of Wild Horse Canyon, Cañada Larga downstream of New Mexico Highway 537, and Cañon Largo downstream of Venado Canyon.

Photographs were collected via UAV at study Sites A, B, and C in August and November 2021 and in July 2022. We collected a total of 6,874 photographs: 1,490 at Site A, 2,519 at Site B, and 2,865 at Site C. Photographs from each flight were loaded into ArcGIS Drone2Map software. We placed eight 61 × 61 cm ground control points (GCPs) on semi-permanent stakes in each study area; the stakes remained in place throughout the study. The latitude, longitude, and elevation of each GCP was surveyed via RTX GPS to an accuracy of <3 cm vertically and <2 cm horizontally. Each of the GCPs was identified in at least 10 individual UAV photographs as a registration marker. The photographs were mosaicked, then processed into a digital surface model (DSM) and digital terrain model (DTM) by Drone2Map. The photomosaic, DSM, and DTM rasters were analyzed in ArcGIS Pro. The DSM and DTM rasters were clipped to a standard area in order to eliminate edge-matching issues; less than 5% was removed around the edges of any raster. We used the Raster Calculator tool to subtract the earlier raster from the later raster (for instance, [July2022Raster] - [August2021Raster]), creating a digital elevation map (DEM) of difference raster. This DEM of difference raster shows elevation change during the study period and is the final analysis product for repeat UAV surveys.

RESULTS

Radiocarbon dating of sediment-hosted charcoal

Twelve sediment-hosted charcoal samples from three map units (young alluvium, older alluvium, and sheetwash deposits) yielded radiocarbon ages ranging from 500 ± 30 YBP to 8,000 ± 50 YBP. Results are summarized in Table 7.1. Full results are included in Appendix A of the *Geologic Map of the Cañon Largo Watershed on the Jicarilla Apache Nation, Rio Arriba and Sandoval Counties, New Mexico*.

Cutbank lateral migration rates

The 12 highest-magnitude selected cutbank sites in the study area underwent lateral migration of 29 to 122 m over a 22-year (3 sites) or 25-year (9 sites) period (Table 7.2). Cutbank lateral migration occurred at rates of 1.16 to 4.88 m/yr. Figures 7.4 through 7.15 show the most-recent available aerial imagery of each location annotated with the position of the cutbank in 1997 (the date of the earliest available aerial imagery) and the path of measurement of cutbank lateral migration.

Table 7.1. Summary ^{14}C ages from charcoal collected within surficial units in the upper Cañon Largo watershed on the Jicarilla Apache Nation.

Summary [14]C Ages from Charcoal within Surficial Sediments in Map Area

Sample Name	Age (YBP)	Latitude	Longitude	Depth Below Surface (cm)	Map Unit
JAN21-01	3,700	36.494481	-107.197067	410	Qao
JAN21-07	1,480	36.459912	-107.312239	300	Qao
JANC-02	2,030	36.228640	-107.380353	400	Qao
JANC-03	4,720	36.253817	-107.382444	200	Qao
JANC-11	1,560	36.320341	-107.220894	400	Qao
JANC-01	8,000	36.304107	-107.204801	400	Qao
JAN21-02	820	36.321576	-107.219529	360	Qay
JAN21-03	950	36.321576	-107.219529	195	Qay
JAN21-04	1,380	36.321685	-107.218415	60	Qay
JANC-08	500	36.323808	-107.406811	70	Qay
JANC-09	560	36.323534	-107.405494	190	Qay/Qf?
JAN21-05	5,810	36.362208	-107.248347	400	Qsw

Note: Margins of error can be found in appendix A of the *Geologic Map of the Cañon Largo Watershed on the Jicarilla Apache Nation, Rio Arriba and Sandoval Counties, New Mexico* report. Geographic coordinates recorded with handheld GPS in NAD83 datum; typical error is ± 4 m. All analyses performed at Beta Analytics Inc.

Table 7.2. Summary data for measured cutbank migration in the upper Cañon Largo watershed. All sites were selected based on their magnitude of lateral cutbank migration, proximity to infrastructure, and alluvial units affected. All sites' cutbanks are eroding into map unit Qao, which is likely to be at least 1,000 years old.

Summary Cutbank Migration Data from Upper Cañon Largo Watershed

Site Number	Initial Photo Date	Final Photo Date	Cutbank Migration Distance (m)	Rate of Migration (m/yr)	Latitude	Longitude
1	1997	2022	29	1.16	36.482	-107.269
2	1997	2022	36	1.44	36.446	-107.403
3	1997	2022	34	1.36	36.443	-107.441
4	1997	2022	34	1.36	36.323	-107.387
5	1997	2022	45	1.80	36.309	-107.329
6	1997	2022	50	2.00	36.320	-107.227
7	1997	2022	45	1.80	36.318	-107.166
8	1997	2019	40	1.82	36.319	-107.159
9	1997	2019	36	1.64	36.304	-107.205
10	1997	2019	45	2.05	36.254	-107.382
11	1997	2022	122	4.88	36.319	-107.413
12	1997	2022	38	1.52	36.468	-107.313

Red line: position of cutbank in 1997.
Yellow line: cutbank migration distance of 29 m.
Lat/long: 36.482°N, -107.269°W

Figure 7.4. Cutbank migration measurement Site 1.

Red line: position of cutbank in 1997.
Yellow line: cutbank migration distance of 36 m.
Lat/long: 36.446°N, -107.403°W

Figure 7.5. Cutbank migration measurement Site 2.

Red line: position of cutbank in 1997.
Yellow line: cutbank migration distance of 34 m.
Lat/long: 36.443°N, -107.441°W

Figure 7.6. Cutbank migration measurement Site 3.

Red line: position of cutbank in 1997.
Yellow line: cutbank migration distance of 34 m.
Lat/long: 36.323°N, -107.387°W

Figure 7.7. Cutbank migration measurement Site 4.

Red line: position of cutbank in 1997.
Yellow line: cutbank migration distance of 45 m.
Lat/long: 36.309°N, -107.329°W

Figure 7.8. Cutbank migration measurement Site 5.

Red line: position of cutbank in 1997.
Yellow line: cutbank migration distance of 50 m.
Lat/long: 36.320°N, -107.227°W

Figure 7.9. Cutbank migration measurement Site 6.

Red line: position of cutbank in 1997.
Yellow line: cutbank migration distance of 45 m.
Lat/long: 36.318°N, -107.166°W

Figure 7.10. Cutbank migration measurement Site 7.

Red line: position of cutbank in 1997.
Yellow line: cutbank migration distance of 40 m.
Lat/long: 36.319°N, -107.159°W

Figure 7.11. Cutbank migration measurement Site 8.

Red line: position of cutbank in 1997.
Yellow line: cutbank migration distance of 36 m.
Lat/long: 36.304°N, -107.205°W

Figure 7.12. Cutbank migration measurement Site 9.

Red line: position of cutbank in 1997.
Yellow line: cutbank migration distance of 45 m.
Lat/long: 36.254°N, -107.382°W

Figure 7.13. Cutbank migration measurement Site 10.

Red line: position of cutbank in 1997.
Yellow line: cutbank migration distance of 122 m.
Lat/long: 36.319°N, -107.413°W

Figure 7.14. Cutbank migration measurement Site 11.

Red line: position of cutbank in 1997.
Yellow line: cutbank migration distance of 38 m.
Lat/long: 36.468°N, -107.313°W

Figure 7.15. Cutbank migration measurement Site 12.

Repeat UAV elevation surveys

Maps of elevation changes between August 2021 and July 2022 are presented in Figures 7.16 through 7.18. Erosion caused up to 3 m of elevation loss at Site A, mostly concentrated in the walls of the steep arroyo in the downstream portion of the study site. There was up to 5 to 25 cm of erosion in roadside gullies. There was sedimentation of 5 to 25 cm in various reaches of arroyos in the study site, and 5 to 25 cm of fan sedimentation on a small alluvial fan on the southwestern edge of the site (Fig. 7.16).

Legend

Value

- ■ -5.51 - -1
- ■ -0.999 - -0.5
- ■ -0.499 - -0.25
- ■ -0.249 - -0.05
- -0.049 - 0.05
- ■ 0.051 - 0.25
- ■ 0.251 - 0.5
- ■ 0.501 - 1
- ■ 1.001 - 7.295

Elevation change between August 17, 2021, and July 28, 2022, at Study Site A. Background orthophotomosaic was collected via UAV on July 28, 2022. Legend values are in meters. Areas on map that are not colored represent values of elevation change less than 0.05 m. The two areas of significant elevation gain in the north-center portion of the map are areas with standing water during at least one of the UAV flights; the calculated values in those two areas do not reflect real conditions.

Figure 7.16. Elevation change between 17 August 2021 and 28 July 2022 at Site A. Much of the supposed elevation gain on the northeastern side of the map is an artifact of data processing and does not reflect observed sedimentation.

At Site B, erosion and sedimentation were largely confined to arroyo walls and beds. In the 12-month period of study, that site experienced up to 3 m of erosion in arroyo walls and up to 1 m of arroyo bed sedimentation. Sedimentation downstream of the major road culvert near the western downstream end of the study site was particularly pronounced but still confined to within arroyo walls. The approximately 1-km-long reach of the arroyo in Site B displayed typical discontinuous arroyo behavior: the arroyo bed experienced alternating erosion and sedimentation of 5 to 25 cm in approximately 300-m-long reaches over the course of the study (Fig. 7.17).
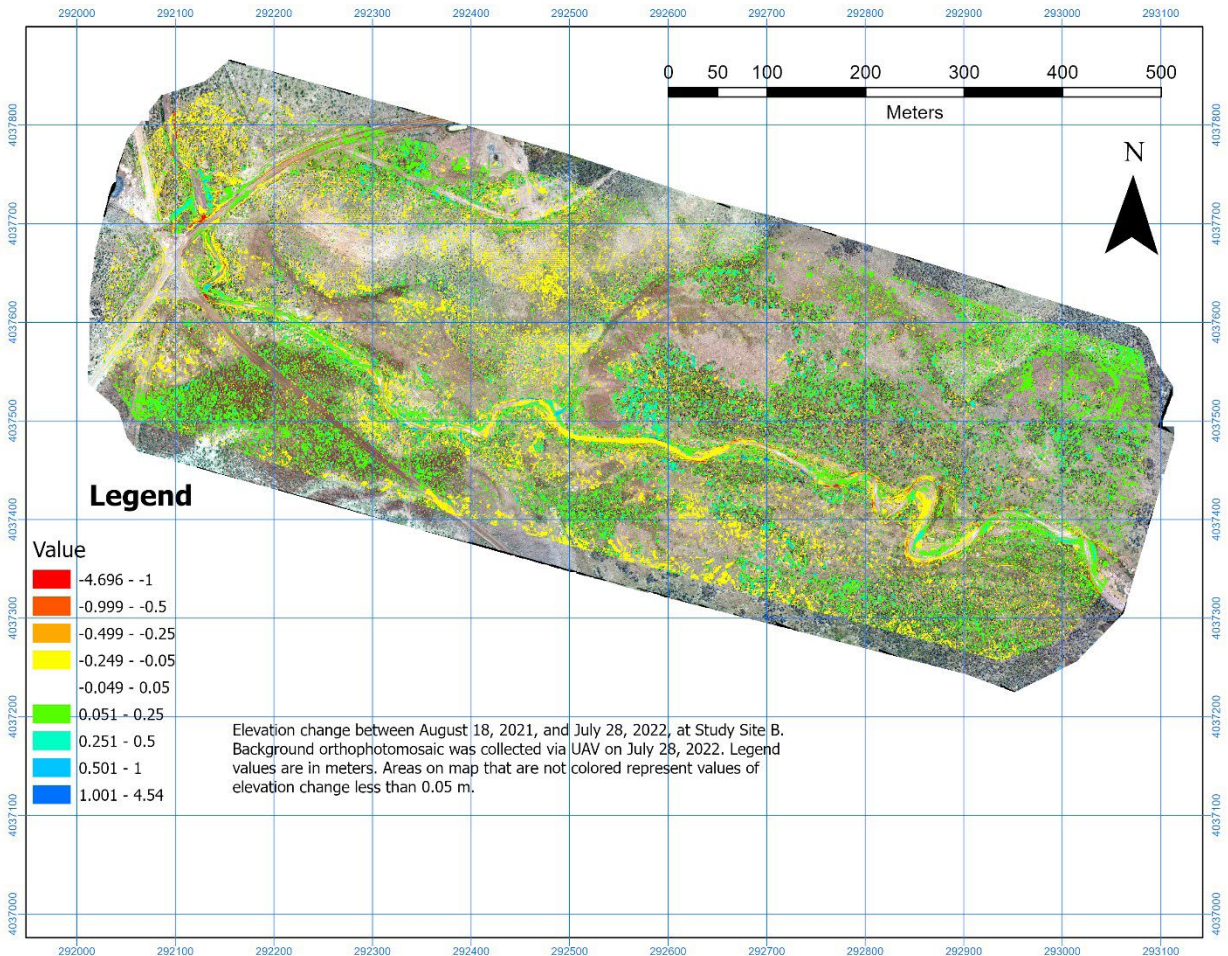
Figure 7.17. Elevation change between 18 August 2021 and 28 July 2022 at Site B.

Site C experienced similar magnitudes of erosion and sedimentation as Sites A and B (Fig. 7.18). Erosion at Site C was concentrated along arroyo walls. Sedimentation at Site C largely occurred in an approximately 0.8-ha (about 2-acre) alluvial fan just upstream of New Mexico Highway 537. This fan underwent an average of 12 cm of sedimentation during the 12-month study period. Multiplied by the 0.8 ha (8,000 m^2) area of sedimentation, these observations show 960 m^3 of sediment deposition between August 2021 and July 2022 on the alluvial fan at Site C.
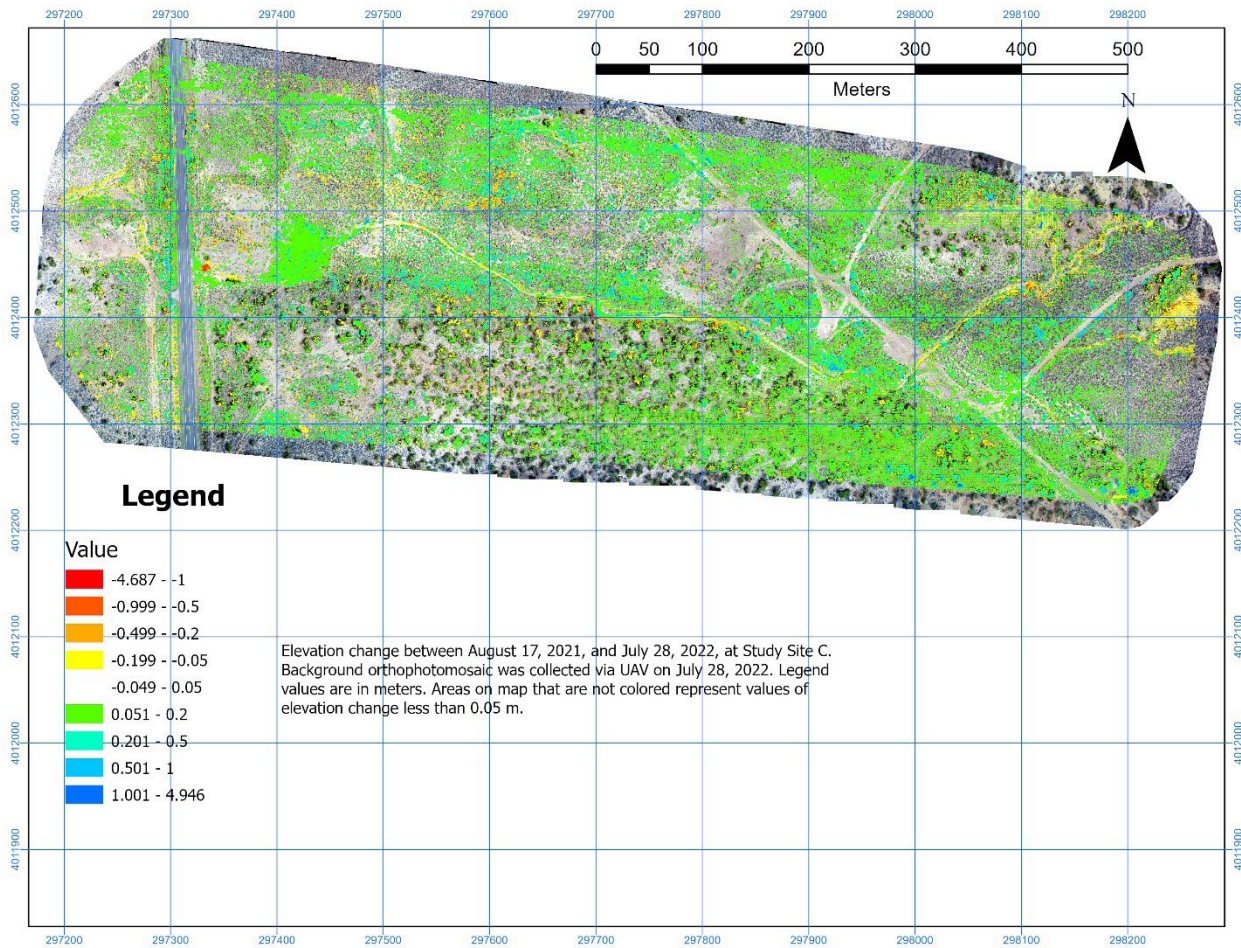
Figure 7.18. Elevation change between 17 August 2021 and 28 July 2022 at Site C. New Mexico Highway 537 is visible on the left side of the image.

INTERPRETATIONS

### Long-term processes (decades to centuries)

Radiocarbon dates from charcoal hosted by sediments of map unit Qao (older alluvium) suggest that the large valleys of the upper Cañon Largo watershed underwent long-term sedimentation from at least 8,000 YBP to approximately 1,500 YBP, an episode of approximately 6,500 years. Field observations of moderately well-developed paleosols within the sediments of Qao suggest that there were also long episodes of stasis during which neither sedimentation nor erosion occurred during the overall aggradational cycle of the middle Holocene. Further work is needed to relate these observations and interpretations to climate and/or geomorphic threshold drivers.

The sediments that make up map unit Qay (young alluvium) are inset into Qao by 1.5 to 7 m, meaning that at least that much erosion occurred after the deposition of Qao but before the deposition of Qay (Fig. 7.19). These erosion estimates are a conservative minimum because they ignore the thickness of map unit Qay. After an erosive episode, map unit Qay was deposited within the small valleys that had been created by the erosion of Qao. This depositional episode began by 1,380 YBP in the Cañada Larga valley, though it may have been later in other valleys in the study areas. Radiocarbon dates of charcoal within Qay show that deposition continued through approximately 500 YBP (approximately the year 1520 CE), though the author observed glass bottles and rubber tires within the sediments of Qay in Tapicito Creek at a depth of 1 m below ground surface. These artifacts were not dated, but are estimated to be 50 to 100 years old, suggesting that in Tapicito Creek, deposition of map unit Qay continued until the twentieth century. The author observed water flow and sedimentation atop the Qay geomorphic surface in September 2022 in Tapicito Creek on a terrace tread standing 1.8 m above the active stream bed, suggesting that minor sedimentation in Qay continues to the present during high-magnitude discharge events.

In all valleys where map unit Qay (young alluvium) exists, it is incised 1.5 to 2.5 m by active stream channels (Fig. 7.20). Under normal streamflow conditions, erosion and/or sedimentation is confined to within this incised portion of valleys. The sediment deposited in these incisions is labelled map unit Qaa (active alluvium). The exact date of the onset of incision into Qay is not known and is likely to be diachronous. Historical photos, anthropogenic detritus found within Qay, and soil development atop Qay suggest that the most-recent incision likely occurred within the twentieth century. This incision continues to the present and is likely to continue as the watershed adjusts to new equilibria.

The ages of major alluvial units in the study area (Qao and Qay), along with field observations of soil development, sediment character, and geomorphic position, suggest that the process rates in the largest-scale cycles of erosion and sedimentation are on the same order as those observed in other historic arroyo studies in the southwestern U.S. (e.g., Schumm and Hadley, 1957; Gellis and Elliott, 2001; Friedman et al., 2015; Townsend et al., 2019; Finley et al., 2022). The decades- to centuries-long duration of erosive and depositional episodes is related to geomorphic thresholds dictated by climate, vegetation, and the base level of the system. In many arroyos in the southwestern U.S. that have experienced incision in the twentieth and twenty-first centuries, human changes in the arroyos' watersheds are at least partially responsible for the geomorphic and/or hydrologic triggers that lead to incision (Matherne, 2006; Aby, 2017).
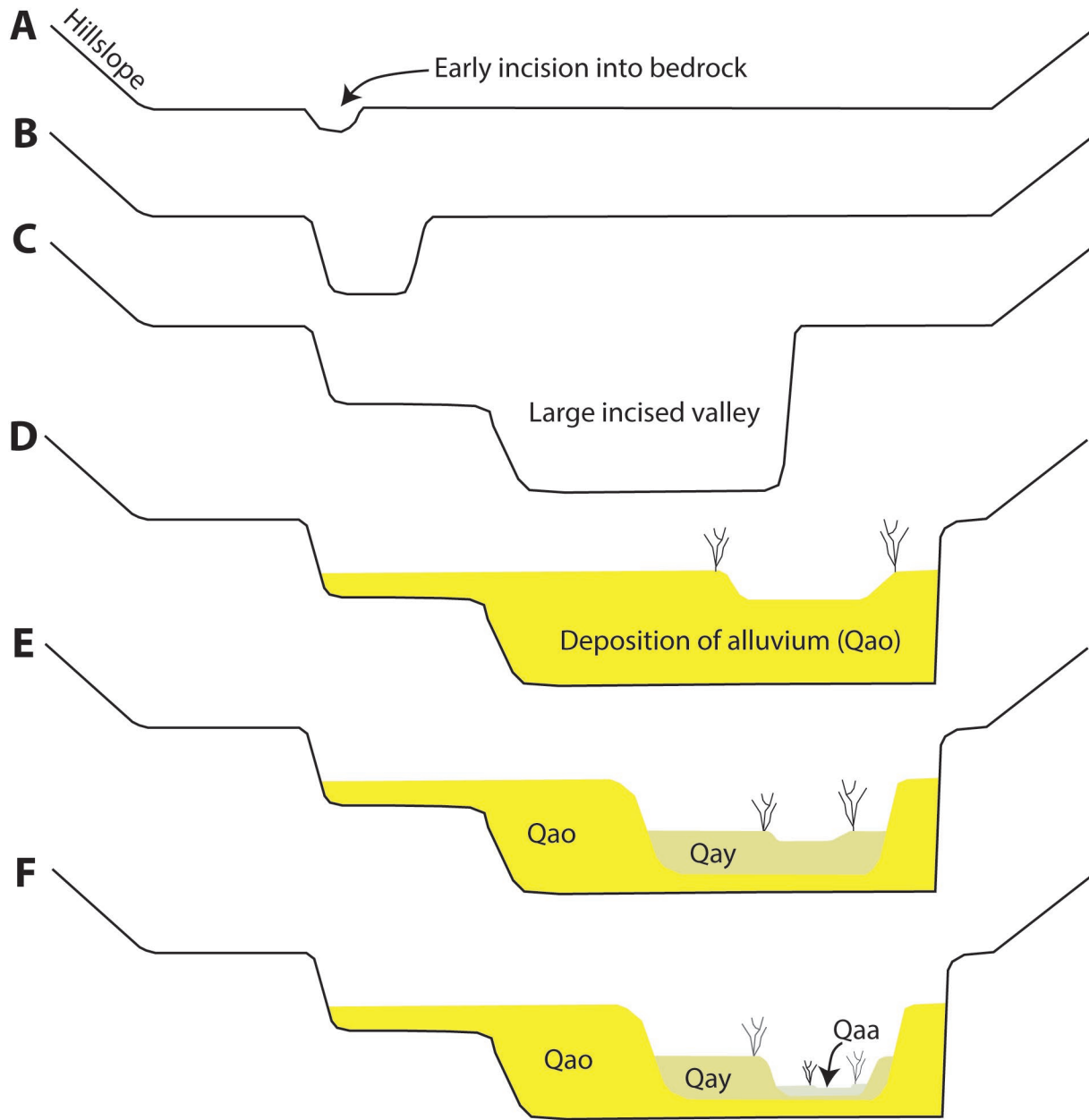
Figure 7.19. Schematic cross sections of the arroyo cycle in the upper Cañon Largo watershed (modified from Friedman et al. [2015]). A: Unincised phase prior to deposition of alluvium, >8,000 YBP. B: Channel incision and widening, >8,000 YBP. C: Concentration of incision at one side of the valley, leaving an erosional terrace on the left, >8,000 YBP. D: First phase of arroyo filling, ca. 8,000 to 1,500 YBP. E: Incision (ca. 1,400 YBP) into older alluvium creates a smaller valley into which younger alluvium is deposited (ca. 1,400 to 100 YBP). F: Another phase of incision and subsequent filling leads to present-day conditions.

Figure 7.20. Three alluvial units in Cañada Larga at approximately 36.321° N, -107.224° W. The oldest unit, Qao, forms the highest bluff on the left. Inset into Qao is Qay, forming the medium cliff in the center and right. The youngest and lowest alluvial unit, Qaa, forms the mostly unvegetated area in the foreground. Photograph taken 24 August 2021. May not be used without permission of the Jicarilla Apache Nation.

Moderate-time-scale processes (years to decades)

As illustrated in Figures 7.4 through 7.15 and in Table 7.2, the erosion of alluvial sediment via the lateral migration of cutbanks in large valleys in the upper Cañon Largo watershed can occur at the rate of tens of cubic meters per year at a single cutbank site. While there are physical limits to the total amount of lateral migration any stream can undergo (Langbein and Leopold, 1966; Schumm and Khan, 1972), most streams in the study area are not at or near those limits, and it is reasonable to expect lateral cutbank migration of similar rates and magnitudes to those described in Table 7.2 to continue for some time. Because the majority of cutbank erosion occurs in major arroyos in large valleys (e.g., Fig. 7.21), it is reasonable to expect that the majority of sediment lost via cutbank migration will be transported out of the study area under present conditions.

Figure 7.21. UAV photographs of cutbank erosion threatening infrastructure in Tapicito Creek approximately 500 m downstream of New Mexico Highway 537. Top photograph shows Tapicito Creek (in bottom left and center, flow direction from left to right) and 6-m-tall cutbank. Note position of road atop cutbank. Photo taken from approximately the same elevation as the road. Bottom photograph shows same location from an altitude of approximately 50 m.

Short-term processes (days to years)

The results of repeat elevation surveys (Figs. 7.16 through 7.18) show that sedimentation and erosion occur on the centimeter to meter scale over relatively short time spans, including during single precipitation events. Erosion on such time scales is largely confined to preexisting stream channels and occurs both as bank collapse and downcutting. All three study sites experienced erosion along roads, an observation in accord with those of Matherne (2006) farther downstream in the Cañon Largo watershed.

Sedimentation at the three study sites occurs in relatively small volumes in arroyo beds. Most sedimentation is instead related to human alterations to the landscape: stock ponds, road culverts, and berms. Sites A and C saw significant sedimentation during the 12-month study period just upstream of road crossings. Blockage of culverts was observed during one flood event at Site B, though there was no significant sedimentation upstream of the culverts during the study period. The culverts at Site C were completely blocked for the duration of the study. Sediment observed on the surface of New Mexico Highway 537 at that site after an August 2021 precipitation event suggests that some sediment is exiting that watershed over the highway due to ineffective culverts. The volume of sediment (around 960 m^3) that is observed to have accumulated on a small alluvial fan just upstream of the blocked culvert at Site C is therefore a minimum estimate for sediment movement in the system during the study period. Using an average sand mass of 1.8 tons/m^3, this volume represents 1,728 tons of sediment. This estimate is less than but on the same order as model estimates for total annual sediment yield at Site C (Table 8.4), lending credence to estimates presented in the next chapter.

VIII. SEDIMENT TRANSPORT ANALYSIS

Clint Richardson and Faustin Kumah

CHAPTER SUMMARY

Three watersheds on the Jicarilla Apache Nation in northern New Mexico were analyzed for peak discharge, runoff volume, and sediment transport using HEC-GeoHMS and an ArcGIS platform to generate and manipulate geospatial data. Available databases were accessed and key attributes were derived to allow for qualitative and quantitative characterization of each watershed with respect to stormwater flow and sediment yield for varied frequency and duration design storms. The analysis shows that high stormwater flows are possible within each watershed, producing significant sediment yields, which supports previous field reconnaissance visual assessments. However, considerable uncertainty lies with the total sediment transport estimates in that the MPM-Woo method used herein for bed material yield depends significantly on the hydraulic coefficients used for stream discharge, velocity, and width and on the D_{50} sediment grain size, with the latter having a pronounced effect on bed material yield. Any uncertainty associated with peak discharge, runoff volume, soil erodibility, and topographic factor would impact the estimate of fine sediment yield, or wash load, as determined using the MUSLE equation. For the analysis herein with a fixed D_{50} of 0.3 mm, the percentage of wash load varied from around 10 to 15% of the total sediment yield; thus, the composite uncertainty in the MUSLE equation may not significantly contribute to the overall uncertainty in the total sediment estimates.

For future sediment management and control decisions, sediment transport estimates were also expressed as mean annual yields. Dominant discharges associated with an increment of discharge that carries the most sediment over a long period of time were determined for each watershed using the mean annual yields. Dominant discharge for Sites A, B, and C is estimated to be 252, 3,230, and 371 cfs, respectively, with mean annual sediment yields of 3,271, 72,676, and 4,365 tons, respectively. Unit soil transport for mean annual yield was 3.85, 11.91, and 8.42 tons/acre/yr, respectively, for Sites A, B, and C. Sediment concentrations in the runoff from the three watersheds lie within what is considered as water flood. Site B has the overall highest sediment concentrations. The mean annual sediment concentration for Site B represents a bulking factor around 1.17. Site A and Site C bulking factor was lower at 1.08.

INTRODUCTION

In this study, several ArcGIS toolboxes and extensions were extensively utilized to process data for modeling various sediment transport processes within the ArcGIS environment. The extensively used extensions include ArcGIS Data Management, ArcGIS Spatial Analyst, ArcGIS 3D Analyst, TauDEM, ArcHydro, and the HEC-GeoHMS.

The ArcHydro tools extension was created cooperatively by Esri and the Center for Research in Water Resources (CRWR) at the University of Texas at Austin. These tools generate multiple datasets that jointly characterize a catchment's drainage patterns. First, data on flow direction, flow accumulation, stream definition, stream segmentation, and watershed delineation are generated using raster analysis. The data are then utilized to create a model in vector form of the watersheds and drainage channels for hydrologic modeling (Esri, 2011).

HEC-GeoHMS (Geospatial Hydrologic Modeling Extension) was developed by the Hydrologic Engineering Center at the U.S. Army Corps of Engineers. Its tools enable its users to do a variety of hydrologic analyses such as delineating watersheds and generating inputs for hydrologic models (Fleming and Doan, 2010).

TauDEM (Terrain Analysis Using Digital Elevation Models) is an open-source ArcGIS extension program created by Utah State University's Hydrology Research Group and purposely employed in this study to take advantage of its ability to compute flow direction and contributing area using a multiple-flow-direction algorithm (D-infinity method). The algorithm channels the flow entering each grid cell to one or two downslope neighbors, thereby eliminating grid bias and unrealistic dispersion induced by the other flow-direction algorithms, such as the D8 method (Tarboton, 1997).

ArcGIS Data Management, Spatial Analyst, and 3D Analyst are popular and powerful ArcGIS tools utilized for a variety of data processing tasks and analyses such as defining projections, clipping rasters to extents, creating surfaces, and raster interpolation.

Primarily, data analyses were performed within the ArcGIS Pro environment due to its efficiency; however, there is no HEC-GeoHMS extension developed for ArcGIS Pro. Hence, terrain processing to derive watershed characteristics was performed within the ArcGIS ArcMap environment.

DATA ACQUISITION METHODS

Digital elevation model

The digital elevation model (DEM) utilized for this study was obtained from the Geologic Mapping Program at the New Mexico Bureau of Geology and Mineral Resources. It is an aerial lidar-based DEM generated between 2016 and 2017, and it features a resolution of 1 × 1 m projected in NAD83 UTM zone 13N. Figure 8.1 shows the DEM with elevation values for the study area.
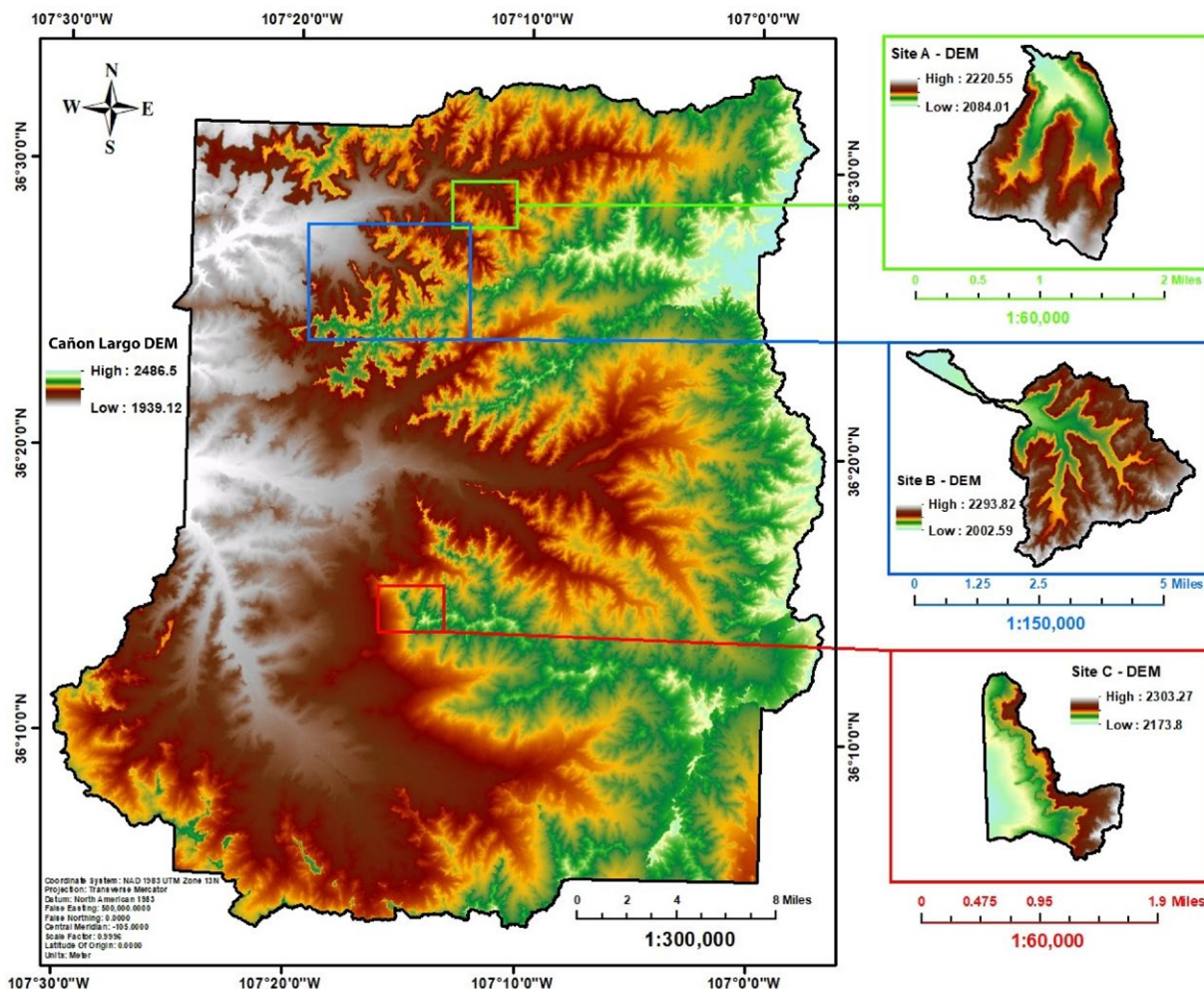

Figure 8.1. Locations of analyzed subbasins on the Cañon Largo watershed and elevations (m).

Land cover

The land cover raster data were downloaded from the Multi-Resolution Land Characteristics (MRLC) Consortium Viewer on 14 February 2022. The MRLC generates and hosts the National Land Cover Database (NLCD) products. For this study, the NLCD 2019 data product, the latest and most comprehensive generation of land cover dataset released by the U.S. Geological Survey (USGS), was utilized. The original cell size of this thematic dataset was 30 × 30 m and features an 8-bit unsigned char pixel type. For this study, this dataset was resampled to 1 × 1 m (nearest neighbor) and reprojected to NAD83 UTM zone 13N. Figure 8.2 shows the classifications for the land cover types of the land cover data for the study area.

Soil Survey Geographic Database

The Soil Survey Geographic Database (SSURGO) is a comprehensive soil database managed by the Natural Resources Conservation Service at the U.S. Department of Agriculture. For the study area, the soil database was downloaded from the Web Soil Survey website on 14 February 2022. The area symbol for the study area is NM698, and the dataset contained both tabular and spatial data (survey area: version 18, 12 September 2021; tabular: version 18, 12 September 2021; spatial: version 5,

15 September 2019), which were used to generate various maps, such as the curve number grid and soil erodibility maps for analyses.

Precipitation

Partial duration precipitation depth data were obtained from the National Oceanic and Atmospheric Administration's (NOAA) National Weather Service Precipitation Frequency Data Server (NOAA Atlas 14, volume 1, version 5). Precipitation frequency estimates in ASCII grid format were downloaded from the same server for different average storm recurrence intervals and durations and prepared in appropriate formats for this study.

Rainfall-runoff erosivity factor

The rainfall-runoff erosivity factor (R-factor) assesses the impacts of raindrops and represents the volume and runoff rate induced by the rain. The R-factor raster was downloaded from the NOAA website in GeoTiff format at a resolution of 800 m in Albers Conic Equal Area, GRS80, NAD83, resampled, and reprojected for this study (see Appendix 2A).

Landsat 8

The USGS's Earth Resources Observation and Science (EROS) Center in Sioux Falls, South Dakota, processes and maintains Landsat images, which
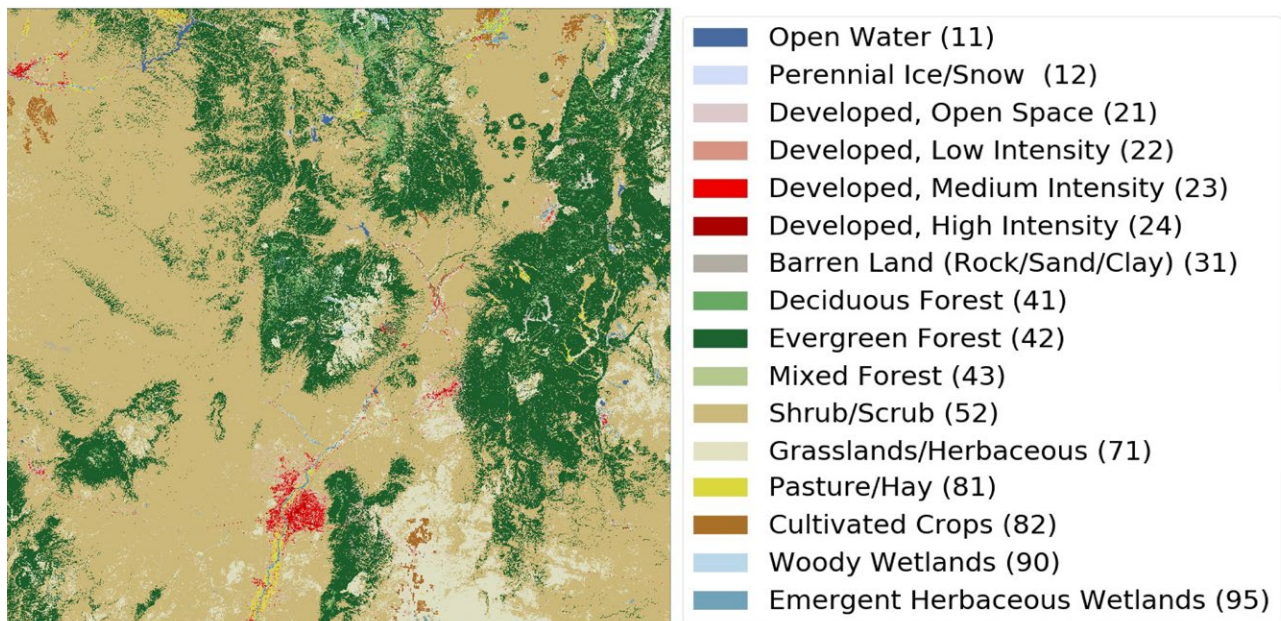

Figure 8.2. NLCD land cover 2019 dataset.

contain valuable information about the earth acquired via satellite-based remote sensing observations (U.S. Geological Survey, 2022). Landsat 8 Level 2 science products for 19 June 2021 and 21 July 2021 were downloaded using the USGS Earth Explorer at a 30-m resolution to compute the mean normalized difference vegetation index (NDVI) for the study area.

DATA PROCESSING METHODS

Curve number grid

The Natural Resources Conservation Service (NRCS) curve number (CN) is a hydrologic measure used to quantify the potential for stormwater runoff in catchments (Mantey and Tagoe, 2013). By incorporating the land cover, soil, CN look-up table, and DEM data, a dimensionless CN raster grid for each watershed was generated using the HEC-GeoHMS extension, which adopts the NRCS TR-55 CN technique. The TR-55 tables present the CN as a function of the catchment's cover type, antecedent runoff condition, hydrologic soil group, treatment, and impervious area. Bare soils are categorized into four hydrologic soil classes based on their minimum infiltration rate after extended wetness: A, B, C, and D (Hydrologic Engineering Center, 2022). For this study, the hydrologic soil groups for the study area were obtained from the SSURGO database. Also, the

NLCD land cover 2019 dataset was reclassified to six levels, and the appropriate CNs for the hydrologic soil groups were chosen based on field reconnaissance to populate the CN look-up table, as shown in Figure 8.3. Figure 8.4 shows the flowchart outlining the procedure to generate the CN grids for the three watersheds. The CN grids generated for the three sites are shown in Appendix 2A.

jana_cnlookuptable

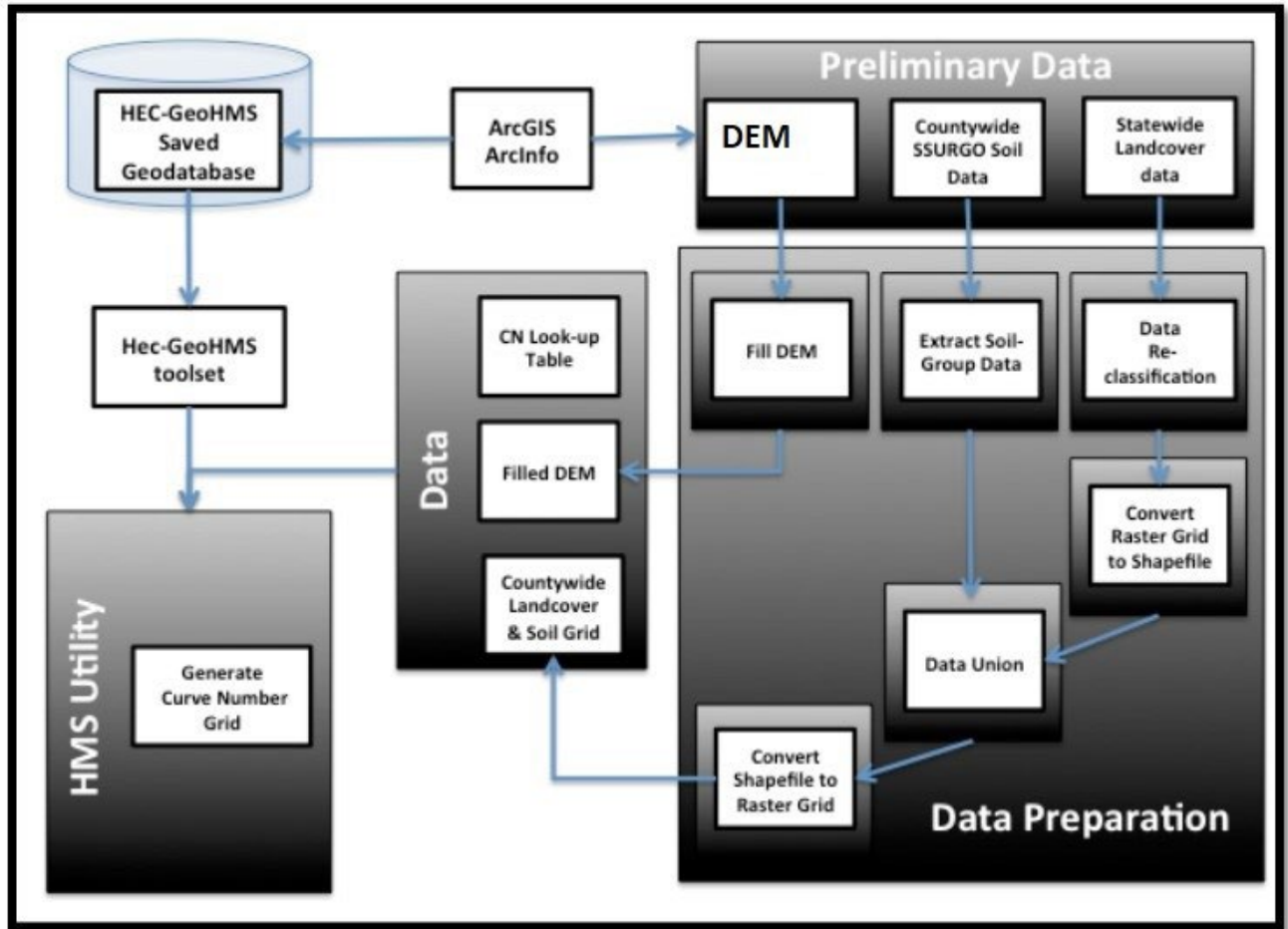| Rowid	OBJECTID	LUVALUE	DESCRIPTION	A	B	C	D
1	1	1	Western Desert Urban	96	96	96	96
2	2	2	Agriculture	68	79	86	89
3	3	3	Rangeland	63	77	85	88
4	4	4	Forest	48	67	77	83
5	5	5	Water	10	10	10	10
6	6	6	Barren	96	96	96	96

Figure 8.3. CN look-up table.

Figure 8.4. CN grid flowchart (modified from Gallegos [2012]).

Stream network

Within the ArcGIS environment, the stream network used for this study was generated from the lidar DEM at flow accumulation thresholds confirmed by field geologists to be a reliable representation of field conditions. Murphy et al. (2008) modeled a stream network using a conventional photogrammetry-generated DEM (10-m resolution) and a lidar-generated DEM (1-m resolution) and compared them with the stream network mapped in the field as the benchmark. They demonstrated that the lidar DEM-derived network was the most exact depiction of the field-mapped network, even more accurate than the photo-derived network. Thus, there is a high level of confidence in the lidar-generated stream network being used in this study. Figure 8.5 shows two stream network extraction methods; Jenson and Domingue's method was adapted for this study.

Terrain processing

At this stage, ArcHydro and HEC-GeoHMS extensions were utilized extensively. ArcHydro was used for terrain preprocessing in the first phase to delineate the stream network, subbasins, watersheds, and other features that jointly describe a basin's drainage patterns for subsequent terrain processing in HEC-GeoHMS.

HEC-GeoHMS is used to develop the hydrologic model for input into HEC-HMS for stormwater simulation and analysis. HEC-GeoHMS generates backdrop map files, meteorological model files, basin files, and a grid cell parameter that HEC-HMS may utilize to build a hydrologic model. The basin model file includes subbasin areas and other hydrologic characteristics that can be computed using geographical data. This extension can create tables summarizing the physical features of streams and watersheds to help estimate hydrologic parameters (Fleming and Doan, 2010). Figures 8.6 and 8.7 are flowcharts outlining the ArcHydro and HEC-GeoHMS procedures adapted for this study from Gallegos (2012). Figures 8.8, 8.9, and 8.10 show the HMS schematic models for Sites A, B, and C, respectively.
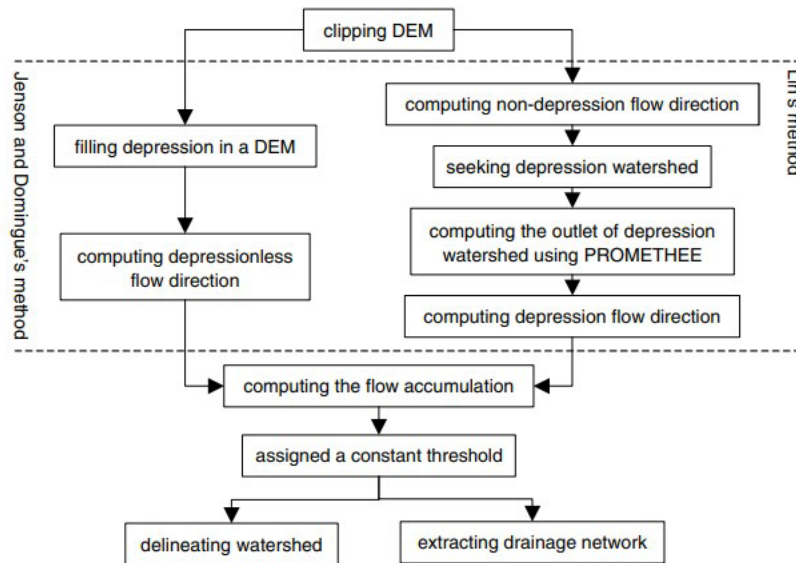

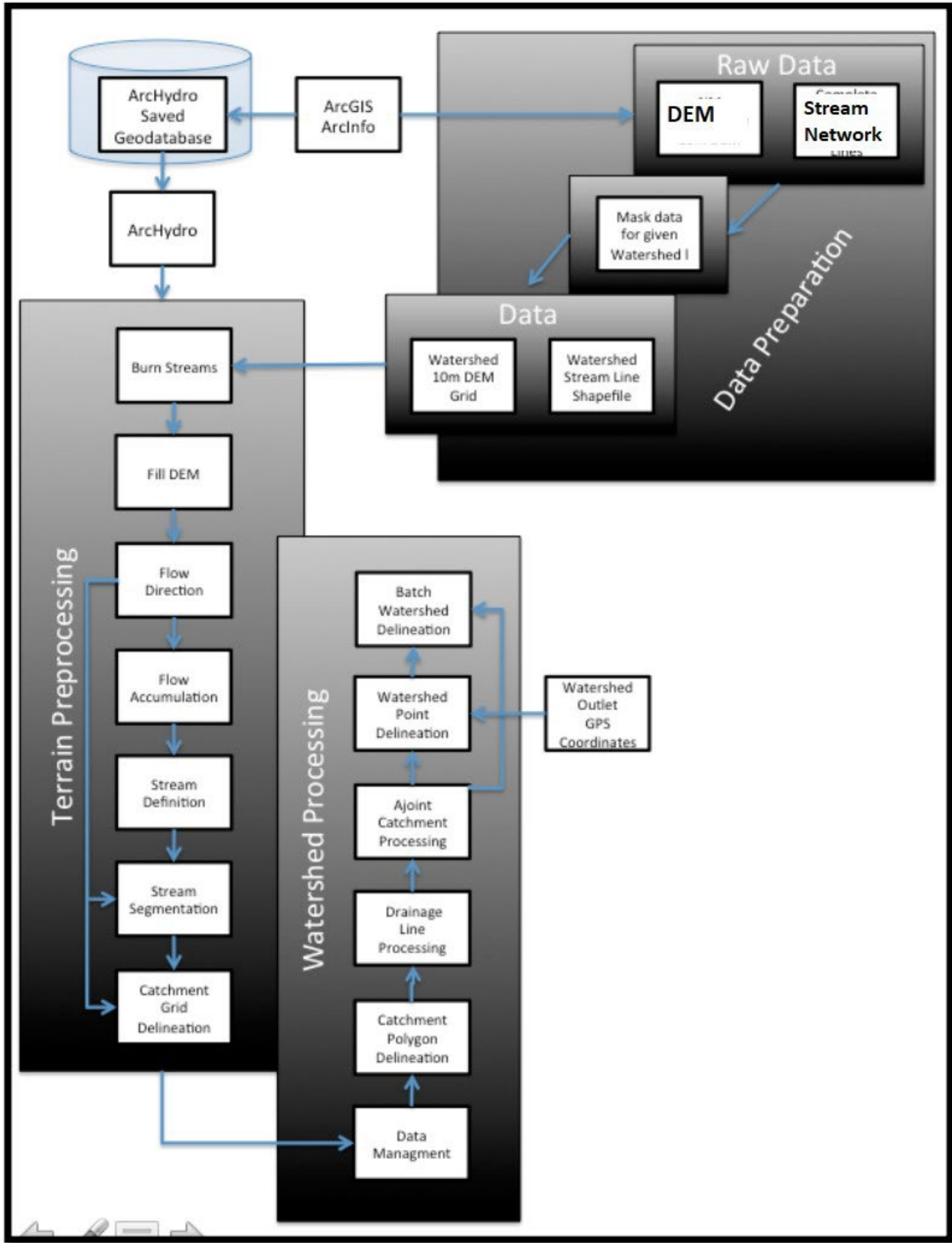**Figure 8.5.** Lin and the Jenson and Domingue stream network extraction methods (Lin et al., 2006).

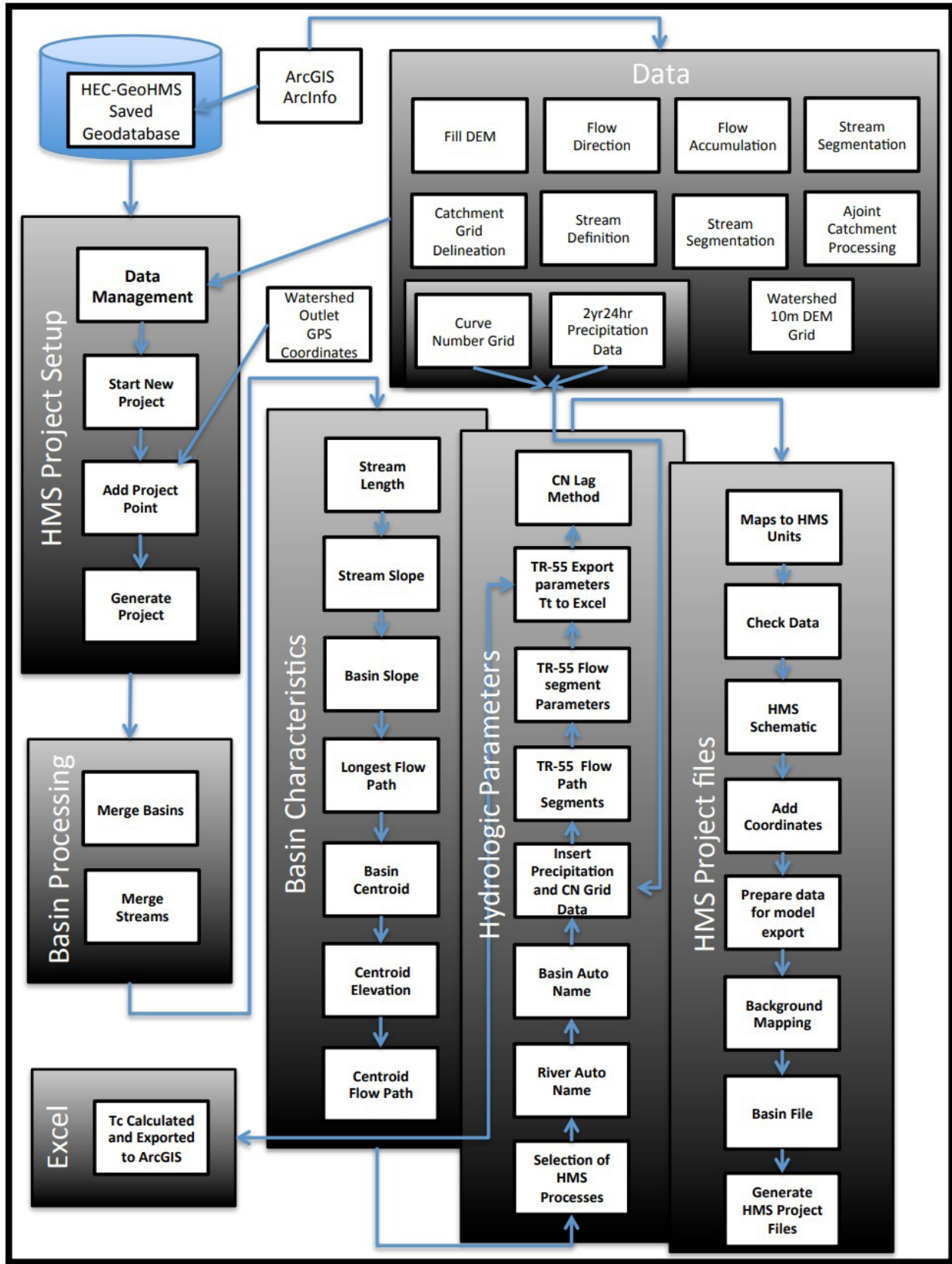**Figure 8.6.** ArcHydro flowchart procedure (modified from Gallegos [2012]).

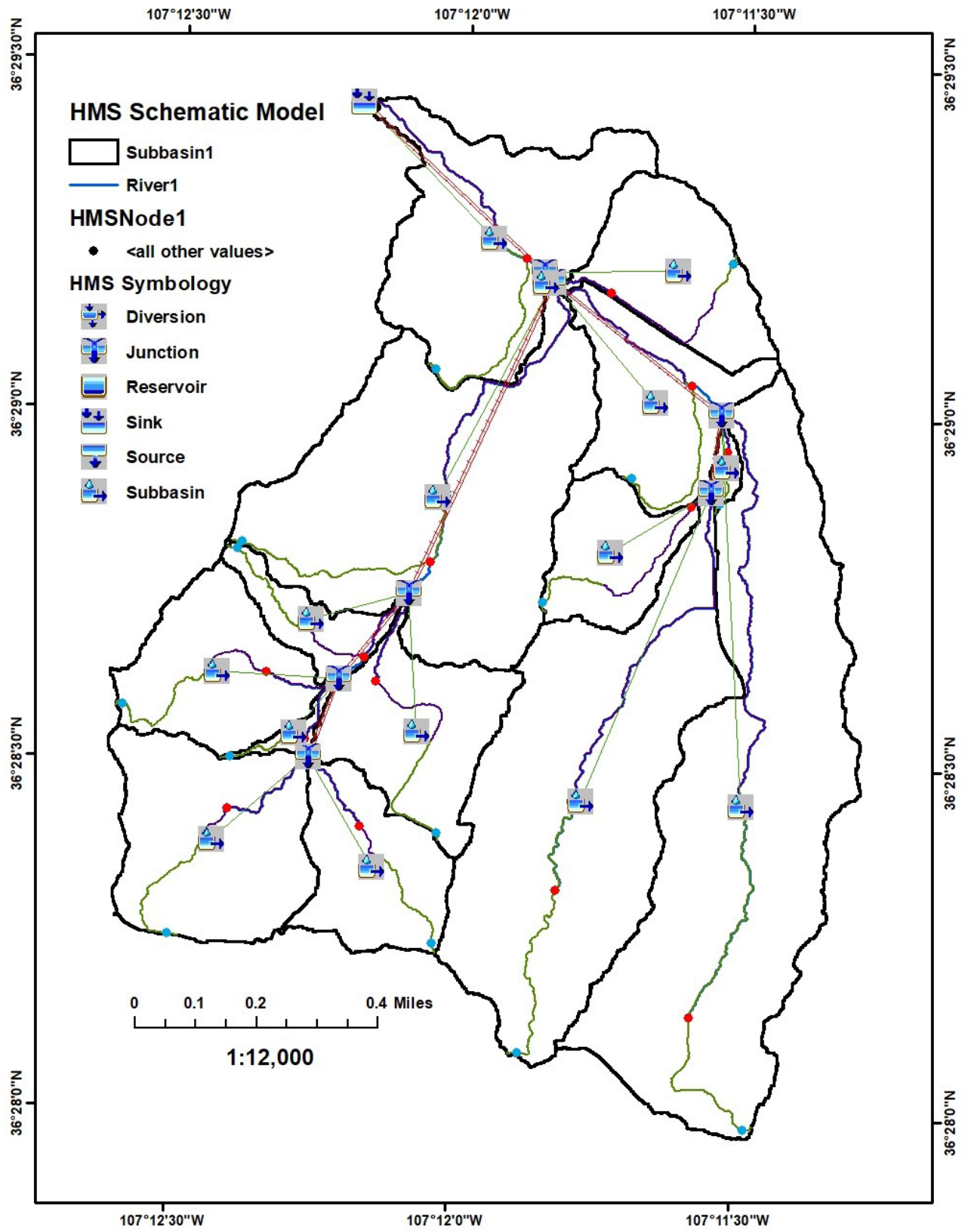**Figure 8.7.** HEC-GeoHMS flowchart procedure (modified from Gallegos [2012]).

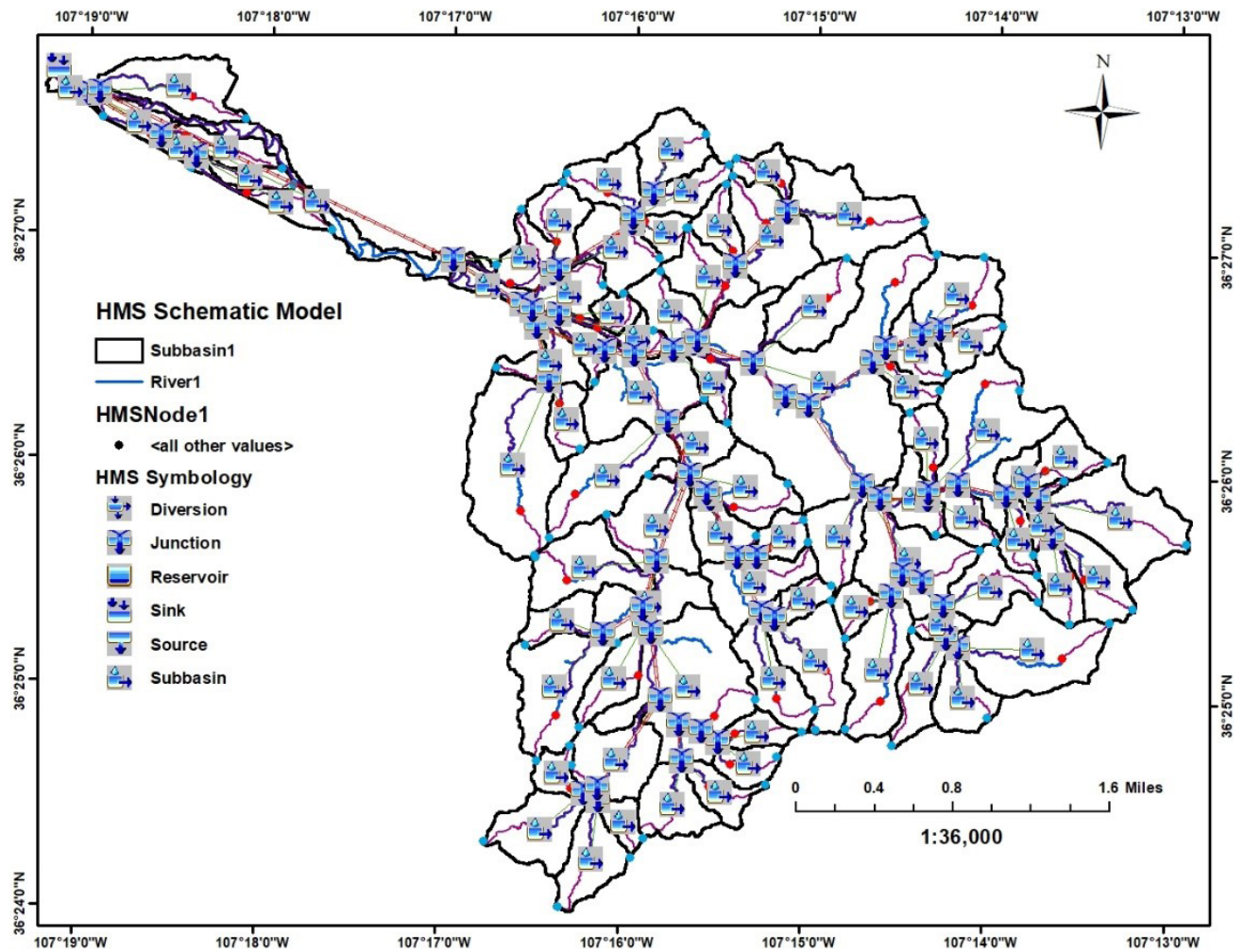**Figure 8.8.** HMS schematic model for Site A.

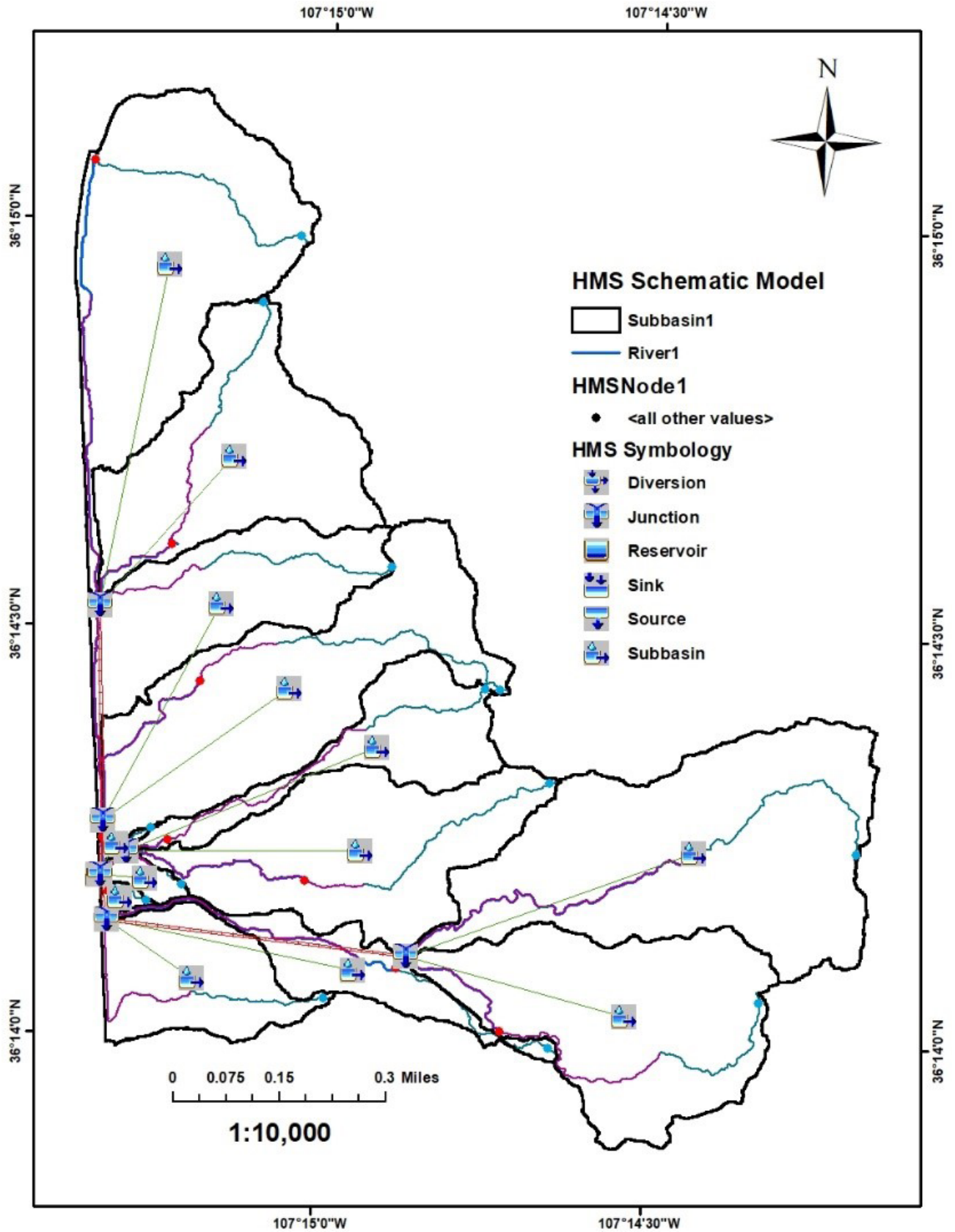**Figure 8.9.** HMS schematic model for Site B.

Figure 8.10. HMS schematic model for Site C.

Peak discharge and runoff volume

Peak flow (cfs) and runoff volume (acre-ft) were computed for each catchment watershed for each frequency-duration storm event and NRCS Type II storm type using the HEC-HMS and imported HMS model.

SEDIMENT TRANSPORT MODELING

For this study, the Modified Universal Soil Loss Equation (MUSLE), MPM-Woo Sediment Transport Equation, and the Unit Stream Power Erosion and Deposition (USPED) models were used to estimate sediment yield and soil erosion and deposition patterns for the three watersheds. D-infinity flow direction and flow accumulation generated using the TauDEM tool were employed for sediment transport modeling in this study. These soil erosion models are discussed below.

MUSLE

Williams (1975) suggested an improved erosivity parameter to account for the runoff shear stress effect on soil detachment in terms of the product of runoff volume and peak discharge for single storms since the USLE frequently fails to consider the effective rainfall that induces surface runoff. Furthermore, the sediment delivery ratio (SDR) changes with storm events, so assuming a constant SDR adds inaccuracy to the estimations (Sadeghi et al., 2014). The model is empirical and does not consider all physical factors impacting sediment yield; however, its variables have a direct conceptual and physical relevance (Williams, 1975). For a given storm, the sediment yield of a watershed can be estimated using the MUSLE equation developed by Williams (1975) and is expressed as

$$Y = \alpha \left(V_{runoff} Q_{peak} \right)^{\beta} \times K \times LS \times C \times P$$

where α is the region-specific calibration factor (unitless), β is the region-specific calibration factor (unitless), Y is the single storm sediment yield (tons), V_{runoff} is the storm runoff volume for a given storm frequency (acre-ft), Q_{peak} is the peak discharge for a given storm frequency (cfs), $\alpha (V_{runoff} Q_{peak})^{\beta}$ is the storm runoff energy factor (R_w), K is the soil erodibility factor (tons·acre·hr/hundreds of acre·ft·ton$_f$·in.),

LS is the slope length factor (ft/ft), C is the cover-management factor (unitless), and P is the support practice factor (unitless).

For α and β, Mussetter Engineering Inc. (2008) used values of 285 and 0.56, respectively, to determine sediment yield for watersheds within the middle Rio Grande basin. Thus, utilizing the storm runoff component makes the MUSLE equation adaptable to semiarid areas in the West where short-duration, high-intensity storms are predominant (Mussetter Engineering Inc., 2008).

MUSLE is adjusted to estimate only the fine sediment (wash load) by multiplying the sediment load by the area-weighted percentage of the watershed soils in the silt and clay size range (i.e., finer than the number 200 sieve). This is computed as

$$Y = \alpha \left(V_{runoff} Q_{peak} \right)^{\beta} \times K \times LS \times C \times P \times P_f$$

where P_f is the fraction of silt and clay in the watershed soil.

MPM-Woo sediment transport equation

The following relationship was developed using multiple regression to compute bed material load in streams carrying high concentrations of suspended sediment (Mussetter Engineering Inc., 2008):

$$Q_{bm} = aWV^b Y^c \left\{ 1 - \frac{C_f}{10^6} \right\}^d$$

where Q_{bm} is the bed material load (cfs), W is the channel width (ft), V is the flow velocity (feet per second [fps]), Y is the flow hydraulic depth (ft), C_f is the fine sediment (silt and clay) concentration by weight (ppm), and coefficient a and exponents b, c, and d are a function of the median bed material size.

The fine sediment concentration, C_f, is computed as

$$C_f = 10^6 \frac{Y_s * 2000}{V_{runoff} * 43560 * \gamma + Y_s * 2000}$$

where γ is the unit weight of runoff water (assumed to be 62.4 lbs/ft^3; 1 ton = 2,000 lbs, 1 acre = 43,560 ft^2).

Concentration of bed material, *Cbm*, as ppm is given by the following relationship:

$$C_{bm} = \frac{SG * 10^6 * Q_{bm}}{V_{runoff} + SG * Q_{bm}}$$

The wash load discharge, *Qf*, as cfs is given by

$$Q_f = \frac{V_r C_f}{SG * 10^6}$$

where *SG* is the specific gravity (assumed to be 2.65 for sand).

Total sediment discharge, *Qstotal*, is therefore equal to the sum of respective discharges:

$$Q_{stotal} = Q_f + Q_{bm}$$

Note that a Colby correction factor (Colby, 1964) may be applied to the sediment yield to account for the increase in the transport capacity of bed material sands when high concentrations (*Cs* [sediment concentration] greater than 10,000 ppm) of wash load are present:

$$q_s = \{1 + (k_1 k_2 - 1)k_3\}q_u = C_c q_u$$

where *qs* is the corrected sediment yield per unit stream width, *qu* is the uncorrected sediment yield per unit stream width, k_1 is the coefficient as a function of flow depth and water temperature, k_2 is the coefficient as a function of flow depth and concentration of fine-material load, k_3 is the coefficient as a function of median size of bed material, and *Cc* is the Colby correction factor.

The total sediment concentration, *Cstotal*, as ppm is given by

$$C_{stotal} = \frac{SG * 10^6 * Q_{stotal}}{V_{runoff} + SG * Q_{stotal}}$$

Dominant discharge and mean annual sediment yield

The dominant or effective discharge for the watershed is associated with the increment of discharge that carries the most sediment over a long period of time.

The mean annual sediment yield for the watershed can be estimated by integrating the sediment yield frequency curve (Chang, 1988):

$$Y_{sm} = \int Y_S PF$$

where Y_s is the individual storm total sediment yield and *PF* is the probability of occurrence of that precipitation event in one year.

Using the 2-, 5-, 10-, 25-, 50-, and 100-year storm events and the trapezoidal rule, the mean annual sediment yield may be numerically approximated by the following relationship (Mussetter Engineering Inc., 2008):

$$Y_{sm} = 0.01Y_{s100} + 0.015Y_{s50} + 0.04Y_{s25} + 0.08Y_{s10} + 0.2Y_{s5} + 0.4Y_{s2}$$

Thus, a correlation of peak discharges with sediment yields coupled with the estimate of mean annual sediment yield above provides a way to estimate the dominant discharge of the watershed.

Bulking factor

Using peak discharge for a given frequency and the resultant total sediment discharge, bulking factor and bulked discharge are respectively given by

$$BF = \frac{Q_{peak} + Q_{stotal}}{Q_{peak}}$$

and

$$Q_{peak\ bulked} = BF * Q_{peak}$$

Hydraulic discharge coefficients

To utilize the MPM-Woo Sediment Transport Equation, values of *W*, *Y*, and *V* must be estimated for a given peak discharge event. Hydraulic geometry relationships for a channel are commonly expressed in the form of power functions of discharge as

$$W = aQ^b$$
$$Y = cQ^f$$
$$V = kQ^m$$

where W is the channel width, Y is the flow depth, V is the flow velocity, Q is the discharge, and a, b, c, f, k, and m are regressed parameters.

The hydraulic variables (width, depth, and velocity) must satisfy the continuity equation for an assumed rectangular channel cross section:

$$Q = WdV$$

Therefore, the coefficients and exponents must satisfy

$$ack = 1$$
$$b + f + m = 1$$

Estimated hydraulic discharge relationships

An analysis of peak flow data from Mussetter Engineering Inc. (2004) for 10 ungaged watershed tributaries to the middle Rio Grande between Bernardo and Elephant Butte Reservoir provided a means to estimate the hydraulic discharge coefficient and exponents needed to apply the MPM-Woo Sediment Transport Equation to the Jicarilla Apache Nation test watersheds. The analysis was constrained to discharges less than 5,000 cfs given the larger watershed size of the referenced watershed basins relative to the smaller test watersheds in this study based on area (mi²). The analysis provided the following correlations:

$$V = 0.883Q^{0.229} \ (r^2 = 0.69)$$
$$Y = 0.062Q^{0.402} \ (r^2 = 0.87)$$
$$W = 18.121Q^{0.369} \ (r^2 = 0.58)$$

where Q is the peak discharge (cfs), V is the average velocity (fps), Y is the average depth (ft), W is the cross section width (ft), and

$$ack = 0.992$$

and

$$b + f + m = 1.00$$

Estimating sediment loads

Since the flow is ephemeral and ungaged for the Jicarilla Apache Nation test watersheds, an HEC-HMS hydrologic model was developed for each watershed to estimate peak discharges for the 2-, 5-, 10-, 25-, 50-, and 100-year recurrence interval events. Output from the individual watershed models was used with a D_{50} sediment grain size (0.3 mm) derived from samples collected on site to develop estimates of total sediment yields for the respective recurrence frequency, as well as the mean annual sediment yield. The wash load fraction of the sediment yield for each watershed was developed using the MUSLE equation, corrected for the fraction of silt and clay. The bed material fraction of the sediment yield was estimated using the MPM-Woo equation and the specified D_{50}. As D_{50} decreases, bed material load increases for a given peak discharge. Note also that the estimated bed material load depends on the hydraulic discharge relationships used, especially as indicated by the influence of the MPM-Woo exponents on the resultant flow velocity and flow depth for a given peak discharge:

$$Q_{bm} = aWV^bY^c\left\{1 - \frac{C_f}{10^6}\right\}^d$$

Using a typical NRCS dimensionless unit hydrograph, a time to peak (t_{peak}) is set to match the runoff volume (V_r) obtained from the HEC-HMS analysis for a given recurrence interval, thereby matching the respective peak discharge (Q_{peak}). The hydraulic conditions (V, D, and W) for each peak discharge are based on the regressed data from Mussetter Engineering Inc. (2004) as indicated above. The bed material component of the total sediment yield is obtained by numerically integrating the bed material transport capacities for individual discharges in the hydrograph over the hydrograph:

$$V_{bm}(t) = Q_{bm}(t) \times dt$$

where $Vbm(t)$ is the incremental bed material transport volume (acre-ft) for each discharge in the hydrograph with appropriate conversion factors applied and $Q_{bm}(t)$ is the bed material transport capacity (cfs).

Normalized difference vegetation index

Vegetation indices, the most extensively used of which is the normalized difference vegetation index (NDVI), are remotely sensed metrics critical for monitoring the ecosystem and evaluating land surface processes (Ke et al., 2015). Theoretically, NDVI is computed as

$$NDVI = \frac{NIR - R}{NIR + R}$$

For this study, a composite band was created with the band 4 (red) and band 5 (near infrared [NIR]) Landsat 8 images for the 19 June 2021 and 21 July 2021 periods, and then the NDVI was generated using the NDVI tool under the Indices Imagery tool in ArcGIS Pro. The Mosaic to New Raster tool (mosaic operator: mean) was used to combine the NDVI raster data (see Appendix 2A).

Estimating the cropping factor

The cropping factor (C-factor) was estimated based on several assumptions using the method of Renard et al. (1997) based on the product of five subfactors:

$$C = SR \times CC \times SC \times PLU \times SM$$

where SR is the surface roughness subfactor (0 to 1), CC is the canopy cover subfactor (0 to 1), SC is the surface cover subfactor (0 to 1), PLU is the prior land use subfactor (0 to 1), and SM is the soil moisture subfactor (0 to 1).

The PLU subfactor was set at 1 assuming no influence on soil erosion of subsurface residual effects from previous cropping or previous tillage practices on soil consolidation. The SM subfactor is set at 1 if the soil is at or near field capacity or 0 if at or near wilting point. To maximize potential surface runoff, SM is set to 1.

Renard et al. (1997) suggest an SR subfactor of 0.60 for rangeland having interspersed piñon-juniper vegetation and an SR subfactor of 0.80 for natural shrub or desert grass. The CC subfactor expresses the ability of vegetation to intercept and reduce the kinetic energy of rainfall striking the soil surface and is a function of the height of vegetation and fraction of the soil surface covered by the vegetative canopy:

$$CC = 1 - FAC * \exp\left(-d_d * H_{eff}\right)$$

where FAC is the fractional vegetative cover, d_d is the mean raindrop diameter falling from the canopy (typically set at 0.10 in.), and H_{eff} is the effective height of canopy (ft; Jakubíková et al., 2006) where

$$H_{eff} = (\frac{1}{3}\{H_{top} - H_{bottom}\} + H_{bottom})$$

The FAC may be estimated using a spectral analysis based on an assumption of a pixel dichotomy model (PDM), wherein the images captured by satellites only contain vegetation and soil:

$$FAC = \frac{NDVI - NDVI_{soil}}{NDVI_{veg} - NDVI_{soil}}$$

where $NDVI_{veg}$ is approximately equal to NDVI with cumulative frequencies of 99% and $NDVI_{soil} \approx$ NDVI with cumulative frequencies of 1%.

The SC subfactor is defined as

$$SC = exp\left\{-b * S_p * \left[\frac{0.24}{R_u}\right]^{0.8}\right\}$$

where b is the empirical coefficient, S_p is the percentage of area covered by surface cover (rocks), and R_u is the surface roughness (in.).

Renard and Simanton (1990) indicated that the C-factor is most sensitive to the SC subfactor of all the subfactors because surface cover has the greatest effect on soil erosion. The empirical coefficient, b, gauges the effectiveness of surface cover in reducing soil erosion, where surface cover includes crop residue and rocks. A value of 0.039 is recommended for rangeland (Renard et al., 1997). The parameter S_p may be taken herein as percentage of rock fragments in and on the soil, a common occurrence on southwestern rangelands. A study by Wilcox and Wood (1989) for the semiarid slopes of the northern Guadalupe Mountains of New Mexico indicated a rock percentage of 14% for slopes of 0 to 17%. Rock fragment percentage summarized from the SSURGO and State Soil Geographic (STATSGO) databases

tabular data for the general vicinity of the Jicarilla Apache Nation test watersheds indicates a range between 10 and 20% (https://databasin.org).

The SR subfactor may be described by the following:

$$SR = exp\{-0.66[R_u - 0.24]\}$$

where 0.24 is the assumed baseline minimum surface roughness (in.; Renard et al., 1997).

Using the Renard et al. (1997) method, a rounded C-factor of 0.20 was estimated for each test watershed. Mussetter Engineering Inc. (2004) used 0.20 to represent relatively sparse vegetation conditions for the analysis of peak discharges in 10 tributary watersheds of the middle Rio Grande between Bernardo and Elephant Butte Reservoir. Table 8.1 summarizes the various input and calculated parameters used to estimate the C-factor.

Soil erodibility factor: rock-free

The soil erodibility factor (K-factor) measures the fine-earth fraction's susceptibility to detachment induced by water. The K-values depend on the proportions of silt, sand, organic matter, saturated hydraulic conductivity (Ksat), and soil structure, with values of K ranging from 0.02 to 0.69. The rock-free K-factor raster data utilized in this study (see Appendix 2A) were generated from the SSURGO soil database.

Table 8.1. Input and calculated cropping factor parameters for test watersheds.

Parameter	Site A	Site B	Site C
FAC[1]	0.48	0.48	0.48
SR subfactor[2]	0.60	0.60	0.60
H_{eff}[3]	2.67	2.67	2.67
S_p (%)[4]	15	15	15
SC subfactor[5]	0.83	0.83	0.83
CC subfactor[6]	0.41	0.41	0.41
C-factor	0.20	0.20	0.20

[1] Based on NDVI cumulative distributions of 1 and 99%, respectively, for $NDVI_{soil}$ and $NDVI_{veg}$.
[2] Based on piñon-juniper interspersed vegetation.
[3] H_{top} = 6 ft, H_{bot} = 1 ft (assumed for piñon-juniper interspersed vegetation).
[4] Estimated average value based on SSURGO and STATSGO data for Jicarilla Apache Nation test watersheds.
[5] S_p = 15%, R_u = 1.01 in., b = 0.039 (typical of rangeland).
[6] Based on FAC and H_{eff}.

Topographic slope length and steepness factor

The impact of topography on erosion is reflected by the slope length and steepness factor (LS-factor), which illustrates that erosion rises with slope angle and length (Mitasova et al., 1996). Many modifications have been proposed to account for the influence of the scale effect of the landscape (Pistocchi et al., 2002). An alternative topographic LS-factor proposed by Mitasova et al. (1996), which takes into account the sediment flux rate on a 2D plane, is used for this study (see Appendix 2A) and is computed as

$$LS \rightarrow A^m(sin\beta)^n$$

where A is the flow accumulation contributing upslope area per unit contour width, β is the slope angle in degrees, and m (= 0.6) and n (= 1.3) are empirical coefficients (value depends on the type of erosion specified: sheet erosion or rill erosion).

USPED

The Unit Stream Power-Based Erosion Deposition (USPED) model is a simple algorithm that forecasts the spatial variability of soil erosion and deposition for steady-state, 2D overland flow under uniform excess precipitation events within a GIS environment (Mitasova et al., 1996). Divergence of the pattern can be evaluated in a gridded-cell computational domain using horizontal planar coordinates in addition to assessing transport capacity (Mitasova et al., 1996). Transport capacity function and soil erosion/deposition pattern maps were created for the three watersheds using the USPED model; the first identifies regions with significant mass transport capacity, while the second generates erosion and deposition patterns within the watershed (Pistocchi et al, 2002; see Appendix 2A).

This approach posits that the carrying power of water flow can only move a limited quantity of sediment (Choudhary et al., 2020). By combining the RUSLE model parameters and contributing upslope area per unit contour width, the USPED transport capacity function predicts the sediment transport, and is therefore expressed as

$$T = RKCPA^m(sin\beta)^n$$

where R is the rainfall-runoff erosivity factor (hundreds of acre·ft·ton$_f$·in./acre·hr·yr); K, C, and P are dimensionless parameters from the MUSLE equation; and A, β, m (= 1.6), and n (= 1.3) are parameters from the topographic LS-factor equation.

The overall soil erosion/deposition patterns, which reveal sediment sinks or sources, were computed as (from Mitasova et al. [1996] and Mitasova [2014])

$$\nabla T = \frac{d(T\cos a)}{dx} + \frac{d(T\sin a)}{dy}$$

where a is the aspect of the terrain surface and dx and dy are the grid resolution (profile and tangential terrain curvature).

GEOMORPHOLOGICAL PARAMETERS

Because the morphometry of the drainage basin, in addition to land cover and anthropogenic activities, highly influences erosion, quantitative examination of morphology becomes essential for understanding the prevalent hydrologic and geomorphic processes that occur within a watershed (Roy et al., 2022). In this study, the sediment delivery ratio (SDR), drainage density ratio (DDR), and stream power index (SPI) were analyzed.

Sediment delivery ratio

The SDR is a metric that measures the efficiency of sediment transport expressed as the percentage of gross erosion conveyed during a certain period from a specific area. It compares the proportion of sediment delivered from eroding sources to a measuring site or watershed outlet to the total amount of soil detached across the same region above that particular point (Lu et al., 2003). The SDR is computed as (see Appendix 2A)

$$SDR = \frac{Flwlength}{(Fac * (Pixel\ size)^2)}$$

where $Flwlength$ is the drainage length raster grid (m), Fac is the flow accumulation grid (unitless), and $Pixel$ is the raster grid pixel size (m).

Drainage density ratio

The DDR is closely related to SDR regarding sediment transport, and it is computed as

$$DDR = \frac{Total\ Flwlength}{Area}$$

where $Total\ Flwlength$ is the total drainage flow length (m) and $Area$ is the total drainage area (m^2).

As DDR increases, the potential for upland erosion being transported to the measurement point increases. A DDR estimate was performed for each watershed.

Stream power index

The rate of energy dissipation with time is defined as stream power and has been extensively used as a metric to evaluate the erosive power of flowing water in erosion and sediment transport studies (Sharma, 2010). Wilson and Gallant (2000) utilized the SPI to determine the erosive effect of targeted surface runoff and identify the optimal locations for employing land conservation measures. The SPIs for the three watersheds were expressed as (Pandey and Sharma, 2017)

$$SPI = ln(A\tan\beta)$$

where A is the flow accumulation contributing upslope area per unit contour width and β is the slope gradient in degrees.

HYDROLOGIC MODELING AND SEDIMENT TRANSPORT ANALYSIS RESULTS AND DISCUSSION

Sediment yield input parameters

Table 8.2 provides an overview of the various input parameters required for the sediment yield analyses for the respective watersheds.

Peak discharge and runoff volume

The selected storm duration for hydrologic analysis must be sufficiently long so that the entire watershed contributes to runoff at the pour point. Most hydrologic designs are now based on either the 24-hr storm duration or a duration equivalent to the time of concentration. For this

hydrologic analysis of the test watersheds, a 24-hr storm duration was selected as the primary focus; however, storm durations of 12 hr and 6 hr were also included.

Tables 8.3, 8.4, and 8.5 summarize the hydrologic data for watershed Sites A, B, and C for 24-hr, 12-hr, and 6-hr storm durations, respectively. Analysis indicates that the peak discharge and runoff volume

for each site are log-normally distributed ($r^2 \approx 1$) in all cases with respect to storm frequency. The magnitude of mean annual peak discharge and mean annual runoff volume increases with increasing storm duration and follows a power-law relationship ($r^2 = 1$). The recurrence interval refers to the mean annual values, which increased as the storm duration decreased for both peak discharge and runoff volume.

Table 8.2. Derived or estimated watershed attributes.

Parameter	Site A	Site B	Site C
Area (mi^2) (ha)	1.33 (344)	9.54 (2,470)	0.81 (210)
$_2P_{24}$ (in.)	1.55	1.55	1.55
$_5P_{24}$ (in.)	1.94	1.94	1.94
$_{10}P_{24}$ (in.)	2.25	2.25	2.25
$_{25}P_{24}$ (in.)	2.69	2.69	2.69
$_{50}P_{24}$ (in.)	3.03	3.03	3.03
$_{100}P_{24}$ (in.)	3.39	3.39	3.39
CN[1]	76	83	87
R-factor[2]	10.11	10.00	10.86
LS-factor[3]	1.13	1.74	1.07
K-factor[4]	0.20	0.31	0.30
C-factor[5]	0.20	0.20	0.20
% Silt and clay[6]	20	20	20
NDVI[7]	0.13	0.13	0.11
FAC[8]	0.48	0.48	0.48
Flow length (m)[9]	11,309	86,805	29,301
SDR (m/m^2)[10]	1.12	1.02	0.32
DDR (m/m^2)[11]	3.29×10^{-3}	3.51×10^{-3}	1.40×10^{-2}
Land slope (%)[12]	19.8	27.6	19.6
SPI (m^2/m)[13]	0.23/14.6	0.19/14.0	-0.17/13.7
D_{50} (mm)[14]	0.30	0.30	0.30

[1] Area-weighted curve number.
[2] Area-weighted R-factor (units of hundreds of ft-ton_f-in./acre-hr-yr).
[3] Area-weighted 2D flow accumulation LS-factor calculated from a 10-m DEM resolution.
[4] Area-weighted K-factor based on SSURGO database and unadjusted for rock fragments.
[5] Based on the five subfactors method of Renard et al. (1997) with estimated FAC from PDM.
[6] Estimated based on soil map units from the Web Soil Survey of the Jicarilla Apache Nation, New Mexico.
[7] Area-weighted NDVI from Landsat 8 spectral reflectance rounded to two decimal places.
[8] Area-weighted FAC based on PDM rounded to two decimal places.
[9] Measured in the downstream direction.
[10] Average based on stream network in the downstream direction.
[11] Average based on stream network in the downstream direction evaluated at a flow accumulation threshold of 50,000 for Sites A and B and 5,000 for Site C.
[12] Mean topographical slope.
[13] Mean and maximum.
[14] Lower estimate from grain size distribution for collected samples.

Table 8.3. Peak discharge and runoff volume (24-hr storm duration).

Frequency (yr)	Site A Peak Discharge (cfs)	Site A Runoff Volume (acre-ft)	Site B Peak Discharge (cfs)	Site B Runoff Volume (acre-ft)	Site C Peak Discharge (cfs)	Site C Runoff Volume (acre-ft)
2	186.8	18.3	2,619.9	224.3	317.7	24.2
5	326.7	31.4	4,286.5	351.4	490.4	36.5
10	454.4	43.4	5,722.2	462.2	635.8	47.0
25	656.1	62.4	7,873.2	630.4	850.1	62.7
50	825.2	78.4	9,612.8	767.1	1,021.0	75.3
100	1,014.0	96.2	11,498.5	916.9	1,204.6	89.0
Mean annual	225.2	21.7	2,937.1	242.9	337.4	25.3
Recurrence interval (yr)	2.60	2.57	2.41	2.34	2.27	2.22

Table 8.4. Peak discharge and runoff volume (12-hr storm duration).

Frequency (yr)	Site A Peak Discharge (cfs)	Site A Runoff Volume (acre-ft)	Site B Peak Discharge (cfs)	Site B Runoff Volume (acre-ft)	Site C Peak Discharge (cfs)	Site C Runoff Volume (acre-ft)
2	106.8	10.9	1,600.4	146.8	208.3	16.4
5	200.0	19.5	2,781.8	236.6	334.8	25.4
10	292.2	28.1	3,886.1	320.7	449.4	33.5
25	445.7	42.6	5,627.5	454.8	626.2	46.3
50	580.2	55.3	7,078.4	567.9	771.3	56.9
100	734.4	69.8	8,686.4	694.1	930.1	68.6
Mean annual	140.0	13.7	1,925.5	165.3	232.2	17.7
Recurrence interval (yr)	2.80	2.74	2.60	2.48	2.42	2.47

Table 8.5. Peak discharge and runoff volume (6-hr storm duration).

Frequency (yr)	Site A Peak Discharge (cfs)	Site A Runoff Volume (acre-ft)	Site B Peak Discharge (cfs)	Site B Runoff Volume (acre-ft)	Site C Peak Discharge (cfs)	Site C Runoff Volume (acre-ft)
2	55.4	6.2	896.4	92.1	129.0	10.6
5	123.1	12.4	1,813.4	163.1	231.7	18.1
10	196.6	19.2	2,741.1	233.5	330.5	25.1
25	318.8	30.6	4,196.8	344.5	481.2	35.8
50	432.9	41.4	5,485.4	443.8	612.0	45.3
100	566.3	53.9	6,930.9	556.4	756.6	55.8
Mean annual	87.4	8.9	1,260.0	114.1	160.4	12.5
Recurrence interval (yr)	3.14	3.00	2.90	2.69	2.67	2.73

A linear relationship between annual runoff volume (acre-ft) and annual peak discharge (cfs) for the test watersheds (storm frequencies 2 yr through 100 yr at 24-hr duration) is evident in Figure 8.11. Additionally, a linear relationship is observed in Figure 8.12 between mean annual runoff volume and mean annual peak discharge for the 24-hr storm duration, as was also observed for the 12-hr and 6-hr storm durations (not shown).

Runoff volume (acre-ft) = 0.0802*Peak discharge (cfs)
$R^2 = 0.99$
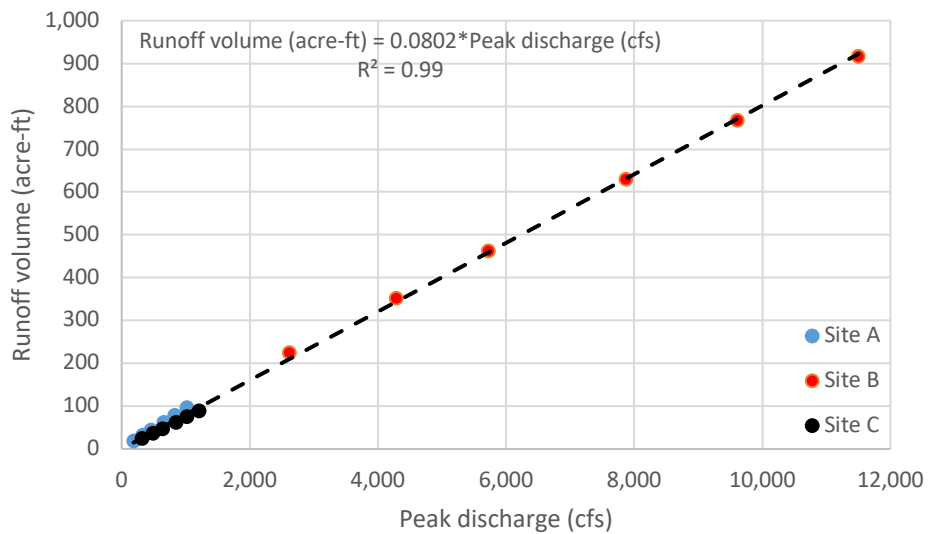
Figure 8.11. Runoff volume versus peak discharge for 24-hr storm duration.

Mean annual runoff volume (acre-ft) = 0.0844*Mean annual peak discharge (cfs)
$R^2 = 0.99$
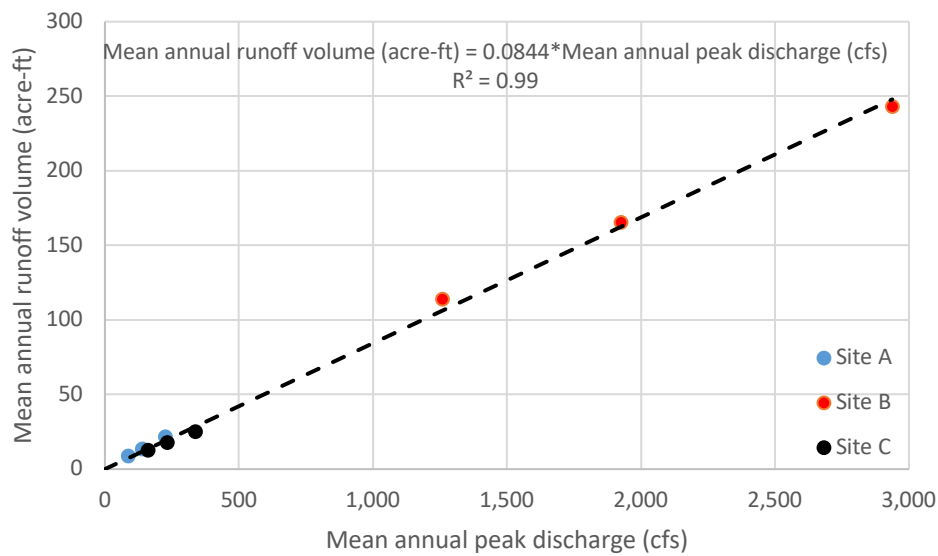
Figure 8.12. Mean annual runoff versus mean annual peak discharge for 24-hr storm duration.
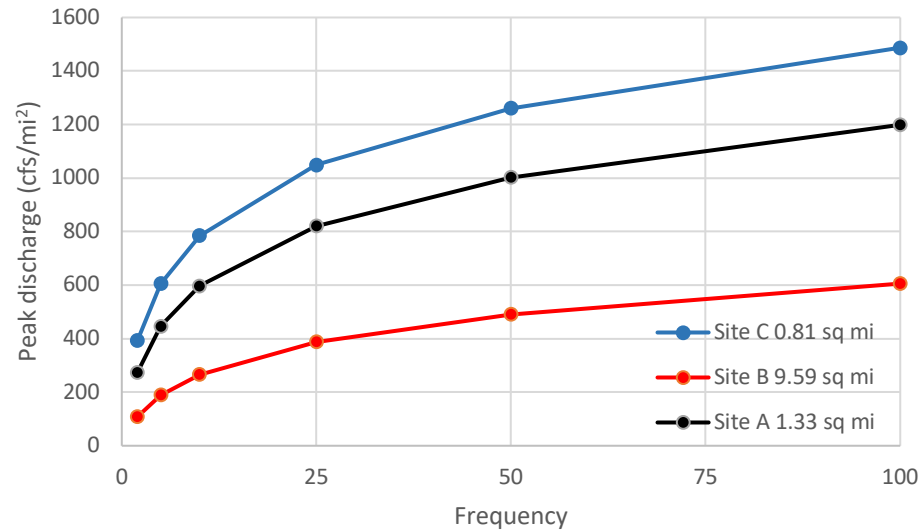
Figure 8.13. Normalized peak discharge versus storm frequency for 24-hr storm duration.

Figure 8.13 provides a plot of peak discharge per unit area (cfs/mi^2) versus storm frequency for a 24-hr storm duration. Similar trends were observed for the 12-hr and 6-hr storm durations. For a given storm frequency, Site C has the highest normalized peak discharge, with Site B having the lowest normalized peak discharge.

Peak discharge is inversely correlated with watershed time of concentration. Fang et al. (2008) estimated time of concentrations for 96 Texas watersheds using various empirical equations to generalize a proportional square root relationship with drainage area. Site B having the larger area would have a longer time of concentration to contribute runoff from the most distant point to the watershed pour point hydraulically. Even though the absolute magnitude of peak discharge is the highest of the three test watersheds, the normalized peak discharge is the lowest for any given storm frequency. Similarly, Site C having the smallest area should have the highest normalized peak discharge for any given storm frequency for comparable land status as per CN.

Total sediment yield and wash load

The bed material fraction of the total sediment yield was estimated for a given frequency of precipitation event and 24-hr storm duration using the MPM-Woo equation and the specified watershed bed material D_{50}. The wash load fraction of the total sediment yield was developed using the MUSLE equation for a given frequency of precipitation event and 24-hr storm duration based on a watershed K-factor, C-factor, P-factor (the support practice factor), and percent silt and clay in the watershed soil.

The watershed coefficients for discharge, velocity, and width previously developed significantly impact the bed material load, not the wash load. In addition, the watershed bed material D_{50} impacts the amount of bed material load, not the wash load. An analysis of the MPM-Woo equation for a given storm frequency and storm duration shows an exponential increase in bed material load for a D_{50} less than about 1.5 mm, asymptotically decreasing in bed material load for D_{50} greater than 1.5 mm. Figure 8.14 shows this exponential relationship for the 100-yr frequency 24-hr storm duration for Site C. Sites A and B exhibit a similar trend.
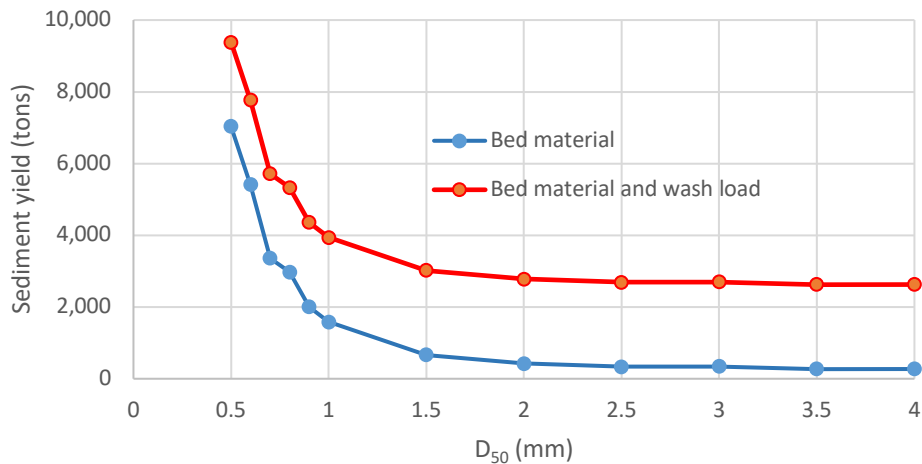
Figure 8.14. Sediment yield versus D_{50} grain size for Site C (100-yr 24-hr design storm).

Table 8.6 summarizes the total sediment yield and wash load data for the three test watersheds, assuming a D_{50} of 0.30 mm. Bulking factors (BF) ranged from 1.08 to 1.12, 1.16 to 1.24, and 1.09 to 1.13 for Sites A, B, and C, respectively, for the 2-yr 24-hr and 100-yr 24-hr design storms, respectively. Bulking factors estimated using the mean annual peak discharge and mean annual runoff volume for Sites A, B, and C were 1.08, 1.17, and 1.08, respectively.

An online Colby correction software (http://ponce.sdsu.edu/onlinecolby.php) was used to ascertain the impact of wash load concentration

on additional transport of bed material based on estimated hydraulic attributes of flow velocity, flow depth, and flow width for each peak discharge. Sediment yields were only slightly lower compared to the sediment yields displayed in Table 8.6, indicating a negligible effect of wash load concentration estimates on sediment transport.

Figure 8.15 displays the normalized total sediment yield for the three watersheds as a function of storm frequency for a storm duration of 24 hr, along with the mean annual yield. The lowest and highest yield correspond to Site A and Site B, respectively. Site A

Table 8.6. Sediment yield and wash load estimates (based on average watershed K-factor, LS-factor, and C-factor with D_{50} = 0.30 mm).

| Frequency (yr) | Site A | | Site B | | Site C | |
	Mean Annual Sediment Yield (tons)	Mean Annual Wash Load (tons)	Mean Annual Sediment Yield (tons)	Mean Annual Wash Load (tons)	Mean Annual Sediment Yield (tons)	Mean Annual Wash Load (tons)
2	2,404	243	59,971	10,114	3,801	540
5	4,653	449	104,669	17,085	6,299	867
10	6,910	647	146,596	23,384	8,567	1,153
25	10,770	975	214,160	33,210	12,159	1,594
50	14,218	1,259	272,032	41,411	15,184	1,956
100	18,237	1,583	337,901	50,546	18,577	2,355
Mean annual	3,271	312	72,676	11,788	4,365	598
Recurrence interval (yr)	2.88	2.76	2.63	2.52	2.50	2.40
Unit soil loss[1]	3.85	0.37	11.91	1.93	8.42	1.15

[1] Unit soil loss (ton/acre/yr) for mean annual yield.

had the lowest CN and K-factor relative to the other two watersheds (Table 8.2). A lower CN results in a lower peak discharge and less runoff volume and, therefore, a lower bed material yield with respect to the MPM-Woo equation. Additionally, the MUSLE predicts that a lower K-factor coupled with lower peak discharge and runoff volume produces a reduced fine sediment yield for comparable watershed attributes of R-factor, LS-factor, and C-factor. The difference in magnitude of these two key attributes helps rationalize the lower estimate of overall sediment yield for Site A.

Mussetter Engineering Inc. (2004) reported that the estimated sediment yield (tons) from 10 tributaries of the Rio Grande was positively correlated with drainage area (mi^2) for all frequencies (2 yr to 100 yr) and for the mean annual yield using power-law regressions. The normalized mean annual yield, however, was inversely correlated with drainage basin size based on a logarithmic fit of the data. García-Ruiz et al. (2015) evaluated direct measurement soil loss data from 3,207 records and noted a negative relationship for normalized erosion rates versus the size of the study area displayed as a log-log plot as shown in Figure 8.15. The estimated sediment yields for the Jicarilla Apache

Nation watershed do not follow previously observed patterns; however, the database is limited to three watershed estimates.

Impact of D_{50} on bed material load

Figure 8.14 illustrates the influence of the selected D_{50} size on bed material yield. The impact of an incremental increase in D_{50} size from 0.30 mm to 0.80 mm was evaluated using mean annual estimates for peak discharge and runoff volume for each watershed and the MPM-Woo equation for a 24-hr storm duration. The bed material load magnitude was reduced as the sediment grain size increased. A reduction of 62, 50, and 60% in sediment yield was noted for Sites A, B, and C, respectively, as the D_{50} size increased from 0.30 to 0.40 mm. An increase from 0.30 to 0.80 mm indicated a sediment yield reduction of 88, 76, and 87%, respectively, for Sites A, B, and C. At a D_{50} of 0.80 mm, the bed material load was approximately the same magnitude (more or less) as the wash load, which is independent of a D_{50} size. Table 8.7 shows the estimated bed material load (tons) as a function of sediment grain size. For comparison, the wash load at the D_{50} of 0.80 mm analysis was 287, 11,260, and 604 tons, respectively, for Sites A, B, and C.
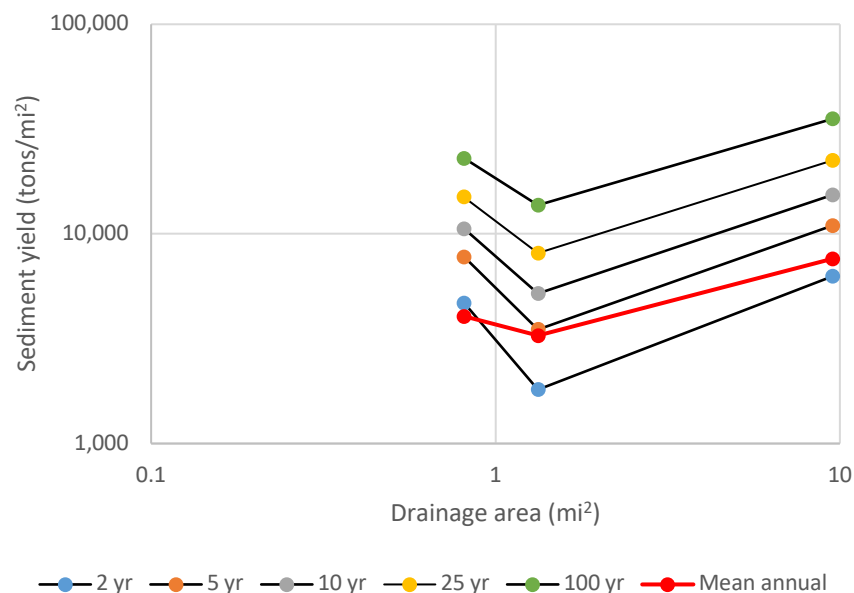
Figure 8.15. Normalized sediment yield versus drainage area for the three test watersheds.

Table 8.7. Bed material load at mean annual discharge and mean annual runoff volume versus D_{50} sediment size.

D_{50} (mm)	Site A	Site B	Site C
		(tons)	
0.30	2,674	55,466	3,454
0.40	1,023	27,770	1,380
0.50	890	27,848	1,228
0.60	620	22,620	877
0.70	379	14,139	540
0.80	309	13,132	449

Dominant discharge estimates

As previously stated, the dominant or effective discharge for the watershed is associated with the increment of discharge that carries the largest volume of sediment over a long period of time. Figures 8.16, 8.17, and 8.18 display the correlation between peak discharge and total sediment yield for each respective test watershed and 24-hr storm duration for a D_{50} of 0.30 mm. Using these correlations and the respective mean annual sediment yield, the dominant discharge for Sites A, B, and C is estimated to be 251.9, 3,229.9, and 371.0 cfs, respectively.

Dominant discharges may also be determined by logarithmic interpolation between the peak discharges and sediment yields for the appropriate recurrence interval storms using the mean annual sediment yield (Mussetter Engineering Inc., 2008). This gives a geometric mean dominant discharge of 244.1, 3,166.7, and 362.7 cfs for Sites A, B, and C,

respectively. The ratio of the 100-yr peak discharge to each dominant discharge estimate was 4.03 and 4.15, 3.56 and 3.63, and 3.25 and 3.32 for Sites A, B, and C, respectively, versus an average of approximately 5.0 for arroyos in the Southern Sandoval County Arroyo Flood Control Authority jurisdictional area (Mussetter Engineering Inc., 2008).

USPED transport capacity and erosion/deposition pattern

An average sediment transport capacity of wash load was estimated based on a watershed 2D flow accumulation, K-factor raster, R-factor raster, constant C-factor of 0.20, and P-factor set at 1 for an area-weighted sediment transport capacity of 0.45 tons/acre/yr (1.02 tonnes/ha/yr) or 386 tons/yr (350 tonnes/yr), 0.80 tons/acre/yr (1.80 tonnes/ha/yr) or 4,879 tons/yr (4,426 tonnes/yr), and 0.70 tons/acre/yr (1.57 tonnes/ha/yr) or 361 tons/yr (327 tonnes/yr) for Sites A, B, and C, respectively.

The erosion/deposition pattern for Sites A, B, and C using divergence of transport capacity indicated an area-weighted net erosion mean of -315, an area-weighted net erosion mean of -44, and an area-weighted net deposition mean of +53, respectively. The divergence map allows one to detect areas where transport capacity increases (erosion) or decreases (deposition), and areas where it is stable. The divergence maps are provided for the respective watersheds in Appendix 2A.

Sediment yield (tons) = 17.85 Discharge (cfs) + 460.17
R² = 1.0
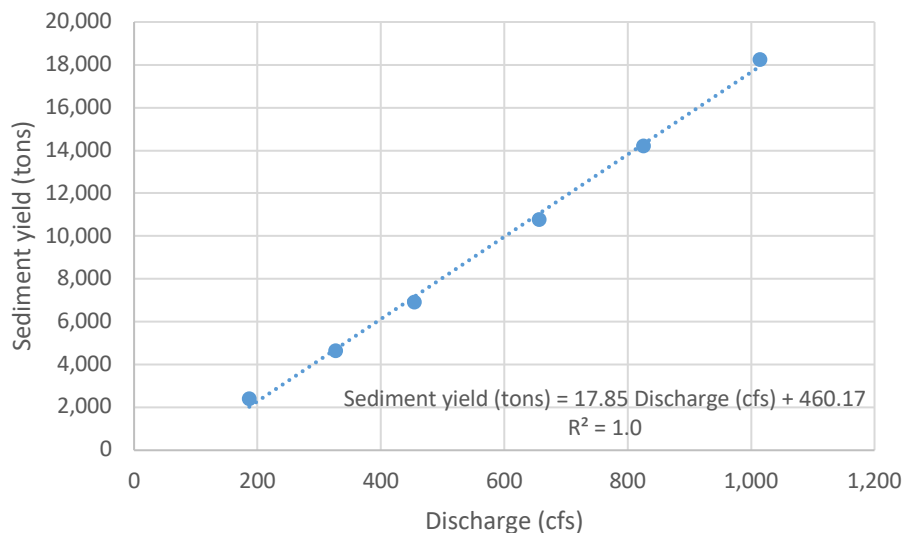
Figure 8.16. Peak discharge versus total sediment yield for Site A.
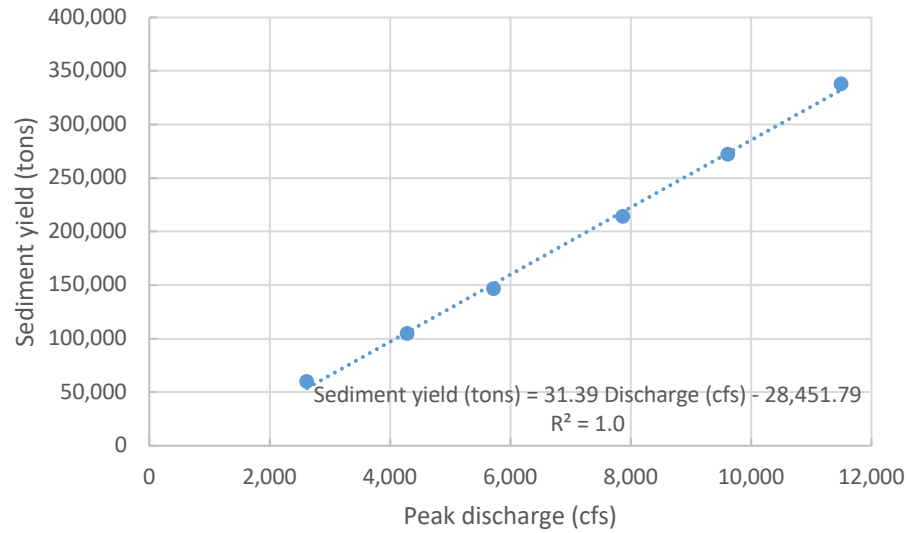
Figure 8.17. Peak discharge versus total sediment yield for Site B.
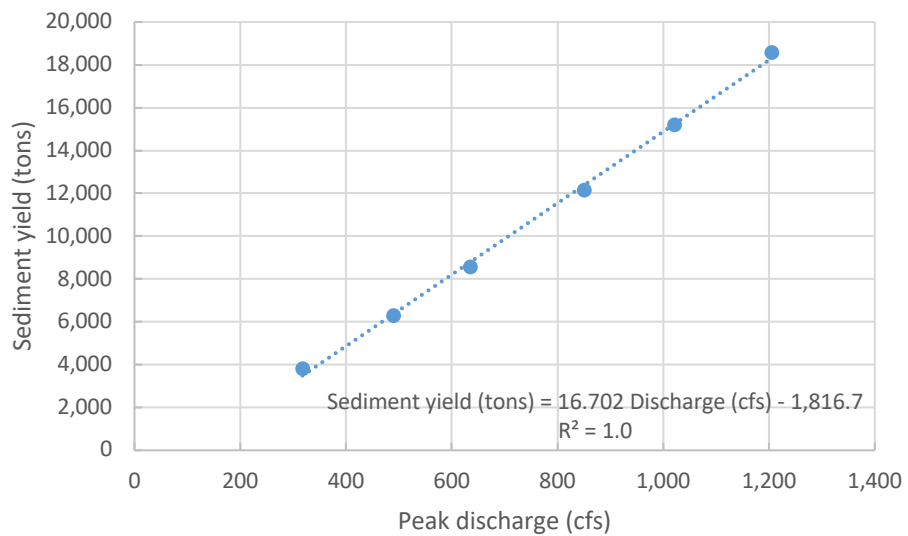
Figure 8.18. Peak discharge versus total sediment yield for Site C.

MUSLE versus USPED

Table 8.8 compares the MUSLE fine sediment yield based on mean annual values for peak discharge and runoff volume, an area-weighted R-factor, an area-weighted K-factor, an area-weighted LS-factor, constant C-factor, and P-factor set at 1, assuming a 24-hr storm duration, with the estimated USPED average sediment transport capacity based on a watershed 2D flow accumulation, R-factor raster, K-factor raster, constant C-factor of 0.20, and P-factor set at 1; the latter estimate is independent of the design storm attributes. Although the methods are analytically different in their approach, the magnitude of fine sediment yield is somewhat comparable on an equivalent annual basis.

Sediment load concentration

Table 8.9 provides an estimate of total sediment concentration given the estimated sediment yields for each watershed and its predicted runoff volumes for a 24-hr storm duration. For comparison, 10,000 mg/L is 1%. These concentrations lie within what is considered as water flood (Mussetter Engineering Inc., 2008). Site B has the overall highest concentrations. The mean annual concentration represents a bulking factor around 1.17.

Contrast of test watershed attributes

Table 8.3 displays derived attributes for the three test watersheds. All three watersheds are comparable as per the vegetative cover (NDVI, FAC, and thus C-factor) and R-factor with respect to potential for fine sediment transport. Site B has the highest LS-factor, whereas Sites A and C have approximately the same LS-factor. A higher composite topographic results in higher fine sediment yield. For comparison, using mean annual yields of bed material and wash load from Table 8.6 indicates a percentage of fine sediment yield to total sediment yield of 9.5, 16.2, and 13.6%, respectively, for Sites A, B, and C.

Site C has the lowest SDR and DDR, which suggests a lower delivery of upland erosion to the watershed pour point. Sites A and B have comparable SDR and DDR values. Site B has the highest overall mean topographic relief compared to Sites A and C, which are approximately equal. Steeper slopes enhance soil erosion. All three watersheds have comparable maximum SPI values; however, Sites A and B have higher mean values of SPI compared to Site C. This is significant because SPI is considered a measure of the main driving forces acting within a stream network, thus influencing the ability of runoff to transport sediments.

Table 8.8. MUSLE versus USPED sediment transport.

Watershed Site	Peak Discharge (cfs)	Runoff Volume (acre-ft)	Wash Load Concentration (ppm)	MUSLE (tons/event)[1]	USPED (tons/yr)	Ratio USPED/ MUSLE
A	225.2	21.7	10,064	297	386	1.30
B	2,957.1	242.9	34,115	11,306	4,879	0.43
C	337.4	25.3	16,644	572	361	0.63

[1] Based on a mean annual event (tons/event = tons/yr).

Table 8.9. Sediment concentrations for the test watersheds.

Watershed Site	2 yr	5 yr	10 yr	25 yr (mg/L)	50 yr	100 yr	Mean Annual
A	97,702	109,083	117,204	127,053	133,498	139,551	110,946
B	196,818	219,265	233,478	250,078	261,049	271,282	220,279
C	115,621	127,038	134,179	142,753	148,438	153,652	127,181

IX. GULLY DEVELOPMENT ANALYSIS

Clint Richardson

CHAPTER SUMMARY

Three watersheds on the Jicarilla Apache Nation in northern New Mexico were analyzed for potential incised gully development. The analysis shows that incisions are possible based on an estimated critical threshold metric, with additional sediment contribution possible to the watershed outlet as a result, which supports previous field reconnaissance visual assessments of gully development. However, considerable uncertainty lies with the theoretical approach in terms of key input variables, such as curve number, watershed slope, rock fragment cover, and contributing drainage area at the headcut area. A slope-area power function was determined for each watershed and compared with a critical threshold coefficient developed by Torri and Poesen (2014). In a relative sense, gully development is possible in all three watersheds based on watershed slope and topographic drainage area. The magnitude and rate of gully development is indeterminate at this stage of investigation.

THRESHOLD MODEL FOR GULLY DEVELOPMENT

Torri and Poesen (2014) presented an extended theoretical approach to describe incised gully development by runoff based on a widely used slope-area power function that describes the critical slope gradient and drainage area for gully initiation at given sites, or

$$SA^b \geq k$$

where S is the slope gradient (m/m), A is the contributing drainage area (ha), b is an exponent related to dominant processes during gully formation,

and k is a constant that depends on soil, rainfall, vegetation cover, and lithology, representing resistance, or threshold, to gully development.

A critical threshold for gully development described above can vary widely depending on site conditions given different k values for dissimilar land cover types (Torri and Poesen, 2014). It is evident in the above approach that drainage area is an important variable; however, the actual contributing drainage area may differ from the topographic drainage area (Torri and Poesen, 2014). Most analyses use the topographic drainage area, which is equal to or greater than the actual contributing drainage area at the headcut.

Based on an extensive review of datasets of S-A relationships for overland flow-induced gully headcuts collected in various parts of the world, Torri and Poesen (2014) analyzed the data to examine trends and magnitudes in both b and k. The NRCS curve number (CN) was implemented to study the effects of vegetation on topographic threshold conditions for gully head development. The traditional maximum potential losses (S_{max}) to runoff determined based on the magnitude of CN was modified to reflect a lower initial abstraction from 0.20 to 0.05, or

$$S_{\text{max}\,0.05} = 0.819 S_{\text{max}\,0.20}^{1.15}$$

With this approach, analysis of the datasets showed that the exponent b (average and median) did not exhibit a trend with the various land use classes, suggesting that b can be represented by a constant value to simplify the critical threshold approach. The trend for the k coefficient increased when moving from tilled soils exposed to runoff to soils protected from erosion by a permanent vegetation cover. Hence, the researchers felt that assuming a constant exponent b does not change the general trend of the k coefficient. Two values of exponent b were arbitrarily

selected to evaluate the threshold values of k for the datasets, resulting in interpolating equations for both as a function of $S_{max\,0.05}$:

$$k = 0.00127S_{max\,0.05} - 0.40$$

for b = 0.38, r^2 = 0.92, and

$$k = 0.00156S_{max\,0.05} - 0.086$$

for b = 0.50, r^2 = 0.81. The researchers reported that an exponent between 0.38 and 0.40 had been previously confirmed based on observations made shortly after a rainstorm that caused the incision of the gully channel. A value of 0.38 was selected for additional analysis based on the higher regression correlation.

The k coefficient was further modified by a multiplier to account for parameter variation not accounted for by $S_{max\,0.05}$. Its value was said to oscillate around 1. In addition, the CN method was corrected for rock fragment cover (RFC) that can significantly affect overall soil infiltration rate. Comparing RFC for the datasets to the ratio of measured k values with predicted k values, an exponential function was derived:

$$k_{corrected} = k/\{0.69exp(1.2RFC)\}$$

Coupled together with the uncorrected k coefficient yields the extended model for gully development, or

$$SA^{0.38} \geq \{0.00127S_{max\,0.05} - 0.40\}c\{0.69exp(1.2RFC)\}$$

where c is a multiplier for additional variation in k.

JICARILLA APACHE NATION WATERSHED POTENTIAL FOR GULLY DEVELOPMENT

A preliminary analysis was performed to evaluate the relative threshold for gully development in each of the test watersheds using the extended approach of Torri and Poesen (2014). Watershed channel slopes were estimated, respectively, from extracted data by Leopold and Miller (1956) for ephemeral streams in New Mexico and also reported by Shaw and Cooper (2008) for ephemeral streams in the semiarid southern Colorado Plateau in Arizona, or

$$S = 0.0204A^{-0.178}, r^2 = 0.99$$

where A is the drainage area (mi^2) and S is the slope (ft/ft), and

$$S = 0.0332A^{-0.179}, r^2 = 0.62$$

where A is the drainage area (km^2) and S is the slope (m/m).

For this relationship, watershed slopes were 0.020 (0.027), 0.021 (0.018), and 0.030 (0.029), respectively, for Sites A, B, and C. Crude estimates were also obtained using Google Earth elevations along transects of stream beds in each watershed. These estimates paralleled those obtained via the Leopold and Miller (1956) and Shaw and Cooper (2008) correlations.

Table 9.1 provides the results of the extended approach for each watershed based on an estimated RFC of 15% and the respective CN, assuming no modifier for the k coefficient. Rock fragment percentage summarized from SSURGO and STATSGO tabular data for the general vicinity of the Jicarilla Apache Nation test watersheds indicates a range between 10 and 20%. The threshold k is exceeded for each watershed. Incised gully development within each watershed is, therefore, possible as evident from field reconnaissance. Any degree of incision would add additional sediment load to the watershed outlet.

Table 9.1. Threshold gully development.

Parameter	Site A	Site B	Site C
CN	76	83	86
Slope (m/m)	0.027	0.018	0.029
Area (ha)	344	2,740	210
SA^{-b}	0.18(0.24)[1]	0.43(0.37)[1]	0.43(0.22)[1]
k	0.10	0.05	0.02

[1] Leopold and Miller (1956) and Shaw and Cooper (2008).

DISCUSSION

A higher CN results in a higher excess rainfall available for overland flow and, hence, a lower critical threshold in accordance with this theoretical approach. A higher watershed slope enhances the likelihood of exceeding the critical threshold. The above analysis assumes a total topographic drainage area contributing to a given headcut area, which would be applicable for an incision occurring at the watershed outlet area. This would not be the case for a gully development within a subarea of total watershed. However, the method could be applied within individual subareas for the three test watersheds given information of drainage slope, drainage area to the subarea outlet, RFC, and CN. This sectionalized assessment could possibly identify subareas with high potential for gully development, which could correlate with spatial and temporal field data. The magnitude and rate of development, however, could not be assessed without further investigation and field reconnaissance. The approach herein is a relative view of potential gully development, not absolute.
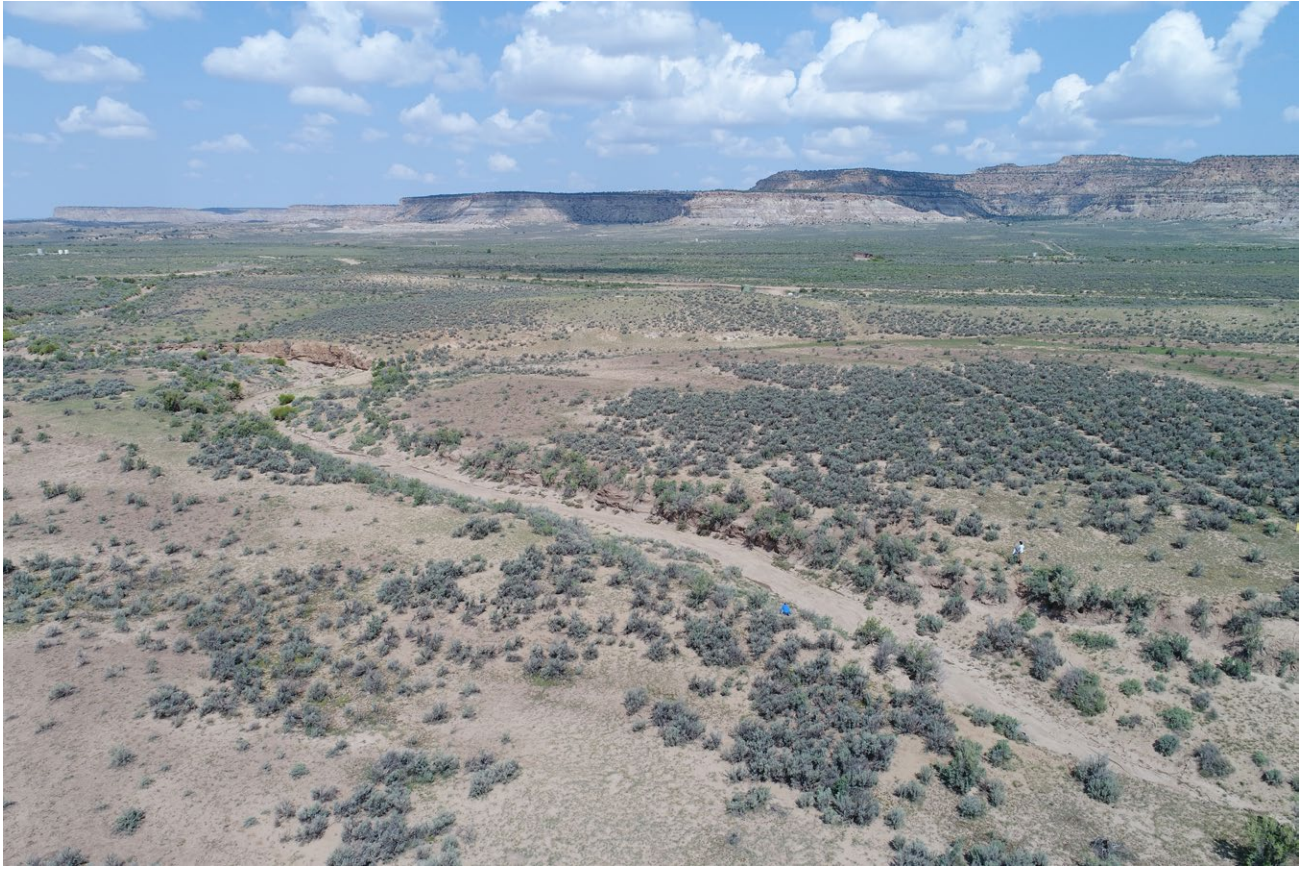
Aerial photograph of Las Norias Canyon, Tapicito Creek, and BS Mesa, Jicarilla Apache Nation. *Photo by New Mexico Bureau of Geology*

X. ENGINEERING RECOMMENDATIONS

Faustin Kumah, Navid Mojtabai, Mehrdad Razavi, and Clint Richardson

INTRODUCTION

The appropriate control for a specific erosion case is determined by considerations that include the stream parameters, the erosion process, construction and maintenance needs, theft, aesthetic appeal, and budget. Countermeasures can be implemented during the earliest establishment of the drainage way or even changed to address issues relating to stability whenever the need arises. An excellent, cost-effective approach, which is also considered a sound engineering convention, is retrofitting because the location, extent, and type of possible stability concerns are usually not visible in many areas at the preliminary progression phase and can take many years to emerge. However, performance is likely the most essential factor in selecting a particular mitigation strategy (Mussetter Engineering Inc., 2008).

Many researchers have proven that integrated watershed management solutions can effectively control soil erosion (Frankl et al., 2016; Teka et al., 2020). Regular monitoring and inspection should be done to ensure timely maintenance and upgrades, and is typically required for almost all soil and water conservation approaches. Detailed design guidelines and specifications for each erosion control technique are available in reference materials utilized to compile this report, including Amimoto (1978), Goldman et al. (1986), FAO (1998), Mussetter Engineering Inc. (2008), Lagasse et al. (2009), Tahoe Regional Planning Agency (2014), Baird et al. (2015), and Garcia-Chevesich (2018).

GEOTEXTILES

Geotextiles tackle engineering challenges such as slope stability, erosion protection, and hydraulic sealing projects (Blond et al., 2019). Even though firms in this industry utilize several solutions for slope rehabilitation and surface protection, geotextiles like biomats, geomats (Fig. 10.1), and meshes have shown to be particularly effective in providing this first protection. Any geotextile offered is built for a particular flow, soil type, slope, and other variables. As a result, manufacturers typically help determine the optimal geotextile solution for any project (Garcia-Chevesich, 2018). In May Ba'ati, Ethiopia, geomembranes were used to build subsurface dams to stabilize gully heads (Frankl et al., 2016). Some types of geotextiles are outlined below.
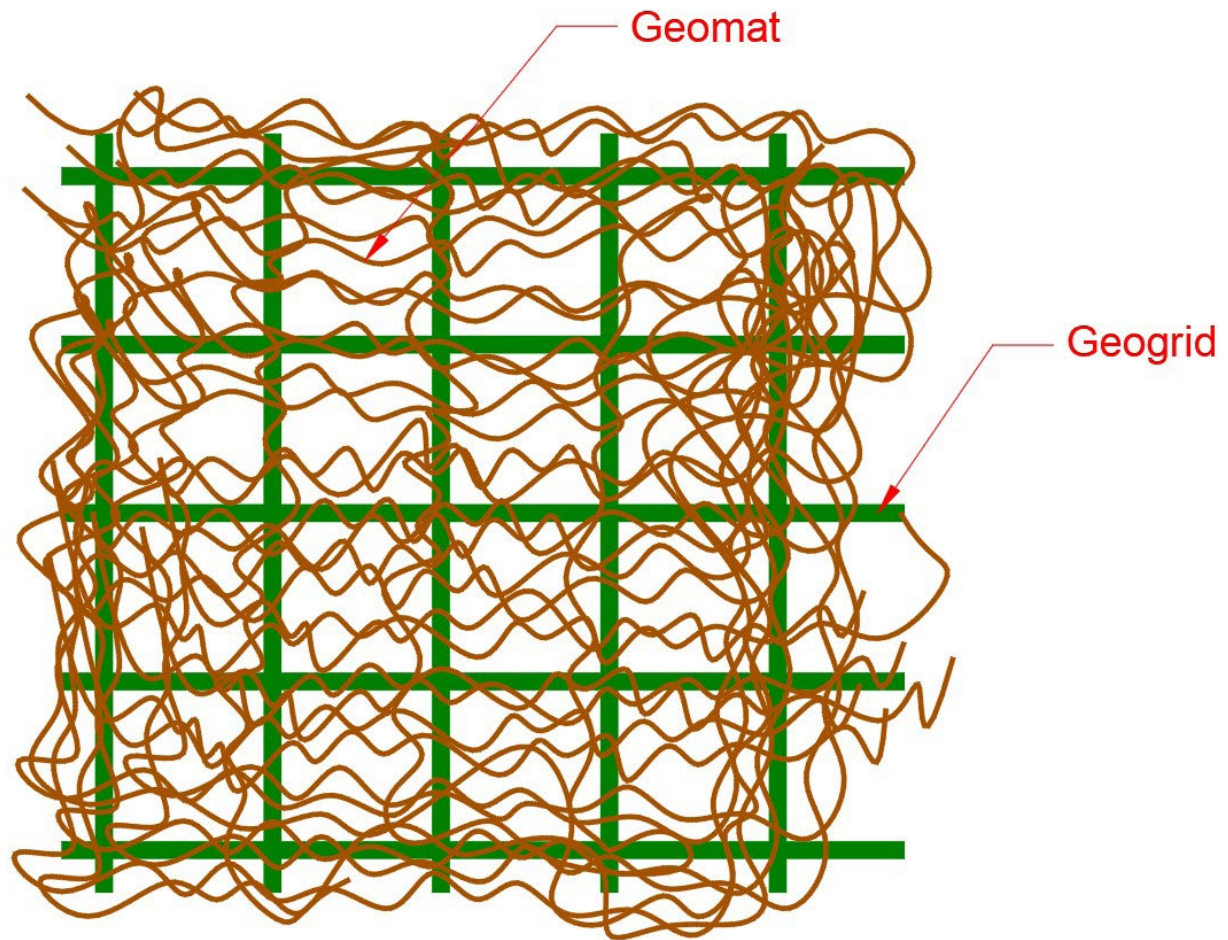
Figure 10.1. Geomats and geogrids.

Biomats

Biomats are typically composed of natural fibers sandwiched between two extremely fine photodegradable polymer nets and sewn in both directions with jute fibers. The composition and availability of the nets and fibers employed will dictate their possible use—slowing sheet erosion across hillsides, covering ditches, lining earth barriers, and providing support for climbing plants—and their application procedures. The contours of gullies and ravines can be covered since the blanket can adapt to the ground irregularities; with the aid of gabions, bioengineering methodologies, or biodegradable (or synthetic) fiber rolls, this provides an option for rehabilitating basin headwaters and channeling (Garcia-Chevesich, 2018).

Geocells

Many scientists have contributed to the advancement of geocell technology, which was initially developed by the U.S. Army Corps of Engineers in the early 1970s for the military (Hegde, 2017). It is a distinctive structure composed of high-density polyethylene (HDPE) welded strips that create open cells. It is available in a variety of cell sizes and cell heights. As a result, geocells (Fig. 10.2) can be filled with concrete, aggregates, and even soils with vegetation potential. Geocells are also viable alternatives to traditional timber concrete forms because they provide a confined frame that adapts to uneven channel subgrades, retaining the concrete and preventing cracks (Garcia-Chevesich, 2018).

Fiber roll

Fiber rolls are tubular structures packed with organic fibers like coconut or cereal straw wrapped in a plastic or organic netting. They are installed perpendicular or parallel to the flow of water to temporarily limit soil sedimentation and erosion caused by the water flow. Furthermore, those with synthetic mesh can endure a more extended life after being silted up with fine particles, whereas organic nets might deteriorate very rapidly if not blanketed by plants (Garcia-Chevesich, 2018).

As a soil erosion control device, a set of fiber rolls is often positioned along the slope's contours to capture sediments and impede overland flow. Biologs can be readily shaped to accommodate uneven terrain for use in drain inlets, around storm drains to block sediments from entering, and as check dams in unlined ditches Even though they are more efficient and last longer than sandbags, they are ineffective during seasons of significant runoff (Tahoe Regional Planning Agency, 2014).

Fiber rolls have become useful in protecting the beds and banks of ephemeral channels when used in tandem with rip-raps, erosion blankets, and other channel stabilization techniques (Garcia-Chevesich, 2018).

ZUNI BOWL

The Zuni bowl (Fig. 10.3) is an in-channel headcut control structure made primarily of rock-lined step falls and plunge pools that inhibits the headcut from migrating upstream by splitting a cascading, eroding headcut into several steps (Sponholtz and Anderson, 2010).

CHECK DAMS

Among the numerous soil and water management approaches, one of the most popular is check dams, which have been devised to minimize soil erosion caused by gullying (Frankl et al., 2016). Check dams (Fig. 10.4) are typically barriers 1 to 2 m high (Fenta et al., 2016) made of sandbags, loose rock, timber, gabion (Fig. 10.5), dried masonry, or a combination of gabion and dried masonry constructed across streams and gullies. Check dams decrease the channel's effective slope, lowering the flow rate of the water, allowing sediment particles to settle, and therefore minimizing erosion of the channel (Fenta et al., 2016).

Check dams can be constructed of porous or nonporous structures. The design of porous check dams is more straightforward, less expensive, and often more effective than nonporous check dams. In addition, these can be constructed entirely by hand and without regard for essential engineering principles. Loose boulders, gabions, waste tires, and logs are commonly used materials to construct porous check dams (Garcia-Chevesich, 2018). Nonporous check dams are made of concrete, metallic sheets, wood, earth, or any other material that is sufficiently impermeable and robust. A deep anchoring is required because the structure must withstand the considerable hydrostatic forces of rushing water

(Garcia-Chevesich, 2018). Through sedimentation, the sediments can fill check dams and form human-made plain areas, which can later be recovered for high-quality agricultural lands due to enrichment of nutrients throughout the erosion processes occurring on the hillslopes (Wang et al., 2011).

Mekonnen et al. (2015) compiled studies done on the amount of sediments trapped by check dams and found that check dams installed at five catchment outlets in China trapped 10,465 Mg/km² per year, three check dams jointly collected 6,162 m³ in Malaysia, and 20 check dams utilized in catchment areas ranging from 1.5 to 317 ha collected 4 to 920 m³ in Spain.

Baird et al. (2015) devised a novel method for assessing hydraulics and the corresponding trends of aggradation and degradation associated with the construction of check dams and other transverse structures. They verified that stream rehabilitation utilizing rock-detention structures is successful over a wide range of time scales. Figure 10.6 shows a rock-detention structure used to detain water and trap sediments.

Frankl et al. (2016) detailed a new approach implemented in northern Ethiopia, which involves installing a vertical geomembrane dam perpendicular to the gully axis to decrease soil cracking by enhancing local soil moisture conditions and restricting bypass flow in soil pipes near the check dam.
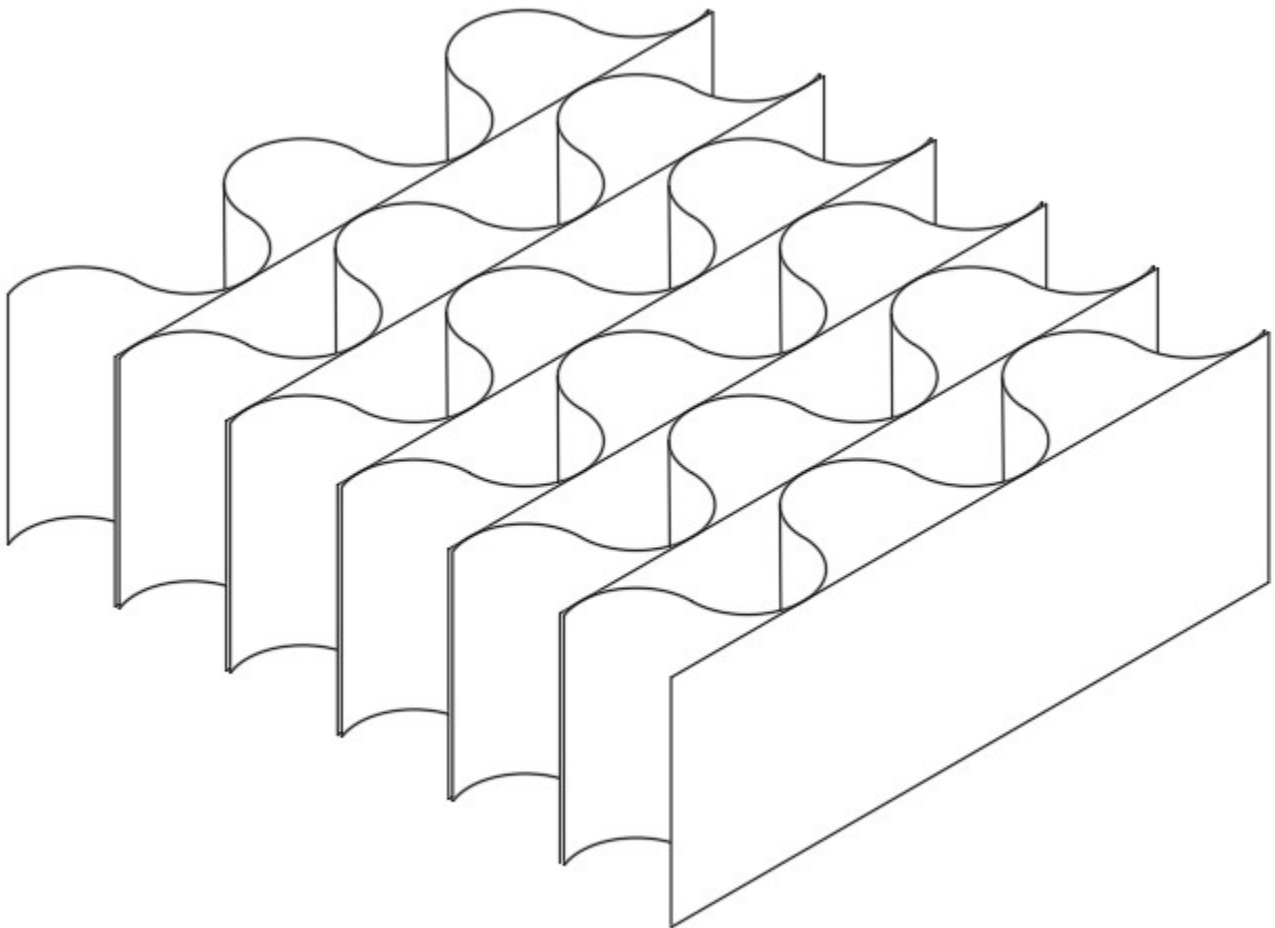
Figure 10.2. Geocell schematic diagram.
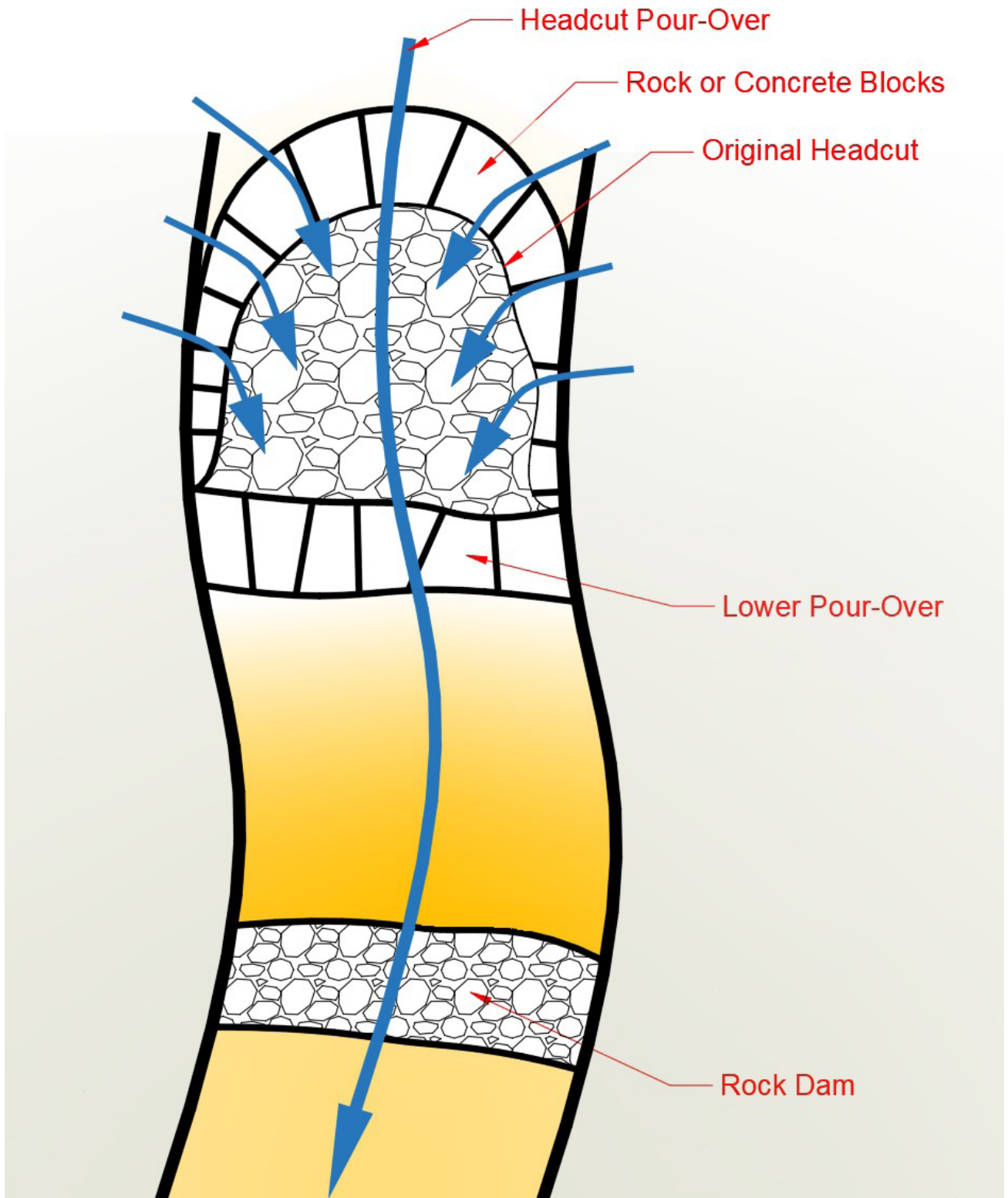
Figure 10.3. Configuration of a Zuni bowl.
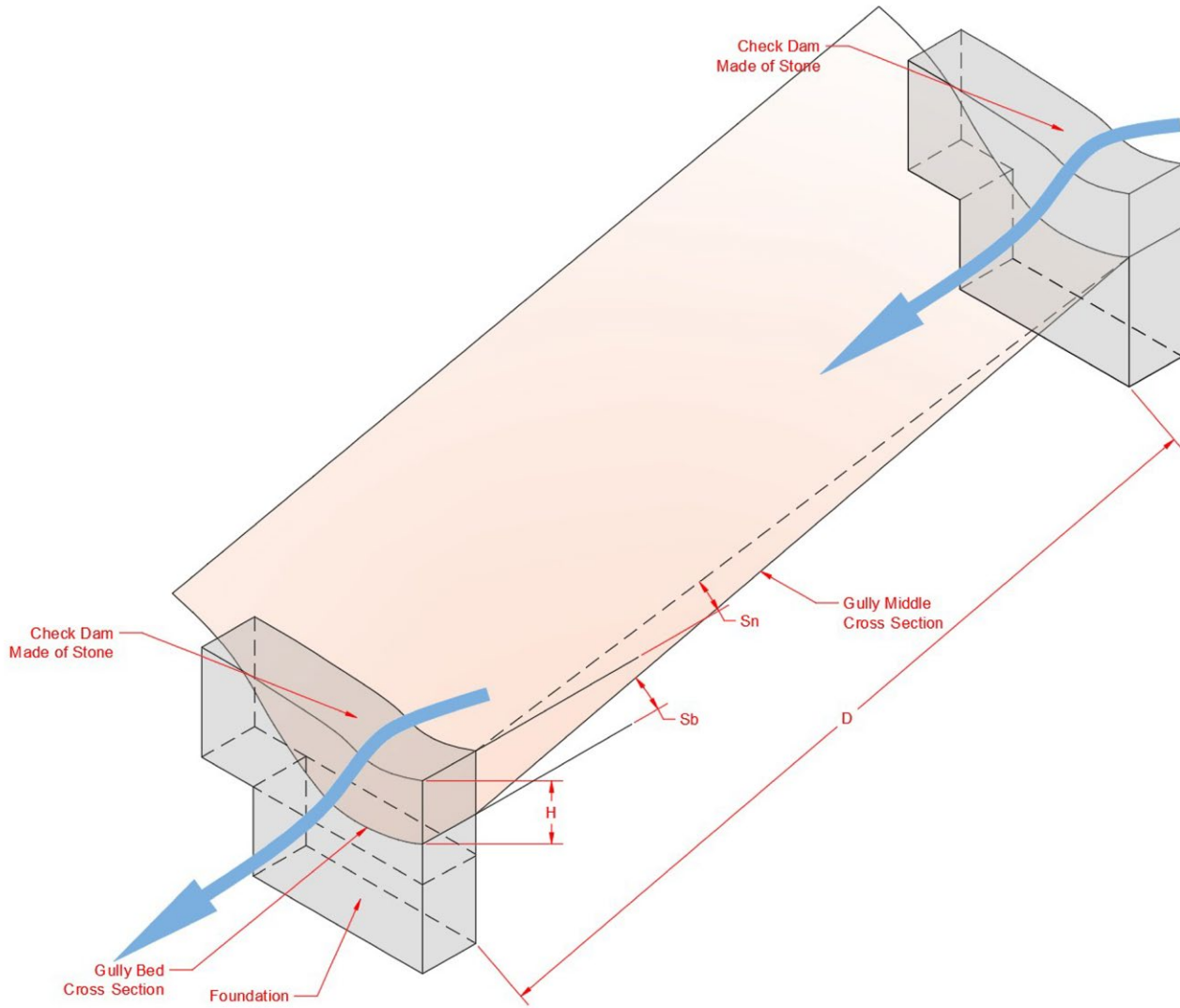
Figure 10.4. Isometric view of a check dam (only left half shown; Sn = gradient of the line joining the foot of the upstream check dam and spillway, H = dam height, D = horizontal distance between two dams, Sb = slope of the channel).
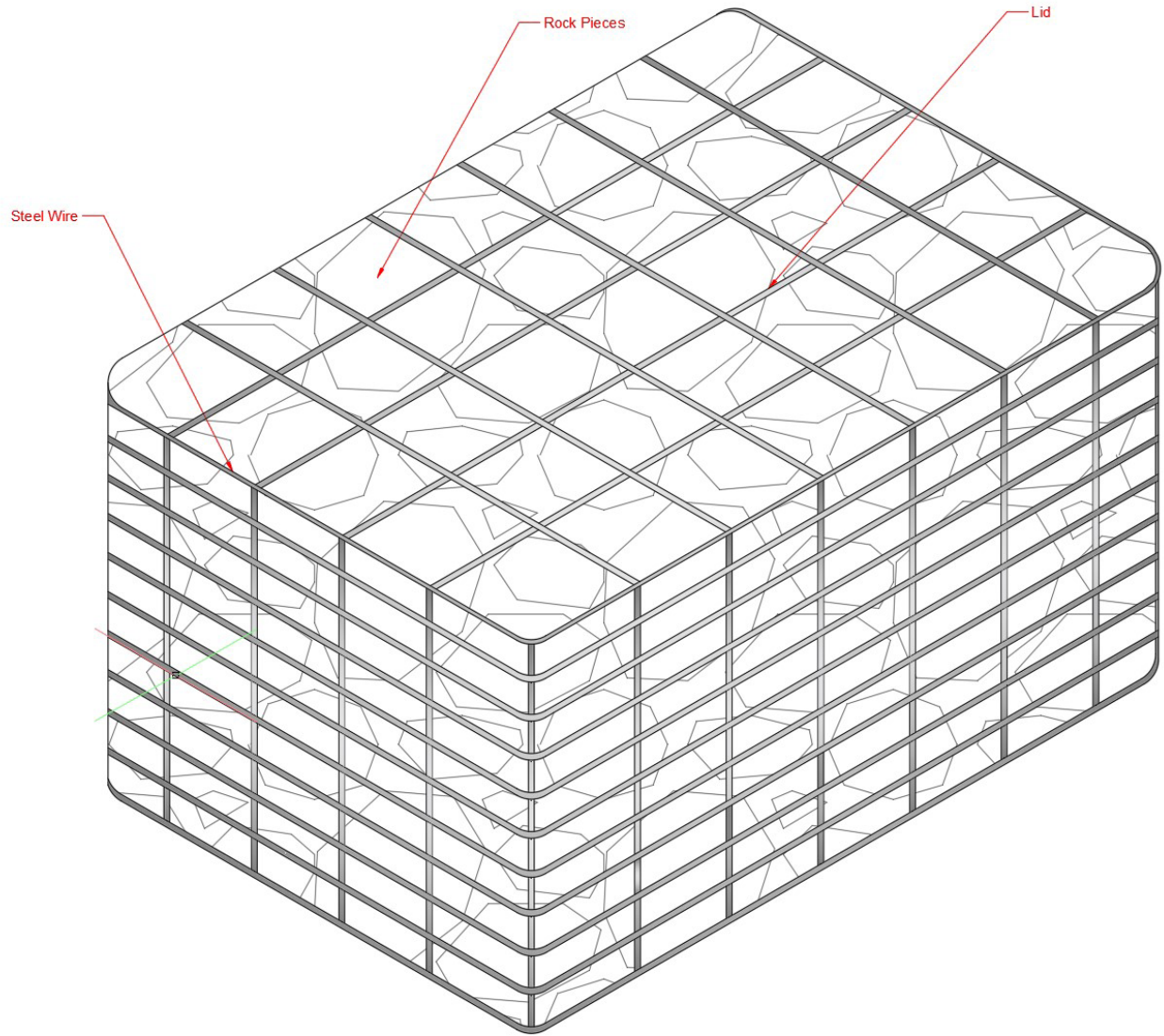
Figure 10.5. A gabion wire basket.
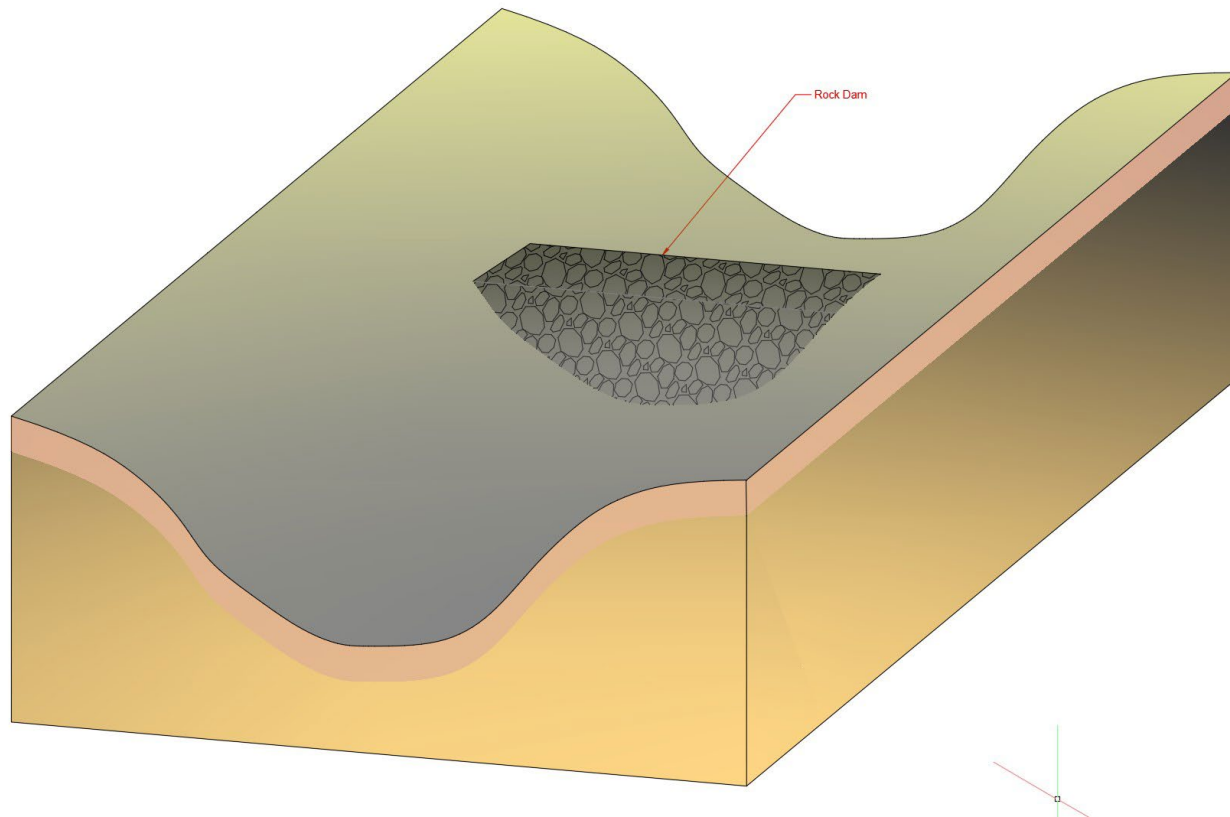
Figure 10.6. Schematic view of a rock dam.

FLEXIBLE DOWN DRAIN

This solution is a tube that is flexible and made of high-grade material or any other fabric that serves as a temporary downhill drain (Amimoto, 1978), as demonstrated in Figure 10.7.

DIVERSION DITCHES

To redirect upslope runoff around disturbed regions, small, temporary diversion ditches, dikes, or slope drains can be designed (Fig. 10.8). Essentially, these ditches gather and slowly transport water laterally along the diversion before being released into a contained environment or discharge conduit (Amimoto, 1978). Off-site water can be routed around the site on a grander scale to reduce the volume of water entering on-site conveyance and treatment systems. By removing off-site flow, on-site channels' discharge and erosion potential are lowered; thus, with overall lower volumes of water, sediment-capturing structures like silt fences and sedimentation basins become significantly more efficient (Harbor, 1999). Descheemaeker et al. (2009) experimented with diverting water flow in gullies into exclosures for other economic activities.
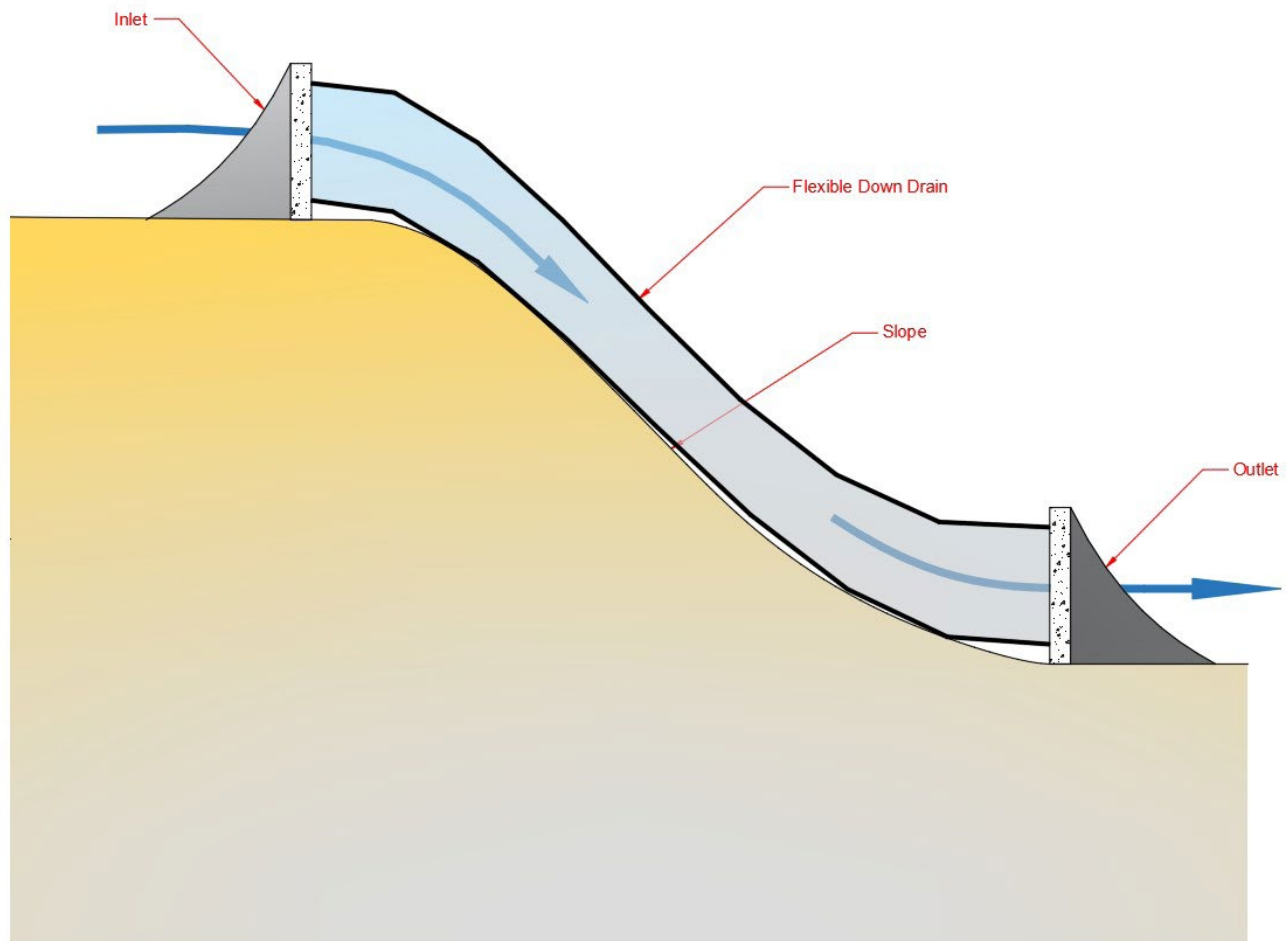
Figure 10.7. Schematic view of a flexible down drain.
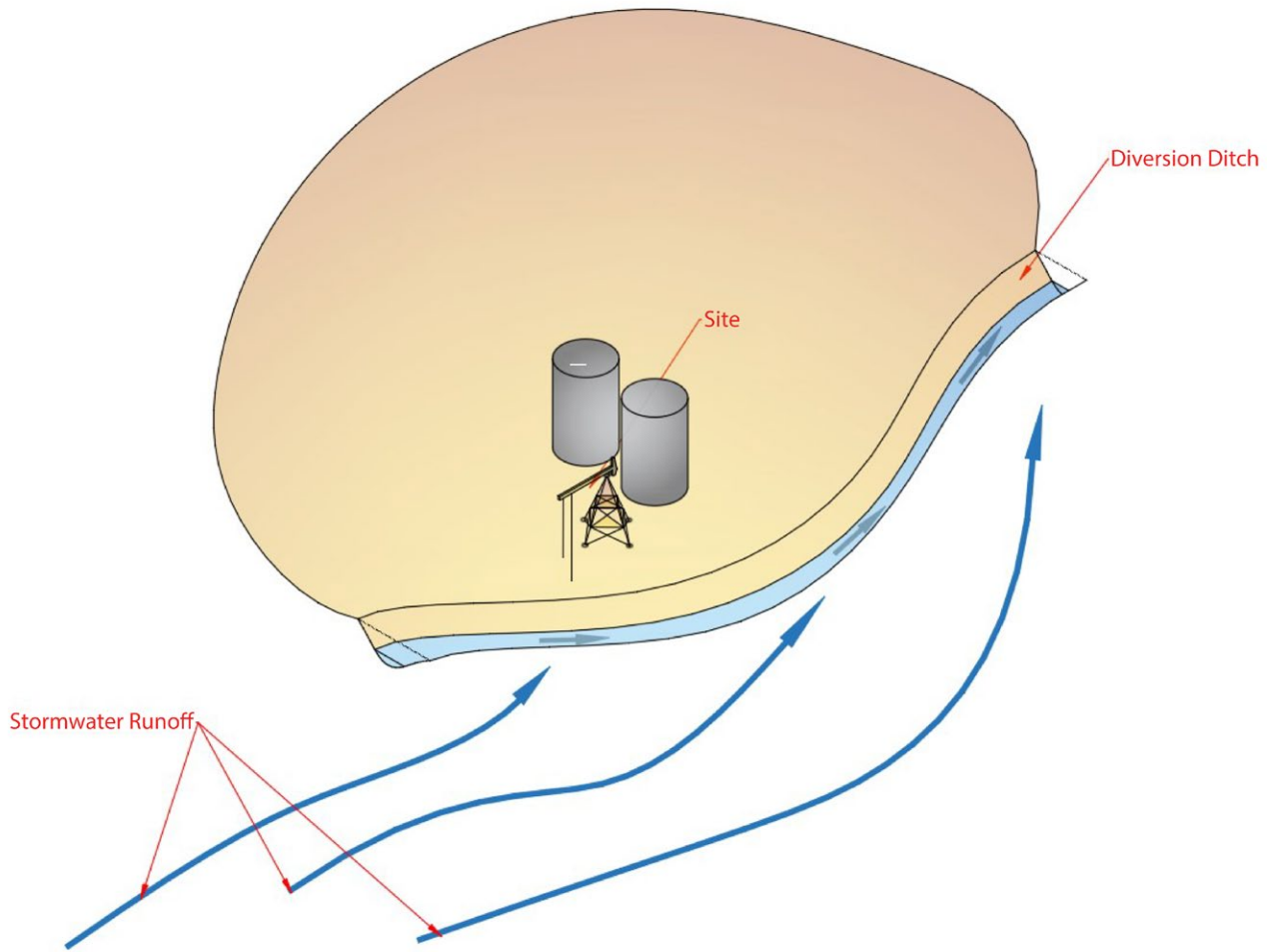
Figure 10.8. Diversion ditch used to protect a site.

STABLE, NON-VEGETATED CHANNEL DESIGN

According to Haan et al. (1994), there are two approaches to designing stable, non-vegetated channels: (a) limit shear force method and (b) limit velocity method. Both approaches include engineering the channel, which entails defining its specifications (height, base, depth, and other parameters) to minimize erosion while considering slope, design flow conditions, and soil type.

Rip-rap

Rip-rap is one of the most practical and adaptable erosion-control strategies. It is utilized to minimize lateral channel bank migration and vertical channel bed degradation, and to mitigate local scour at grade-control structures, channel drops, abutments, spurs, and guide banks (Mussetter Engineering Inc., 2008). Rip-rap is a barrier of large rocks placed on the banks of a stream to prevent erosion or undercutting of the

weaker ground beneath (Baird et al., 2015). In the design of stable channels with high water flow rates, rip-raps are typically employed when vegetation is non-existent (Garcia-Chevesich, 2018).

Baird et al. (2015) outlined three methods of installing rip-rap:

1. Rip-rap revetment: The rocks are laid starting from the toe of the bank and moving upward. The rocks can be placed solely on the toe, leaving the top bank intact, or vegetation can be grown above the stone toe.

2. Rip-rap windrow: Rocks are heaped above possible erosion areas in the expectation that the river would conclude the job by eroding to the windrow's base. Erosion near the stockpile's toe protects the slope by enabling the rock rip-rap to cascade down the channel bank.

3. Trench-filled rip-rap: These are identical to rip-rap windrows; however, the rocks are stacked in an excavated trench at a designated position and in designed alignments.

RIGID LININGS

Rigid linings are made of asphalt, concrete, grouted rock, sacked concrete, and/or soil cement. These stiff materials are designed for lining channels. Because of their low roughness coefficient, rigid linings have the highest flow capacity. Uplift forces, frost action, water seeping through the joints, or water spilling over the channel sidewalls and washing away the supporting earth should all be avoided in constructing rigid channels (Amimoto, 1978).

Soil cement

Soil cement has a distinct benefit for grade control and channel protection because a significant amount of material can very cheaply be supplied to counteract erosion forces. Soil cement may also solve various arroyo stability issues, such as channel banks, grade-control structures, and access roads. On channel banks with moderately steep slopes, a stair-step soil cement construction is recommended. In the arid Southwest, a grade of up to 1:1 is commonly used for stair-stepped soil cement (Mussetter Engineering Inc., 2008).

DIRT ROAD EROSION CONTROL

In reality, one of the significant sediment-producing anthropogenic activities in natural ecosystems is constructing dirt roads; thus, the higher the road density, the more sediment is discharged (Garcia-Chevesich, 2018). Also, Nyssen et al. (2002) concluded that road development redirects concentrated stormwater runoff to other catchments and thus is one likely source of gully erosion.

Two approaches have been suggested for erosion control of dirt roads—road stabilization and drainage control—and incorporating these approaches with continuous monitoring and maintenance produces the best results (Garcia-Chevesich, 2018).

Road stabilization

Presently, soil reinforcement approaches have been utilized for dirt road stabilization rather than the traditional soil compaction technique, which tends to fail during heavy precipitation events and high vehicular traffic (Garcia-Chevesich, 2018).

Geotextiles are a well-known soil reinforcement technique (Elleboudy et al., 2017) that improves bearing capacity and induces tension membrane effect and lateral restraints in the soil (Giroud and Noiray, 1981). Due to the restricted load capacity of soils for use in road fills, practically all soil movement activities now require some reinforcing element (Garcia-Chevesich, 2018). Geotextiles (particularly geogrids) are viable alternatives to soil deformation challenges due to their strong resilience and minimal elongation (Garcia-Chevesich, 2018). Geogrids are cost-effective and not biodegradable, hence their wide geotechnical applications (Visser et al., 2011).

Elleboudy et al. (2017) demonstrated that a geogrid layer is most effective when placed at the topmost quarter of the base course layer. An extra layer of geogrid placed at the boundary between the subgrade and base course layer reduced vertical deformation depth by 26%. They also proved that using two geogrid layers concurrently enhanced bearing capacity while reducing roughly 34% the thickness of the required base course layer.

Road drainage

The goal of road drainage is primarily to minimize surface runoff on the road and adjacent areas. A suitable dirt road drainage design begins with the grading pattern of the road's cross section. The purpose is to prevent water from accumulating on the road's surface and control the water to flow gently to one or both edges, depending on the scenario (Garcia-Chevesich, 2018). On steep or unpaved roads, lateral drainage prevents ruts from channeling water longitudinally over the road surface (FAO, 1998).

Intercepting dips

The utility of intercepting dips is restricted to road gradients of less than 10%, and they control the flow of water that is longitudinal to the road. The dip's outflow end must be rock-armored or fitted with a flexible down drain to counteract fill erosion (FAO, 1998).

Fords

Fords are typically constructed using rock gabions or pipes and are widely utilized in ephemeral streams. They are a practical approach to channel crossing in roadway locations prone to flash floods, cyclically intense precipitation peak runoff, or regular passage of avalanches or heavy debris (Garcia-Chevesich, 2018).

Portable bridges

Portable bridges are prescribed for unmaintained roads or skid trails. They are simple to install and are a cheaper alternative to pipe culverts and other permanent structures (New York State Forestry, 2011).

Open-top culverts

Open-top culverts can be constructed from treated timber or poles that are durable, or pre-engineered from corrugated, galvanized steel. These are most beneficial on higher road gradients, and they control water flow longitudinal to the road. To counteract plugging, the gradient of open-top culverts needs to be at least 4%, and the culvert should be tilted 30° downslope, as with dips. The trough should be 3 to 4 inches deep and 4 to 8 inches wide (FAO, 1998).

Culvert design

The bulking factor increases the clear water Q to account for the sediment occupying a portion of the total volume, as expressed as

$$Q_{bulked} = Q_{clear} \times Bulking\ Factor$$

Q_{bulked} is then used to size the culvert based on an inlet or outlet control scenario. At higher bulking factors (greater than 1.2) or higher concentrations of sediment (greater than 200,000 mg/L), the suspended sediment affects the water properties and the sediment transport behavior, which requires adjustment of the roughness coefficient, especially for debris flows. Culvert roughness, slope, length, and entrance conditions must be evaluated because these influence the culvert's flow profile. These parameters are essential in defining the headwater depth (HW) to prevent the culvert from overtopping. Peak flows with suspended sediments are higher than clear water peak flows, hence the recommendation of the simple approach for sediment concentrations less than 20%.

The construction should be designed such that water flows directly into and out of the culvert, with no sharp directional changes at either end, since this will slow the flow rate and produce erosion, ponding, or accumulation of debris at the portal of the culvert. The culvert's intake design should be built to screen out elements that will not flow through the culvert. Likewise, the outlet should be planned to restore non-erosive flow downstream of the road. During periods of low flow, energy dissipators downstream must be able to self-clean (FAO, 1998).

Diversions

Simple flow diversions are frequently created on dirt roads over extensive flat landscapes. These diversions are simple to implement using the same equipment used to build the road (Garcia-Chevesich, 2018).

SUBSURFACE DRAINAGE

When surface drainage cannot efficiently remove or intercept surface flow (Garcia-Chevesich, 2018) or groundwater (FAO, 1998), subsurface drainage solutions are necessary. Perforated pipe underdrains are conventional subdrainage systems inserted at the bottom of a narrow trench and filled with coarse sand or another filter material. The drains must be at least 6 inches in diameter and built of bituminous fiber, concrete, asbestos-cement, metal, or clay. To intercept groundwater, the excavated trench must be excavated below the groundwater level and into a lower, more impervious layer of soil (FAO, 1998).

Depending on the soil qualities and availability of materials, several techniques may be employed to prevent clogging. The first step is to wrap the perforated pipe in geotextile fabric. Next, encase the pipe with open-graded aggregate material and wrap it with a piece of fabric. Using cloth precludes the need for an inverted filter made up of different sand layers and sizes of gravel. Alternatively, a graded aggregate filter could surround the pipe if fabric is unavailable (FAO, 1998).

CONCLUSIONS

Disclaimer

These site-specific engineering recommendations provide a general guideline for the project's design phase. These recommendations are based on site visits, limited soil tests, numerical hydrological models, close-range photogrammetry results, topography, and site geology at the initiation phase. Extensive data collection of geotechnical engineering tests and precise long-term monitoring data are required to determine the erosion control structures' types, locations, and dimensions. Besides, more research must be done to select a safe and effective soil stabilization method. Therefore, under no circumstances can the results of this phase immediately be used to design any erosion control structure or ground improvement technique.

A summary of the observed problems at different sites

Figure 10.9 shows the locations of different sites on the map and the infrastructure on these sites. Table 10.1 presents a summary of the observed problems in the field at different sites.
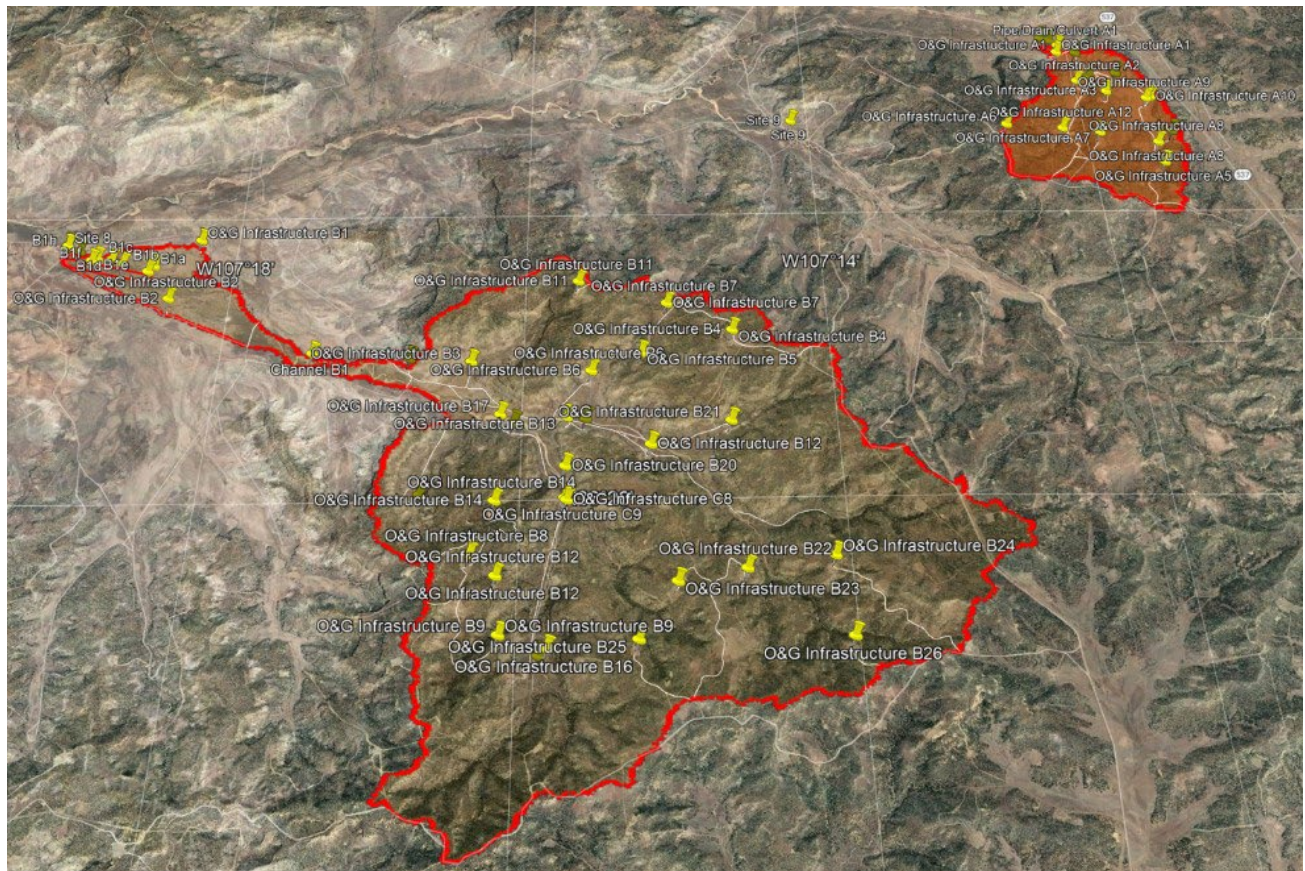
Figure 10.9. Locations of the different sites and infrastructure on the map (Google Earth).

Table 10.1. Summary of problems observed in the field at different sites by Kevin Hobbs in March 2021 (Hobbs and Pearthree, 2022).

Latitude	Longitude	Name	Problem Description
36.260659	-107.227047	Site 1	North-draining tributary of Burro Canyon. Near headwaters. Water is running down the road, causing an incision on the west side of the road.
36.250015	-107.226456	Site 2	North-draining tributary of Burro Canyon (same drainage as Sites 1 and 3). Approximately 7 m of the incision through alluvial sediments within historic time. Bedrock outcrops uphill approximately 100 m west of this site likely lead to overland flow and headcutting at culverts, as we saw on 12 March 2021.
36.248078	-107.228137	Site 3	Same north-draining tributary of Burro Canyon as Sites 1 and 2. This is the upstream end of headcutting in this tributary. The headcut has moved upstream approximately 25 m since 1997. There is an oil pump and tanks approximately 50 m upstream of the headcut. Only 4 km^2 of the drainage area are upstream of this site.
36.350882	-107.315636	Site 4	South-draining tributary to Cañada Larga with a 6-m incision in recent times. Headcut threatens oil pump and well pad. This site is relatively high in the watershed.
36.235863	-107.255214	Site 5	West-draining tributary to Cañon Largo at New Mexico Highway 537 crossing. The site was visited on 12 March 2021. Culvert cannot accommodate runoff, and sediment deposition is occurring on the upstream side of the highway. There has been approximately 1 m of deposition in the past 10 (?) years, burying a barbed-wire fence. Very high in the watershed—there is less than 1 km^2 upstream of this point.
36.253963	-107.382042	Site 6	Junction of Venado Canyon with Cañon Largo. A laterally migrating cutbank has caused the main road through Cañon Largo here to be pushed 30 m east since 1997. Pearthree and Hobbs observed soil piping in the road, suggesting ongoing lateral erosion. This site is much lower in its watershed than Sites 1–7, with a larger area contributing runoff and sediment. The road being eroded here is the main route through Cañon Largo.
36.437281	-107.354305	Site 7	North-draining tributary to Tapicito Creek. This site is offered as a potential study site because of the breached retention dam at a headcut here. The headcut has existed since at least 1997. The dam was built in 2011 and was breached by headcutting sometime between 2013 and 2016.
36.462030	-107.319805	Site 8	Road culvert at Las Norias Canyon. The team visited here on 12 March 2021. The culvert was recently rebuilt and is a major route providing access to oil and gas infrastructure.
36.478365	-107.235628	Site 9	Small headcut in a tributary to Wild Horse Canyon. This site has been problematic since at least 1997 and is routinely repaired with a bulldozer. This might be a good site to determine the causes/effects of headcutting on roads.
36.438096	-107.407426	Site 10	Incision and headcutting in the small north-draining tributary canyon to Tapicito Creek. Erosion has rerouted the road and threatened the well pad.
36.124120	-107.099189	Site 11	Headwaters site in far upstream reach of Five Lakes Canyon near the Continental Divide. Major earthmoving here in 2016–2017 to prevent incision. The dam was breached by October 2017. The only infrastructure threatened here is a minor north-south road, but this might be a good site to observe an attempt at erosion control.

The study area was divided into three main sites—A, B, and C—shown in Figures 10.10 through 10.12. A thorough review of the observed problems in the field (Table 10.1) reveals that these sites have almost no engineering structures to prevent or slow the erosion rate, and the current human-made structures to control erosion do not seem to work effectively. On the other hand, it is not feasible to protect the entire site due to the vast area, the geology, the severity of storms, and the cost. However, employing engineering techniques to divert the flow, slow down and spread the flow, protect infrastructure locally, and stabilize the soil would be a practical solution to reduce erosion and protect infrastructure.
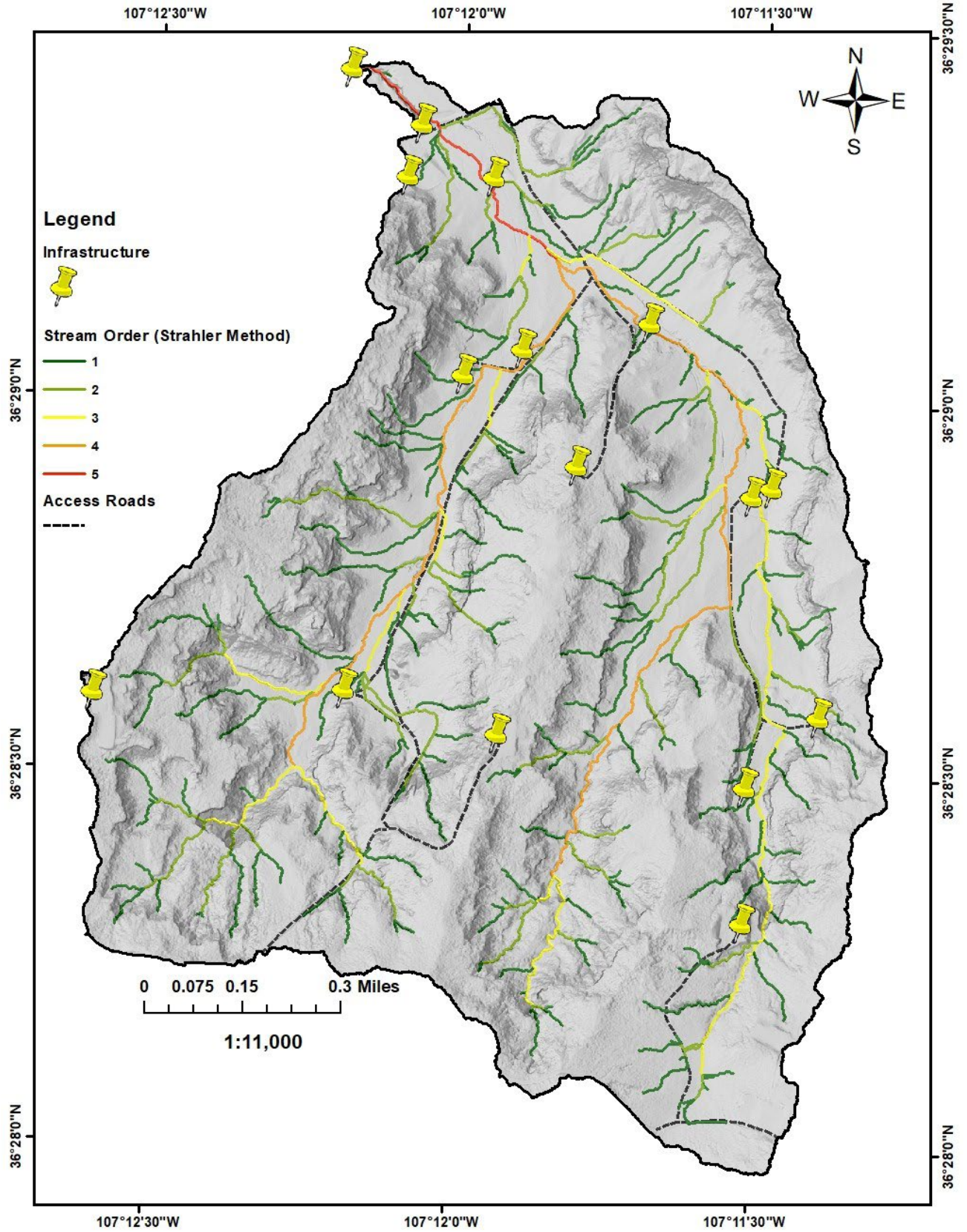
Figure 10.10. Stream orders in Site A.
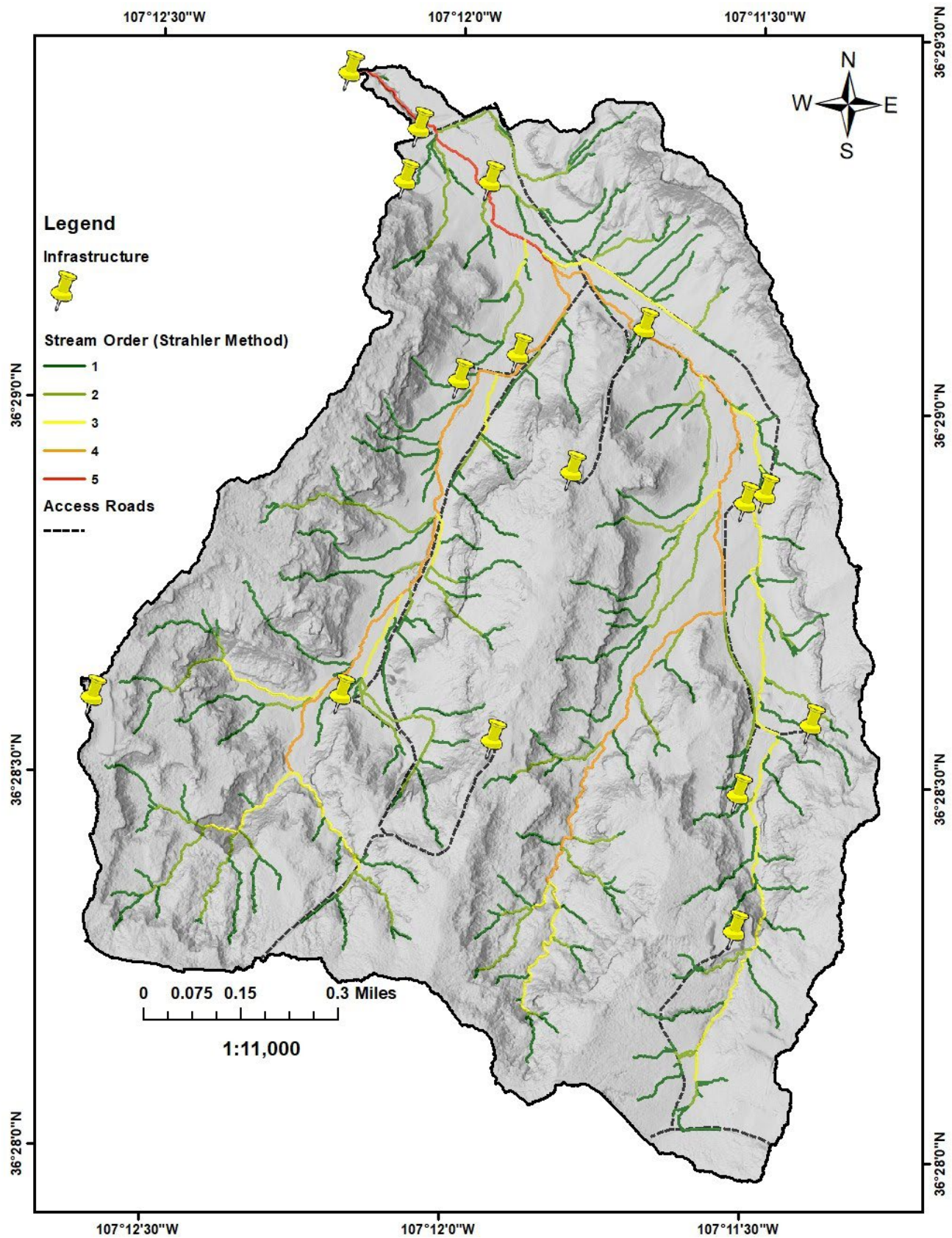
Figure 10.11. Stream orders in Site B.
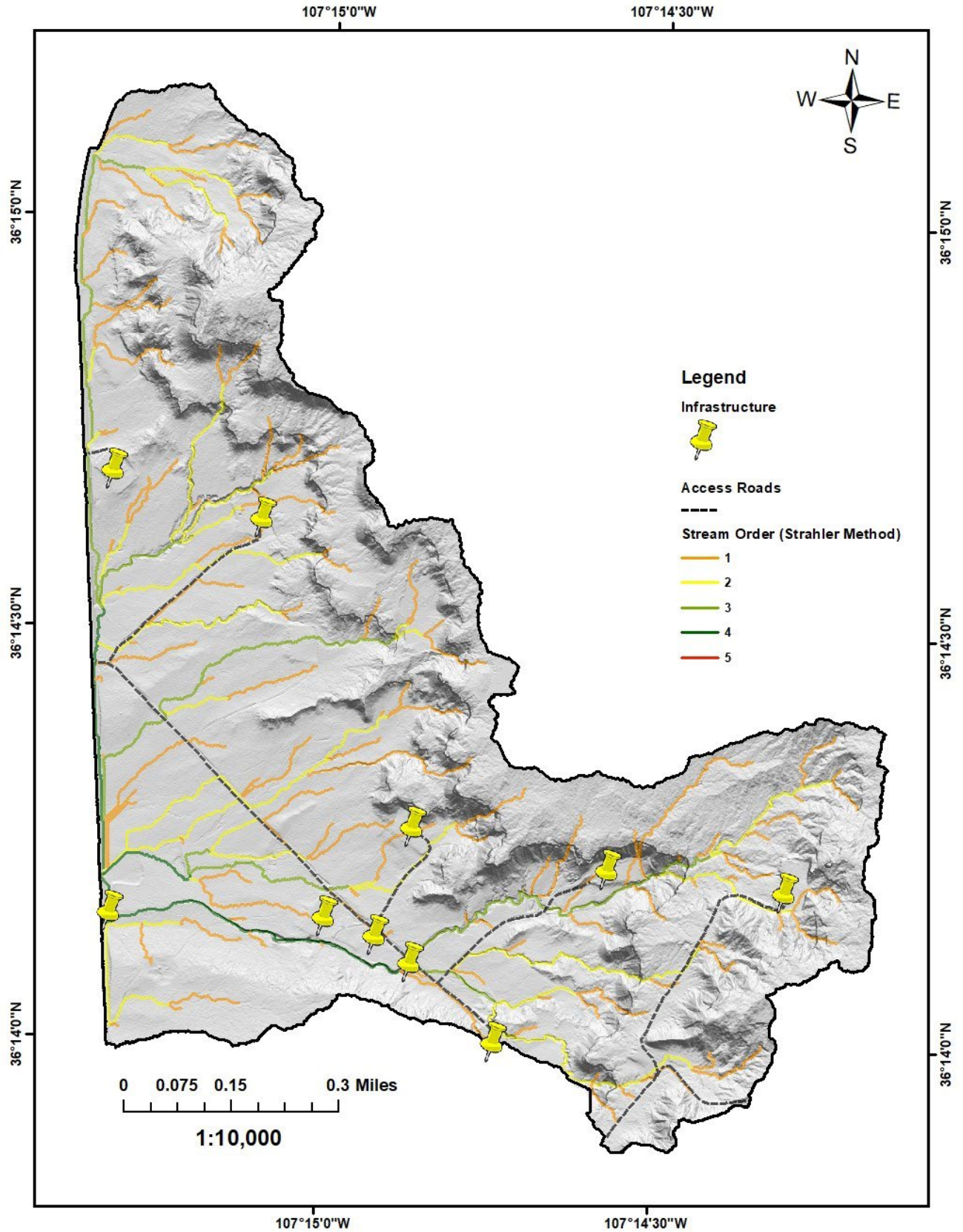
Figure 10.12. Stream orders in Site C.

Engineering recommendations for Sites A, B, and C

Figures 10.13 through 10.15 show the slope angle, stream order, and locations of structures for Sites A, B, and C, respectively. For Site A, the area is 1.33 mi², the estimated mean annual peak discharge is 225.2 cfs, and the slope angle varies between 0 and 84°; for Site B, the area is 9.54 mi², the estimated mean annual peak discharge is 2,937.1 cfs, and the slope angle varies between 0 and 85°; and finally for Site C, the area is 0.81 mi², the estimated mean annual peak discharge is 337.4 cfs, and the slope angle varies between 0 and 84°. Engineering recommendations for each site and the infrastructure are as follows. The large peak discharge, steep slopes, and geology of these sites require that a combination of engineering techniques must be employed to deal with the extreme erosion problem and protect structures.

Land and channels

Though all general engineering recommendations listed in this chapter can be applied to reduce and control the erosion of these sites, the focus on site-specific engineering recommendations is on less-expensive methods. That being said, check dams (Fig. 10.4) built at stream order locations 4 and 5 for Sites A and B and stream order locations 6 and 7 for Site C will reduce erosion significantly. Diversion ditches (Fig. 10.8) built around the buildings, roads, and structures are recommended to protect the structures. Zuni bowls (Fig. 10.3) are recommended to control in-channel headcuts. The contractor must avoid using the native rocks to build check dams and Zuni bowls due to the high erodibility of the native materials.

Dirt roads

The dirt roads must be compacted at the optimal water content of the soil ± 2% to at least 90% of the maximum dry density attained in a standard Proctor test according to ASTM D-698. Chemical soil stabilization of the road surface to a depth of 1 ft provides better protection against erosion. Cement is used as a typical additive to stabilize the soil, and the typical weight of the cement to dry weight of the soil is less than 15%. However, more research must be done to determine the right type of additive, its percentage, and its environmental impact. Adequate drainage must be provided along the roads to intercept and convey stormwater effectively.

Slopes

Natural and human-made slopes near infrastructure must be protected to reduce erosion and the risk of slope failure. Rip-raps and gabion baskets (Fig. 10.5) made of non-native materials to protect slopes are recommended. Use of terraces for steep slopes and slopes with a height of 10 ft or more is standard practice. Based on the angle of repose of the soil samples (about 32°), the maximum slope must be less than 1:2 (about 27°). In the case of flow through the slope or when the erosion potential of the slope toe is high, a toe drain must be built to prevent piping.

Culverts

Field observations show that the diameter of most culverts is not large enough to handle the stormwater discharge and sediment load, and the size and angle must be based on an engineering design. In addition, the locations and slopes must be optimized. The sides of the culverts up to some distance and the bed near both ends must be protected by reinforced concrete structures or equivalent revetment.

Oil pipelines

Adding to the measures stated above, the oil pipelines must be supported by engineering structures that can handle vertical and lateral loads. The oil pipeline supports must also allow lateral and vertical displacements to some extent. For the areas where a gully or incision can form, the pipeline must be supported by piles.

Monitoring and maintenance

It is important to remember that this problem has no permanent solution. Building any new structure in the way of water will change the local flow patterns and, as a result, the erosion pattern. The site and structures must be monitored at regular intervals and after each stormwater event to maintain the functionality of the infrastructure. Additionally, design revisions may be unavoidable depending on the actual performance of the engineering methods and structures to control erosion.
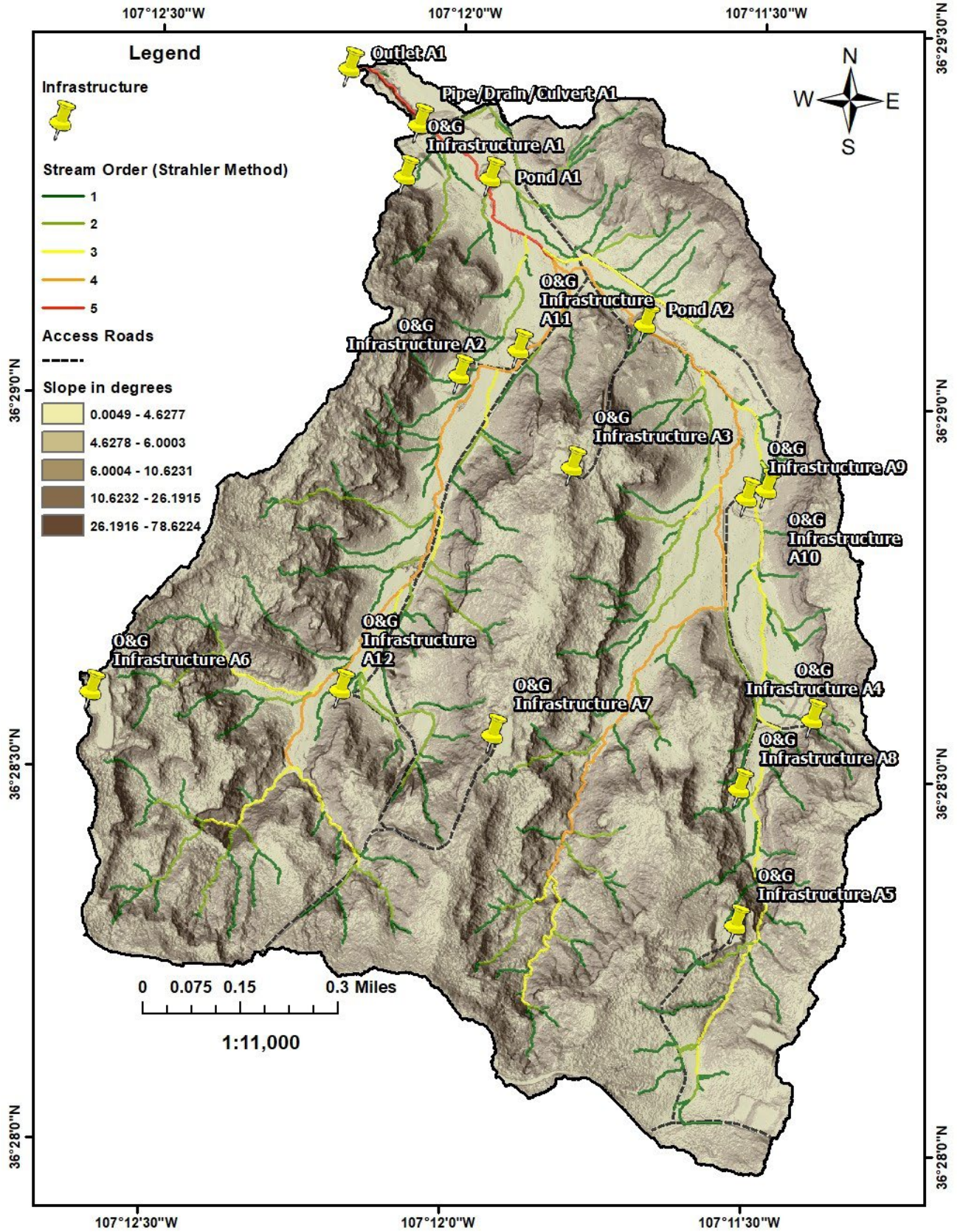
Figure 10.13. Slope angle, stream orders, and infrastructure at Site A. O&G = oil and gas.
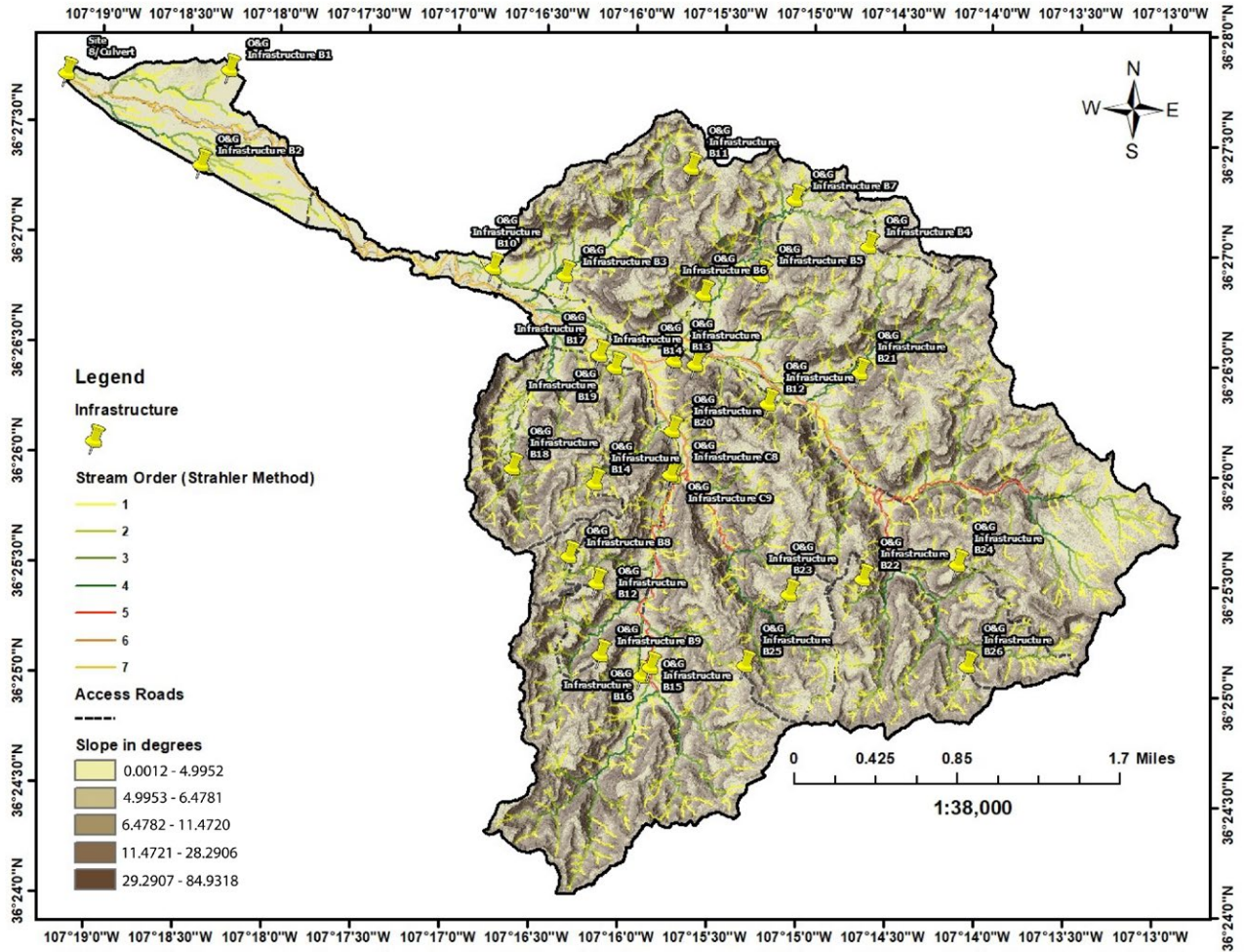
Figure 10.14. Slope angle, stream orders, and infrastructure at Site B. O&G = oil and gas.
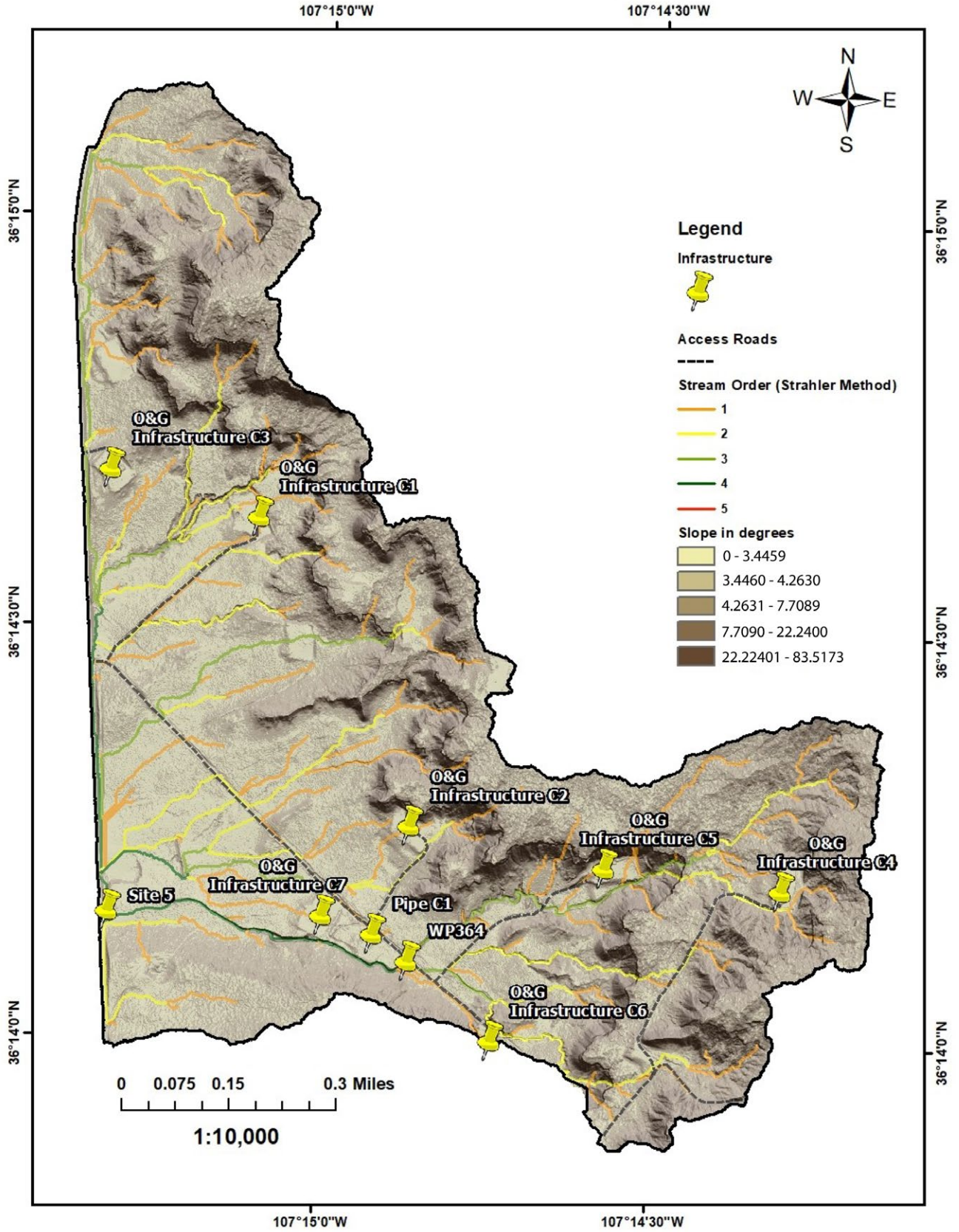
Figure 10.15. Slope angle, stream orders, and infrastructure at Site C. O&G = oil and gas, WP = well pad.

REFERENCES

Abdullah, M., Feagin, R., and Musawi, L., 2017, The use of spatial empirical models to estimate soil erosion in arid ecosystems: Environmental Monitoring and Assessment, v. 189. https://doi.org/10.1007/s10661-017-5784-y

Aby, S.B., 2017, Date of arroyo cutting in the American Southwest and the influence of human activities: Anthropocene, v. 18, p. 76–88. https://doi.org/10.1016/j.ancene.2017.05.005

Affleck, R., Carr, M., and West, B., 2014, Flow control and design assessment for drainage system at McMurdo Station, Antarctica: U.S. Army Engineer Research and Development Center report ERDC/CRREL TR-14-26, 91 p.

Afrin, T., Kaye, N.B., Khan, A.A., and Testik, F.Y., 2016, Parametric study of perforated pipe underdrains surrounded by loose aggregate: Journal of Hydraulic Engineering, v. 142, no. 12. https://doi.org/10.1061/(ASCE)HY.1943-7900.0001214

Ahmad, I., 2018, Digital elevation model (DEM) coupled with geographic information system (GIS)—An approach towards erosion modeling of Gumara watershed, Ethiopia: Environmental Monitoring and Assessment, v. 190. https://doi.org/10.1007/s10661-018-6888-8

Aiello, A., Adamo, M., and Canora, F., 2015, Remote sensing and GIS to assess soil erosion with RUSLE3D and USPED at river basin scale in southern Italy: CATENA, v. 131, p. 174–185. https://doi.org/10.1016/j.catena.2015.04.003

Aksoy, H., and Kavvas, M.L., 2005, A review of hillslope and watershed scale erosion and sediment transport models: CATENA, v. 64, no. 2–3, p. 247–271. https://doi.org/10.1016/j.catena.2005.08.008

Amimoto, P.Y., 1978, Erosion and sediment control handbook: U.S. Environmental Protection Agency, Water Planning Division, 197 p.

Anders, N., Valente, J., Masselink, R., and Keesstra, S., 2019, Comparing filtering techniques for removing vegetation from UAV-based photogrammetric point clouds: Drones, v. 3, no. 3, p. 1–14. https://doi.org/10.3390/drones3030061

Arriola-Valverde, S., Villalobos-Avellán, L.C., Villagra-Mendoza, K., and Rimolo-Donadio, R., 2020, Erosion quantification in runoff agriculture plots by multitemporal high-resolution UAS digital photogrammetry: IEEE Journal of Selected Topics in Applied Earth Observations and Remote Sensing, v. 13, p. 6326–6336. https://doi.org/10.1109/JSTARS.2020.3027880

Baird, D.C., Fotherby, L., Klumpp, C.C., and Sculock, S.M., 2015, Bank stabilization design guidelines: U.S. Department of the Interior, Bureau of Reclamation, 319 p. https://www.usbr.gov/tsc/techreferences/mands/mands-pdfs/A-BankStab-final6-25-2015.pdf

Best Mexican Beach Pebbles, 2019, River rock-filled gabion walls: https://bestmexicanbeachpebbles.com/river-rock-filled-gabion-walls/ (accessed December 2022).

Biswas, A., and Krishna, A.M., 2017, Geocell-reinforced foundation systems—A critical review: International Journal of Geosynthetics and Ground Engineering, v. 3. https://doi.org/10.1007/s40891-017-0093-7

Blond, E., Boyle, S., Ferrara, M., Herlin, B., Plusquellec, H., Rimoldi, P., and Stark, T., 2019, Applications of geosynthetics to irrigation, drainage and agriculture: Irrigation and Drainage, v. 68, no. 1, p. 67–83. https://doi.org/10.1002/ird.2300

Borrelli, P., Märker, M., Panagos, P., and Schütt, B., 2014, Modeling soil erosion and river sediment yield for an intermountain drainage basin of the Central Apennines, Italy: CATENA, v. 114, p. 45–58. https://doi.org/10.1016/j.catena.2013.10.007

Borrelli, P., et al., 2017, An assessment of the global impact of 21st century land use change on soil erosion: Nature Communications, v. 8. https://doi.org/10.1038/s41467-017-02142-7

Borrelli, P., et al., 2021, Soil erosion modelling—A global review and statistical analysis: Science of the Total Environment, v. 780. https://doi.org/10.1016/j.scitotenv.2021.146494

Bull, W.B., 1997, Discontinuous ephemeral streams: Geomorphology, v. 19, no. 3–4, p. 227–276. https://doi.org/10.1016/S0169-555X(97)00016-0

Bump, A.P., and Davis, G.H., 2003, Late Cretaceous–early Tertiary Laramide deformation of the northern Colorado Plateau, Utah and Colorado: Journal of Structural Geology, v. 25, no. 3, p. 421–440. https://doi.org/10.1016/S0191-8141(02)00033-0

Chandramohan, T., Venkatesh, B., and Balchand, A.N., 2015, Evaluation of three soil erosion models for small watersheds: Aquatic Procedia, v. 4, p. 1227–1234. https://doi.org/10.1016/j.aqpro.2015.02.156

Chang, H., 1988, Fluvial Processes in River Engineering: Hoboken, New Jersey, John Wiley & Sons Inc., 432 p.

Choudhary, S., Jaiswal, R.K., Nema, A.K., Thakur, A., and Gangwar, A., 2020, Watershed prioritization for soil conservation measures using USPED model in Nagwan Watershed: Journal of Soil and Water Conservation, v. 19, no. 3, p. 235–243. http://dx.doi.org/10.5958/2455-7145.2020.00032.6

Clark, J.S., and Patterson III, W.A., 1997, Background and local charcoal in sediments—Scales of fire evidence in the paleorecord, in Clark, J.S., Cachier, H., Goldammer, J.G., and Stocks, B., eds., Sediment Records of Biomass Burning and Global Change: NATO ASI Series, v. 51, p. 23–48. https://doi.org/10.1007/978-3-642-59171-6_3

Colby, B.R., 1964, Practical computations of med-material discharge: Journal of the Hydraulics Division, Proceedings of the American Society of Civil Engineers, v. 90, no. 2, p. 217–264.

Compton, R.R., 1962, Manual of Field Geology: Hoboken, New Jersey, John Wiley & Sons Inc., 378 p.

Coulthard, T.J., Hancock, G.R., and Lowry, J.B.C., 2012, Modelling soil erosion with a downscaled landscape evolution model: Earth Surface Processes and Landforms, v. 37, no. 10, p. 1046–1055. https://doi.org/10.1002/esp.3226

Craig, R.F., 2004, Craig's Soil Mechanics (seventh edition): New York, Spon Press, 464 p.

Cramer, M., 2008, Photogrammetric sensors, in Shekhar, S., and Xiong, H., eds., Encyclopedia of GIS: Boston, Springer, p. 871–875. https://doi.org/10.1007/978-0-387-35973-1_983

d'Oleire-Oltmanns, S., Marzolff, I., Peter, K.D., and Ries, J.B., 2012, Unmanned aerial vehicle (UAV) for monitoring soil erosion in Morocco: Remote Sensing, v. 4, no. 11, p. 3390–3416. https://doi.org/10.3390/rs4113390

da Luz, M.P., Ardila, M.A.A., Junior, R.D.D.S., Valentin, C.A., Schliewe, M.S., Coelho, A.T., and da Silva, J.L., 2021, Geomats used to control erosion on reservoir margins in Brazilian hydroelectric power plants: Water, v. 13, no. 11. https://doi.org/10.3390/w13111444

Darrach, A.G., Sauerwein, W.J., and Halley, C.E., 1981, Building water pollution control into small private forest and ranchland roads: U.S. Department of Agriculture, Forest Service and Soil Conservation Service.

Das, B.M., and Sobhan, K., 2014, Principles of Geotechnical Engineering (eighth edition): Stamford, Connecticut, Cengage Learning, 704 p.

de Vente, J., and Poesen, J., 2005, Predicting soil erosion and sediment yield at the basin scale— Scale issues and semi-quantitative models: Earth-Science Reviews, v. 71, no. 1–2, p. 95–125. https://doi.org/10.1016/j.earscirev.2005.02.002

de Vente, J., Poesen, J., Arabkhedri, M., and Verstraeten, G., 2007, The sediment delivery problem revisited: Progress in Physical Geography—Earth and Environment, v. 31, no. 2, p. 155–178. https://doi.org/10.1177/0309133307076485

de Vente, J., Poesen, J., Verstraeten, G., Govers, G., Vanmaercke, M., Van Rompaey, A., Arabkhedri, M., and Boix-Fayos, C., 2013, Predicting soil erosion and sediment yield at regional scales— Where do we stand?: Earth-Science Reviews, v. 127, p. 16–29. https://doi.org/10.1016/j.earscirev.2013.08.014

Delaney, P.T., Pollard, D.D., Ziony, J.I., and McKee, E.H., 1986, Field relations between dikes and joints—Emplacement processes and paleostress analysis: Journal of Geophysical Research, v. 91, no. B5, p. 4920–4938. https://doi.org/10.1029/JB091iB05p04920

Descheemaeker, K., Nyssen, J., Poesen, J., Raes, D., Terryn, L., Haile, M., Muys, B., and Deckers, J., 2009, Water harvesting and sediment trapping in exclosures—A gully diversion experiment in the Tigray Highlands, Ethiopia: Geophysical Research Abstracts, v. 11.

Elleboudy, A.M., Saleh, N.M., and Salama, A.G., 2017, Assessment of geogrids in gravel roads under cyclic loading: Alexandria Engineering Journal, v. 56, no. 3, p. 319–326. https://doi.org/10.1016/j.aej.2016.09.023

Eltner, A., and Sofia, G., 2020, Structure from motion photogrammetric technique: Developments in Earth Surface Processes, v. 23, p. 1–24. https://doi.org/10.1016/B978-0-444-64177-9.00001-1

Eltner, A., Baumgart, P., Maas, H-G., and Faust, D., 2015, Multi-temporal UAV data for automatic measurement of rill and interrill erosion on loess soil: Earth Surface Processes and Landforms, v. 40, no. 6, p. 741–755. https://doi.org/10.1002/esp.3673

Eltner, A., Kaiser, A., Castillo, C., Rock, G., Neugirg, F., and Abellán, A., 2016, Image-based surface reconstruction in geomorphometry—Merits, limits and developments: Earth Surface Dynamics, v. 4, no. 2, p. 359–389. https://doi.org/10.5194/esurf-4-359-2016

Esri, 2011, Arc Hydro tools—Tutorial, Version 2.0: http://downloads.esri.com/archydro/archydro/tutorial/doc/arc%20hydro%20tools%202.0%20-%20tutorial.pdf (accessed November 2022).

Fang, X., Thompson, D.B., Cleveland, T.G., Pradhan, P., and Malla, R., 2008, Time of concentration estimated using watershed parameters determined by automated and manual methods: Journal of Irrigation and Drainage Engineering, v. 134, no. 2, p. 202–211. https://doi.org/10.1061/(ASCE)0733-9437(2008)134:2(202)

FAO, 1998, Watershed management field manual—Road design and construction in sensitive watersheds: FAO Conservation Guide 13/5, Food and Agriculture Organization of the United Nations, http://www.fao.org/docrep/006/T0099E/T0099E00.HTM (accessed November 2022).

Fenta, A.A., Yasuda, H., Shimizu, K., Haregeweyn, N., and Negussie, A., 2016, Dynamics of soil erosion as influenced by watershed management practices—A case study of the Agula watershed in the semi-arid highlands of northern Ethiopia: Environmental Management, v. 58, p. 889–905. https://doi.org/10.1007/s00267-016-0757-4

Finley, J.B., Robinson, E., and DeRose, R.J., 2022, Arroyo formation impacts on an early dryland agricultural community in northeastern Utah, USA: Geoarchaeology, v. 38, no. 1. https://doi.org/10.1002/gea.21942

Fleming, M.J., and Doan, J.H., 2010, HEC-GeoHMS geospatial hydrologic modeling extension user's manaul: https://www.hec.usace.army.mil/software/hec-geohms/documentation/hec-geohms_users_manual_5.0.pdf (accessed November 2022).

Frankl, A., Deckers, J., Moulaert, L., Van Damme, A., Haile, M., Poesen, J., and Nyssen, J., 2016, Integrated solutions for combating gully erosion in areas prone to soil piping—Innovations from the drylands of northern Ethiopia: Land Degradation and Development, v. 27, no. 8, p. 1797–1804. https://doi.org/10.1002/ldr.2301

Friedman, J.M., Vincent, K.R., Griffin, E.R., Scott, M.L., Shafroth, P.B., and Auble, G.T., 2015, Processes of arroyo filling in northern New Mexico, USA: GSA Bulletin, v. 127, no. 3–4, p. 621–640. https://doi.org/10.1130/B31046.1

Gallegos, J.B., 2012, A GIS-based characterization of eight small watersheds in New Mexico—Development and correlation of a sediment load hydraulic bulking factor [MS thesis]: Socorro, New Mexico Institute of Mining and Technology.

Garcia-Chevesich, P.A., 2018, Erosion Control and Land Restoration: Parker, Colorado, Outskirts Press Inc., 466 p.

García-Ruiz, J.M., Beguería, S., Nadal-Romero, E., González-Hidalgo, J.C., Lana-Renault, N., and Sanjuán, Y., 2015, A meta-analysis of soil erosion rates across the world: Geomorphology, v. 239, p. 160–173. https://doi.org/10.1016/j.geomorph.2015.03.008

Gellis, A.C., and Elliott, J.G., 2001, Arroyo changes in selected watersheds of New Mexico, United States, in Anthony, D.J., Harvey, M.D., Laronne, J.B., and Mosley, M.P., eds., Applying Geomorphology to Environmental Management: Littleton, Colorado, Water Resources Publications LLC, p. 225–240.

Giménez, R., Marzolff, I., Campo, M.A., Seeger, M., Ries, J.B., Casalí, J., and Álvarez-Mozos, J., 2009, Accuracy of high-resolution photogrammetric measurements of gullies with contrasting morphology: Earth Surface Processes and Landforms, v. 34, no. 14, p. 1915–1926. https://doi.org/10.1002/esp.1868

Giroud, J.-P., and Noiray, L., 1981, Geotextile-reinforced unpaved road design: Journal of the Geotechnical Engineering Division, v. 107, no. 9, p. 1233–1254. https://doi.org/10.1061/AJGEB6.0001187

Glendell, M., et al., 2017, Testing the utility of structure-from-motion photogrammetry reconstructions using small unmanned aerial vehicles and ground photography to estimate the extent of upland soil erosion: Earth Surface Processes and Landforms, v. 42, no. 12, p. 1860–1871. https://doi.org/10.1002/esp.4142

Goldman, S.J., Jackson, K., and Bursztynsky, T.A., 1986, Erosion and Sediment Control Handbook: New York, McGraw-Hill, 454 p.

Golkarian, A., Khosravi, K., Panahi, M., and Clague, J.J., 2023, Spatial variability of soil water erosion—Comparing empirical and intelligent techniques: Geoscience Frontiers, v. 14, no. 1. https://doi.org/10.1016/j.gsf.2022.101456

Griffith, G.E., Omernik, J.M., McGraw, M.M., Jacobi, G.Z., Canavan, C.M., Schrader, T.S., Mercer, D., Hill, R., and Moran, B.C., 2006, Ecoregions of New Mexico (color poster with map, descriptive text, summary tables, and photographs): U.S. Geological Survey, scale 1:1,400,000.

Gudino-Elizondo, N., Biggs, T.W., Castillo, C., Bingner, R.L., Langendoen, E.J., Taniguchi, K.T., Kretzschmar, T., Yuan, Y., and Liden, D., 2018, Measuring ephemeral gully erosion rates and topographical thresholds in an urban watershed using unmanned aerial systems and structure from motion photogrammetric techniques: Land Degradation and Development, v. 29, no. 6, p. 1896–1905. https://doi.org/10.1002/ldr.2976

Guduru, J.U., and Jilo, N.B., 2022, Assessment of rainfall-induced soil erosion rate and severity analysis for prioritization of conservation measures using RUSLE and multi-criteria evaluations technique at Gidabo watershed, Rift Valley Basin, Ethiopia: Ecohydrology & Hydrobiology, v. 23, no. 1, p. 30–47. https://doi.org/10.1016/j.ecohyd.2022.09.002

Haan, C.T., Barfield, B.J., and Hayes, J.C., 1994, Design Hydrology and Sedimentology for Small Catchments: San Diego, California, Academic Press, 608 p.

Harbor, J., 1999, Engineering geomorphology at the cutting edge of land disturbance—Erosion and sediment control on construction sites: Geomorphology, v. 31, no. 1–4, p. 247–263. https://doi.org/10.1016/S0169-555X(99)00107-5

Hegde, A., 2017, Geocell reinforced foundation beds-past findings, present trends and future prospects—A state-of-the-art review: Construction and Building Materials, v. 154, p. 658–674. https://doi.org/10.1016/j.conbuildmat.2017.07.230

Hobbs, K.M., and Pearthree, K.S., 2023, Geologic map of the Cañon Largo watershed on the Jicarilla Apache Nation, Rio Arriba and Sandoval Counties, New Mexico: New Mexico Bureau of Geology and Mineral Resources Open-File Report 620A, scale 1:50,000. https://doi.org/10.58799/OFR-620A

Hydrologic Engineering Center, 2022, HEC-HMS technical reference manual: U.S. Army Corps of Engineers. https://www.hec.usace.army.mil/confluence/hmsdocs/hmstrm

Igwe, P.U., Onulgbo, A.A., Chinedu, O.C., Ezeaku, I.I., and Muoneke, M.M., 2017, Soil erosion—A review of models and applications: International Journal of Advanced Engineering Research and Science, v. 4, no. 12, p. 138–150. https://dx.doi.org/10.22161/ijaers.4.12.22

Indian Roads Congress, 2018, Guidelines for design and installation of gabion structures: https://law.resource.org/pub/in/bis/irc/irc.gov.in.sp.116.2018.pdf (accessed December 2022).

Issaka, S., and Ashraf, M.A., 2017, Impact of soil erosion and degradation on water quality—A review: Geology, Ecology, and Landscapes, v. 1, no. 1, p. 1–11. https://doi.org/10.1080/24749508.2017.1301053

Jakeman, A.J., Green, T.R., Beavis, S.G., Zhang, L., Dietrich, C.R., and Crapper, P.F., 1999, Modelling upland and instream erosion, sediment and phosphorus transport in a large catchment: Hydrological Processes, v. 13, no. 5, p. 745–752. https://doi.org/10.1002/(SICI)1099-1085(19990415)13:5%3C745::AID-HYP777%3E3.0.CO;2-E

Jakubíková, A., Janeček, M., and Tippl, M., 2006, Field determination of the specific input characteristics to calculate the value of C factor of time-variable crops for the revised universal soil loss equation (RUSLE): Soil and Water Research, v. 1, no. 1, p. 10–15. https://doi.org/10.17221/6500-SWR

Karydas, C.G., Panagos, P., and Gitas, I.Z., 2014, A classification of water erosion models according to their geospatial characteristics: International Journal of Digital Earth, v. 7, no. 3, p. 229–250. https://doi.org/10.1080/17538947.2012.671380

Ke, Q., and Zhang, K., 2022, Interaction effects of rainfall and soil factors on runoff, erosion, and their predictions in different geographic regions: Journal of Hydrology, v. 605. https://doi.org/10.1016/j.jhydrol.2021.127291

Ke, Y., Im, J., Lee, J., Gong, H., and Ryu, Y., 2015, Characteristics of Landsat 8 OLI-derived NDVI by comparison with multiple satellite sensors and in-situ observations: Remote Sensing of Environment, v. 164, p. 298–313. https://doi.org/10.1016/j.rse.2015.04.004

Kim, Y., Lee, G., An, H., and Yang, J.E., 2015, Uncertainty assessment of soil erosion model using particle filtering: Journal of Mountain Science, v. 12, p. 828–840. https://doi.org/10.1007/s11629-014-3408-3

Kirkby, M.J., Abrahart, R., McMahon, M.D., Shao, J., and Thornes, J.B., 1998, MEDALUS soil erosion models for global change: Geomorphology, v. 24, no. 1, p. 35–49. https://doi.org/10.1016/S0169-555X(97)00099-8

Kourgialas, N.N., Koubouris, G.C., Karatzas, G.P., and Metzidakis, I., 2016, Assessing water erosion in Mediterranean tree crops using GIS techniques and field measurements—The effect of climate change: Natural Hazards, v. 83, p. 65–81. https://doi.org/10.1007/s11069-016-2354-5

Kucuker, D.M., and Giraldo, D.C., 2022, Assessment of soil erosion risk using an integrated approach of GIS and analytic hierarchy process (AHP) in Erzurum, Turkiye: Ecological Informatics, v. 71, p. 101788. https://doi.org/10.1016/j.ecoinf.2022.101788

Lagasse, P.F., Clopper, P.E., Pagán-Ortiz, J.E., Zevenbergen, L.W., Arneson, L.A., Schall, J.D., and Girard, L.G., 2009, Bridge scour and stream instability countermeasures—Experience, selection, and design guidance (third edition): U.S. Department of Transportation Federal Highway Administration Hydraulic Engineering Circular No. 23.

Lal, R., 2001, Soil degradation by erosion: Land Degradation & Development, v. 12, no. 6, p. 519–539. https://doi.org/10.1002/ldr.472

Langbein, W.B., and Leopold, L.B., 1966, River meanders—Theory of minimum variance: U.S. Geological Survey Professional Paper 422-H, 20 p. https://doi.org/10.3133/pp422H

Laporte-Fauret, Q., Marieu, V., Castelle, B., Michalet, R., Bujan, S., and Rosebery, D., 2019, Low-cost UAV for high-resolution and large-scale coastal dune change monitoring using photogrammetry: Journal of Marine Science and Engineering, v. 7, no. 3. https://doi.org/10.3390/jmse7030063

le Roux, J., Morake, L., Van Der Waal, B., Anderson, R.L., and Hedding, D.W., 2022, Intra-gully mapping of the largest documented gully network in South Africa using UAV photogrammetry—Implications for restoration strategies: Progress in Physical Geography, v. 46, no. 5, p. 772–789. https://doi.org/10.1177/03091333221101057

Leopold, L.B., and Miller, J.P., 1956, Ephemeral streams—Hydraulic factors and their relation to drainage net: U.S. Geological Survey Professional Paper 282-A, 37 p. https://doi.org/10.3133/pp282A

Levy, B., and McCuen, R., 1999, Assessment of storm duration for hydrologic design: ASCE Journal of Hydrologic Engineering, v. 4, no. 3, p. 209–213. https://doi.org/10.1061/(ASCE)1084-0699(1999)4:3(209)

Li, P., Mu, X., Holden, J., Wu, Y., Irvine, B., Wang, F., Gao, P., Zhao, G., and Sun, W., 2017, Comparison of soil erosion models used to study the Chinese Loess Plateau: Earth-Science Reviews, v. 170, p. 17–30. https://doi.org/10.1016/j.earscirev.2017.05.005

Li, W., Bertin, S., and Friedrich, H., 2018, Combining structure from motion and close-range stereo photogrammetry to obtain scaled gravel bar DEMs: International Journal of Remote Sensing, v. 39, no. 23, p. 9269–9293. https://doi.org/10.1080/01431161.2018.1530809

Liao, K., Song, Y., Xie, S., and Zheng, H., 2019, Monitoring of Benggang erosion based on UAV photogrammetry technology: IOP Conference Series—Earth and Environmental Science, v. 330, no. 5. https://doi.org/10.1088/1755-1315/330/5/052003

Lin, C.-Y., Lin, W.-T., and Chou, W.-C., 2002, Soil erosion prediction and sediment yield estimation—The Taiwan experience: Soil and Tillage Research, v. 68, no. 2, p. 143–152. https://doi.org/10.1016/S0167-1987(02)00114-9

Lin, W.-T., Chou, W.-C., Lin, C.-Y., Huang, P.-H., and Tsai, J.-S., 2006, Automated suitable drainage network extraction from digital elevation models in Taiwan's upstream watersheds: Hydrological Processes, v. 20, no. 2, p. 289–306. https://doi.org/10.1002/hyp.5911

Lisle, R.J., Brabham, P.J., and Barnes, J.W., 2011, Basic Geological Mapping (fifth edition): Hoboken, New Jersey, John Wiley & Sons Inc., 217 p.

Lu, H., Moran, C.J., Prosser, I.P., Raupach, M.R., Olley, J. and Petheram, C., 2003, Hillslope erosion and sediment delivery—A basin wide estimation at medium catchment scale: CSIRO Land and Water Technical Report 15/03.

Ma, X., Zhao, C., and Zhu, J., 2021, Aggravated risk of soil erosion with global warming—A global meta-analysis: CATENA, v. 200. https://doi.org/10.1016/j.catena.2020.105129

Mali, V.K., and Kuiry, S.N., 2018, Assessing the accuracy of high-resolution topographic data generated using freely available packages based on SfM-MVS approach: Measurement, v. 124, p. 338–350. https://doi.org/10.1016/j.measurement.2018.04.043

Mali, V.K., Venu, P., Nagaraj, M.K., and Kuiry, S.N., 2021, Demonstration of structure-from-motion (SfM) and multi-view stereo (MVS) close range photogrammetry technique for scour hole analysis: Sādhanā, v. 46, no. 4, p. 1–13. https://doi.org/10.1007/s12046-021-01758-2

Mantey, S., and Tagoe, N.D., 2013, Spatial modelling of Soil Conservation Service curve number grid and potential maximum soil water retention to delineate flood prone areas—A case study: Research Journal of Environmental and Earth Sciences, v. 5, no. 8, p. 449–456. http://dx.doi.org/10.19026/rjees.5.5673

Maruffi, L., Stucchi, L., Casale, F., and Bocchiola, D., 2022, Soil erosion and sediment transport under climate change for Mera River, in Italian Alps of Valchiavenna: Science of the Total Environment, v. 806, no. 2. https://doi.org/10.1016/j.scitotenv.2021.150651

Matherne, A.M., 2006, Effects of roads and well pads on erosion in the Largo Canyon watershed, New Mexico, 2001–02: U.S. Geological Survey Scientific Investigations Report 2006-5039, 42 p. https://doi.org/10.3133/sir20065039

Megahan, W.F., 1977, Reducing erosional impacts of roads, in Guidelines for Watershed Management: Rome, Food and Agriculture Organization, United Nations, p. 237–261.

Mekonnen, M., Keesstra, S.D., Stroosnijder, L., Baartman, J.E.M., and Maroulis, J., 2015, Soil conservation through sediment trapping—A review: Land Degradation and Development, v. 26, no. 6, p. 544–556. https://doi.org/10.1002/ldr.2308

Merritt, W.S., Letcher, R.A., and Jakeman, A.J., 2003, A review of erosion and sediment transport models: Environmental Modelling & Software, v. 18, no. 8–9, p. 761–799. https://doi.org/10.1016/S1364-8152(03)00078-1

Mitas, L., and Mitasova, H., 1998, Distributed soil erosion simulation for effective erosion prevention: Water Resources Research, v. 34, no. 3, p. 505–516. https://doi.org/10.1029/97WR03347

Mitasova, H., 2014, Soil erosion and deposition modeling—Theoretical background: https://ncsu-geoforall-lab.github.io/erosion-modeling-tutorial/erdep_theory.html (accessed November 2022).

Mitasova, H., Hofierka, J., Zlocha, M., and Iverson, L.R., 1996, Modelling topographic potential for erosion and deposition using GIS: International Journal of Geographical Information Systems, v. 10, no. 5, p. 629–641. https://doi.org/10.1080/02693799608902101

Murphy, P.N.C., Ogilvie, J., Meng, F-R., and Arp, P., 2008, Stream network modelling using lidar and photogrammetric digital elevation models—A comparison and field verification: Hydrological Processes, v. 22, no. 12, p. 1747–1754. https://doi.org/10.1002/hyp.6770

Mussetter Engineering Inc., 2004, Sediment yields from ungaged tributaries to the middle Rio Grande between Bernardo and Elephant Butte Reservoir: https://www.ose.state.nm.us/Basins/RioGrande/SanAcacia/SedimentTributaryReport-11-24-04.pdf (accessed November 2022).

Mussetter Engineering Inc., 2008, Sediment and erosion design guide: https://www.sscafca.org/development/documents/sediment_design_guide/Sediment%20Design%20Guide%2012-30-08.pdf (accessed November 2022).

Najafi, M., Salem, S., Bhattachar, D., Salman, B., and Patil, R., 2008, An asset management approach for drainage infrastructure and culverts: Midwest Regional University Transportation Center, University of Wisconsin–Madison. https://www.researchgate.net/publication/228685906

Nearing, M.A., 1998, Why soil erosion models over-predict small soil losses and under-predict large soil losses: CATENA, v. 32, no. 1, p. 15–22. https://doi.org/10.1016/S0341-8162(97)00052-0

New York State Forestry, 2011, New York State Forestry best management practices for water: https://www.dec.ny.gov/docs/wildlife_pdf/yfiforestrybmp.pdf (accessed November 2022).

Niu, B., Qu, J., Zhang, X., Liu, B., Tan, L., and An, Z., 2019, Quantifying provenance of reservoir sediment using multiple composite fingerprints in an arid region experiencing both wind and water erosion: Geomorphology, v. 332, p. 112–121. https://doi.org/10.1016/j.geomorph.2019.02.011

Nyssen, J., Poesen, J., Moeyersons, J., Luyten, E., Veyret-Picot, M., Deckers, J., Haile, M., and Govers, G., 2002, Impact of road building on gully erosion risk—A case study from the northern Ethiopian highlands: Earth Surface Processes and Landforms, v. 27, no. 12, p. 1267–1283. https://doi.org/10.1002/esp.404

Nyssen, J., Veyret-Picot, M., Poesen, J., Moeyersons, J., Haile, M., Deckers, J., and Govers, G., 2004, The effectiveness of loose rock check dams for gully control in Tigray, northern Ethiopia: Soil Use and Management, v. 20, no. 1, p. 55–64. https://doi.org/10.1111/j.1475-2743.2004.tb00337.x

Pandey, M., and Sharma, P.K., 2017, Remote sensing and GIS based watershed prioritization, in Proceedings, IEEE International Geoscience & Remote Sensing Symposium, Fort Worth, TX, 23–28 July 2017, p. 6182–6185. https://doi.org/10.1109/IGARSS.2017.8128420

Pandey, A., Himanshu, S.K., Mishra, S.K., and Singh, V.P., 2016, Physically based soil erosion and sediment yield models revisited: CATENA, v. 147, p. 595–620. https://doi.org/10.1016/j.catena.2016.08.002

Peternel, T., Kumelj, Š., Oštir, K., and Komac, M., 2017, Monitoring the Potoška planina landslide (NW Slovenia) using UAV photogrammetry and tachymetric measurements: Landslides, v. 14, p. 395–406. https://doi.org/10.1007/s10346-016-0759-6

Pham, T.G., Degener, J., and Kappas, M., 2018, Integrated universal soil loss equation (USLE) and geographical information system (GIS) for soil erosion estimation in A Sap basin, Central Vietnam: International Soil and Water Conservation Research, v. 6, no. 2, p. 99–110. https://doi.org/10.1016/j.iswcr.2018.01.001

Phinzi, K., and Ngetar, N.S., 2019, The assessment of water-borne erosion at catchment level using GIS-based RUSLE and remote sensing—A review: International Soil and Water Conservation Research, v. 7, no. 1, p. 27–46. https://doi.org/10.1016/j.iswcr.2018.12.002

Pimentel, D., 2006, Soil erosion—A food and environmental threat: Environment, Development and Sustainability, v. 8, p. 119–137. https://doi.org/10.1007/s10668-005-1262-8

Pineux, N., Lisein, J., Swerts, G., Bielders, C.L., Lejeune, P., Colinet, G., and Degré, A., 2017, Can DEM time series produced by UAV be used to quantify diffuse erosion in an agricultural watershed?: Geomorphology, v. 280, p. 122–136. https://doi.org/10.1016/j.geomorph.2016.12.003

Pistocchi, A., Cassani, G., and Zani, O., 2002, Use of the USPED model for mapping soil erosion and managing best land conservation practices, *in* Proceedings, 1st International Congress on Environmental Modelling and Software, Lugano, Switzerland, June 24–27, 2002, p. 163–168. https://scholarsarchive.byu.edu/iemssconference/2002/all/191

Poesen, J., 2018, Soil erosion in the Anthropocene—Research needs: Earth Surface Processes and Landforms, v. 43, no. 1, p. 64–84. https://doi.org/10.1002/esp.4250

Rajabi, A.M., Yavari, A., and Cheshomi, A., 2022, Sediment yield and soil erosion assessment by using empirical models for Shazand watershed, a semi-arid area in center of Iran: Natural Hazards, v. 112, p. 1685–1704. https://doi.org/10.1007/s11069-022-05244-8

Raza, A., Ahrends, H., Habib-Ur-Rahman, M., and Gaiser, T., 2021, Modeling approaches to assess soil erosion by water at the field scale with special emphasis on heterogeneity of soils and crops: Land, v. 10, no. 4. https://doi.org/10.3390/land10040422

Renard, K.G., and Simanton, J.R., 1990, Application of RUSLE to rangelands, *in* Riggins, R.E., Jones, E.B., Singh, R., and Rechard, P.A., eds., Watershed planning and analysis in action: American Society of Civil Engineers, p. 164–173.

Renard, K.G., Foster, G.R., Weesies, G.A., McCool, D.K., and Yoder, D.C., 1997, Predicting soil erosion by water—A guide to conservation planning with the revised universal soil loss equation (RUSLE): U.S. Department of Agriculture, Agricultural Research Service Agriculture Handbook Number 703, 385 p.

Renschler, C.S., Mannaerts, C., and Diekkrüger, B., 1999, Evaluating spatial and temporal variability in soil erosion risk—Rainfall erosivity and soil loss ratios in Andalusia, Spain: CATENA, v. 34, no. 3–4, p. 209–225. https://doi.org/10.1016/S0341-8162(98)00117-9

Richardson, E.V., and Simons, D.B., 1984, Use of spurs and guidebanks for highway crossings, *in* Second Bridge Engineering Conference: National Academies of Sciences, Engineering, and Medicine Transportation Research Board, p. 184–193.

Roy, S., Das, S., and Sengupta, S., 2022, Predicting terrain erosion susceptibility from drainage basin morphometry using ALOS-PALSAR DEM—Analysis from PCA-weighted AHP approach in a river system of Eastern India: Environment, Development and Sustainability, v. 25, p. 9589–9617. https://doi.org/10.1007/s10668-022-02450-z

Sadeghi, S.H.R., Gholami, L., Darvishan, A.K., and Saeidi, P., 2014, A review of the application of the MUSLE model worldwide: Hydrological Sciences Journal, v. 59, no. 2, p. 365–375. https://doi.org/10.1080/02626667.2013.866239

Santos, C.A.G., Watanabe, M., and Suzuki, K., 1998, A conceptual soil erosion model: Proceedings of Hydraulic Engineering, v. 42, p. 1033–1038. https://doi.org/10.2208/prohe.42.1033

Schumm, S.A., and Hadley, R.F., 1957, Arroyos and the semiarid cycle of erosion [Wyoming and New Mexico]: American Journal of Science, v. 255, no. 3, p. 161–174. https://doi.org/10.2475/ajs.255.3.161

Schumm, S.A., and Khan, H.R., 1972, Experimental study of channel patterns: GSA Bulletin, v. 83, no. 6, p. 1755–1770. https://doi.org/10.1130/0016-7606(1972)83[1755:ESOCP]2.0.CO;2

Senanayake, S., Pradhan, B., Alamri, A., and Park, H.-J., 2022, A new application of deep neural network (LSTM) and RUSLE models in soil erosion prediction: Science of the Total Environment, v. 845. https://doi.org/10.1016/j.scitotenv.2022.157220

Sharma, A., 2010, Integrating terrain and vegetation indices for identifying potential soil erosion risk area: Geo-spatial Information Science, v. 13, no. 3, p. 201–209. https://doi.org/10.1007/s11806-010-0342-6

Shaw, J.R., and Cooper, D.J., 2008, Linkages among watersheds, stream reaches, and riparian vegetation in dryland ephemeral stream networks: Journal of Hydrology, v. 350, no. 1–2, p. 68–82. https://doi.org/10.1016/j.jhydrol.2007.11.030

Sikdar, K., 2019, Mohave County low impact development guide for flood protection and water sustainability: Holistic Engineering and Land Management Inc., 80 p. http://dx.doi.org/10.13140/RG.2.2.22030.79689

Sponholtz, C., and Anderson, A.C., 2010, Erosion control field guide: Quivira Coalition, 12 p.

State of California, 1971, Environmental impact of urbanization of the foothill and mountainous lands of California: Division of Soil Conservation, 4 p.

Stöcker, C., Eltner, A., and Karrasch, P., 2015, Measuring gullies by synergetic application of UAV and close range photogrammetry—A case study from Andalusia, Spain: CATENA, v. 132, p. 1–11. https://doi.org/10.1016/j.catena.2015.04.004

Straffelini, E., Pijl, A., Otto, S., Marchesini, E., Pitacco, A., and Tarolli, P., 2022, A high-resolution physical modelling approach to assess runoff and soil erosion in vineyards under different soil managements: Soil and Tillage Research, v. 222. https://doi.org/10.1016/j.still.2022.105418

Stroosnijder, L., 2005, Measurement of erosion—Is it possible?: CATENA, v. 64, no. 2–3, p. 162–173. https://doi.org/10.1016/j.catena.2005.08.004

Tahoe Regional Planning Agency, 2014, Best management practices handbook: https://tahoebmp.org/bmphandbook.aspx (accessed November 2022).

Tarboton, D.G., 1997, A new method for the determination of flow directions and upslope areas in grid digital elevation models: Water Resources Research, v. 33, no. 2, p. 309–319. https://doi.org/10.1029/96WR03137

Teka, K., Haftu, M., Ostwald, M., and Cederberg, C., 2020, Can integrated watershed management reduce soil erosion and improve livelihoods? A study from northern Ethiopia: International Soil and Water Conservation Research, v. 8, no. 3, p. 266–276. https://doi.org/10.1016/j.iswcr.2020.06.007

The Constructor, 2021, What is culvert? Its types, materials and location: https://theconstructor.org/construction/types-of-culverts-material-construction/12926/ (accessed December 2022).

Torri, D., and Poesen, J., 2014, A review of topographic threshold conditions for gully head development in different environments: Earth-Science Reviews, v. 130, p. 73–85. https://doi.org/10.1016/j.earscirev.2013.12.006

Townsend, K.F., Nelson, M.S., Rittenour, T.M., and Pederson, J.L., 2019, Anatomy and evolution of a dynamic arroyo system, Kanab Creek, southern Utah, USA: GSA Bulletin, v. 131, no. 11–12, p. 2094–2109. https://doi.org/10.1130/B35195.1

Uri, N.D., 2001, The environmental implications of soil erosion in the United States: Environmental Monitoring and Assessment, v. 66, p. 293–312. https://doi.org/10.1023/A:1006333329653

U.S. Environmental Protection Agency, 1972, Guidelines for erosion and sediment control planning and implementation: Environmental Protection Technology Series EPA-R2-72-015.

U.S. Geological Survey, 2022, Landsat satellite missions: https://www.usgs.gov/landsat-missions/landsat-satellite-missions (accessed November 2022).

Uysal, M., Toprak, A.S., and Polat, N., 2015, DEM generation with UAV photogrammetry and accuracy analysis: Measurement, v. 73, p. 539–543. https://doi.org/10.1016/j.measurement.2015.06.010

Visser, S.M., Sterk, G., and Ribolzi, O., 2004, Techniques for simultaneous quantification of wind and water erosion in semi-arid regions: Journal of Arid Environments, v. 59, no. 4, p. 699–717. https://doi.org/10.1016/j.jaridenv.2004.02.005

Visser, R., Tinnelly, B., and Fairbrother, S., 2011, Installation of geogrid to improve forest roads construction: FORMEC Austria, 8 p.

Vrieling, A., 2006, Satellite remote sensing for water erosion assessment—A review: CATENA, v. 65, no. 1, p. 2–18. https://doi.org/10.1016/j.catena.2005.10.005

Wang, Y., Fu, B., Chen, L., Lü, Y., and Gao, Y., 2011, Check dam in the loess plateau of China—Engineering for environmental services and food security: Environmental Science and Technology, v. 45, no. 24, p. 10298–10299. https://doi.org/10.1021/es2038992

Wang, Y., Dong, Y., Su, Z., Mudd, S.M., Zheng, Q., Hu, G., and Yan, D., 2020, Spatial distribution of water and wind erosion and their influence on the soil quality at the agropastoral ecotone of north China: International Soil and Water Conservation Research, v. 8, no. 3, p. 253–265. https://doi.org/10.1016/j.iswcr.2020.05.001

Wang, H., Zuo, H., Jia, X., Li, K., and Yan, M., 2021, Full particle size distribution characteristics of land surface sediment and their effect on wind erosion resistance in arid and semiarid regions of northwest China: Geomorphology, v. 372. https://doi.org/10.1016/j.geomorph.2020.107458

Wilcox, B.P., and Wood, M.K., 1989, Factors influencing interrill erosion from semiarid slopes in New Mexico: Journal of Range Management, v. 42, no. 2, p. 66–70. https://doi.org/10.2307/3899661

Williams, J.R., 1975, Sediment routing for agricultural watersheds: Journal of the American Water Resources Association, v. 11, no. 5, p. 965–974. https://doi.org/10.1111/j.1752-1688.1975.tb01817.x

Wilson, J.P., and Gallant, J.C., 2000, Digital terrain analysis, *in* Wilson, J.P., and Gallant, J.C., eds., Terrain Analysis—Principles and Applications: Hoboken, New Jersey, John Wiley & Sons Inc., p. 1–27.

Wrobel, B.P., 1991, The evolution of digital photogrammetry from analytical photogrammetry: The Photogrammetric Record, v. 13, no. 77, p. 765–776. https://doi.org/10.1111/j.1477-9730.1991.tb00738.x

Yang, D., Kanae, S., Oki, T., Koike, T., and Musiake, K., 2003, Global potential soil erosion with reference to land use and climate changes: Hydrological Processes, v. 17, no. 4, p. 2913–2928. https://doi.org/10.1002/hyp.1441

Zhang, L., O'Neill, A.L., and Lacey, S., 1996, Modelling approaches to the prediction of soil erosion in catchments: Environmental Software, v. 11, no. 1–3, p. 123–133. https://doi.org/10.1016/S0266-9838(96)00023-8

Zhang, W., Zhou, J., Feng, G., Weindorf, D.C., Hu, G., and Sheng, J., 2015, Characteristics of water erosion and conservation practice in arid regions of central Asia—Xinjiang Province, China as an example: International Soil and Water Conservation Research, v. 3, no. 2, p. 97–111. https://doi.org/10.1016/j.iswcr.2015.06.002

Zhang, W., Qu, J., Tan, L., Jing, Z., Bian, K., and Niu, Q., 2016, Environmental dynamics of a star dune: Geomorphology, v. 273, p. 28–38. https://doi.org/10.1016/j.geomorph.2016.08.005

Zhang, Z., Luo, J., and Chen, B., 2020, Spatially explicit quantification of total soil erosion by RTK GPS in wind and water eroded croplands: Science of the Total Environment, v. 702. https://doi.org/10.1016/j.scitotenv.2019.134716

Zi, T., Kumar, M., Kiely, G., Lewis, C., and Albertson, J., 2016, Simulating the spatio-temporal dynamics of soil erosion, deposition, and yield using a coupled sediment dynamics and 3D distributed hydrologic model: Environmental Modelling & Software, v. 83, p. 310–325. https://doi.org/10.1016/j.envsoft.2016.06.004

APPENDIX I.
UAV-DERIVED MAPS OF STUDY AREAS
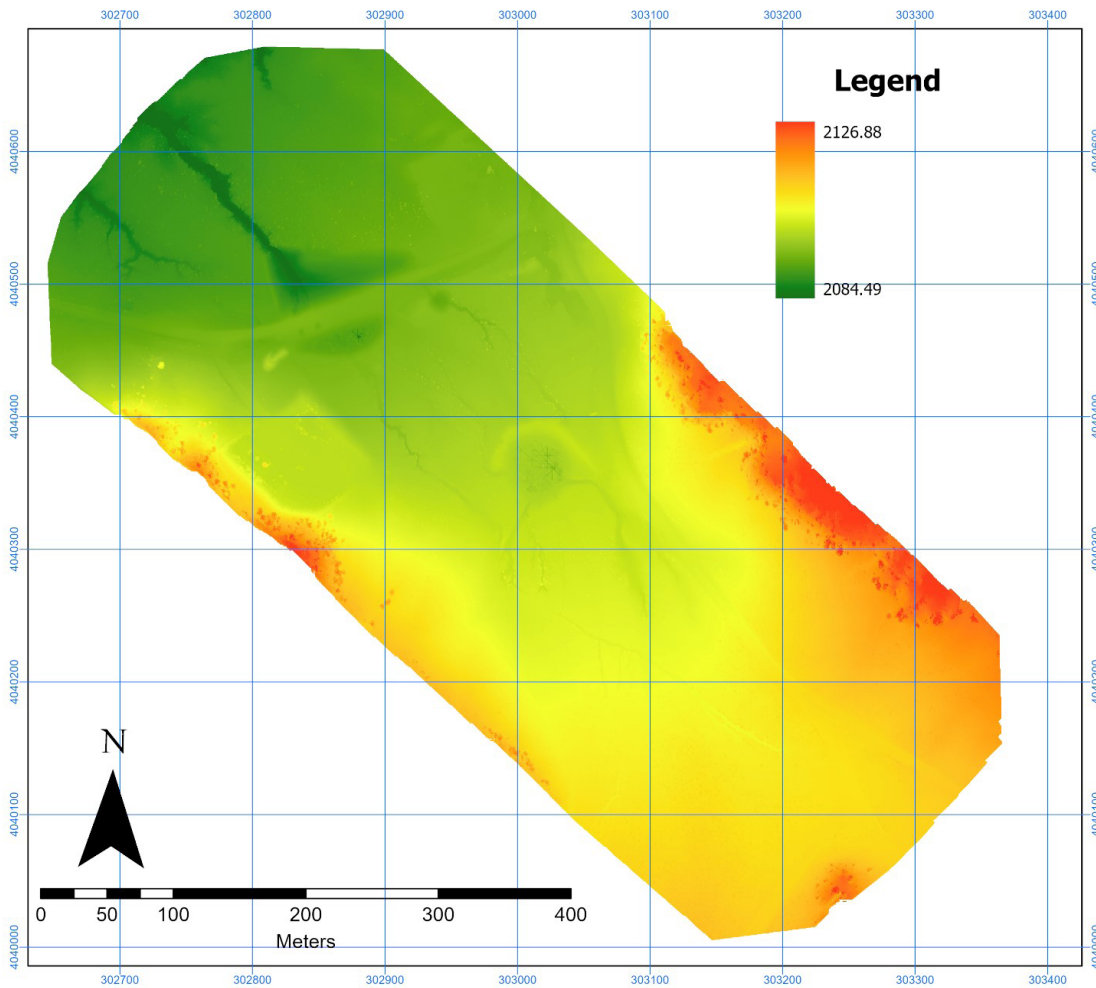
Appendix 1.1. Digital surface model of Site A, August 2021. Scale units are meters above sea level.
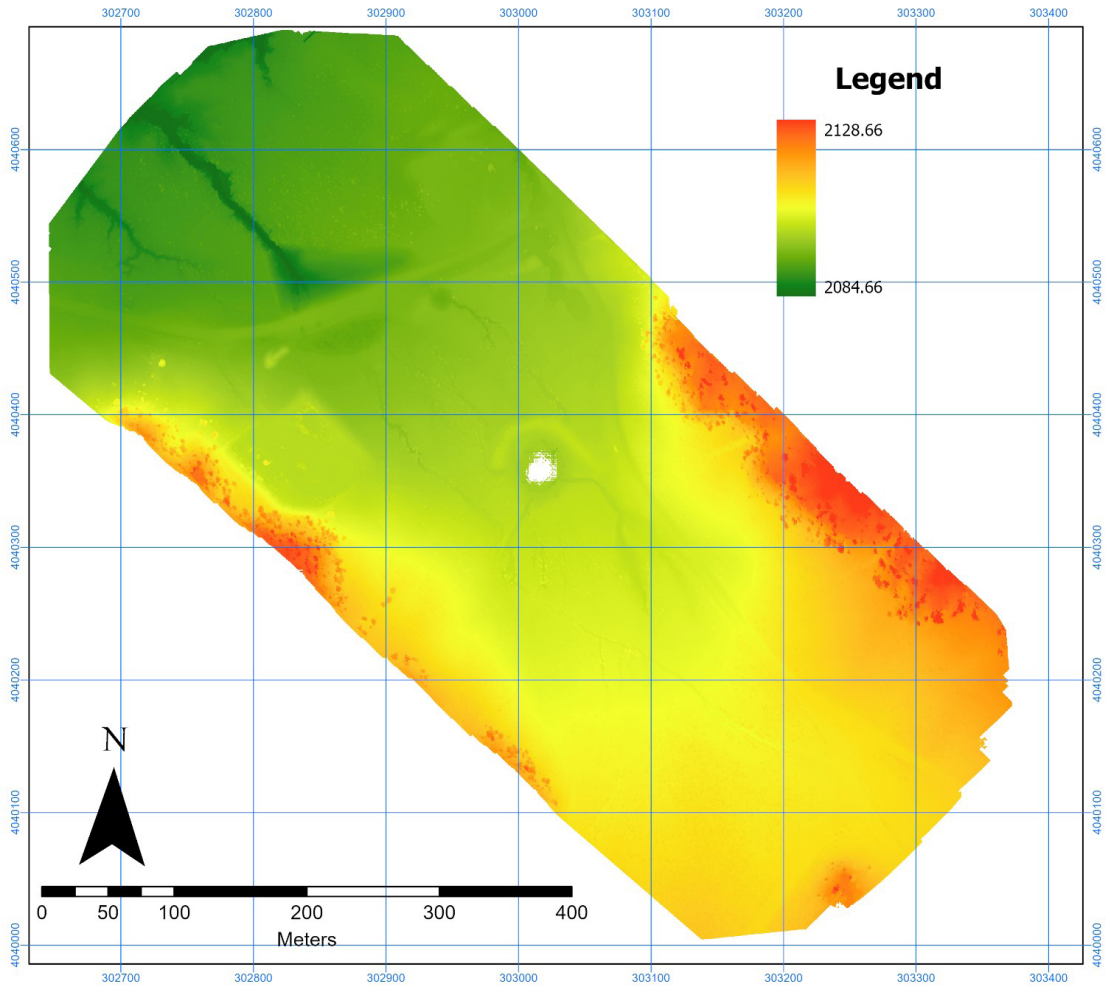
Appendix 1.2. Digital surface model of Site A, July 2022. Scale units are meters above sea level.
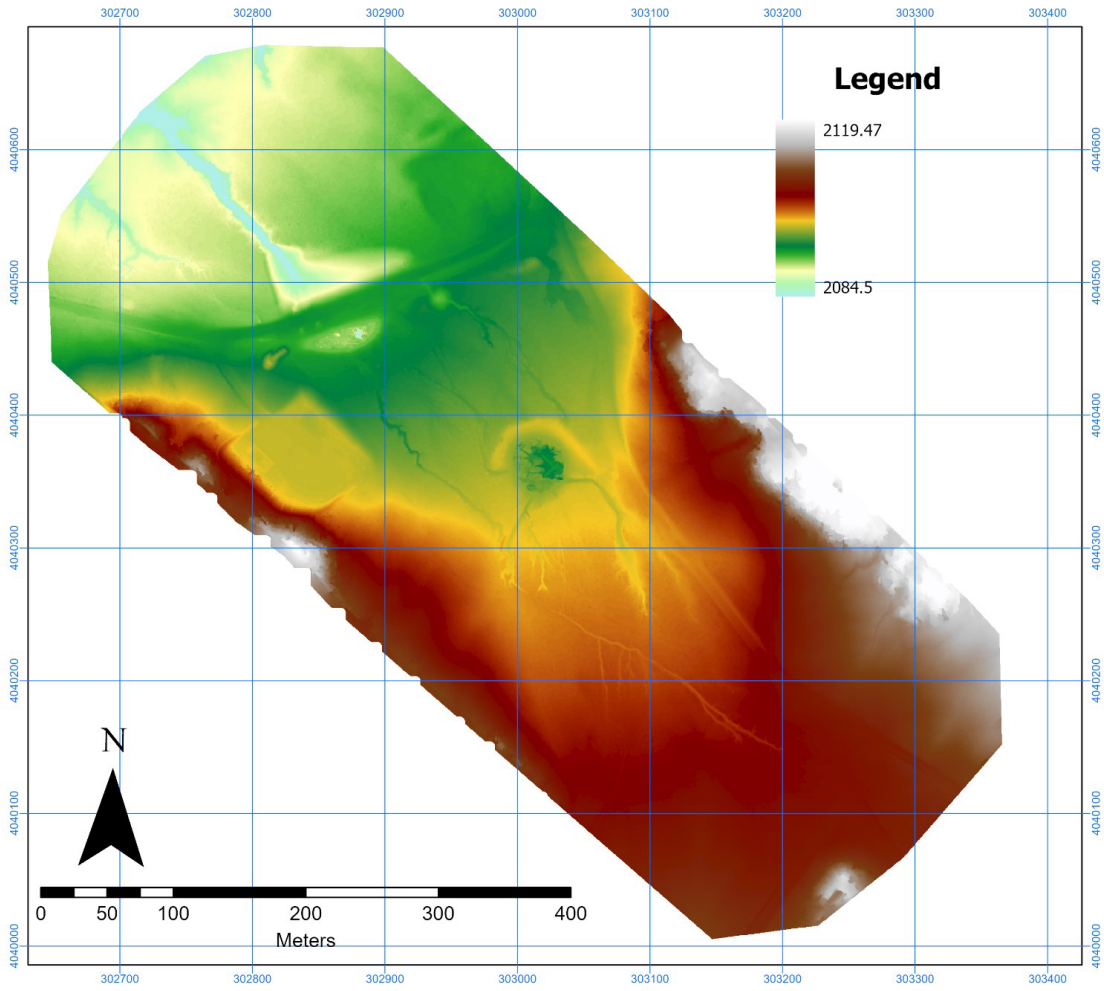
Appendix 1.3. Digital terrain model of Site A, August 2021. Scale units are meters above sea level.
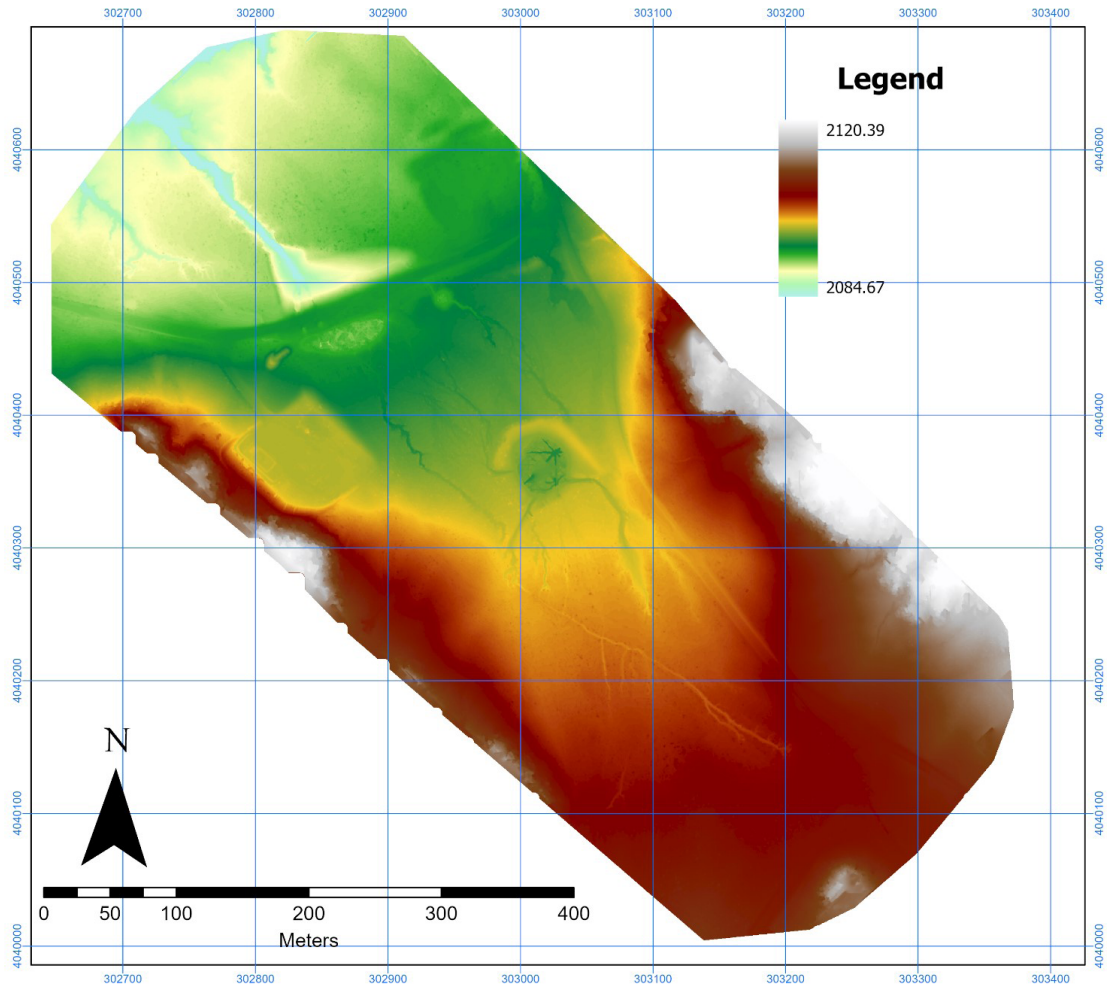
Appendix 1.4. Digital terrain model of Site A, July 2022. Scale units are meters above sea level.
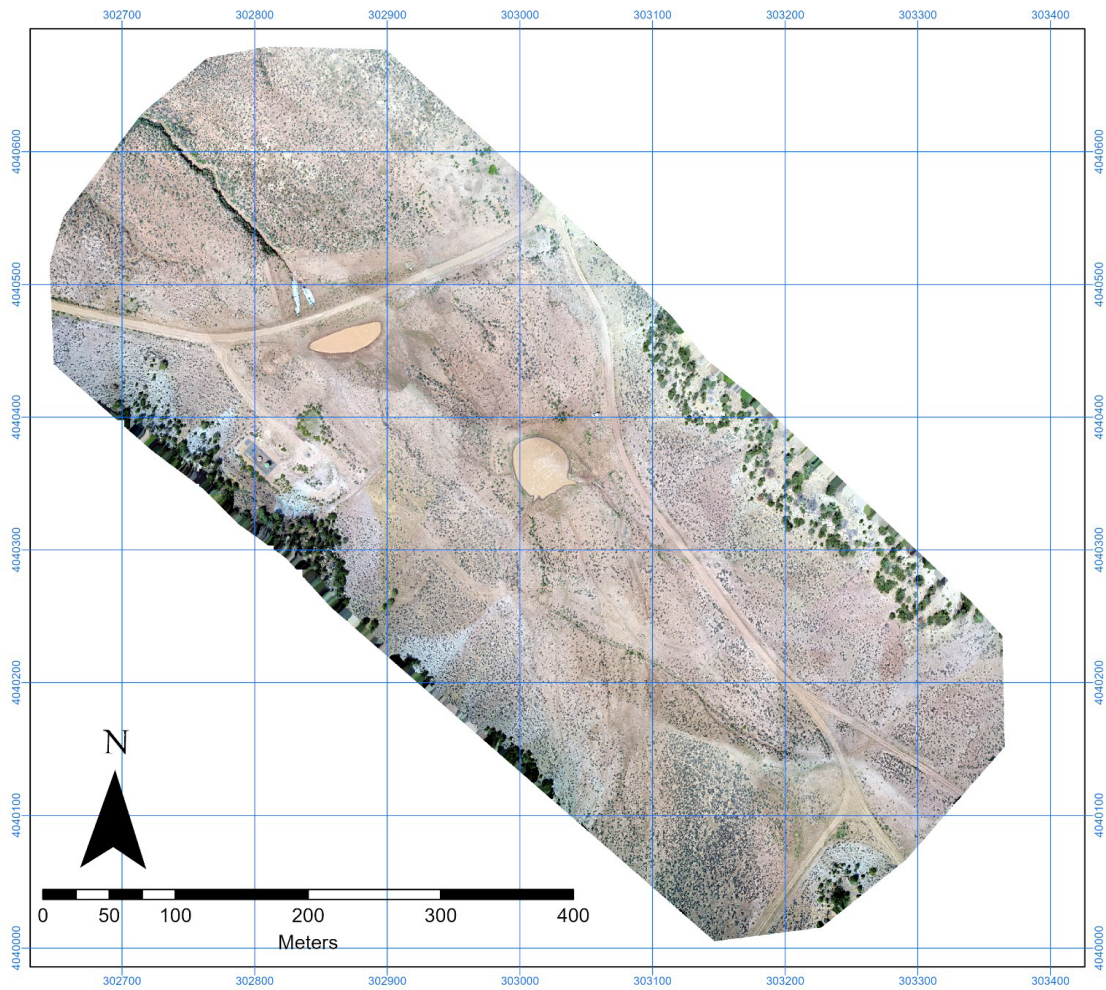
Appendix 1.5. Digital orthomosaic of Site A, August 2021.
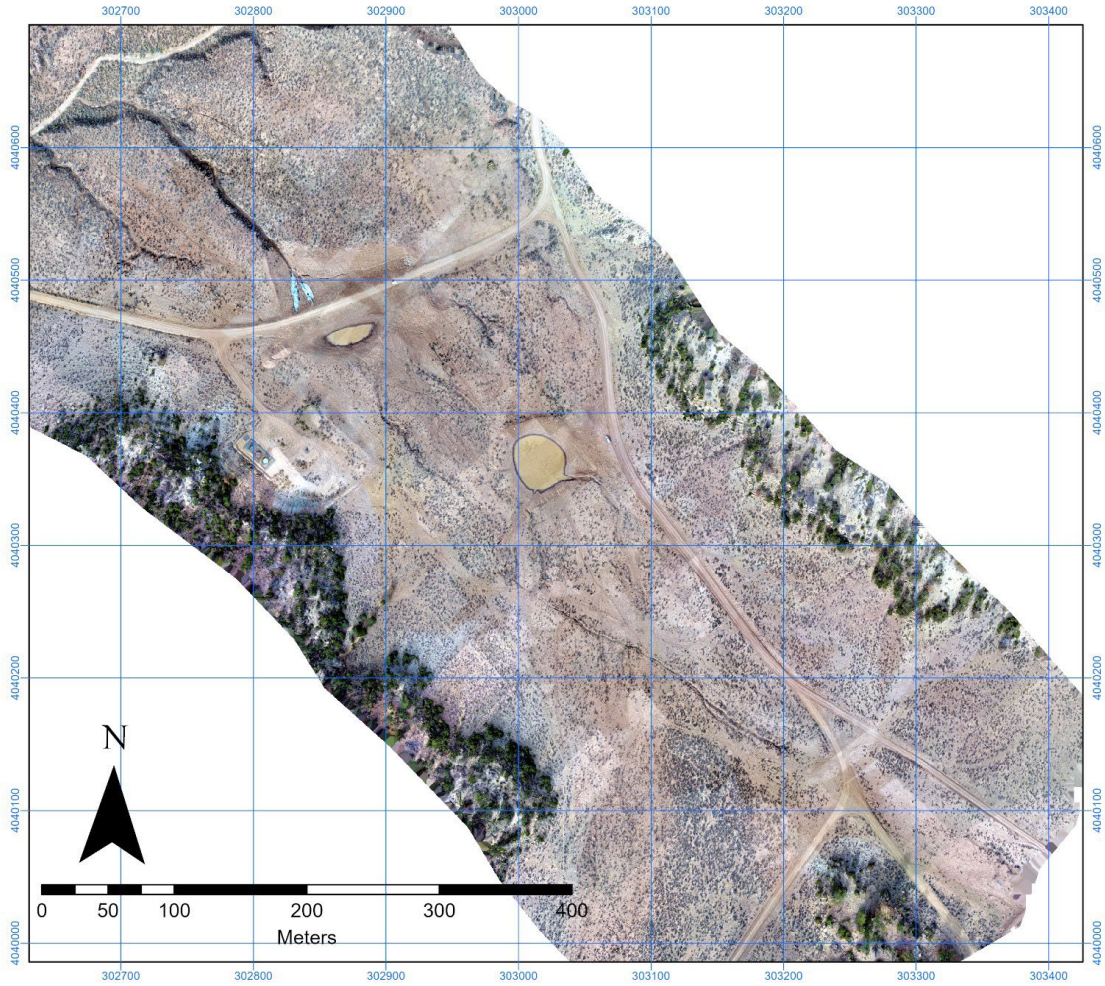
Appendix 1.6. Digital orthomosaic of Site A, November 2021.
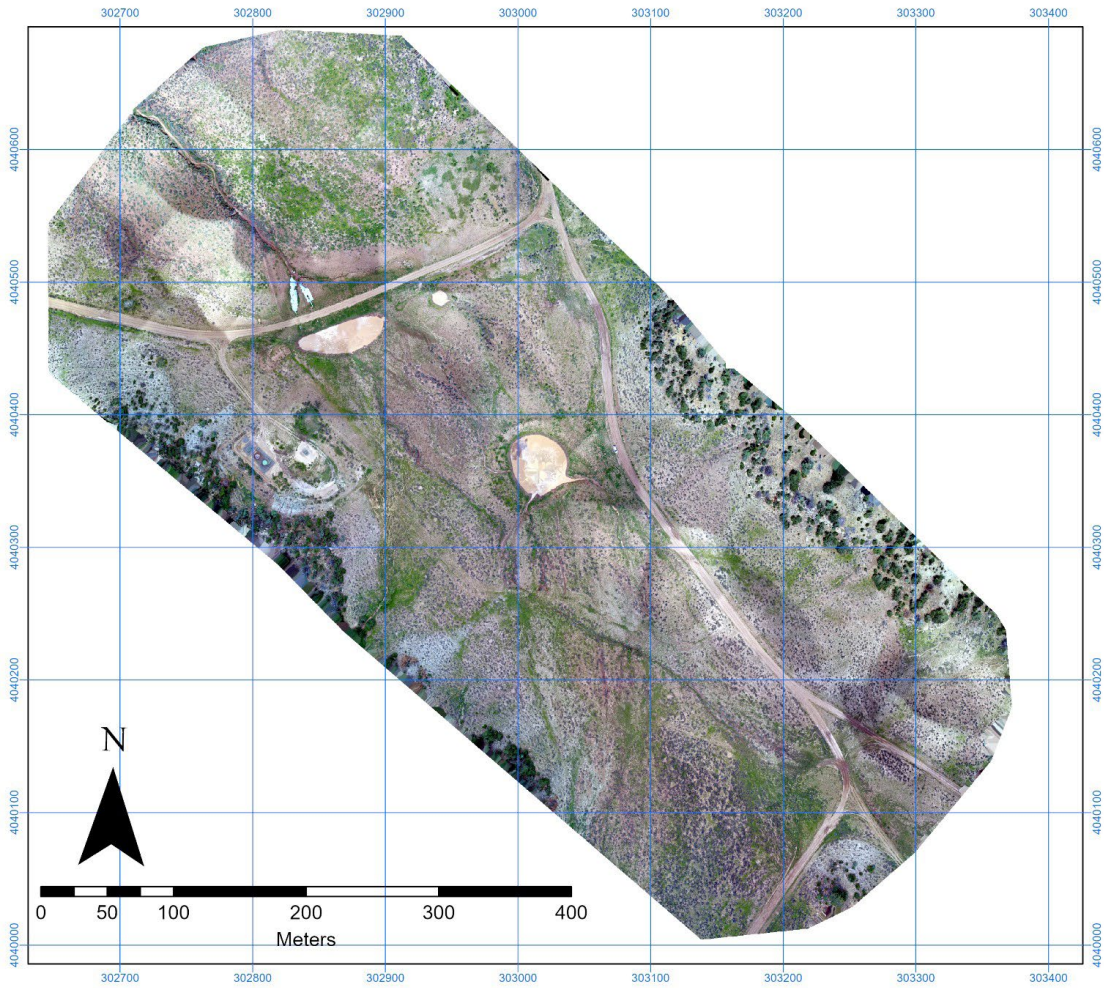
Appendix 1.7. Digital orthomosaic of Site A, July 2022.
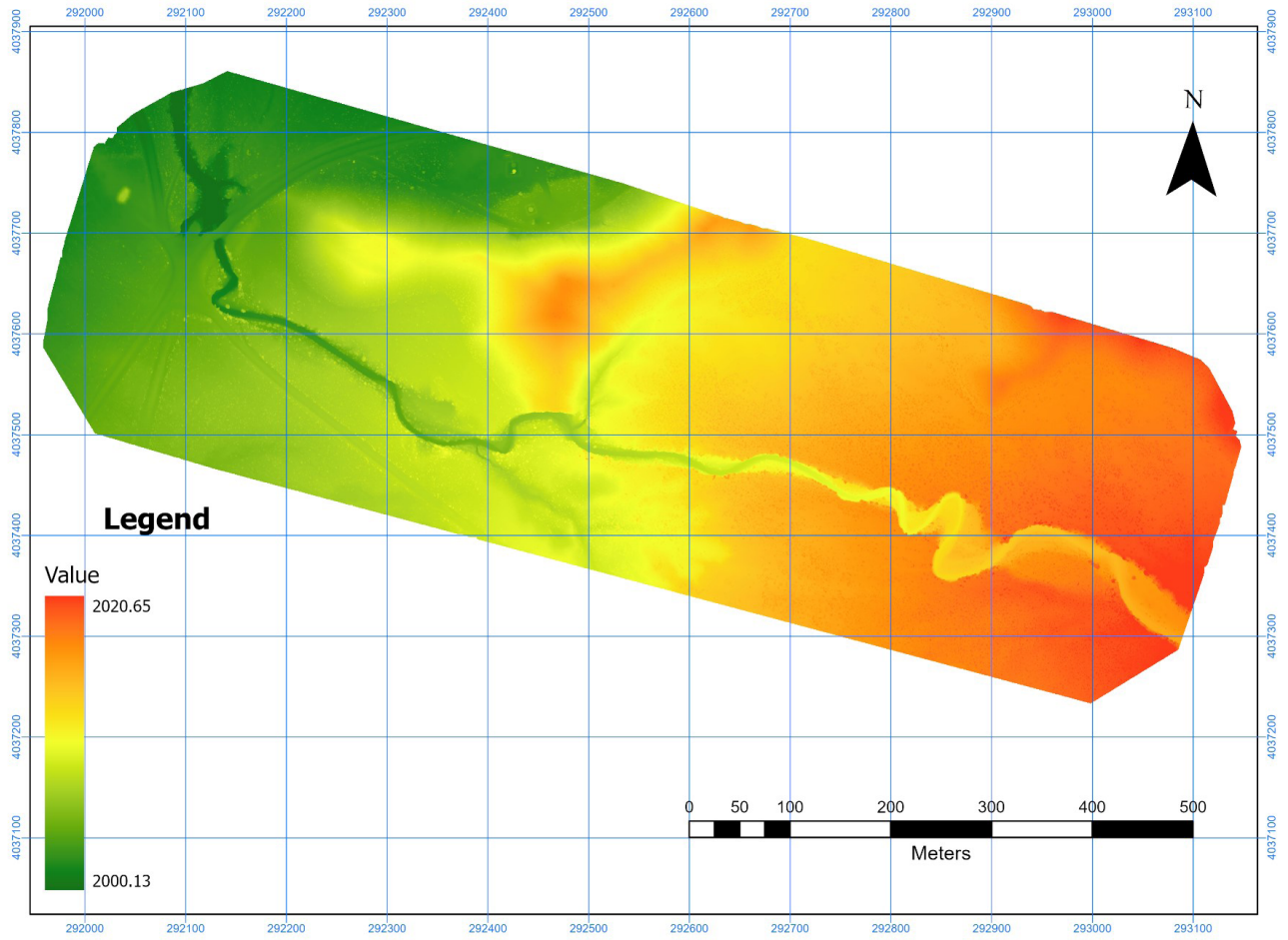
Appendix 1.8. Digital surface model of Site B, August 2021. Scale units are meters above sea level.
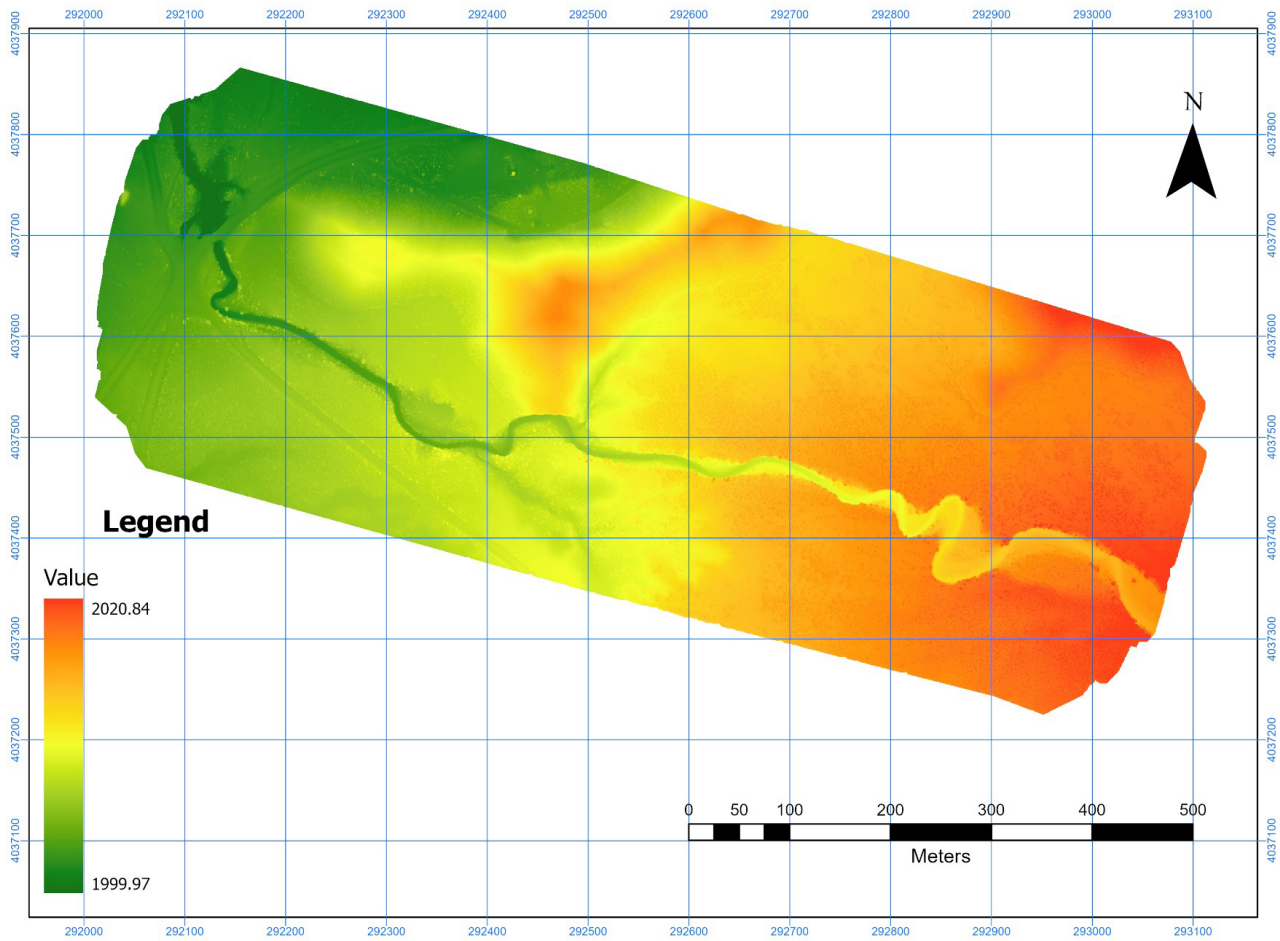
Appendix 1.9. Digital surface model of Site B, July 2022. Scale units are meters above sea level.
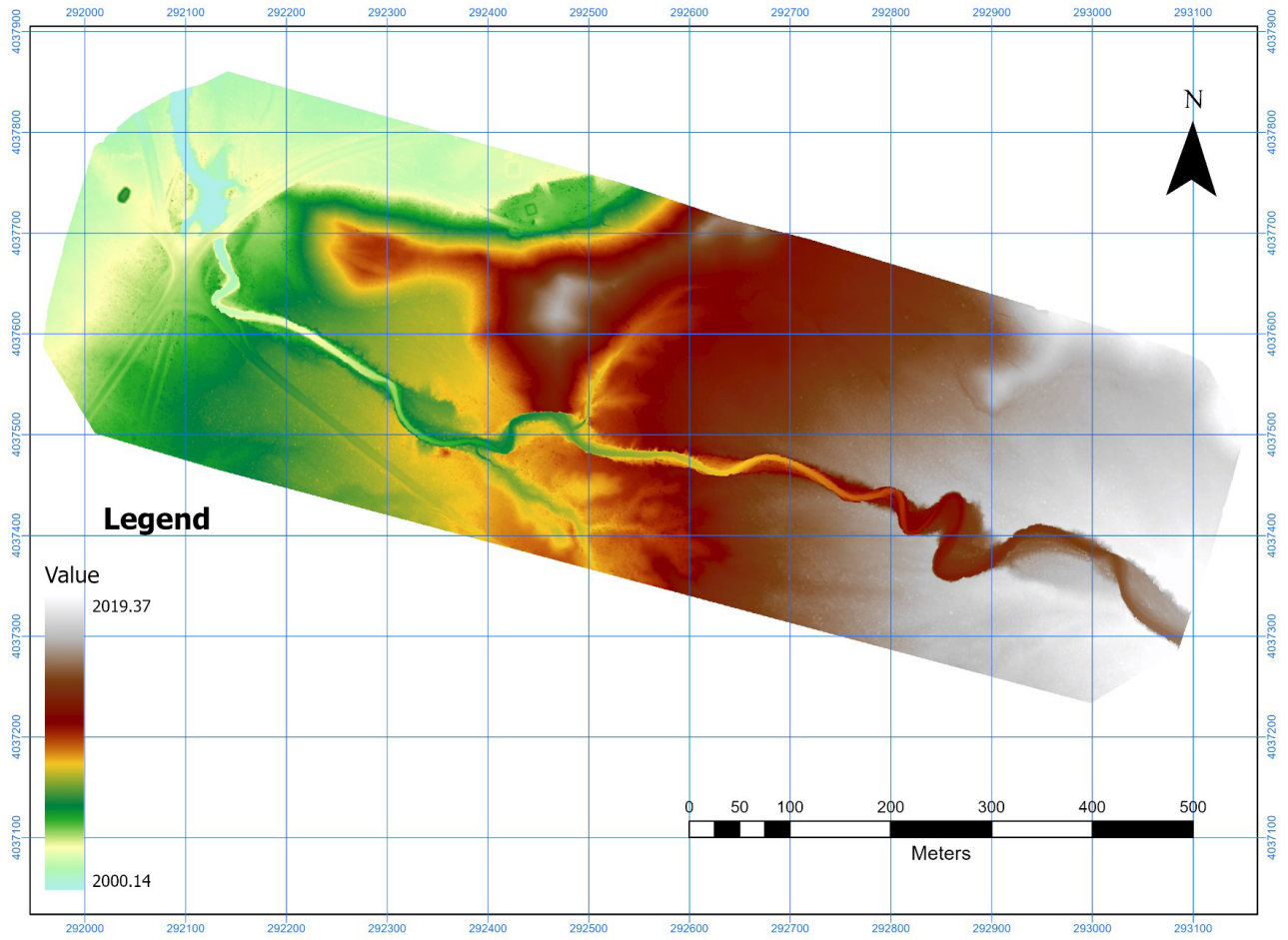
Appendix 1.10. Digital terrain model of Site B, August 2021. Scale units are meters above sea level.
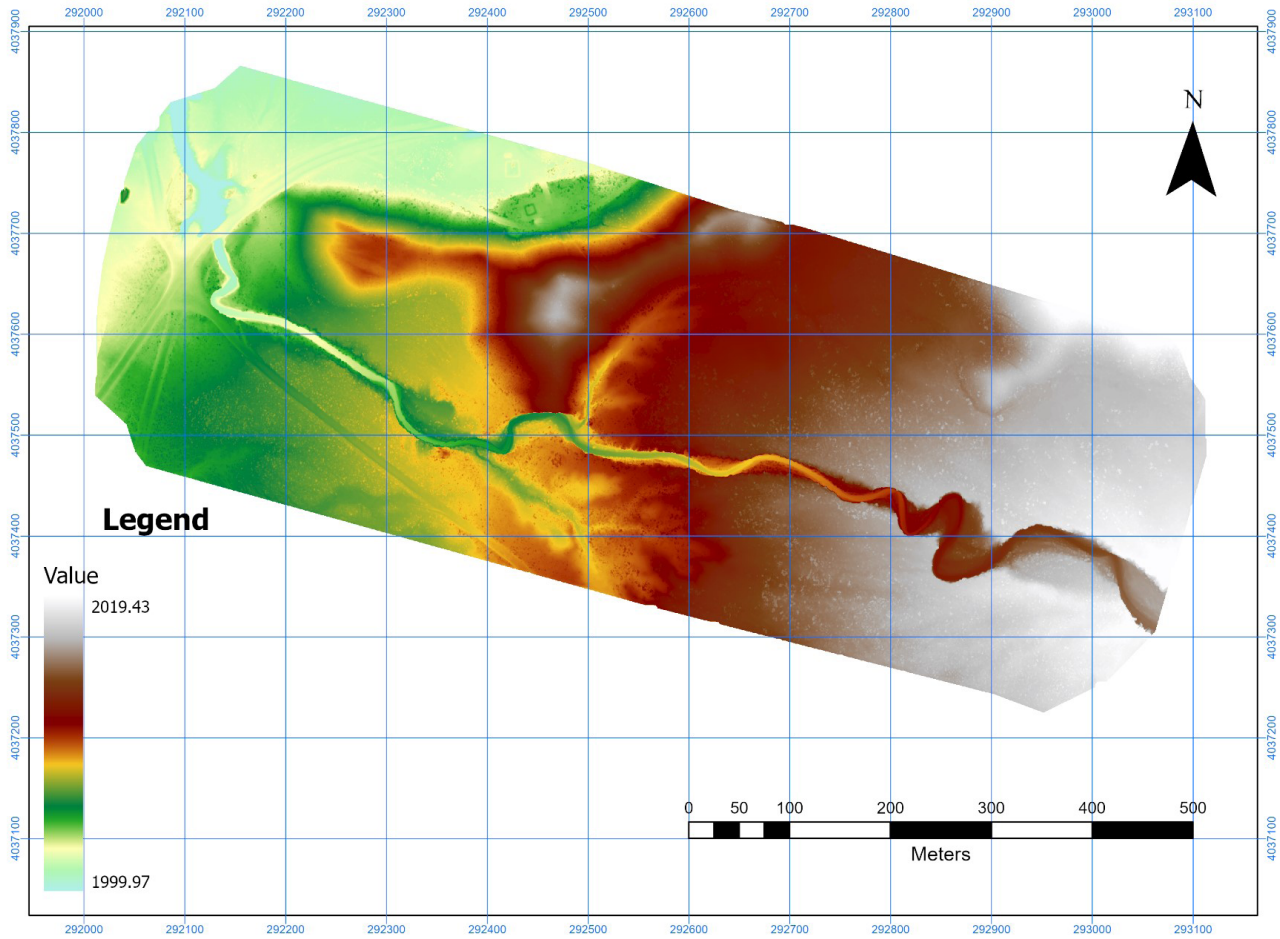
Appendix 1.11. Digital terrain model of Site B, July 2022. Scale units are meters above sea level.
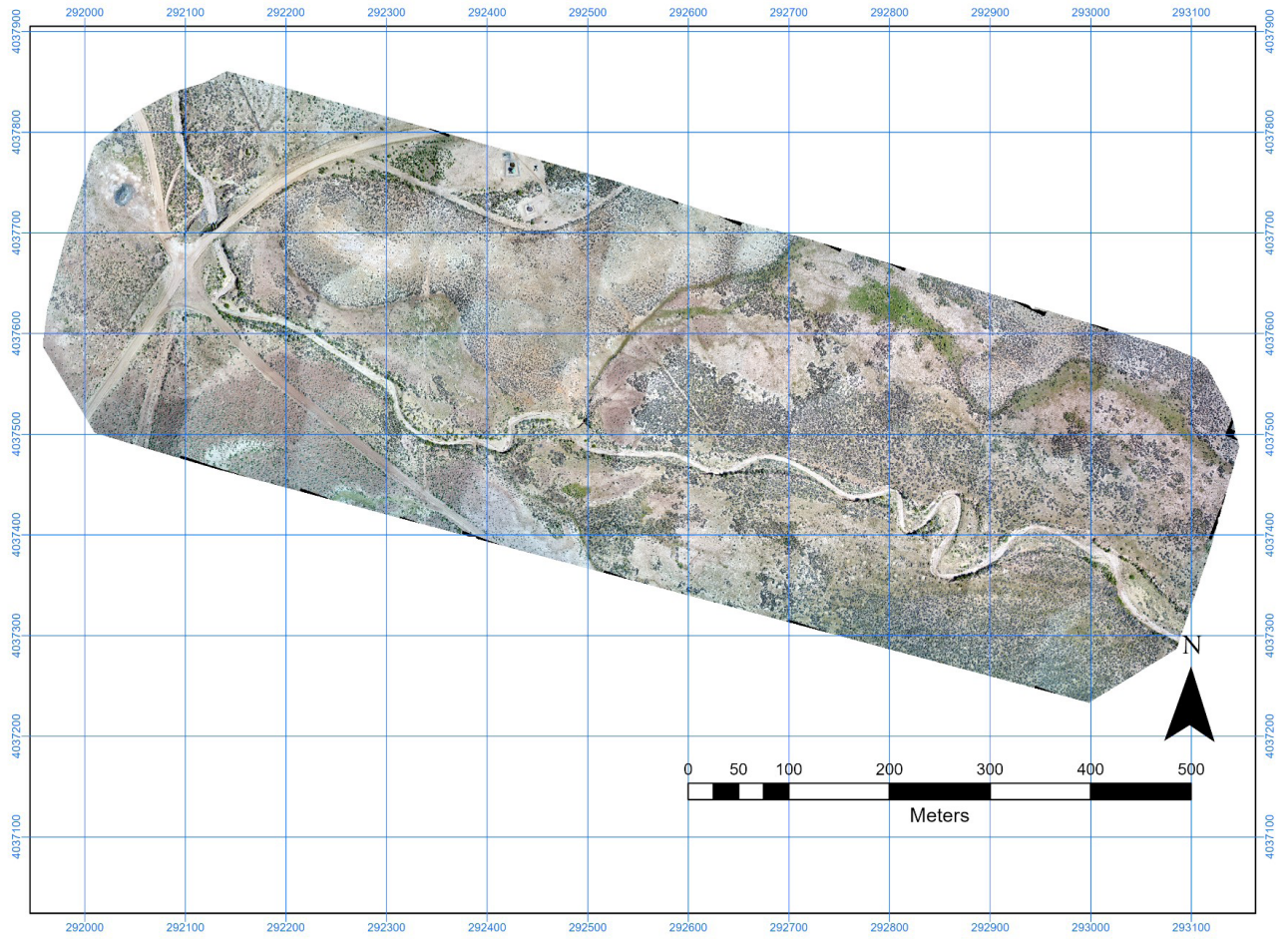
Appendix 1.12. Digital orthomosaic of Site B, August 2021.
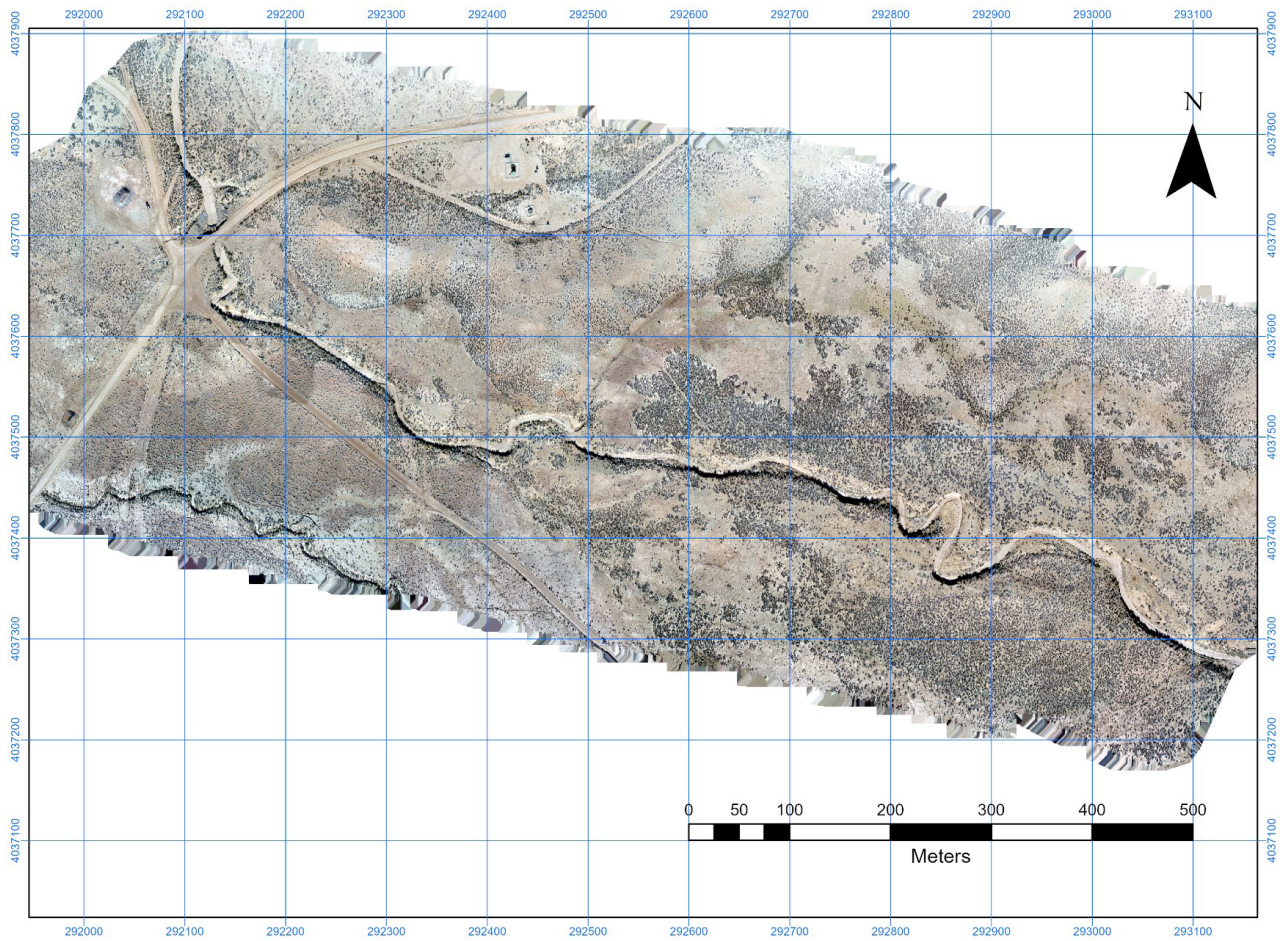
Appendix 1.13. Digital orthomosaic of Site B, November 2021.
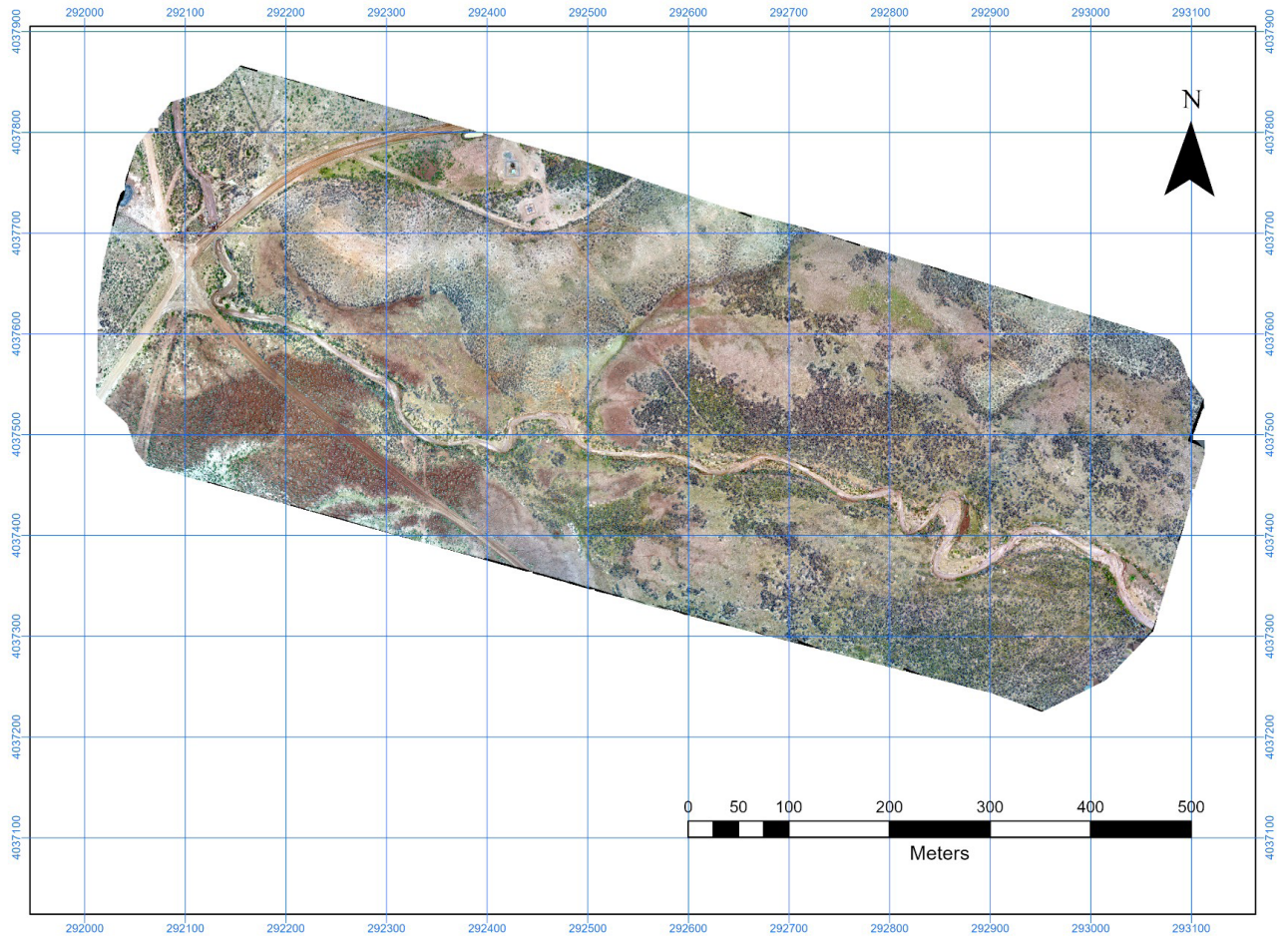
Appendix 1.14. Digital orthomosaic of Site B, July 2022.
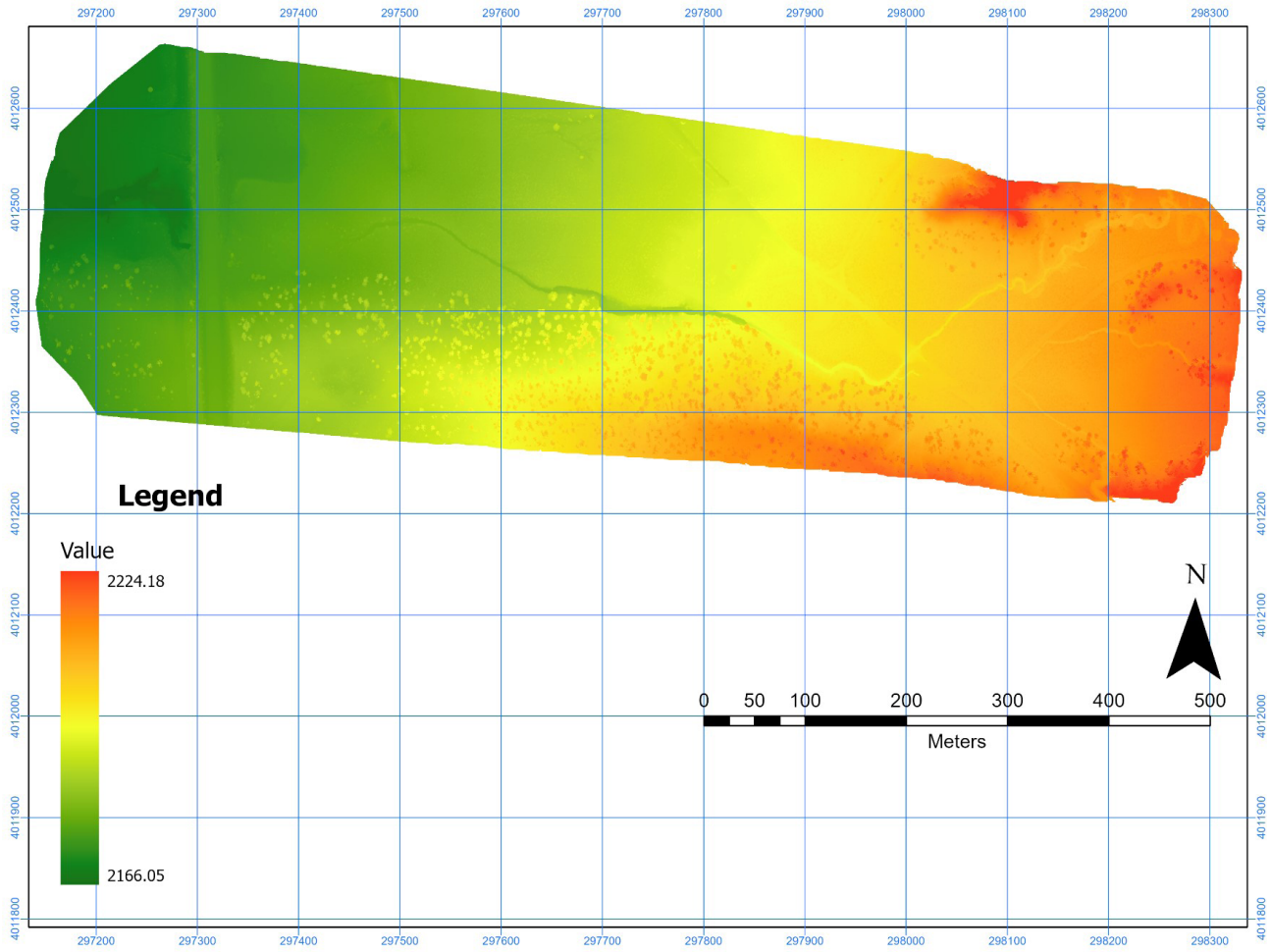
Appendix 1.15. Digital surface model of Site C, August 2021. Scale units are meters above sea level.
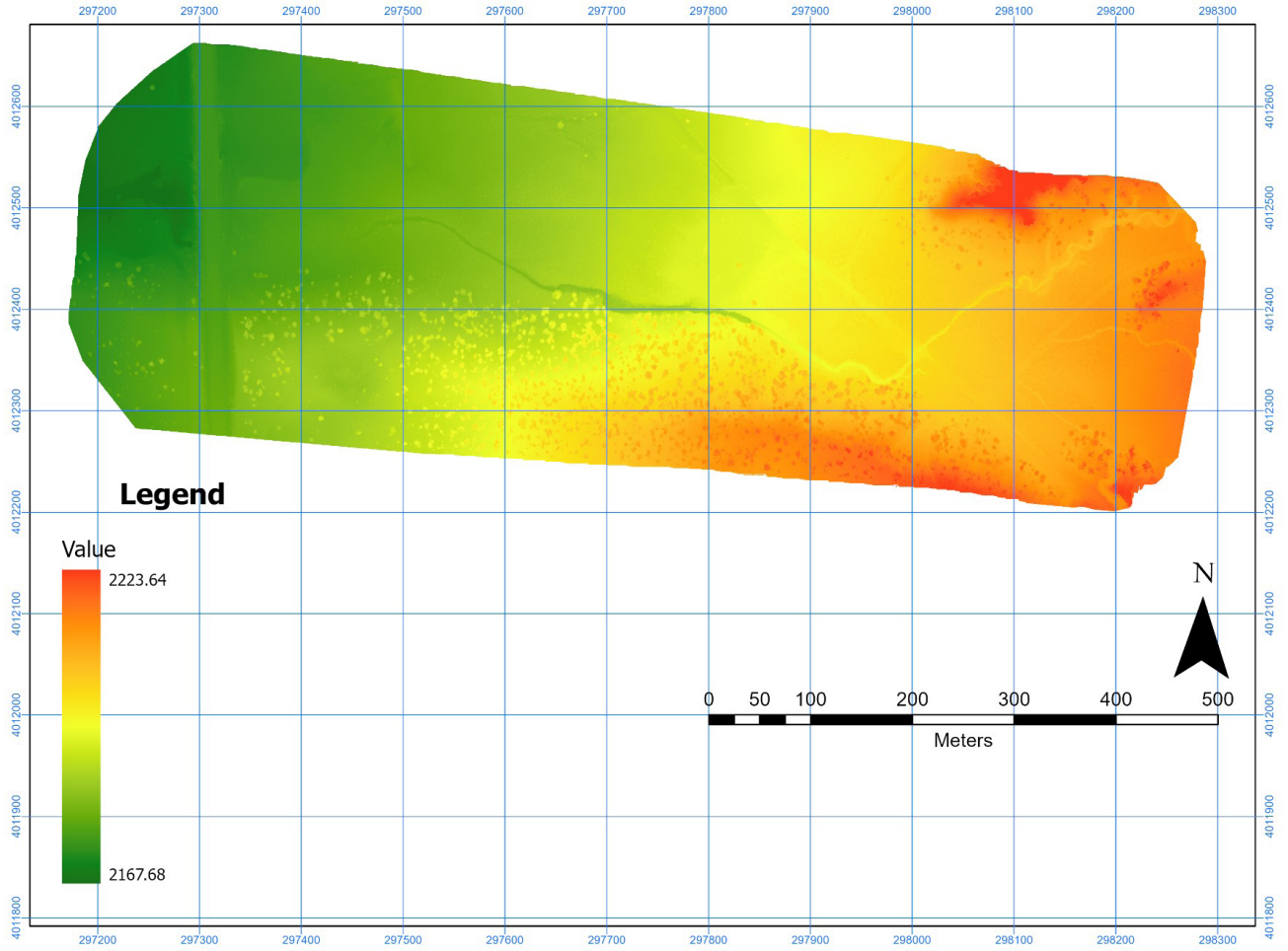
Appendix 1.16. Digital surface model of Site C, July 2022. Scale units are meters above sea level.
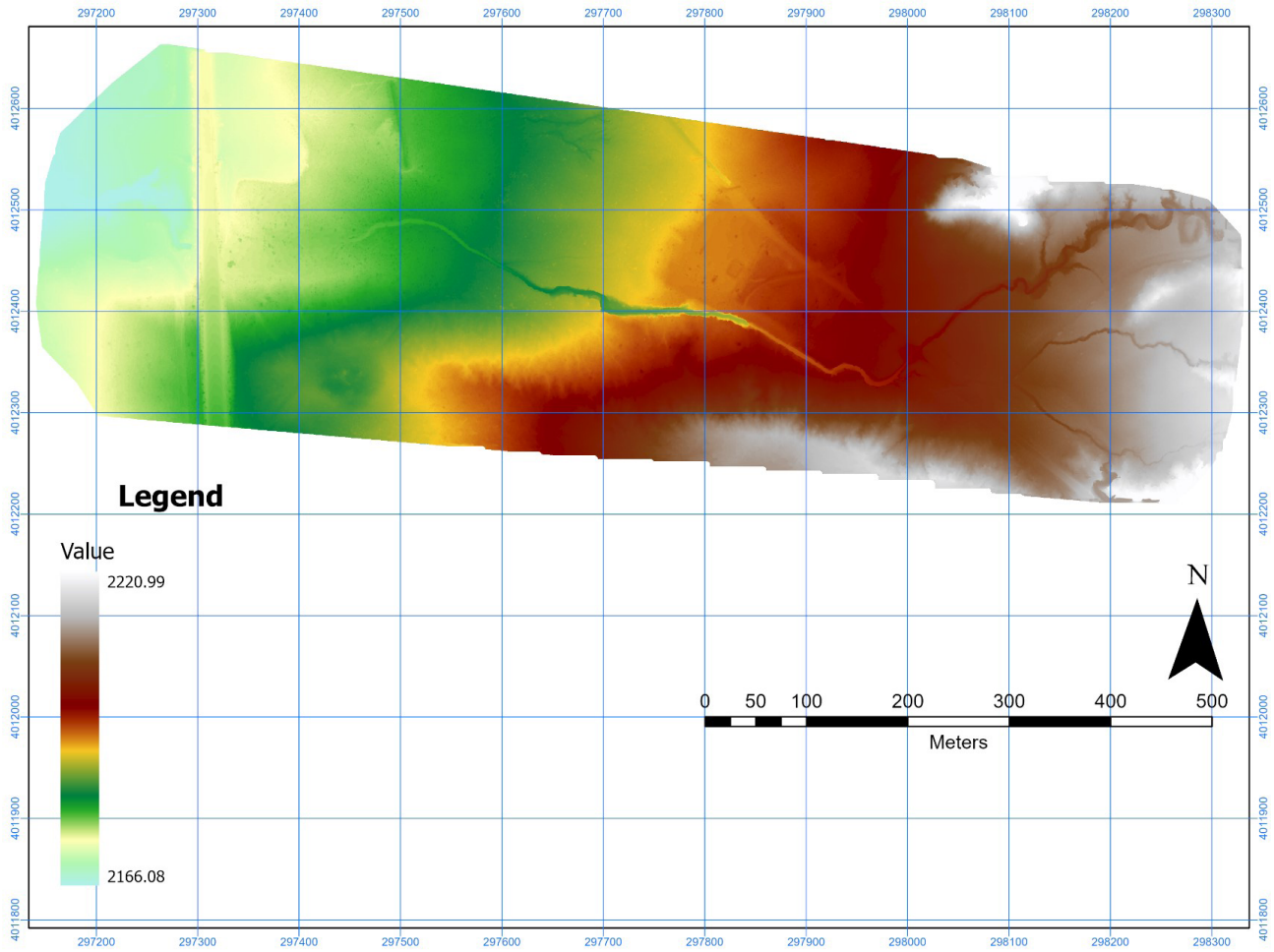
Appendix 1.17. Digital terrain model of Site C, August 2021. Scale units are meters above sea level.
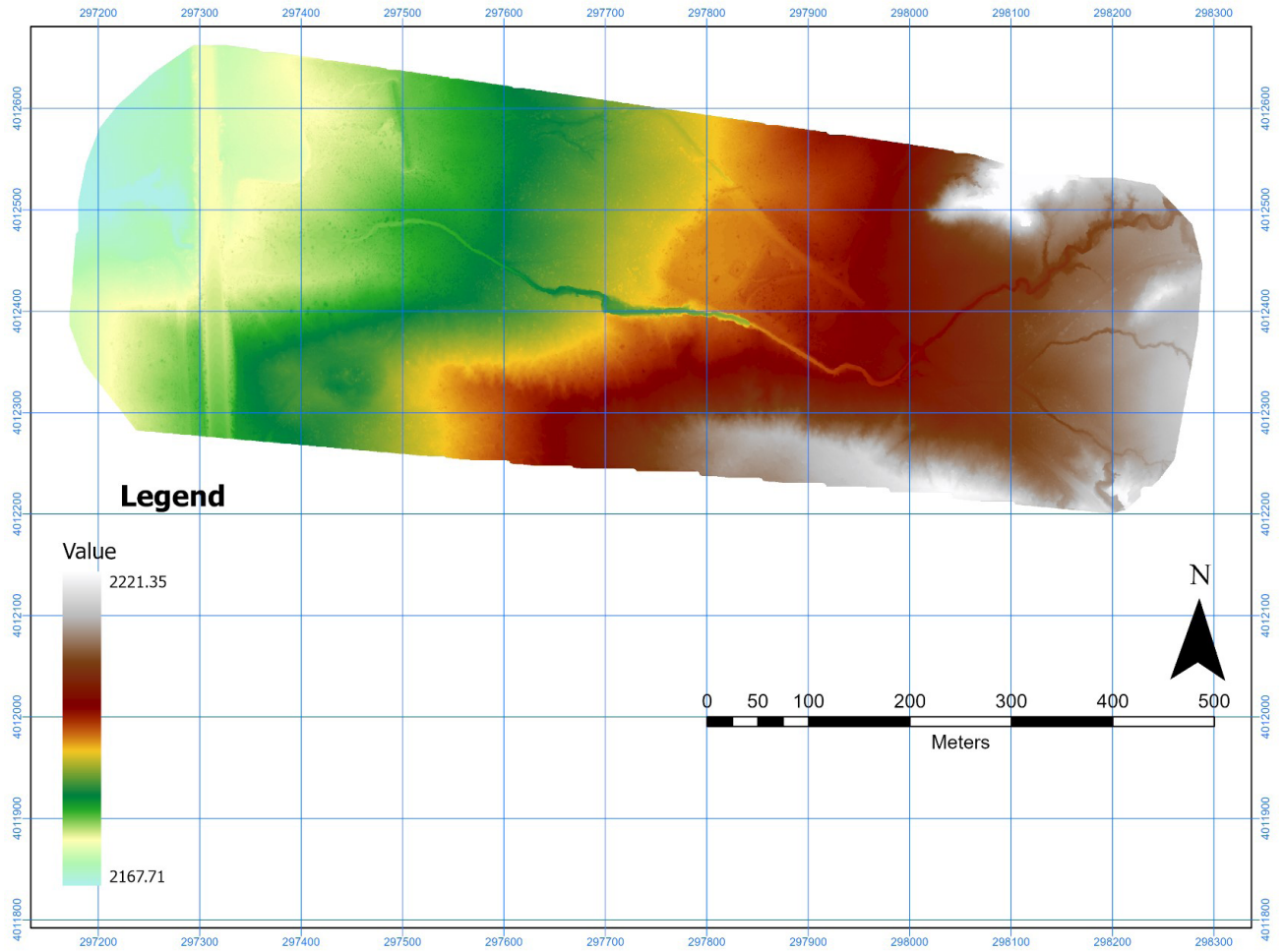
Appendix 1.18. Digital terrain model of Site C, July 2022. Scale units are meters above sea level.
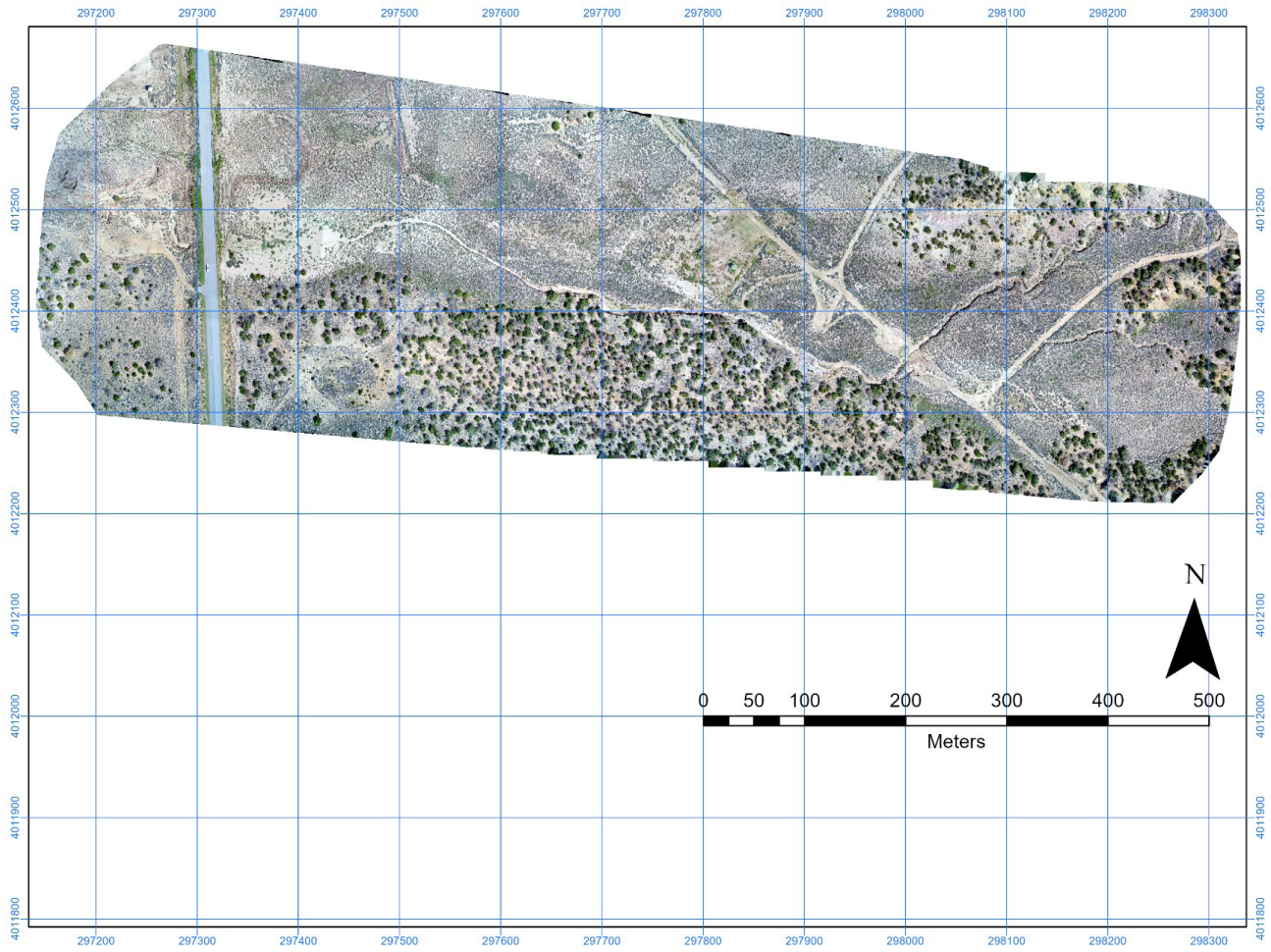
Appendix 1.19. Digital orthomosaic of Site C, August 2021.
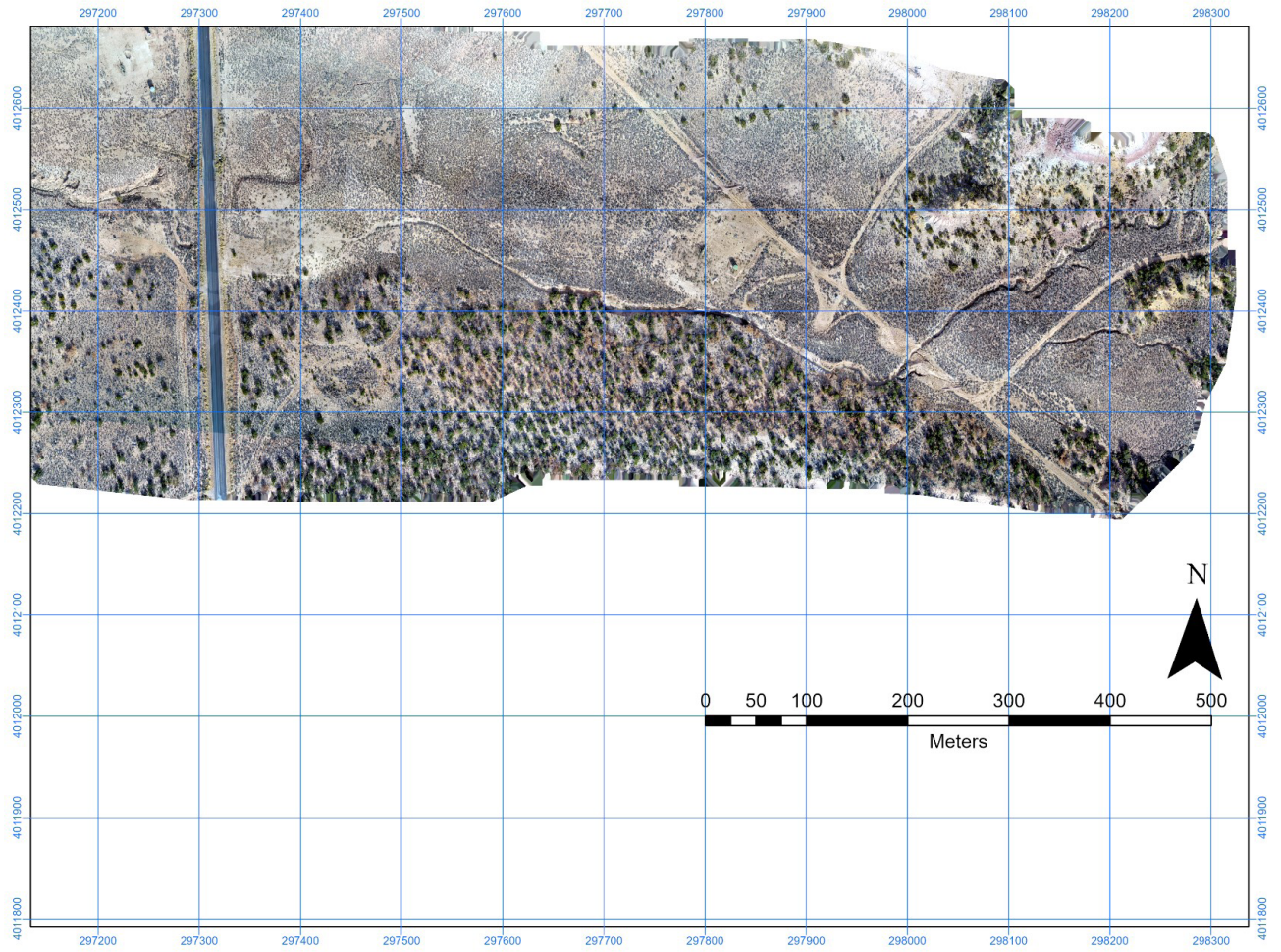
Appendix 1.20. Digital orthomosaic of Site C, November 2021.
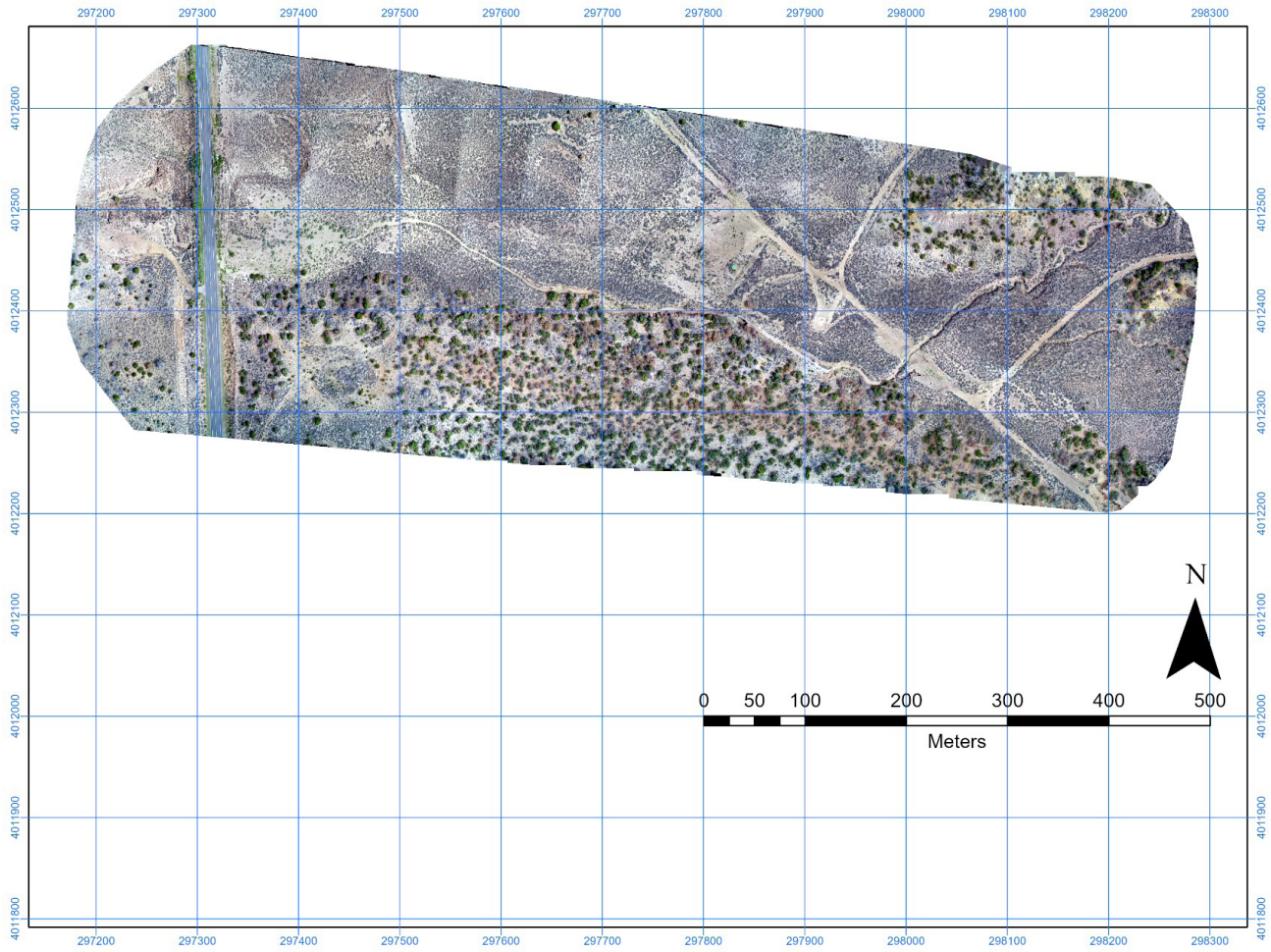
Appendix 1.21. Digital orthomosaic of Site C, July 2022.

APPENDIX 2.

2A: DERIVED MAPS FOR SITE A

Appendix 2A.1. Site A Google Earth overlay.
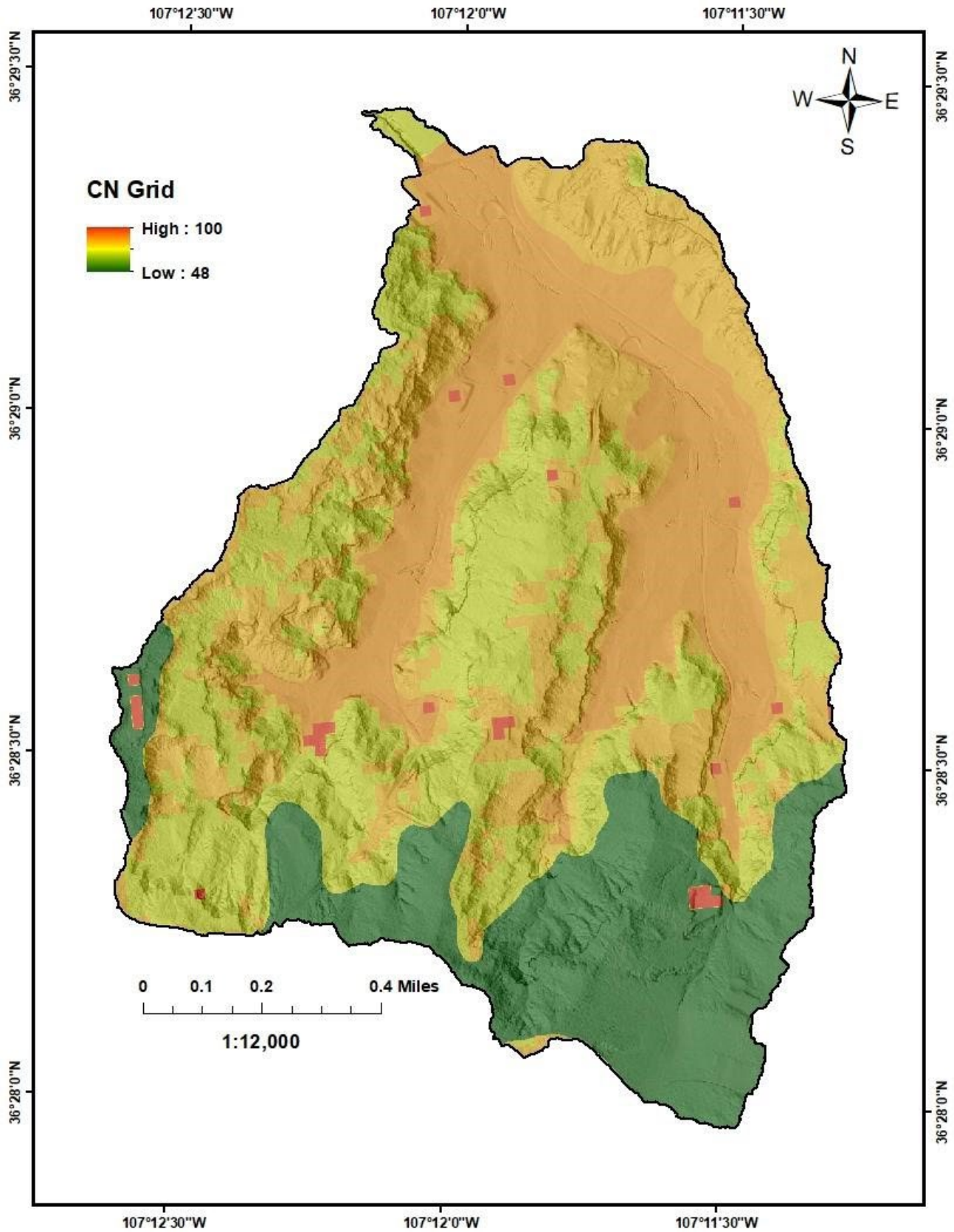
Appendix 2A.2. Site A curve number.
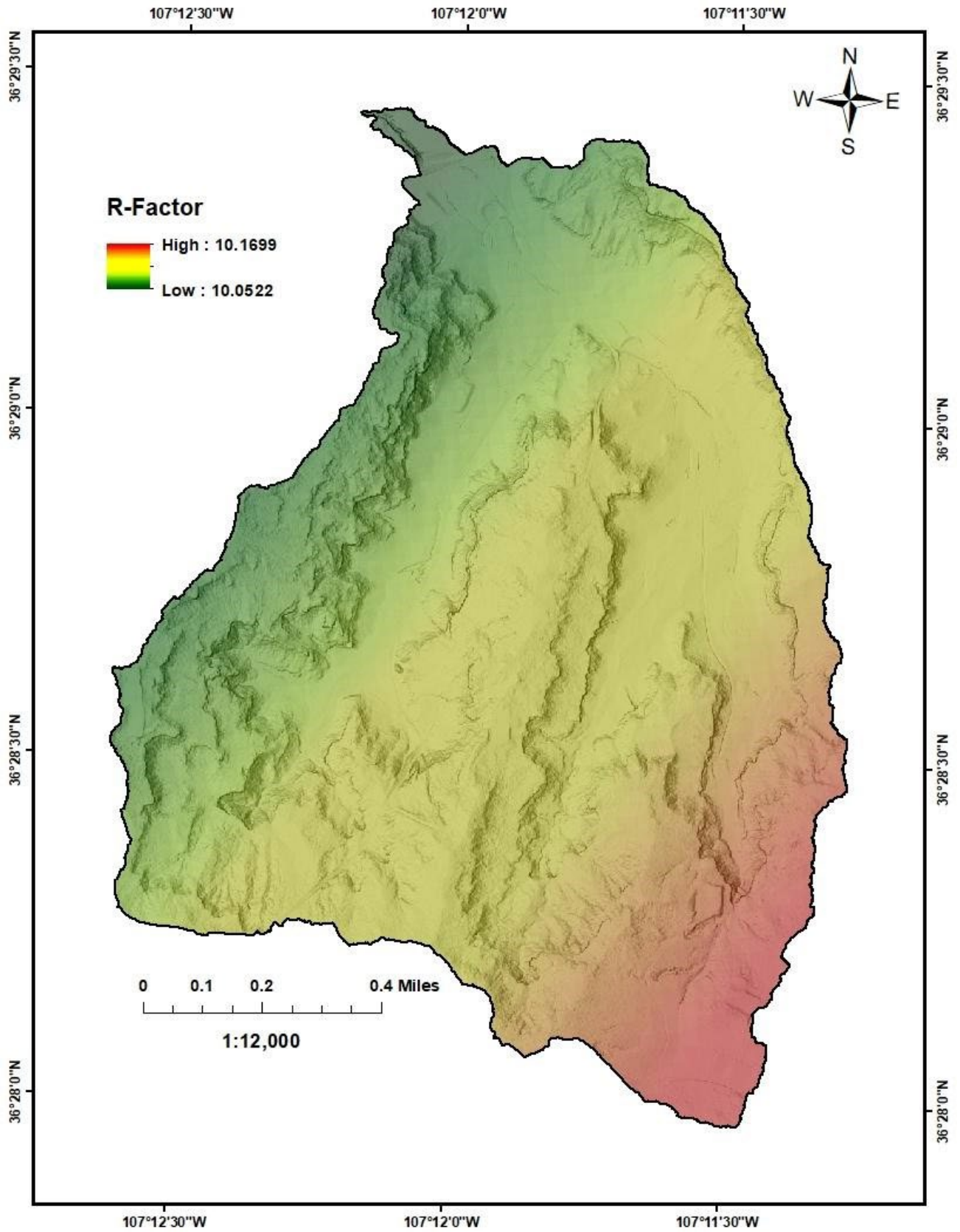
Appendix 2A.3. Site A rainfall erosivity R-factor.
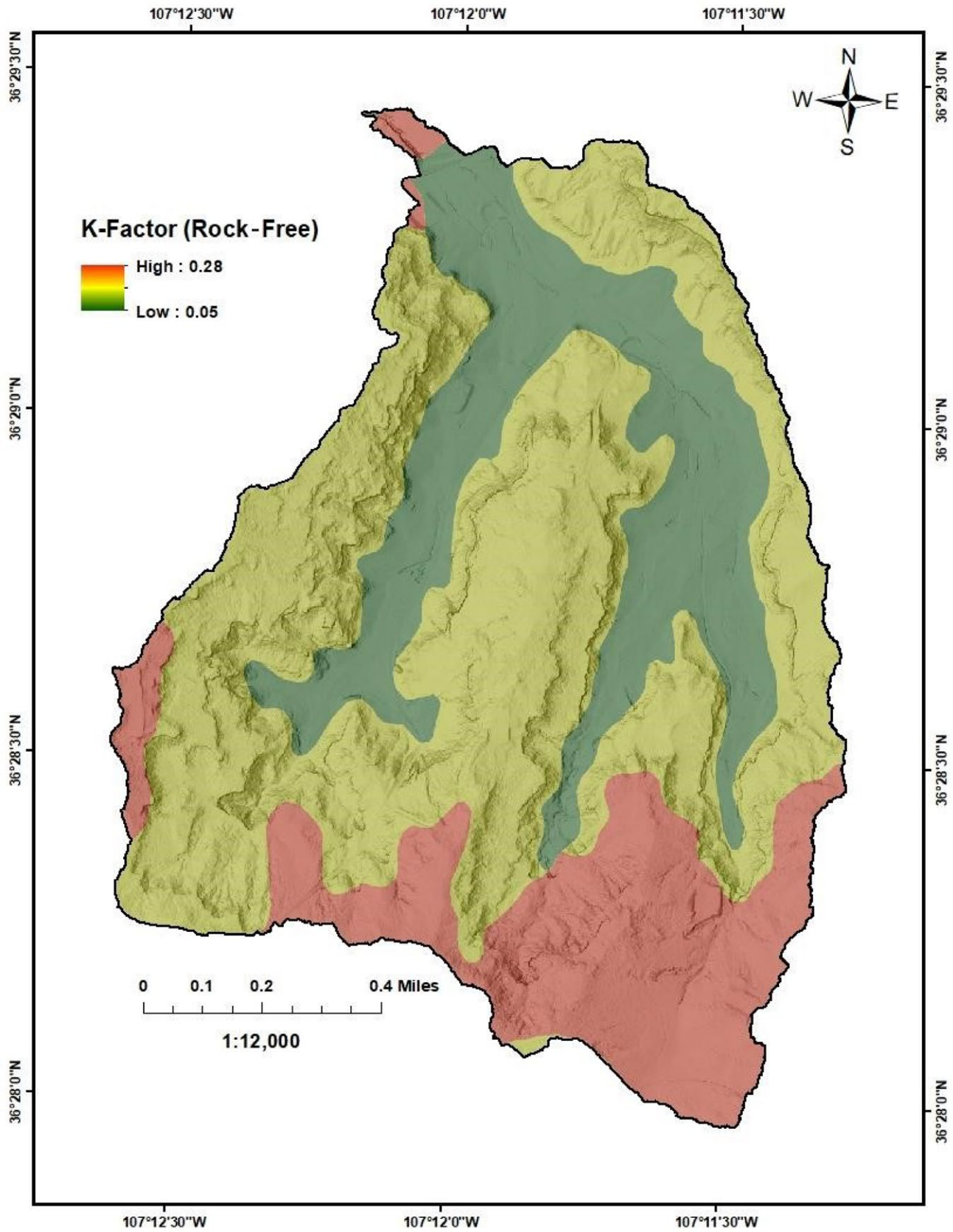
Appendix 2A.4. Site A soil erodibility K-factor.
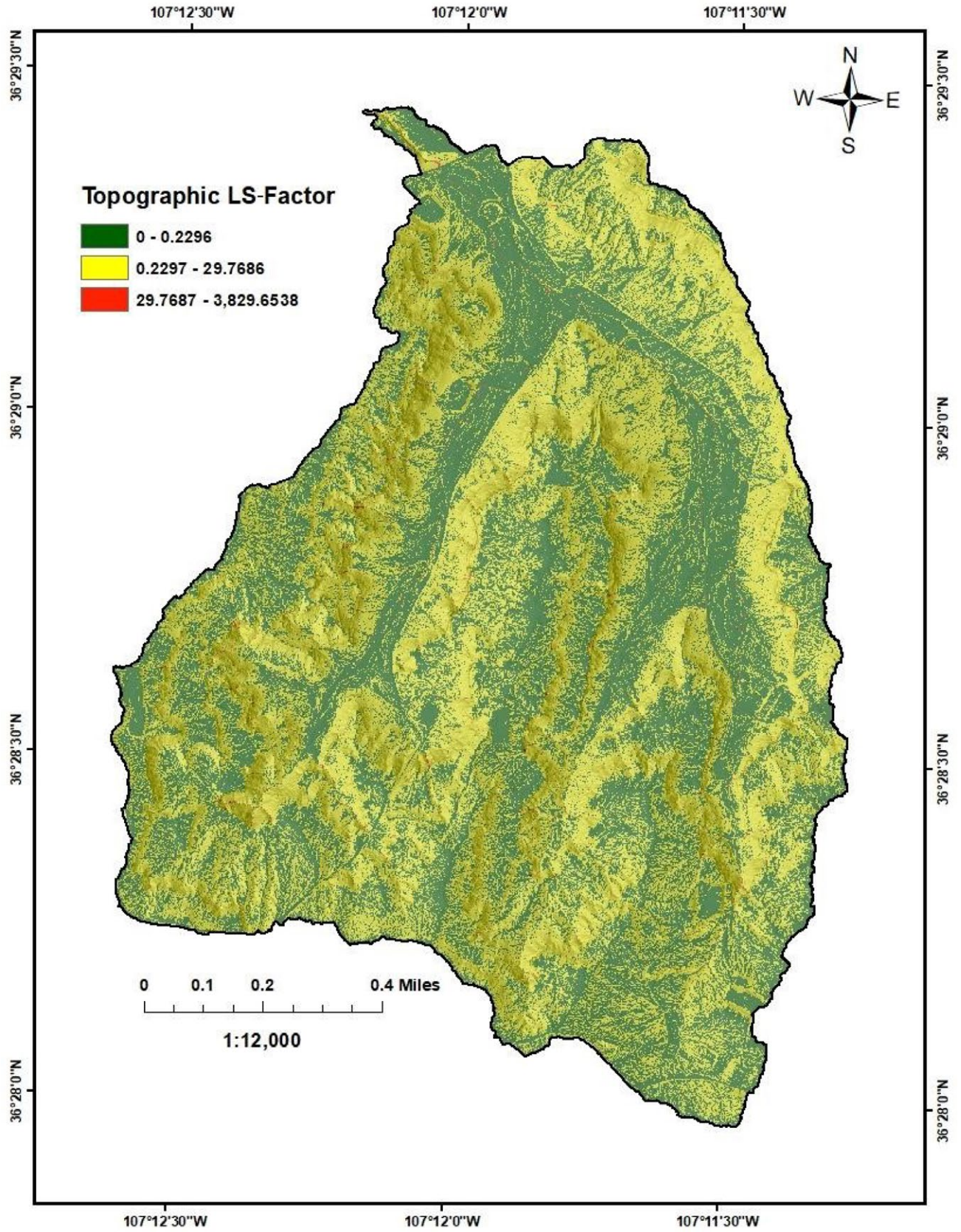
Appendix 2A.5. Site A topographic LS-factor.
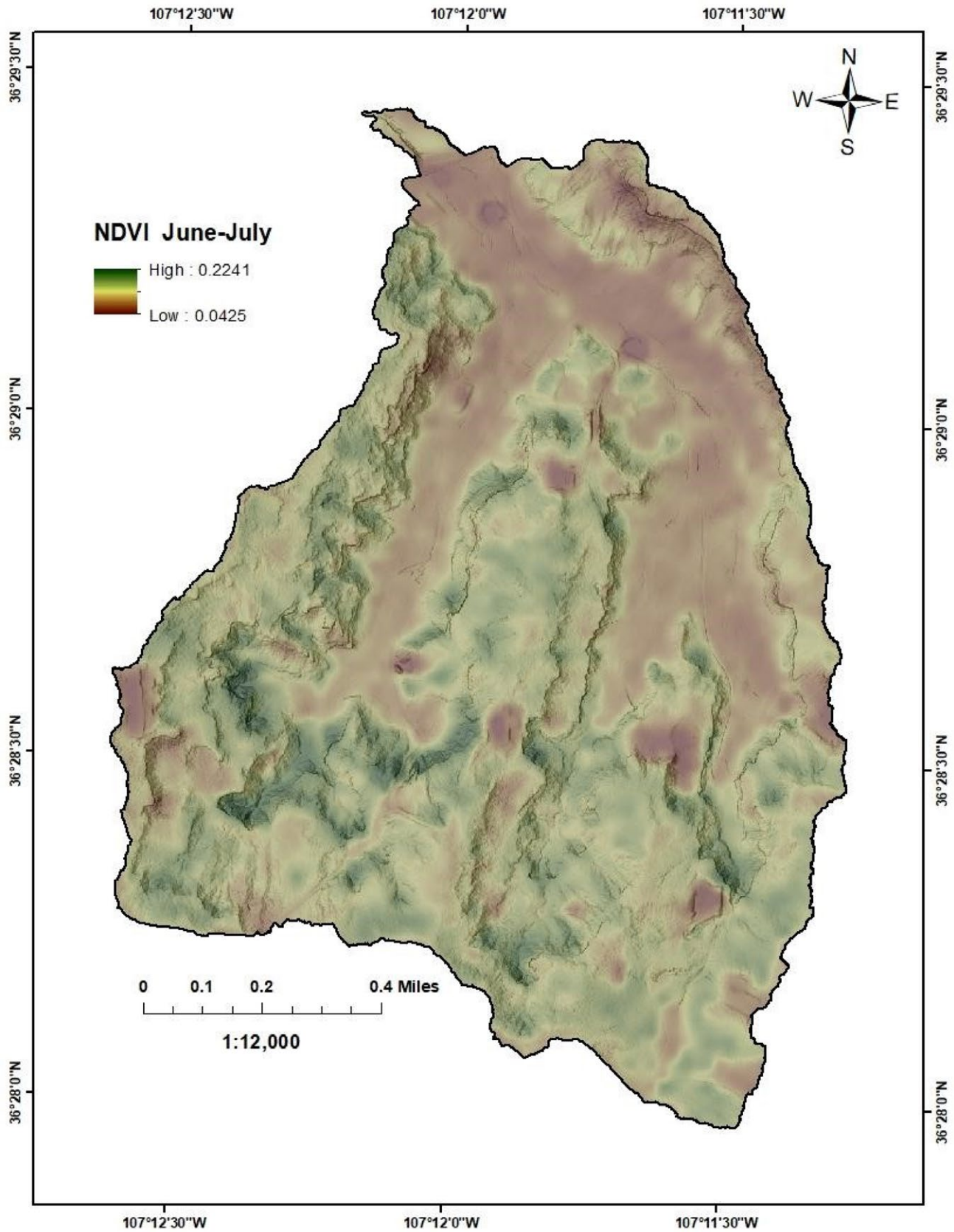
Appendix 2A.6. Site A normalized difference vegetation index.
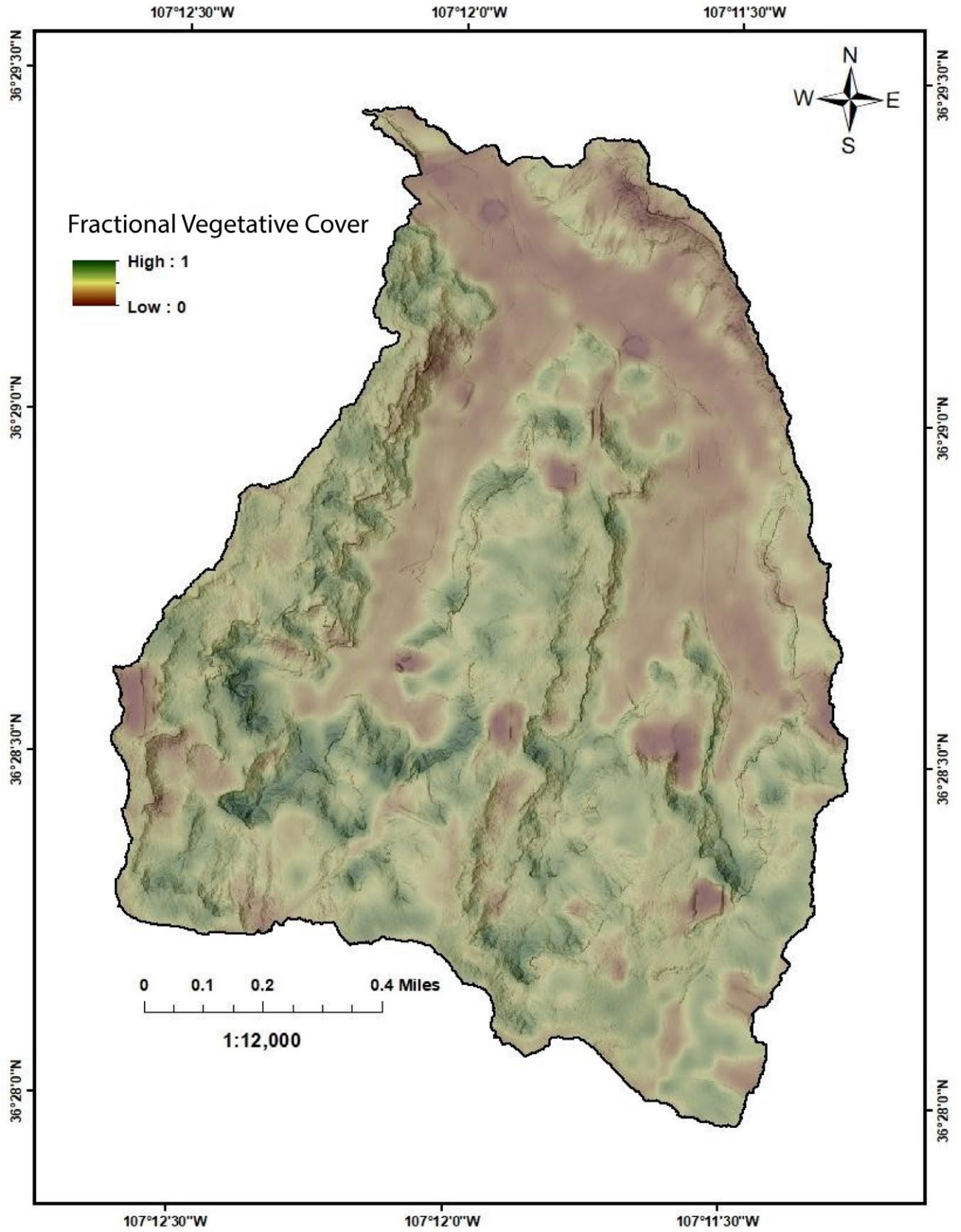
Appendix 2A.7. Site A fractional vegetative cover.
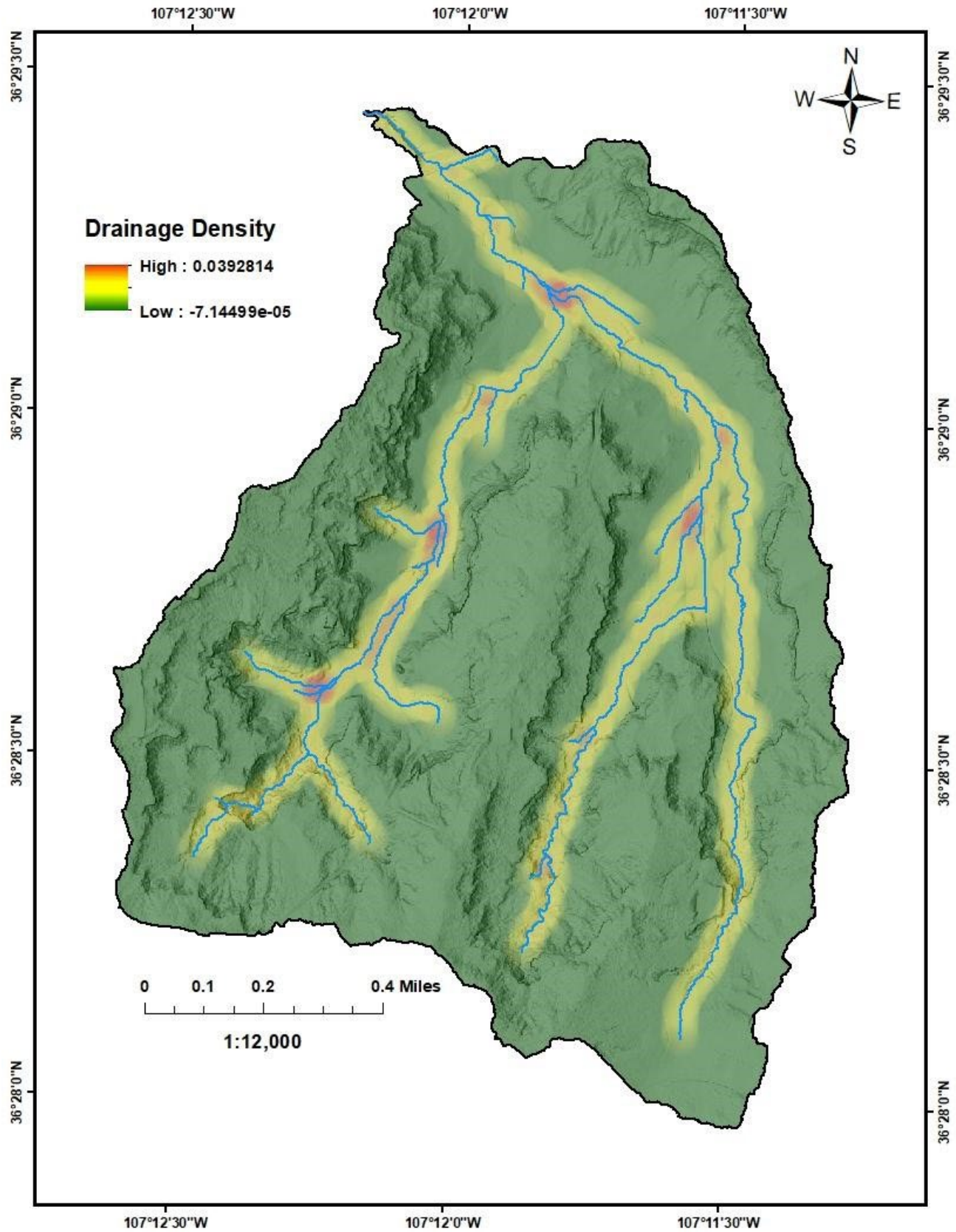
**Appendix 2A.8.** Site A drainage density.
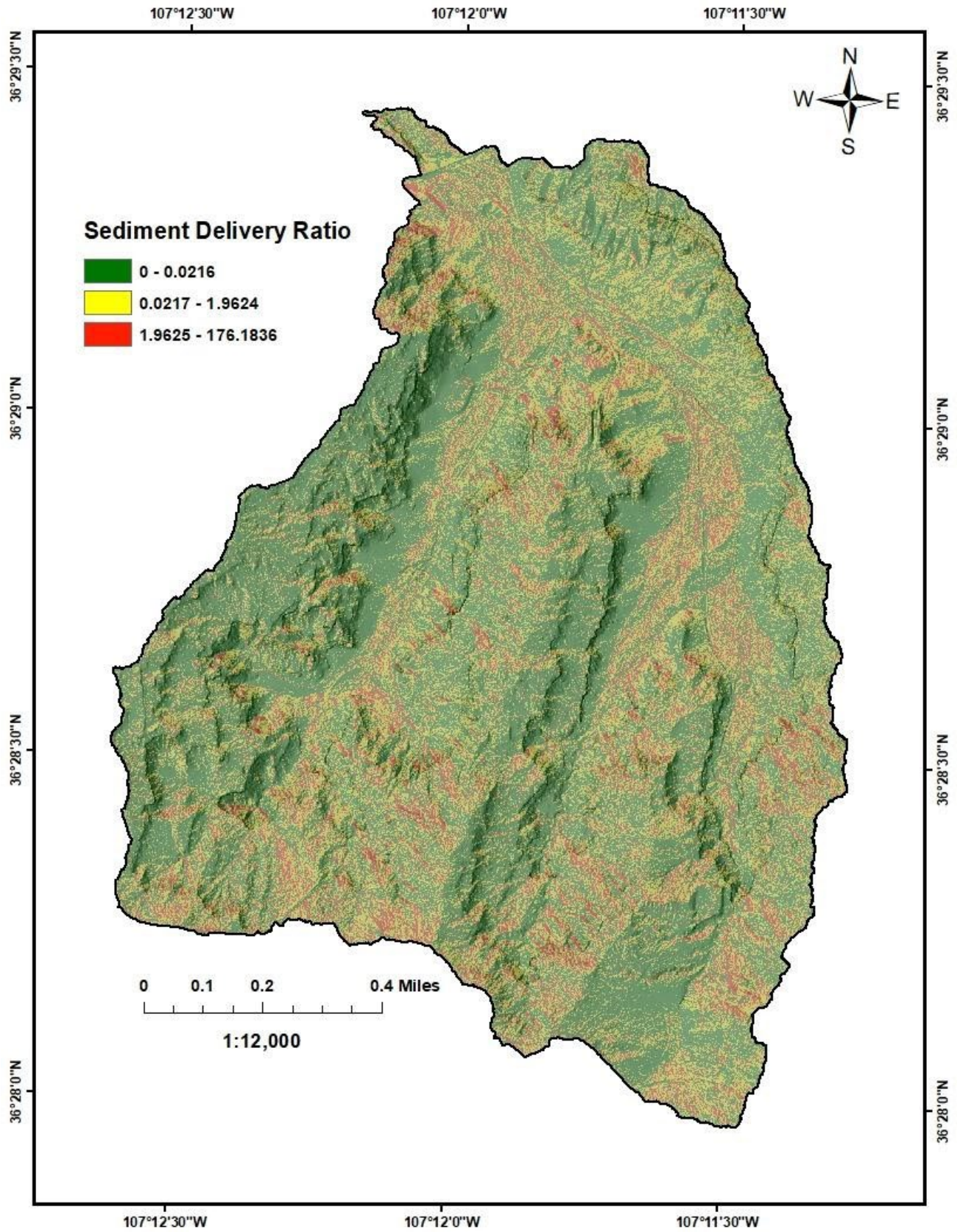
Appendix 2A.9. Site A sediment delivery ratio.
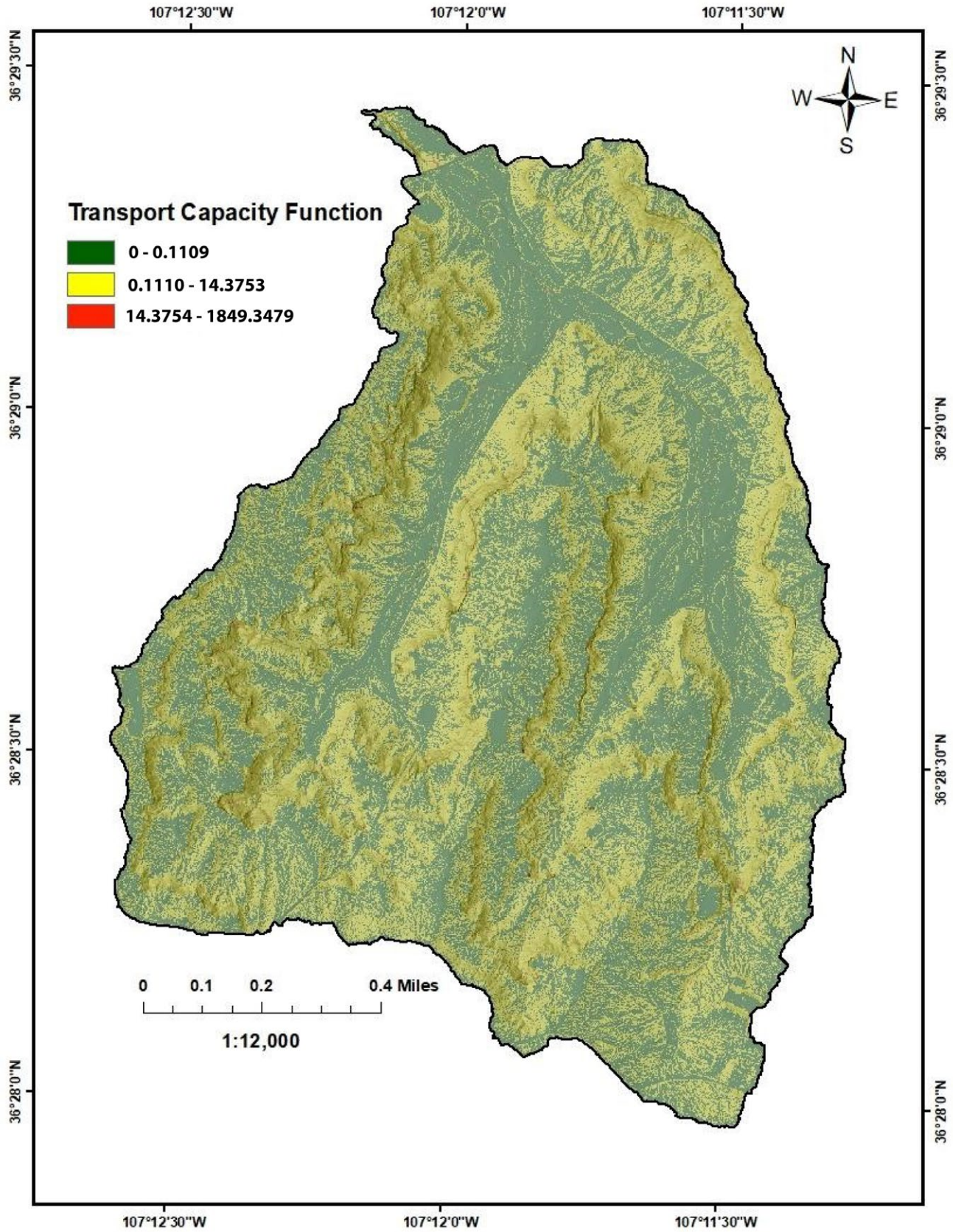
Appendix 2A.10. Site A sediment transport capacity.
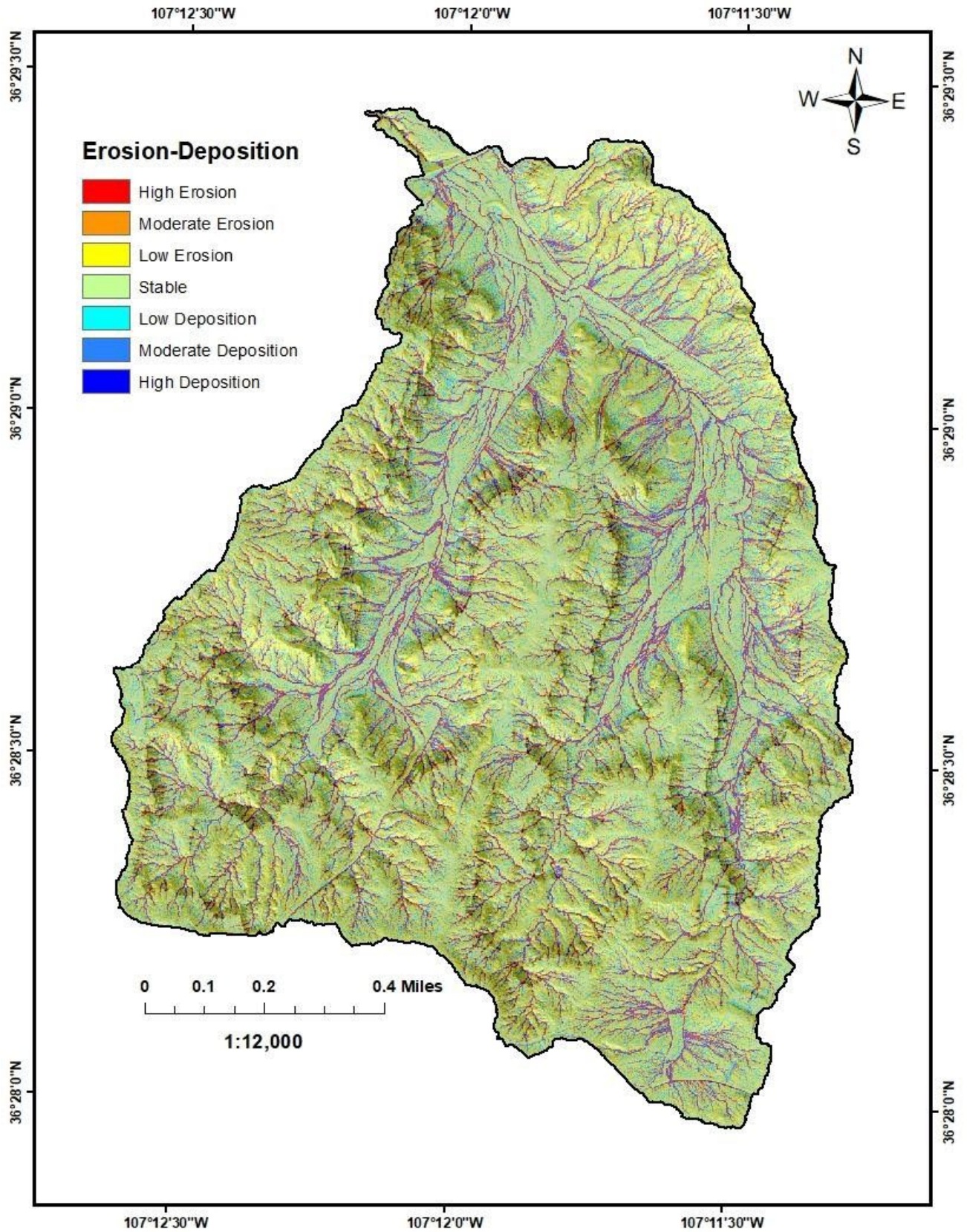
Appendix 2A.11. Site A sediment transport divergence.

Slope - Percent Rise

- 0.0086 - 7.4308
- 7.4309 - 8.4116
- 8.4117 - 15.8338
- 15.8339 - 71.9947
- 71.9948 - 496.9473
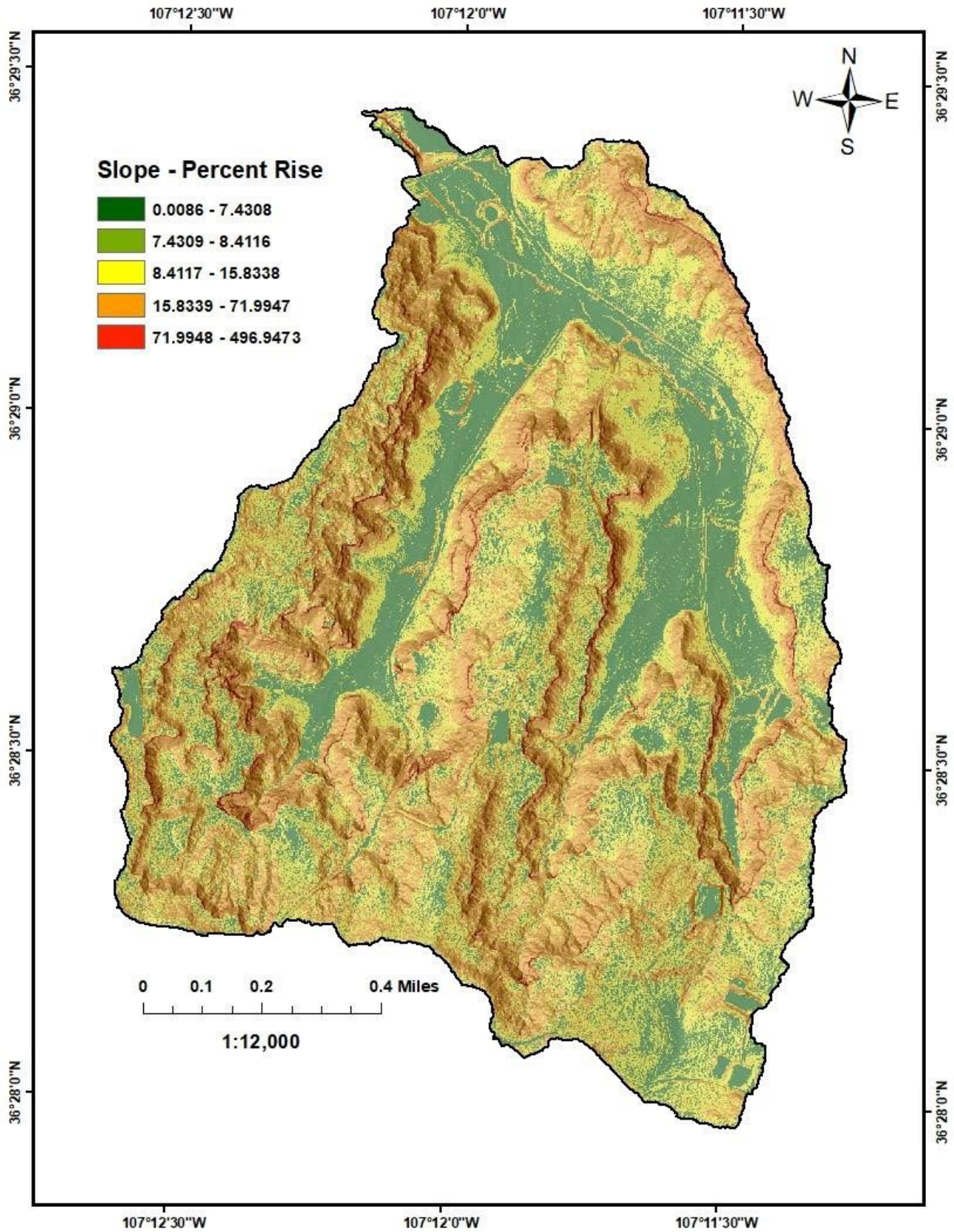
Appendix 2A.12. Site A slope as percent rise.
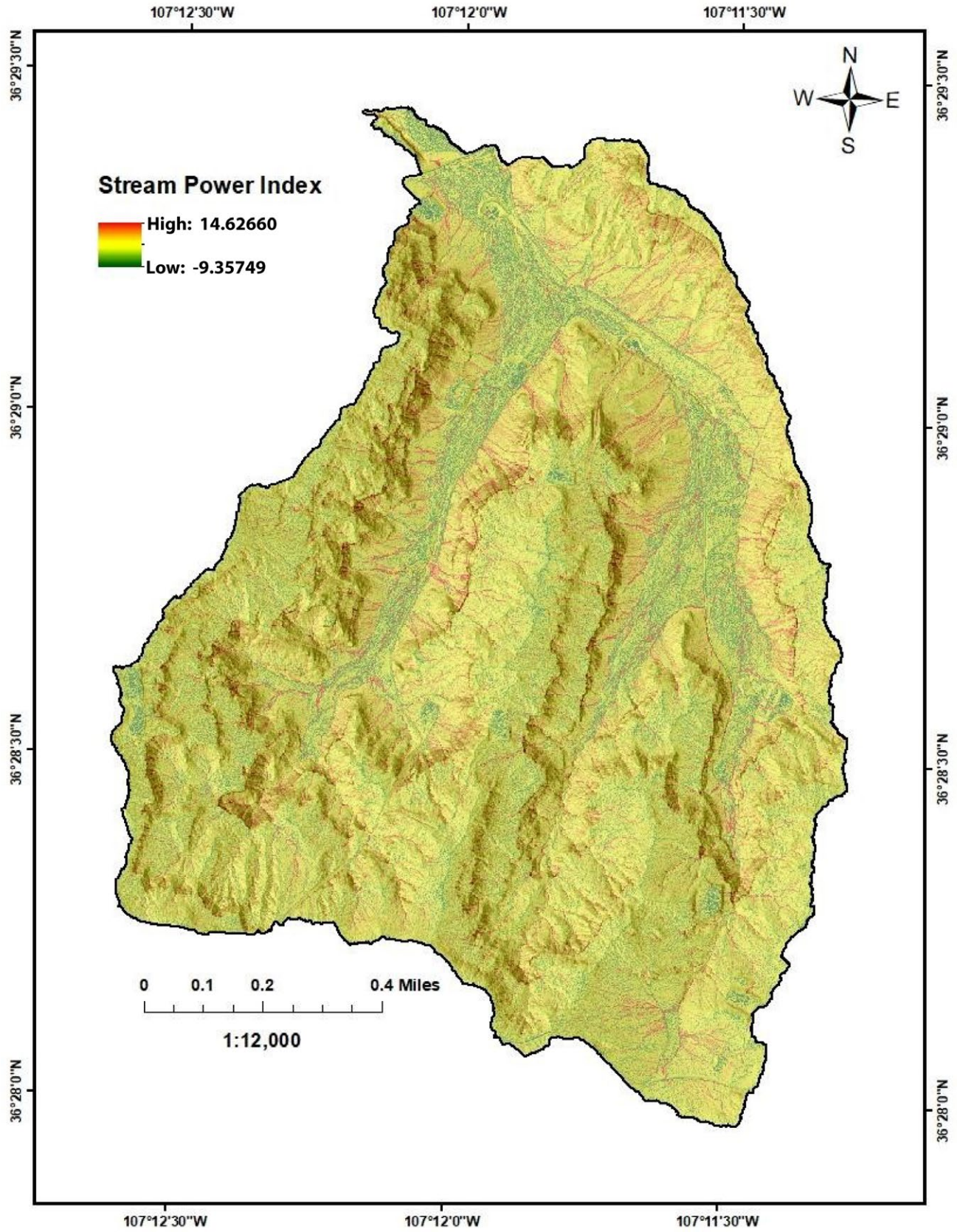
Appendix 2A.13. Site A stream power index.

2B: DERIVED MAPS FOR SITE B

Appendix 2B.1. Site B Google Earth overlay.
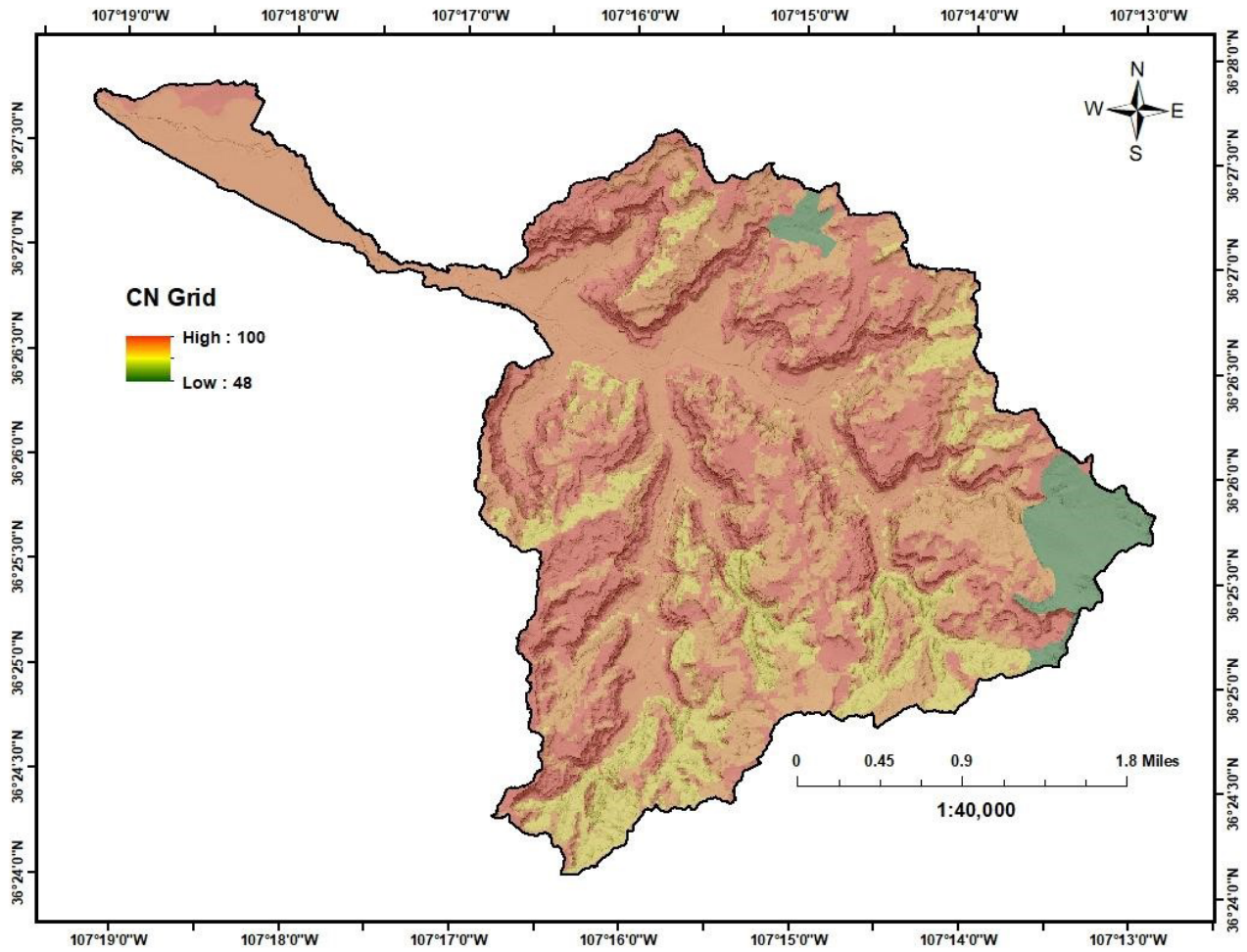
Appendix 2B.2. Site B curve number.
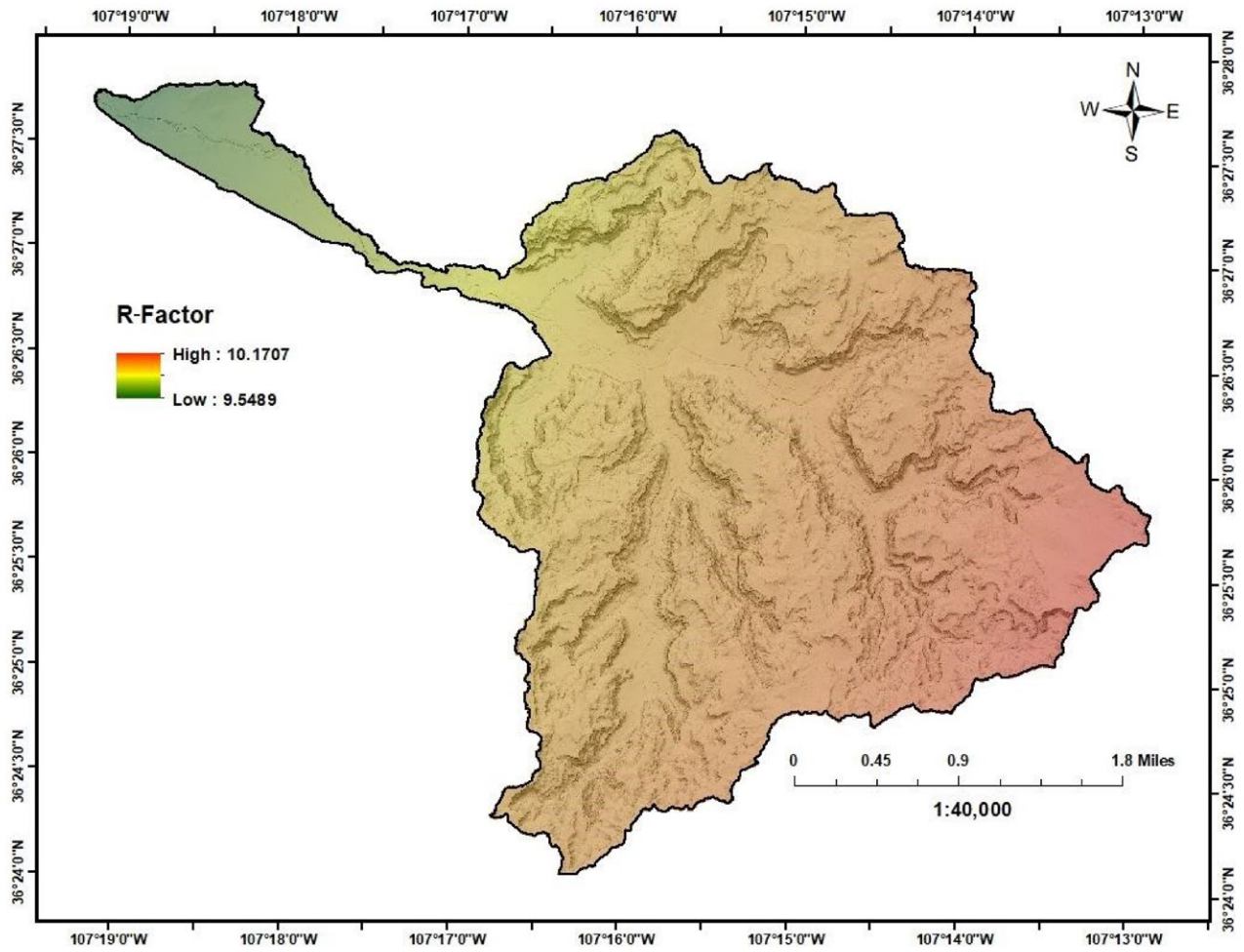
Appendix 2B.3. Site B rainfall erosivity R-factor.
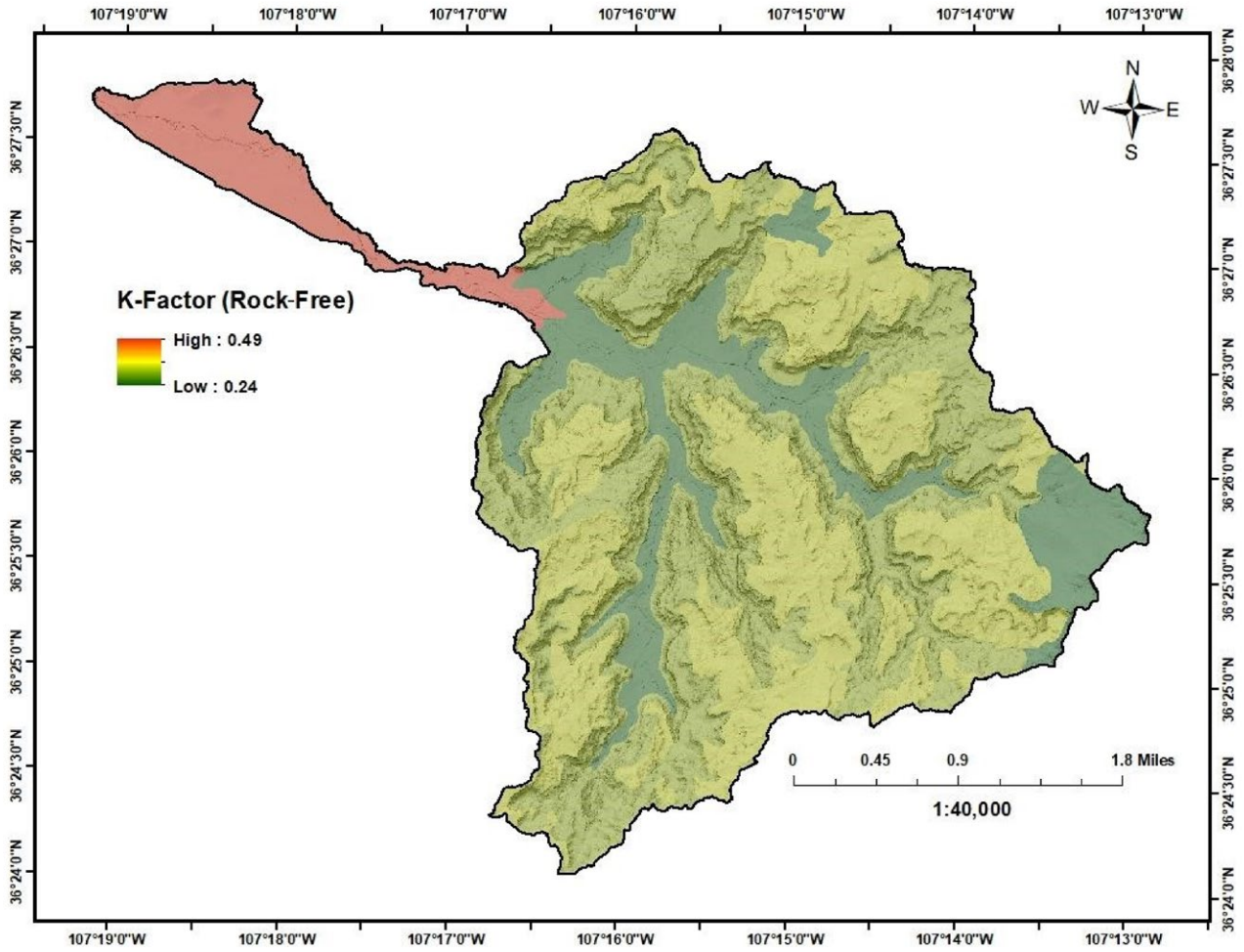
Appendix 2B.4. Site B soil erodibility K-factor.
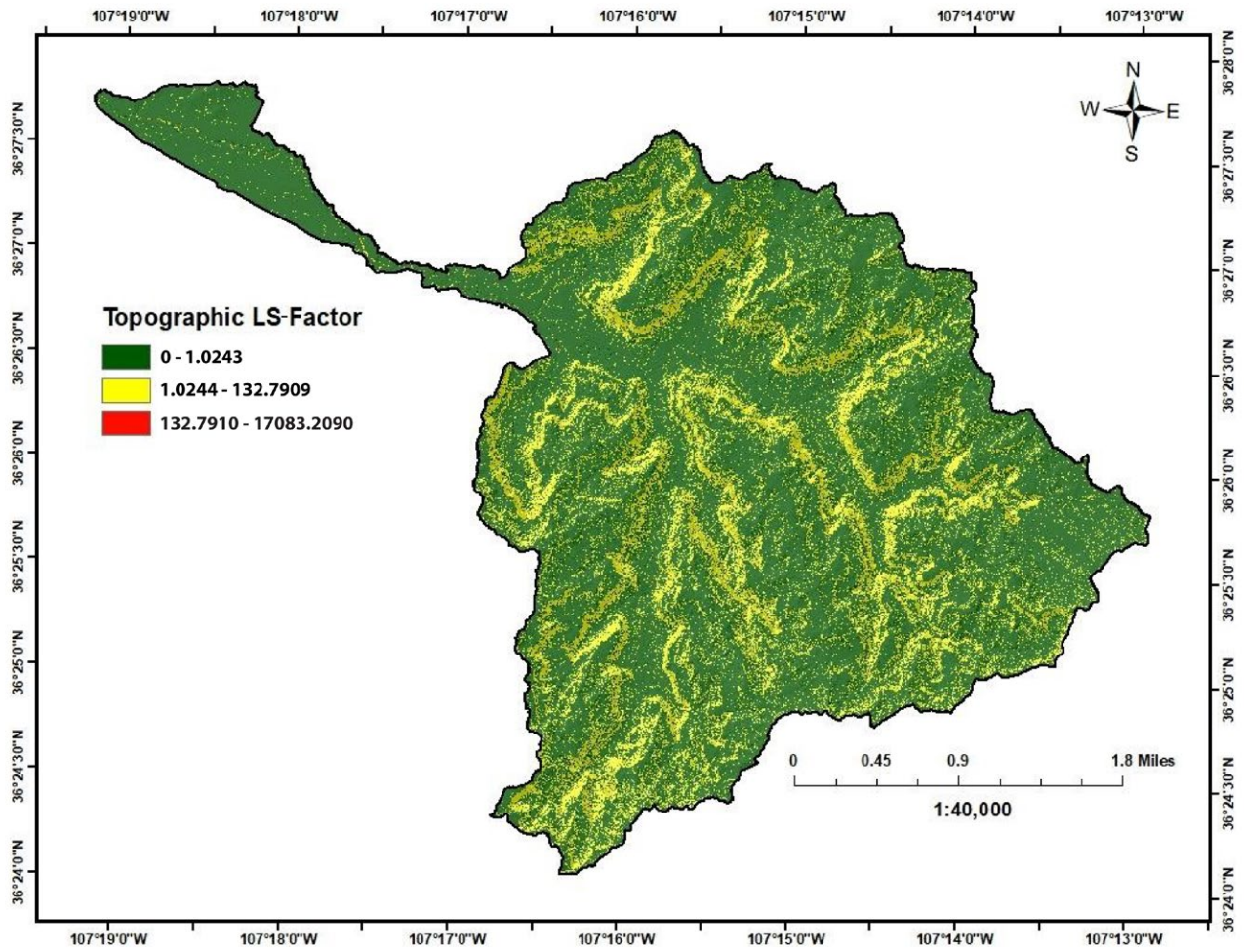
Appendix 2B.5. Site B topographic LS-factor.
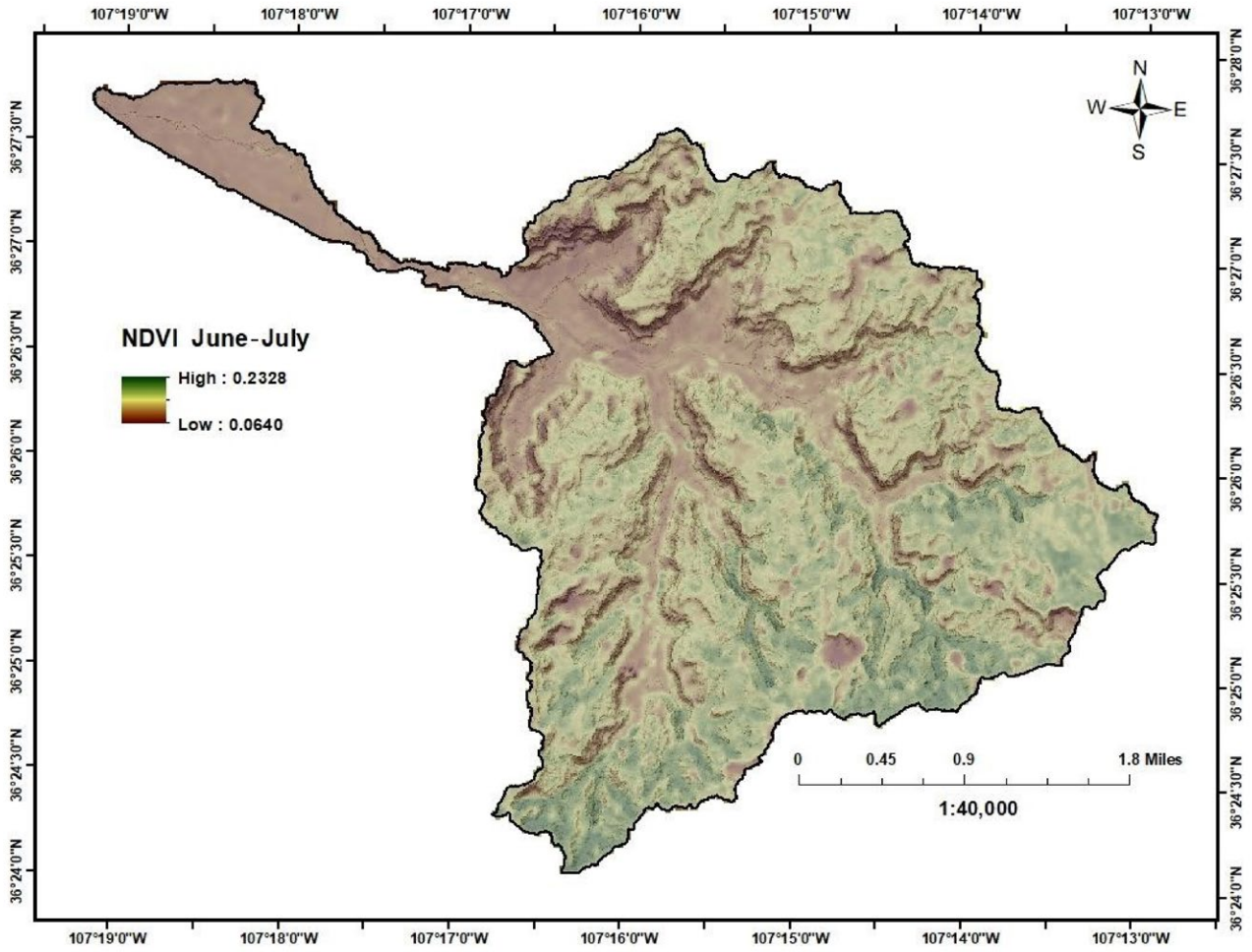
Appendix 2B.6. Site B normalized difference vegetation index.
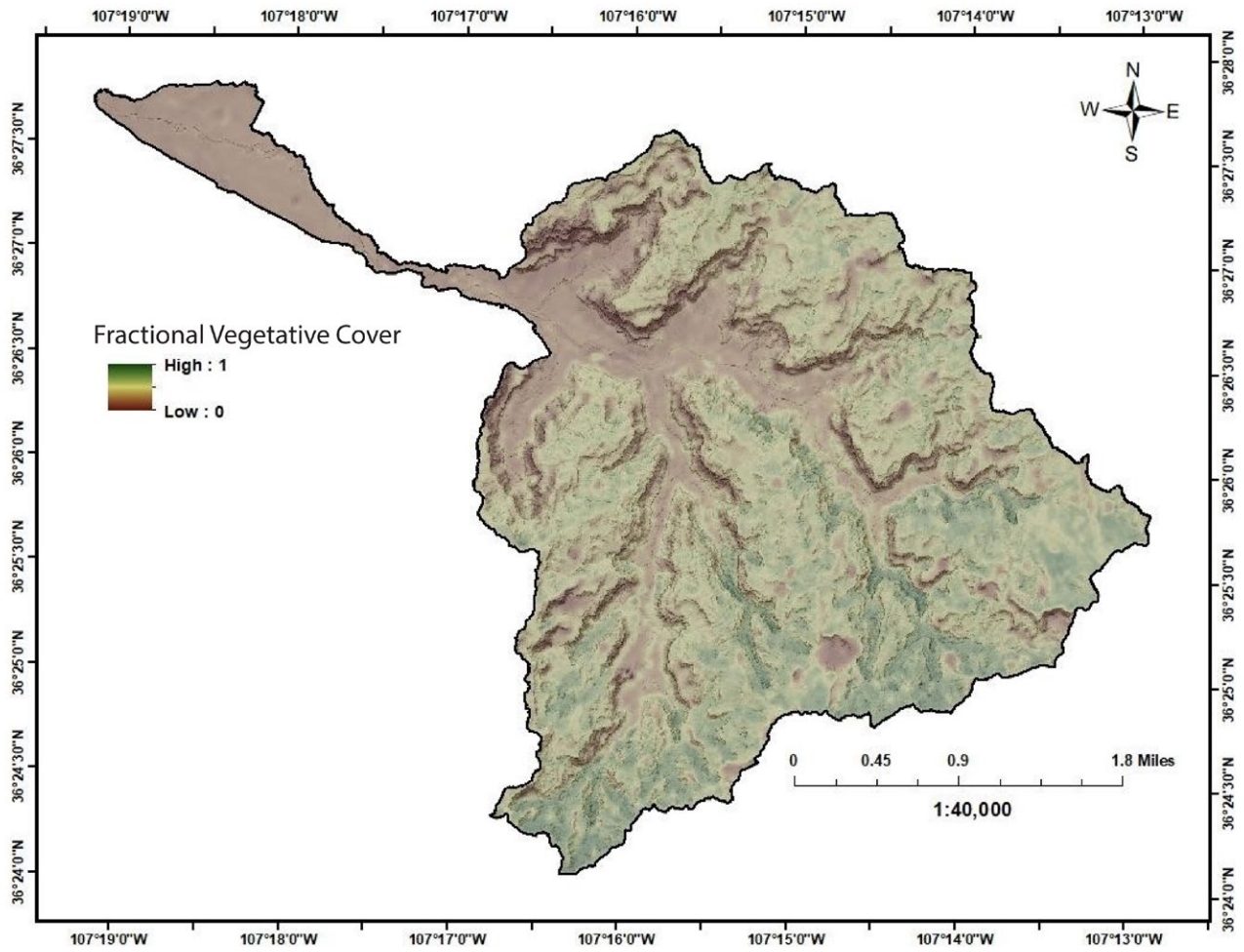
Appendix 2B.7. Site B fractional vegetative cover.
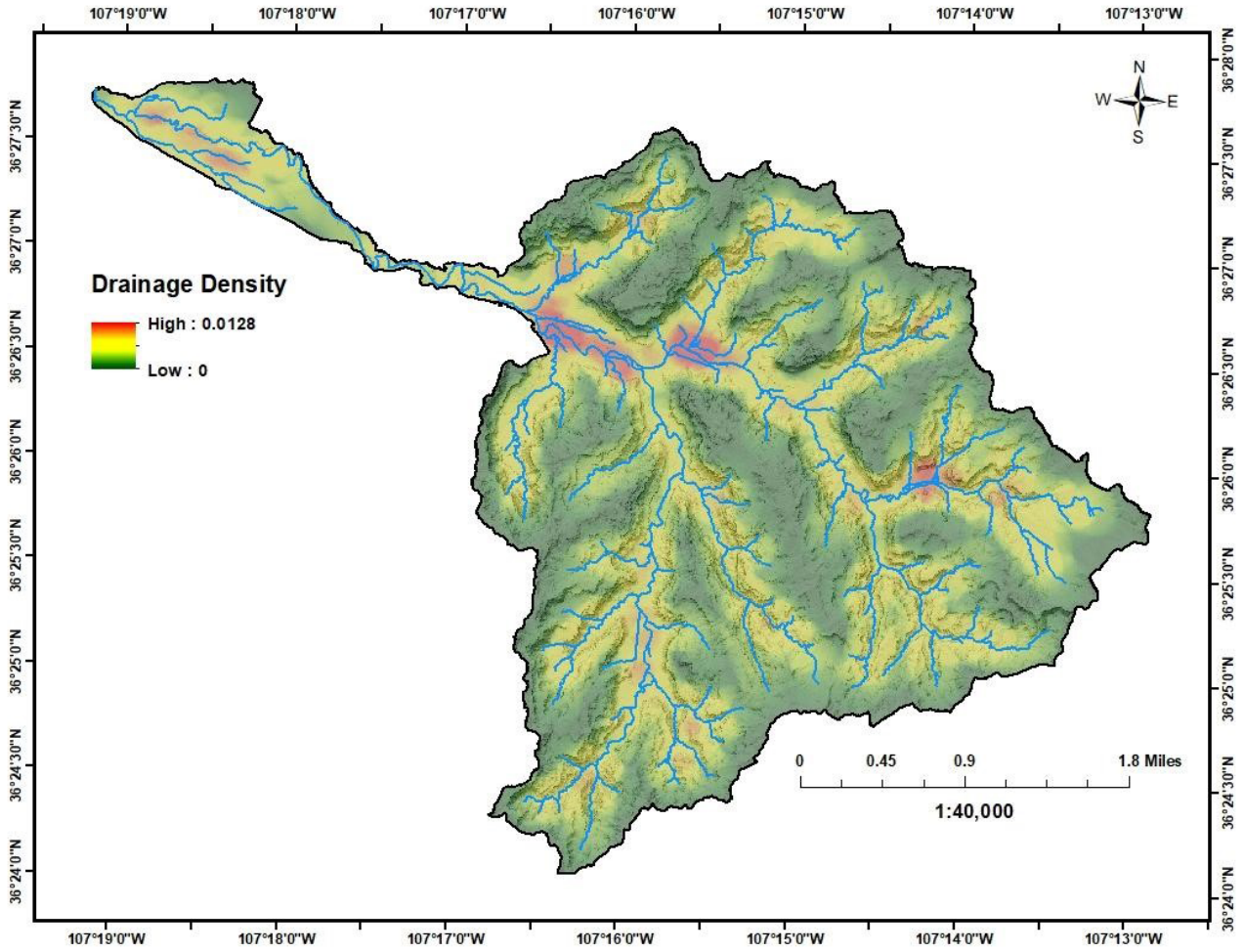
Appendix 2B.8. Site B drainage density.
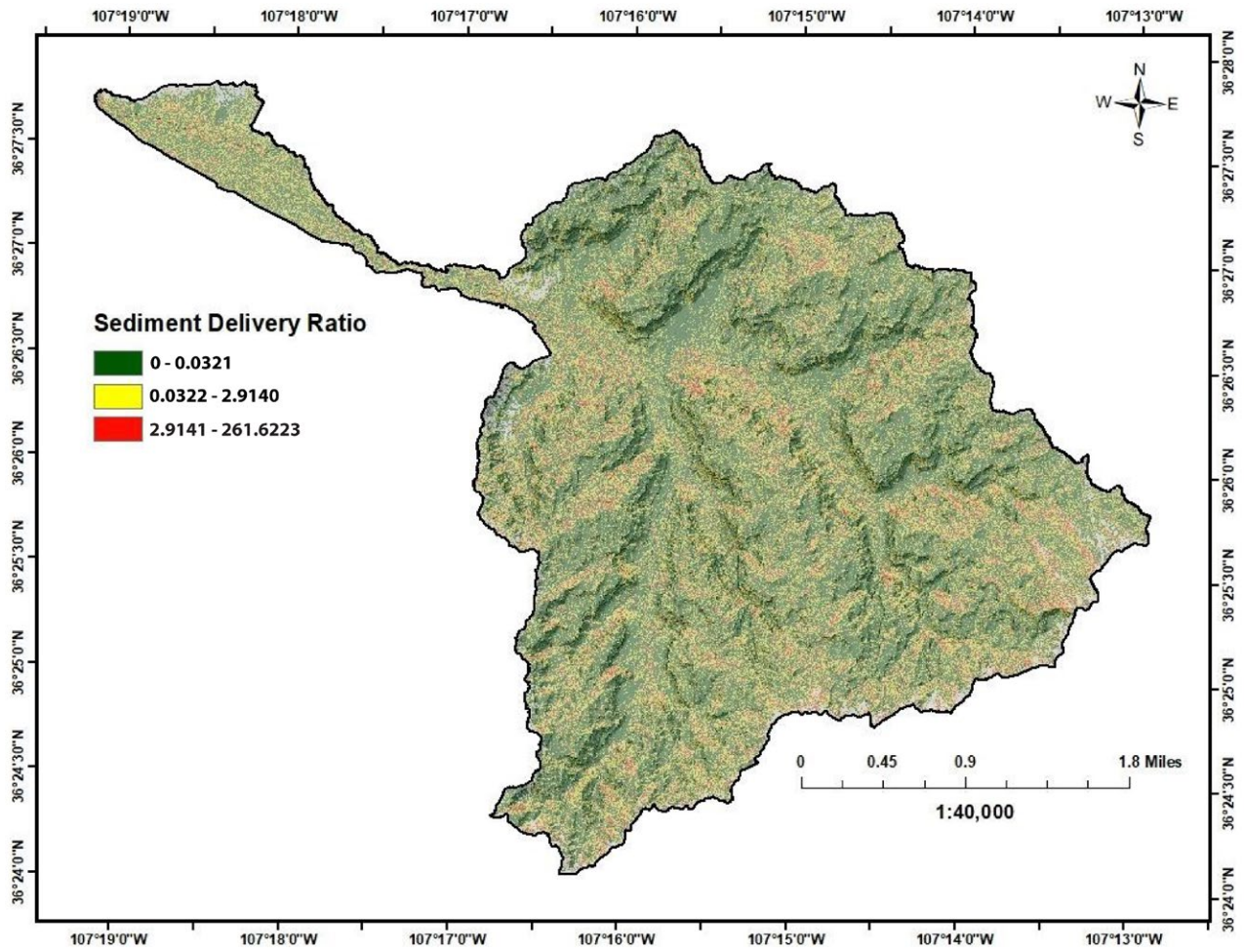
Appendix 2B.9. Site B sediment delivery ratio.
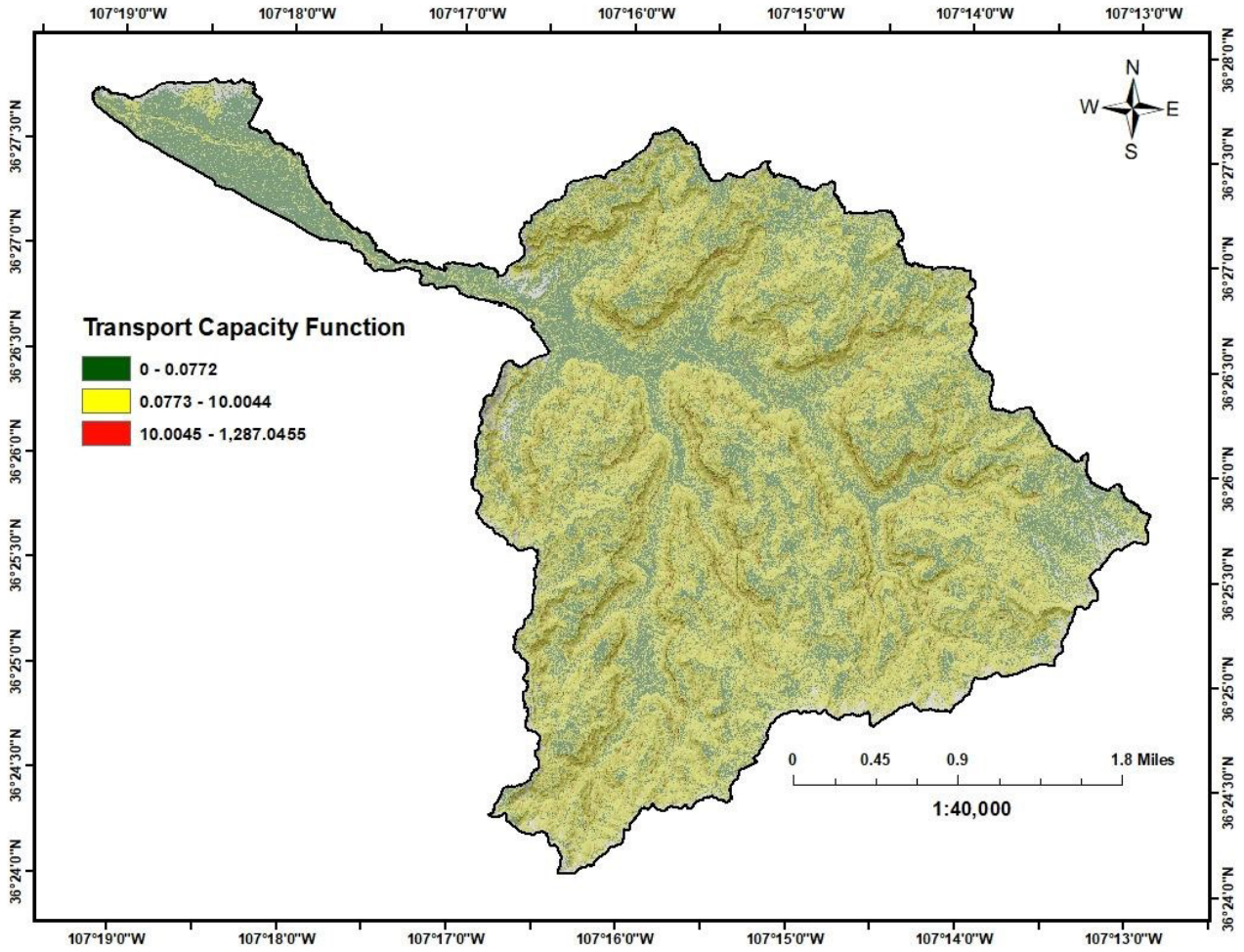
Appendix 2B.10. Site B sediment transport capacity.
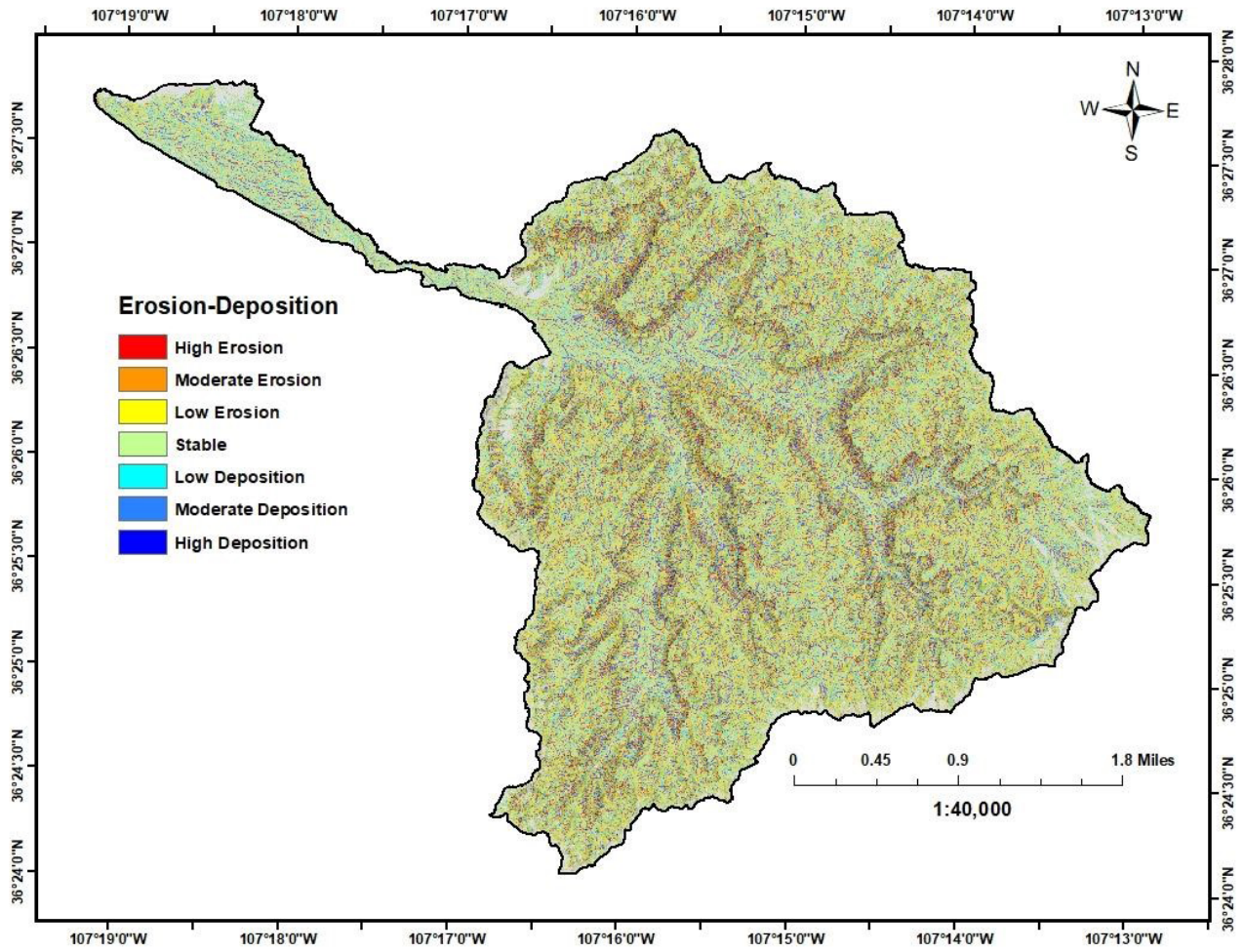
Appendix 2B.11. Site B sediment transport divergence.
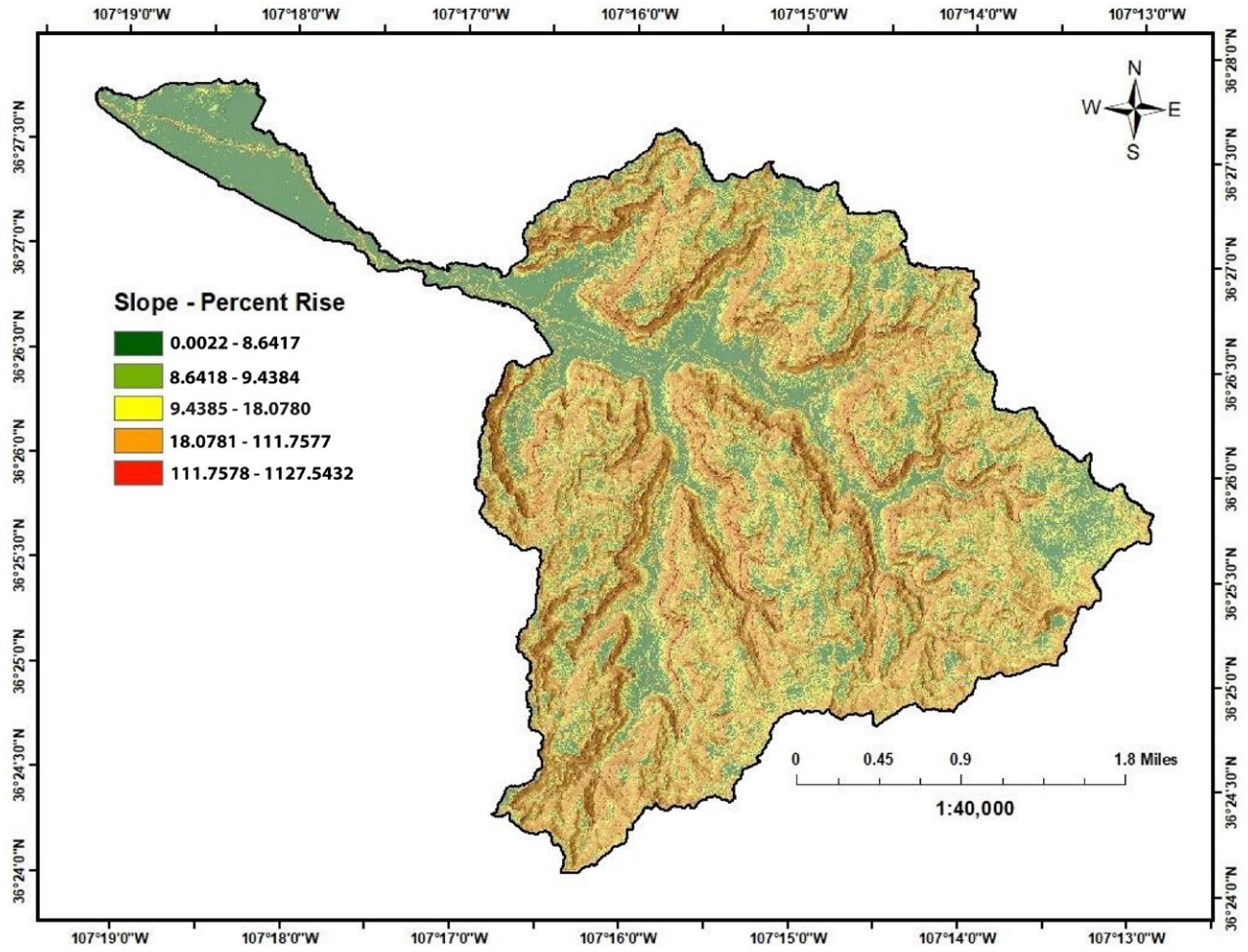
Appendix 2B.12. Site B slope as percent rise.
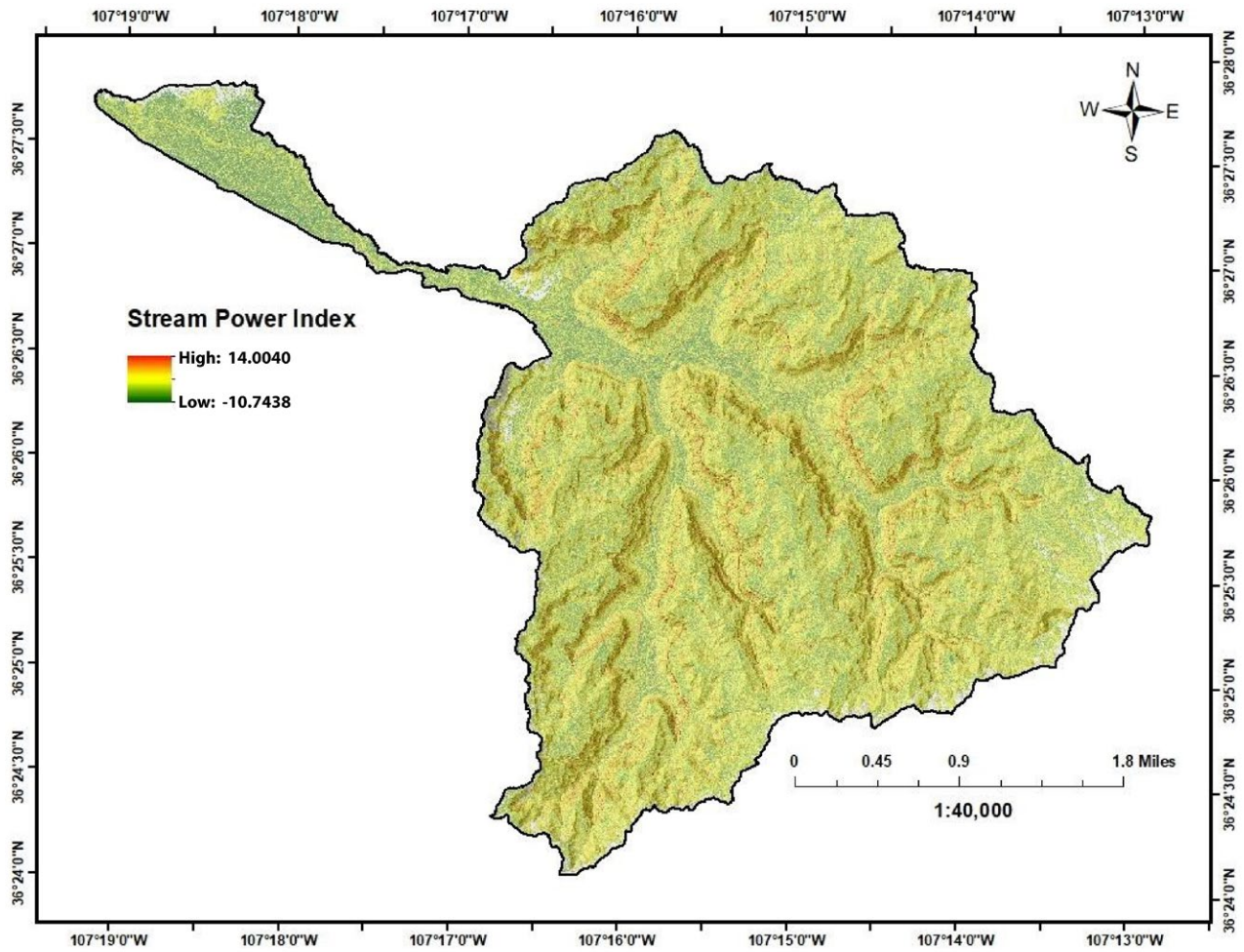
Appendix 2B.13. Site B stream power index.

2C: DERIVED MAPS FOR SITE C

Appendix 2C.1. Site C Google Earth overlay.
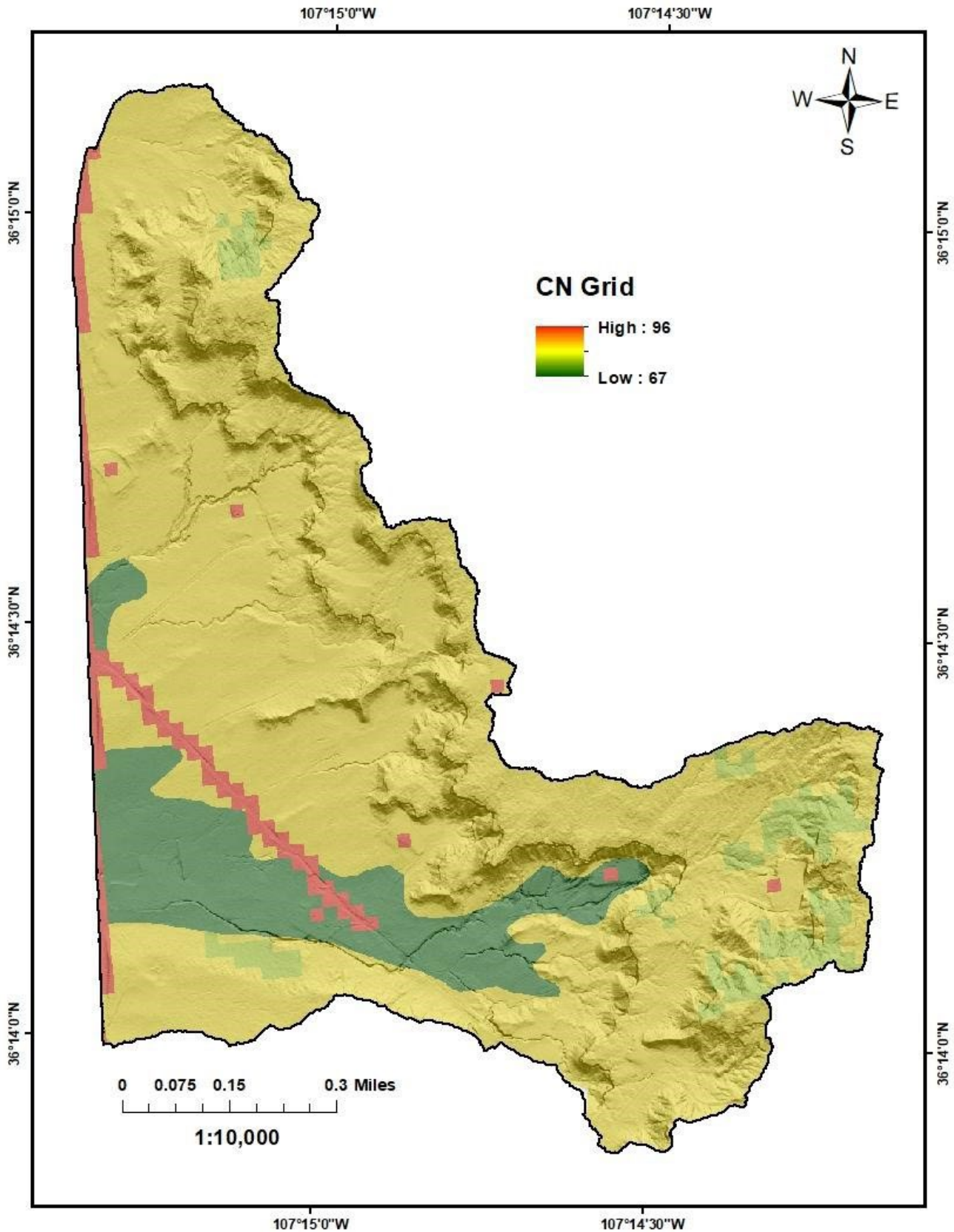
Appendix 2C.2. Site C curve number.
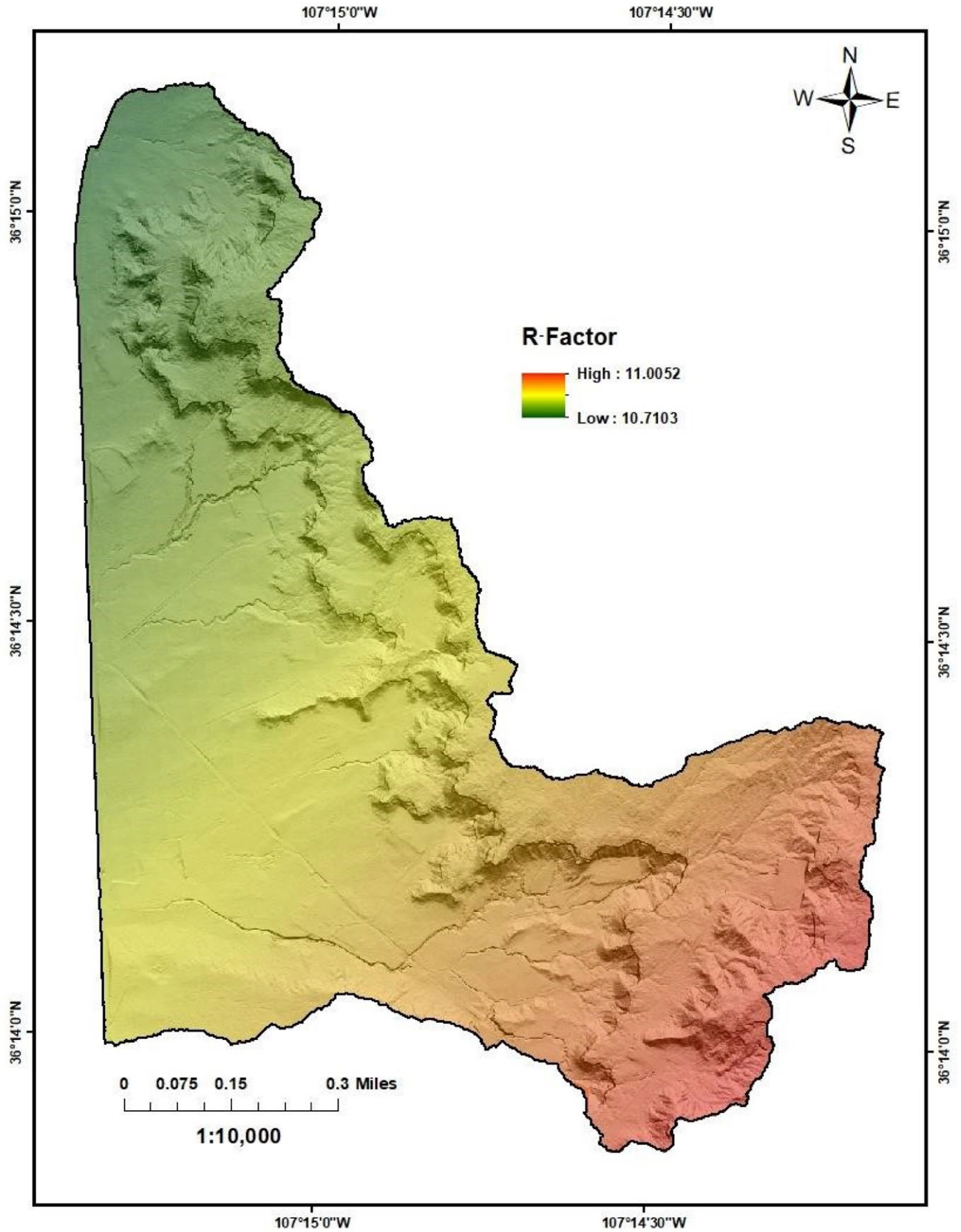
Appendix 2C.3. Site C rainfall erosivity R-factor.
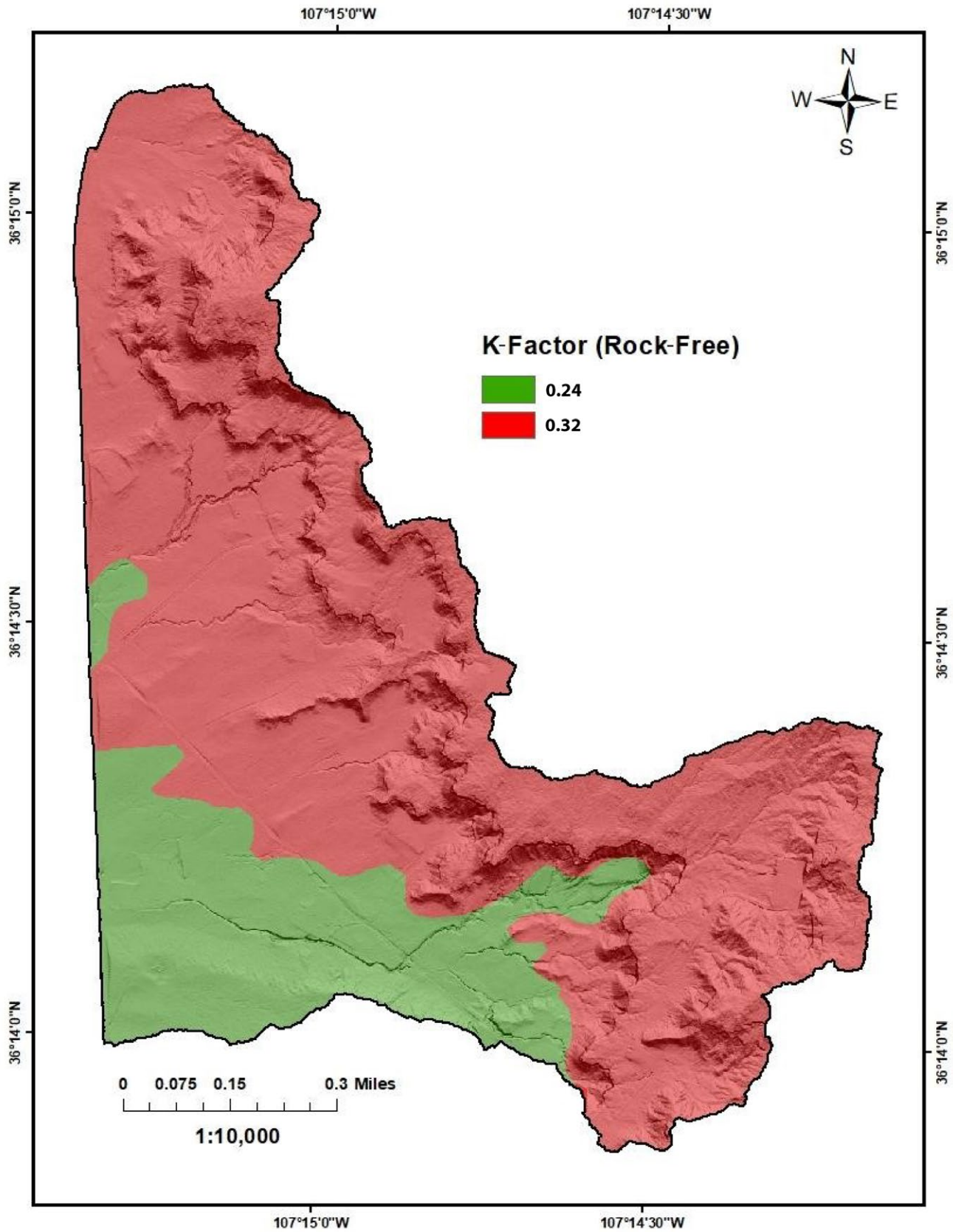
Appendix 2C.4. Site C soil erodibility K-factor.
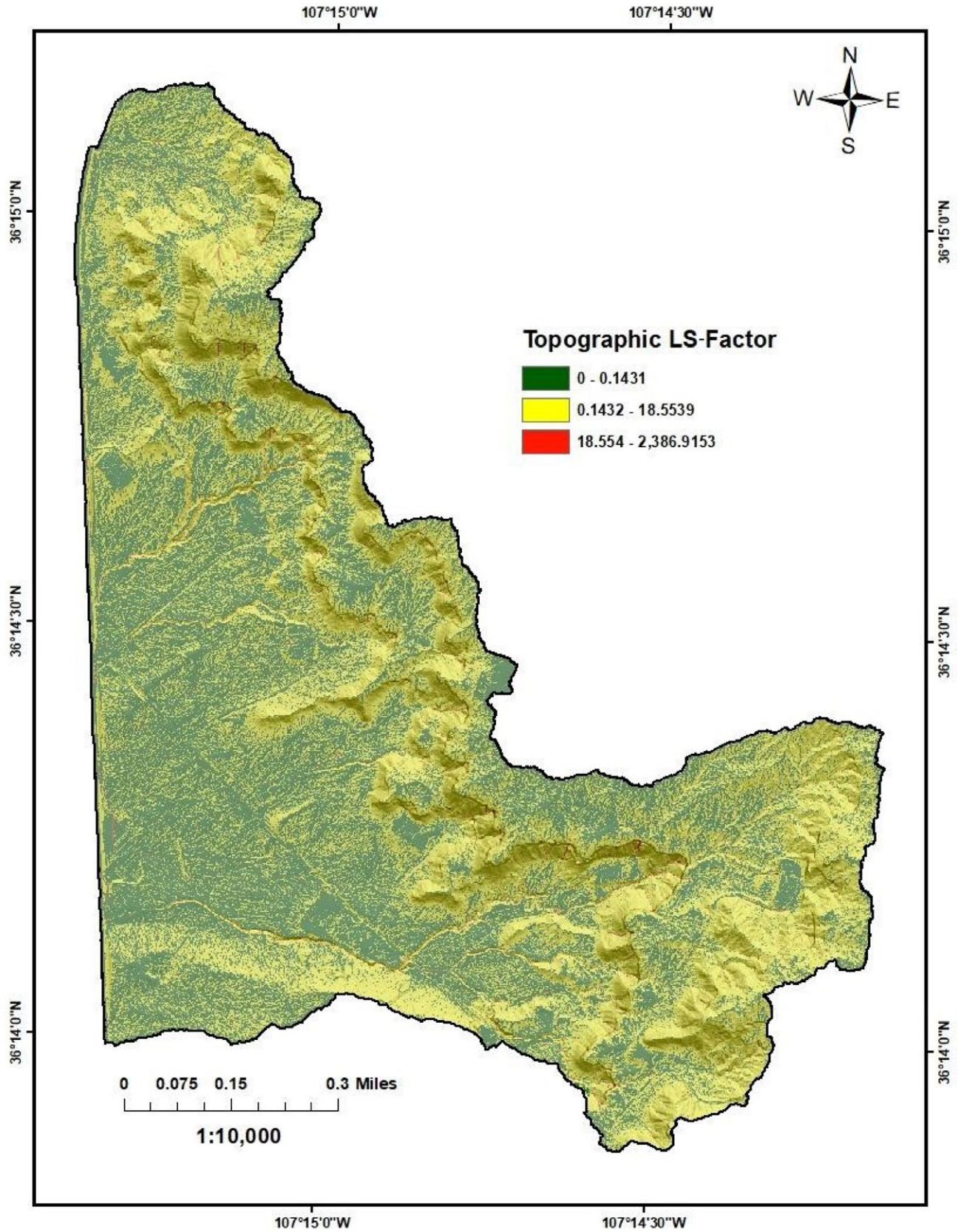
Appendix 2C.5. Site C topographic LS-factor.
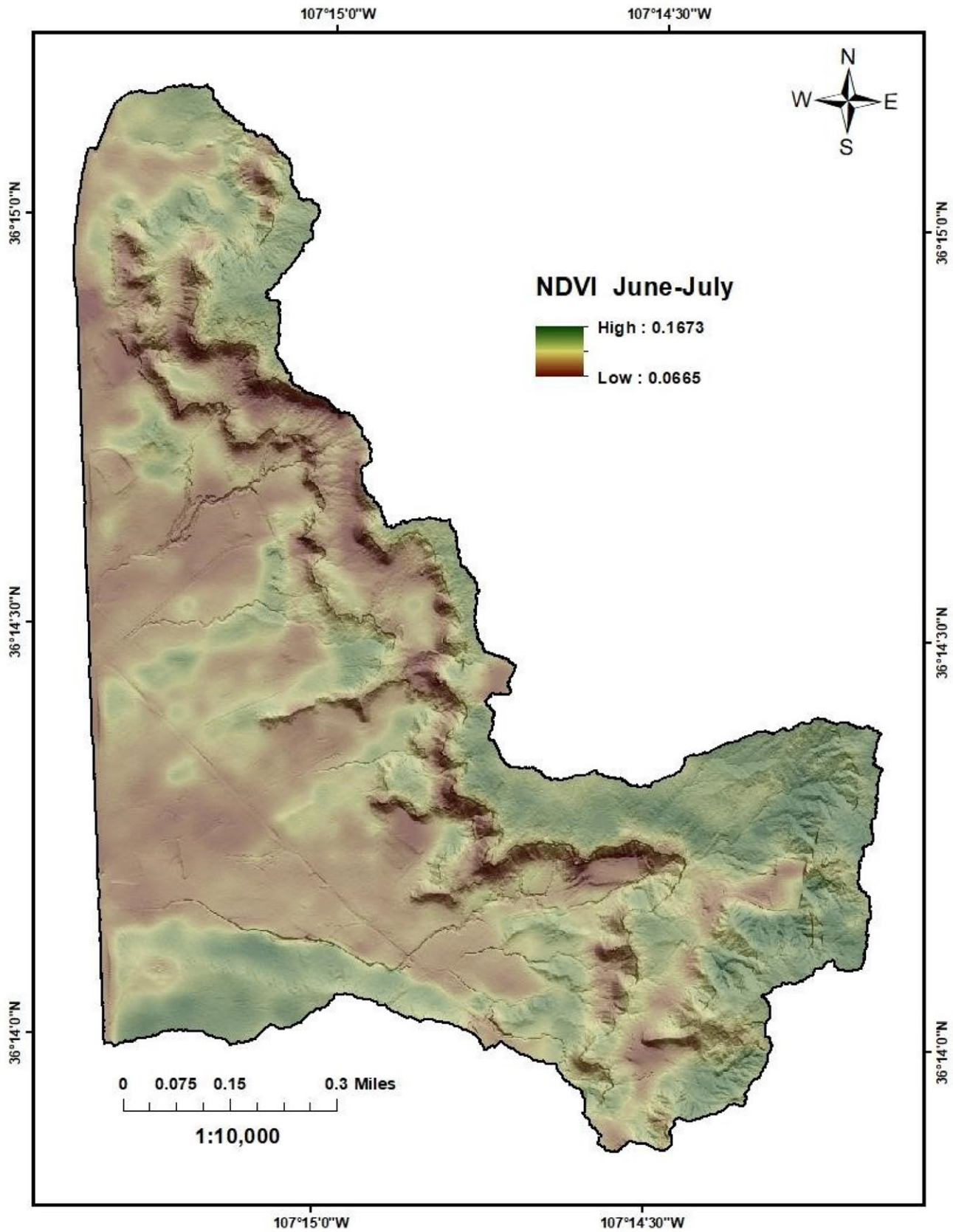
Appendix 2C.6. Site C normalized difference vegetation index.
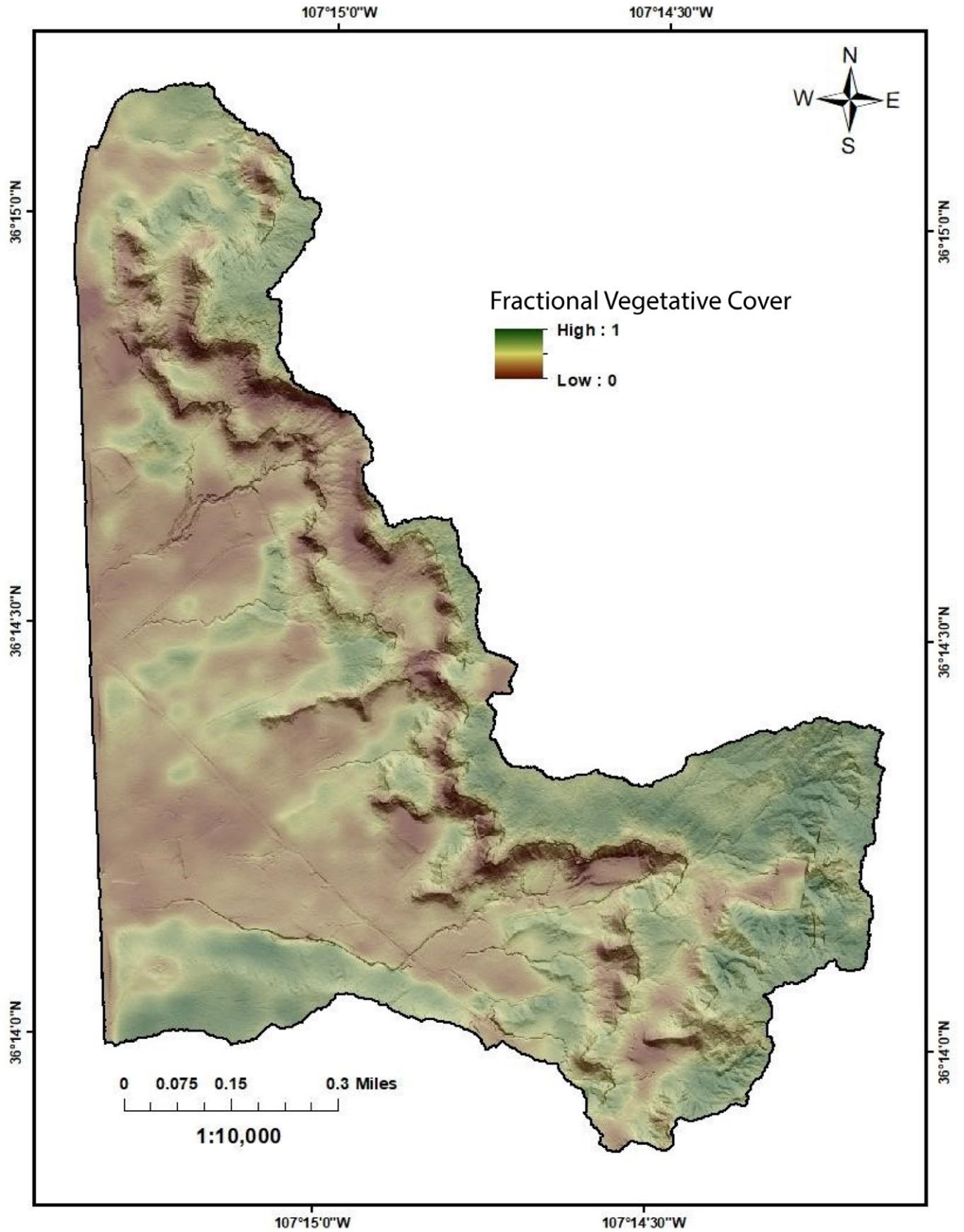
Appendix 2C.7. Site C fractional vegetative cover.
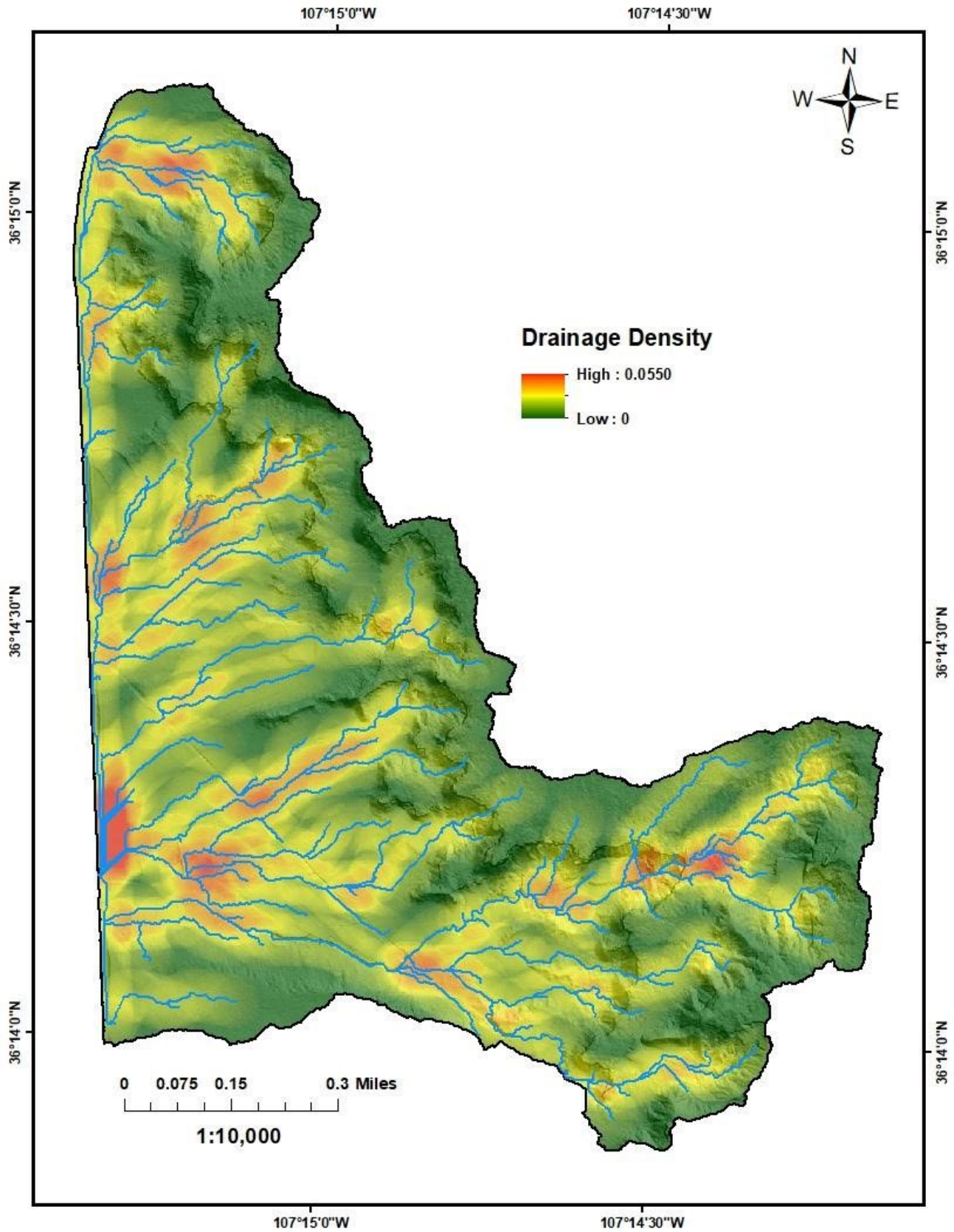
Appendix 2C.8. Site C drainage density.
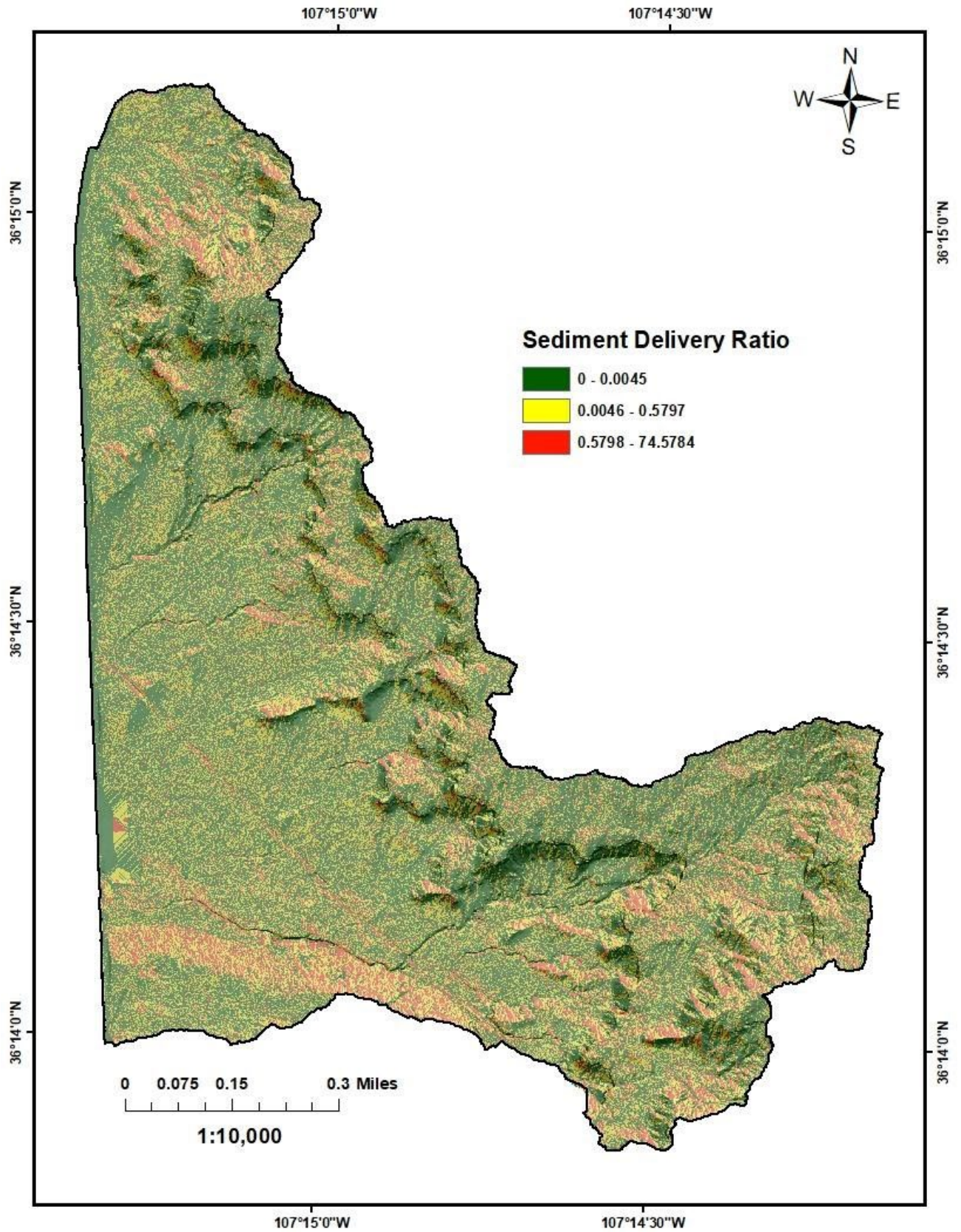
Appendix 2C.9. Site C sediment delivery ratio.
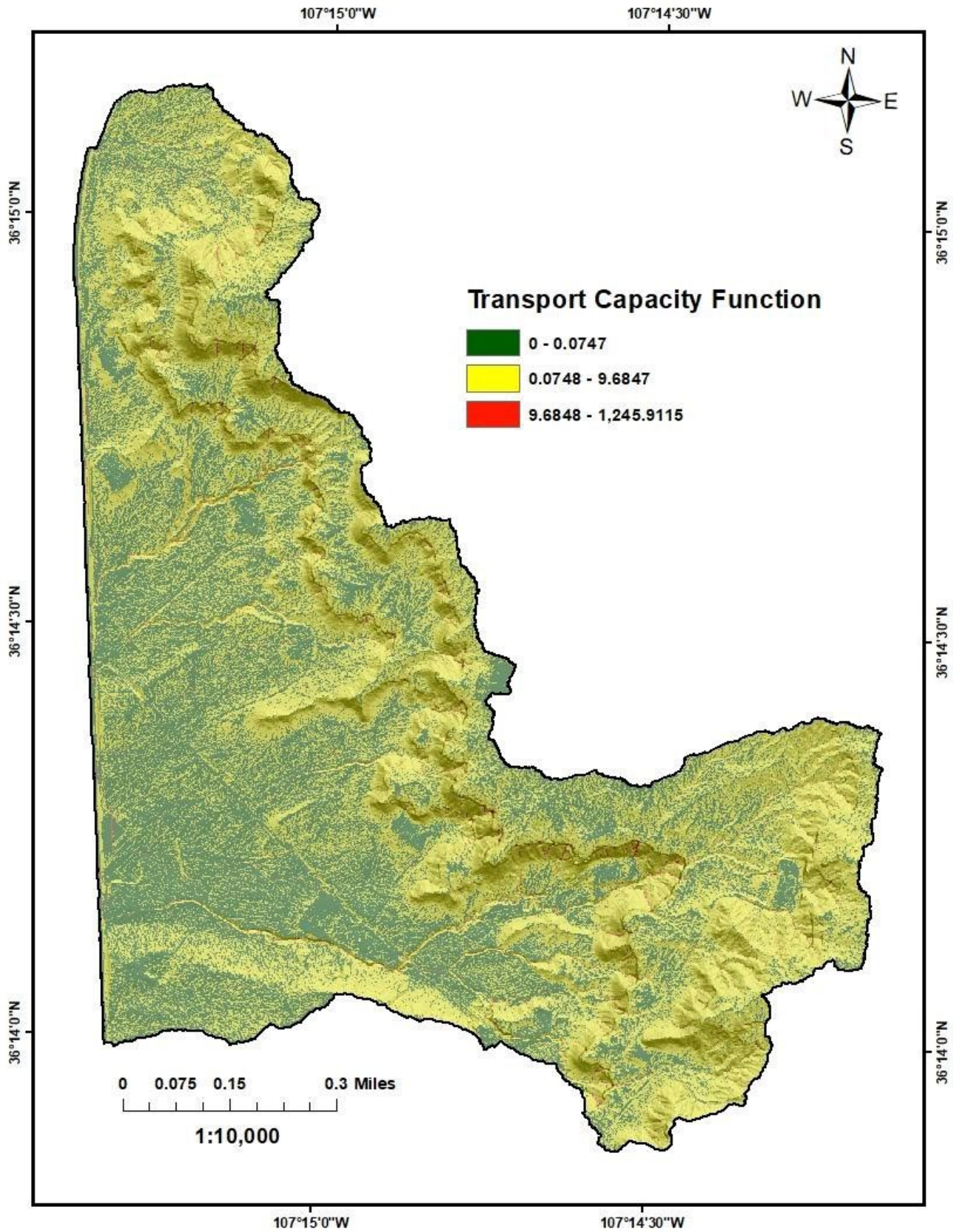
Appendix 2C.10. Site C sediment transport capacity.
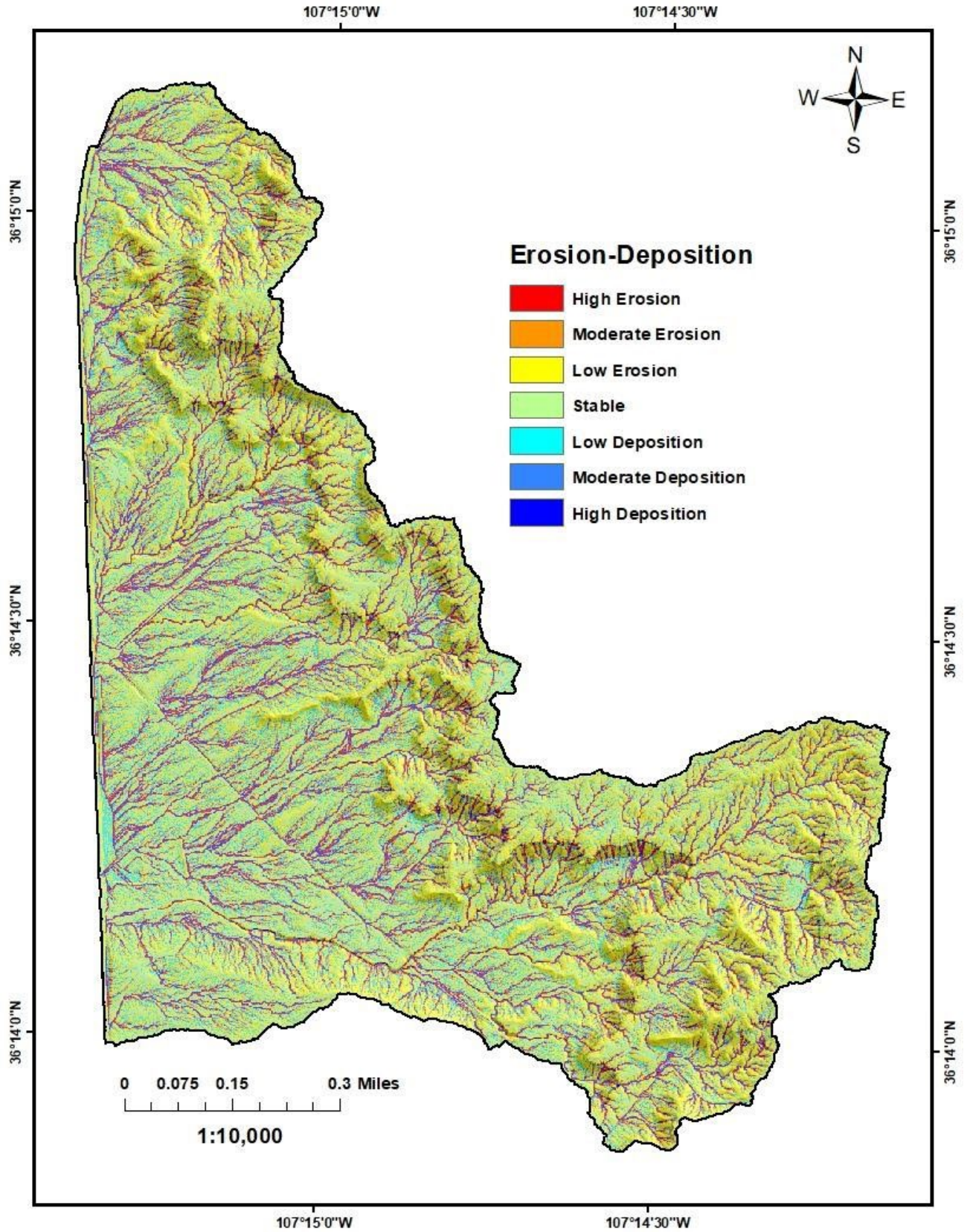
Appendix 2C.11. Site C sediment transport divergence.
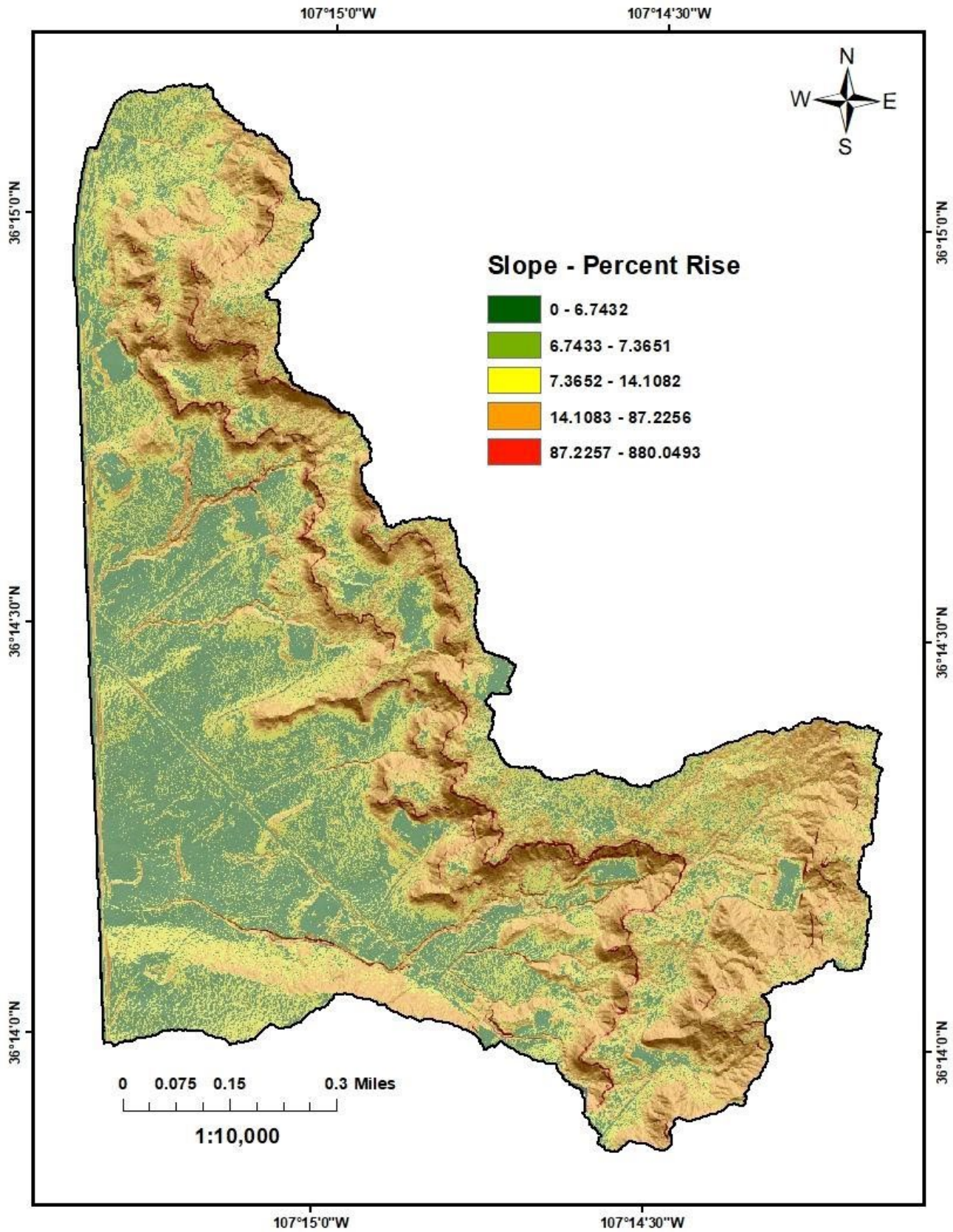
Appendix 2C.12. Site C slope as percent rise.
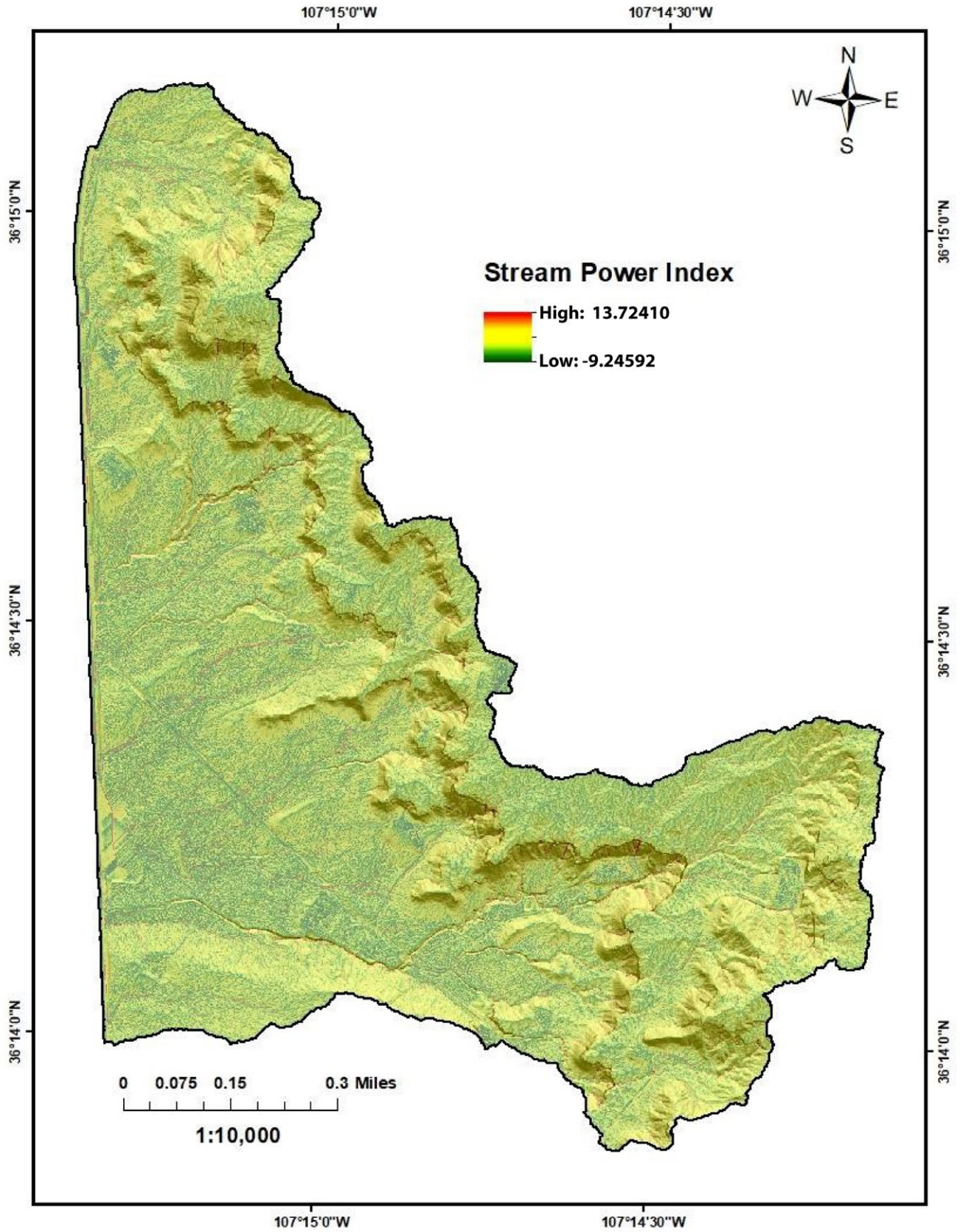
Appendix 2C.13. Site C stream power index.